

Alma Mater Studiorum - University of Bologna

---

Scuola di Dottorato in Ingegneria Civile ed Architettura

Dottorato di Ricerca in Ingegneria Civile ed Ambientale

Tesi di Dottorato

Aeroelastic stability of structures:  
flutter analysis using  
Computational Fluid Dynamics

Settore Concorsuale di Afferenza 08/B2  
Settore Scientifico Disciplinare ICAR/08

Relatore:

Chiar.mo Prof. **Francesco Ubertini**

Candidato:

**Luca Patruno**

Correlatori:

Ill.mo Prof. **Stefano de Miranda**

Ill.mo Prof. **Giuseppe Vairo**

Coordinatore del Dottorato:

Chiar.mo Prof. **Alberto Lamberti**

---

Esame finale Anno 2014 - Ciclo XXVI





"Ecco il mio segreto. È molto semplice:  
non si vede bene che col cuore.  
L'essenziale è invisibile agli occhi."

-Le Petit Prince-

to Jeng Yi.



# Introduzione

A causa della crescente snellezza e leggerezza delle strutture permesse dalle nuove tecniche costruttive e dai materiali innovativi ad alta resistenza, l'effetto del vento sulle strutture è diventato nelle ultime decadi un campo di ricerca di grande importanza in Ingegneria Civile. Nonostante le origini di tale campo di ricerca si possano rintracciare nei primi sviluppi dell'aeronautica all'inizio del ventesimo secolo, la sua applicazione sistematica nel campo delle grandi infrastrutture si può certamente identificare con il collasso del primo ponte di Tacoma il 7 Novembre 1940.

Da quello sfortunato evento, grandi passi avanti sono stati fatti nella comprensione dell'interazione tra vento e strutture, arrivando alla definizione di linee guida e modalità di analisi che hanno provato indubbia efficacia nel prevenire comportamenti indesiderati e il collasso delle strutture.

L'aeroelasticità, ovvero lo studio dell'effetto combinato del vento e della deformabilità delle strutture, è dunque un campo di ricerca relativamente giovane in Ingegneria Civile e rappresenta il suo punto più vicino a quell'insieme di conoscenze normalmente identificate con l'aeronautica.

Sebbene al tempo del collasso del ponte di Tacoma molti dei concetti di base necessari allo studio dei fenomeni aeroelastici fossero già ben noti in campo aeronautico, la loro applicazione al campo dell'Ingegneria Civile ha introdotto numerosi problemi che sono ancora oggi oggetto di ricerca.

Come risultato della scarsità di soluzioni analitiche disponibili in tale settore, le analisi sono in gran parte basate sulla valutazione di coefficienti empirici, normalmente estratti grazie a tests in galleria del vento su modelli in scala ridotta. Le tecniche adottate per estrarre tali parametri, le convenzioni adottate per la loro rappresentazione, i set-up sperimentali e le analisi usate per inferire da questi il comportamento della struttura reale, anche se ben definiti, sono ancora largamente non uniformi nella comunità tecnico-scientifica.

Inoltre, benchè da un punto di vista tecnico molti problemi siano stati affrontati con successo, intendendo che esiste una soluzione tecnica affidabile atta a risolverli, da un punto di vista teorico la loro comprensione è ancora da considerarsi immatura perchè il loro esatto meccanismo di generazione è tuttora non chiaro e l'effetto dei parametri in gioco noto solo in casi particolari testati in condizioni ben definite che non possono essere generalizzate con sicurezza. Tale spiccata variabilità è senza dubbio una conseguenza della grande non-linearità del comportamento meccanico del fluido, specialmente se si considerano corpi tozzi.

Recentemente, grazie al sensibile aumento nella potenza computazionale disponibile, le simulazioni numeriche stanno diventando una valida attività complementare ai tests

in galleria del vento e una alternativa attraente per il futuro.

Grazie alla sua flessibilità, durante gli ultimi anni, l'approccio computazionale ha guadagnato importanza rispetto alle consuete procedure sperimentali. Tuttavia, ancora oggi, tale approccio ai problemi di interazione fluido-struttura non è così largamente utilizzato come si potrebbe pensare. La principale ragione di ciò sono le difficoltà insite nella modellazione numerica dei flussi che si sviluppano attorno ai corpi tozzi, caratterizzati da generazione di turbolenza e marcate instazionarietà.

La turbolenza è un fenomeno caotico, intrinsecamente tridimensionale, caratterizzato dalla presenza di una grande quantità di strutture con scale spaziali e temporali diverse, le quali rendono la sua simulazione numerica praticamente impossibile per applicazioni di tipo tecnico anche con l'utilizzo di HPC supercomputers. Il modo in cui la turbolenza è simulata è la più importante causa di inconsistenze tra i risultati sperimentali e quelli numerici. Nonostante tale problema sia meramente tecnologico, come verrà in seguito spiegato, la sua soluzione pratica non sembra raggiungibile nel prossimo futuro.

In tale contesto, lo scopo di questa tesi è di esplorare i limiti di applicabilità dei modelli numerici attualmente disponibili per la simulazione dell'instabilità aeroelastica dei ponti di grande luce. Nonostante esista un'ampia letteratura riguardante lo studio numerico delle proprietà aerodinamiche degli impalcati da ponte, poco è stato fatto per quanto concerne la validazione di tali modelli su strutture in movimento.

La tesi è organizzata come segue. Per prima cosa si propone una breve introduzione all'aeroelasticità, alla dinamica dei fluidi, alla modellazione della turbolenza e alle tecniche normalmente utilizzate per studiare la stabilità dei ponti. Successivamente, si descrive e si discute nel dettaglio un modello di carico sintetico che generalizza l'approccio di Wagner al caso di corpi moderatamente tozzi. In seguito, si presenta una validazione ampia e sistematica delle performance di simulazioni basate su modelli di turbolenza RANS nel predire le derivate di flutter di semplici prismi rettangolari. Infine, la strategia di simulazione è testata su diverse tipologie di impalcati da ponte discutendo le limitazioni dell'approccio proposto e proponendo linee guida per l'impostazione delle analisi e l'interpretazione dei risultati ottenuti.

# Contents

<b>1</b>	<b>Introduction</b>	<b>11</b>
<b>2</b>	<b>Aeroelasticity</b>	<b>13</b>
2.1	Dimensional analysis . . . . .	13
2.1.1	Time . . . . .	14
2.1.2	Frequency . . . . .	14
2.1.3	Forces and moments . . . . .	15
2.1.4	Reynolds number . . . . .	16
2.2	Streamlined and bluff bodies . . . . .	19
2.3	Vortex shedding and lock-in . . . . .	21
2.4	Torsional divergence . . . . .	22
2.5	Buffeting . . . . .	23
2.6	Galloping . . . . .	24
2.6.1	Other forms of galloping . . . . .	26
2.7	Flutter . . . . .	26
2.8	General remarks on aeroelastic phenomena . . . . .	28
<b>3</b>	<b>Inviscid flows</b>	<b>29</b>
3.1	Conservation laws . . . . .	29
3.2	Mass conservation . . . . .	30
3.3	Momentum conservation . . . . .	31
3.4	Energy conservation . . . . .	32
3.5	Inviscid flows . . . . .	33
3.5.1	Bernoulli's theorem . . . . .	34
3.5.2	Potential flows . . . . .	34
3.6	The thin airfoil . . . . .	40
3.6.1	Static aerodynamic loads on the thin airfoil . . . . .	43
3.6.2	Motion-induced loads on the thin airfoil . . . . .	43
<b>4</b>	<b>Viscous and turbulent flows</b>	<b>47</b>
4.1	Boundary layer . . . . .	48
4.2	Viscosity . . . . .	50
4.3	Momentum conservation for viscous fluids . . . . .	51
4.3.1	Origin of the boundary layer . . . . .	52
4.4	Origin of turbulence . . . . .	53
4.5	Turbulent flows . . . . .	54

4.6	Kolmogorov's energy spectrum . . . . .	56
4.7	Time-averaged Navier-Stokes equations . . . . .	57
4.7.1	Scalar transport equation . . . . .	58
4.8	Turbulence modelling using RANS models . . . . .	59
4.8.1	Prandtl's mixing length . . . . .	59
4.8.2	Two equation models . . . . .	61
4.8.3	Reynolds Stress Models . . . . .	67
4.9	Large Eddies Simulations . . . . .	68
4.10	Scale-Resolving Simulations . . . . .	69
<b>5</b>	<b>Flutter derivatives</b> . . . . .	<b>73</b>
5.1	Introduction . . . . .	74
5.2	Scanlan formulation . . . . .	74
5.3	Flutter derivative estimation . . . . .	76
5.3.1	Forced vibration method . . . . .	77
5.3.2	The free vibration method . . . . .	78
5.4	Computational fluid dynamics estimation . . . . .	82
5.4.1	Combined forced vibration method . . . . .	86
5.5	Critical flutter speed evaluation . . . . .	88
5.5.1	Flutter determinant . . . . .	89
5.5.2	Iterative eigenvalue analysis . . . . .	91
5.5.3	Motion equations integration . . . . .	92
5.6	Fully coupled simulations . . . . .	93
<b>6</b>	<b>The thin airfoil theory and its generalization</b> . . . . .	<b>97</b>
6.1	Introduction . . . . .	98
6.1.1	Motion-induced loads on bridge deck sections . . . . .	100
6.2	A consistent time-domain description . . . . .	102
6.2.1	Time-frequency duality . . . . .	103
6.3	Identification of model parameters . . . . .	105
6.3.1	Asymptotic regimes . . . . .	105
6.3.2	Response to quasi-step motions . . . . .	106
6.3.3	Response to an angular harmonic motion . . . . .	108
6.4	A numerical approach . . . . .	109
6.4.1	The numerical model . . . . .	109
6.4.2	Aerodynamic data evaluation procedure . . . . .	110
6.4.3	Response to vertical motions . . . . .	112
6.5	Numerical results: the FTP case . . . . .	113
6.5.1	Harmonic motions . . . . .	113
6.5.2	Quasi-step motion . . . . .	113
6.5.3	Application of the identification procedure . . . . .	114
6.6	Numerical results: the CBS case . . . . .	116

<b>7</b>	<b>Flutter derivatives extraction: rectangular prisms</b>	<b>123</b>
7.1	Introduction . . . . .	124
7.2	Some comments on aeroelastic forces . . . . .	125
7.3	Simulation approach . . . . .	126
7.3.1	Numerical setup . . . . .	127
7.4	Preliminary numerical analysis . . . . .	128
7.4.1	Comparison of turbulence models on <i>R4</i> . . . . .	128
7.4.2	Calibration of the standard $k - \omega$ on <i>R4</i> . . . . .	129
7.5	Numerical results . . . . .	131
7.5.1	<i>R2</i> . . . . .	131
7.5.2	<i>R3</i> . . . . .	133
7.5.3	<i>R4</i> . . . . .	140
7.5.4	<i>R5</i> , <i>R8</i> and <i>R10</i> . . . . .	144
7.5.5	<i>R12p5</i> , <i>R15</i> and <i>R20</i> . . . . .	150
7.5.6	Critical flutter wind speed evaluation . . . . .	150
7.6	Conclusions on rectangular prisms . . . . .	151
<b>8</b>	<b>Flutter derivatives extraction: bridge decks</b>	<b>159</b>
8.1	Introduction . . . . .	159
8.2	Investigation results . . . . .	161
8.2.1	<i>R8</i> . . . . .	162
8.2.2	Severn . . . . .	164
8.2.3	Gibraltar . . . . .	165
8.2.4	Chongqing . . . . .	167
8.2.5	Tacoma . . . . .	175
8.2.6	Adige . . . . .	180
8.3	Conclusions on bridge decks . . . . .	182
<b>9</b>	<b>Conclusions</b>	<b>187</b>





# Introduction

Thanks to the increasing slenderness and lightness allowed by new construction techniques and materials, the effects of wind on structures became in the last decades a research field of great importance in Civil Engineering. Although its origins date back to the early stages of aeronautics, at the beginning of the 20th century, its systematic application in the infrastructure construction field is more recent and can be certainly related to the famous collapse of the first Tacoma bridge on November the 7th 1940.

Since that unfortunate event, many successful achievements have been accomplished in the comprehension of the interactions between wind and structures, leading to the definition of design guidelines and analyses that proved to be effective in the prevention of undesired behaviours and structural failure.

Aeroelasticity, the study of the combined effect of the wind and the deformability of the structure, is then a relatively recent field of interest in Civil Engineering and represents its closest point to the ensemble of knowledge traditionally framed in the domain of aeronautics.

Although at the time of the Tacoma Bridge failure many of the basic concepts needed to tackle wind loading and wind-structure interaction were already developed and well known in the aeronautical field, their application to Civil Engineering introduced a wide range of new peculiar difficulties which are still under research nowadays.

As a result of the lack of widely applicable analytical developments, the analyses strongly rely on the evaluation of empirical parameters that are usually extracted through wind tunnel tests on reduced scale models. The techniques adopted to extrapolate such parameters from reduced scale tests, their representation conventions, the experimental apparatus and the analyses used to extrapolate the full-scale structure behaviour, although well defined, are still largely non-uniform in the technical and scientific community.

Furthermore, although from a technical point of view many problems are well understood, meaning that a reliable solution exists to predict their effects or avoid their development, from the theoretical point of view, their comprehension can be still considered immature as their exact development mechanism is still unclear and the effect of a variety of parameters known only with respect to particular cases tested under well defined conditions which cannot be generalized with confidence. Such a great variability is indeed a consequence of the high non-linearity of the fluid behaviour especially when

non-aerodynamic bodies are considered.

More recently, thanks to the advances in computers power, the numerical simulation of wind tunnel tests has become a valid complementary activity and an attractive alternative for the future.

Due to its flexibility, during the last years, the computational approach gained importance with respect to the traditional experimental investigation. However, still today, the computational approach to fluid-structure interaction problems is not as widely adopted as it could be expected. The main reason for this lies in the difficulties encountered in the numerical simulation of the turbulent, unsteady flow conditions generally encountered around bluff bodies.

Turbulence is a highly chaotic flow regime, inherently three-dimensional, characterized by the presence of a wide range of length and time scales which make its numerical description almost impossible for technical applications even with modern HPC supercomputers. The way turbulence is accounted for in the computational simulations, represents the main source of discrepancies between the experimental and the simulated results but, although such a problem might appear to be merely technological, as it will be later explained, its practical solution seems still not attainable in the close future.

In this context, the aim of this thesis is to explore the limit of applicability of the available computational methods in the simulation of aerodynamic instability of long span bridges. Although a wide literature exists on the computational characterization of the aerodynamic properties of bridge decks, little has been done to test the performances and reliability of available models in the case of moving structures.

The thesis is organized as follows. Firstly, a synthetic introduction to aeroelasticity, fluid dynamics, turbulence modelling and standard procedures used to assess bridge stability are presented. Then, a synthetic wind loading model, which generalizes the Wagner approach to mildly bluff bodies, is described and discussed in detail. Afterwards, a comprehensive and systematic validation of RANS based simulations performance in predicting flutter derivatives of simple rectangular prisms is presented. Finally, the simulation strategy is tested on bridge deck sections of technical interest highlighting the limitations of the proposed approach and setting guidelines for the simulation strategy and the interpretation of the results.

# Chapter 2

## Aeroelasticity

In this chapter an introduction to the basic concepts of aerodynamics and aeroelasticity is presented.

Dimensional analysis, which played a crucial role in the development of fluid dynamics and aerodynamics, is introduced and applied in order to deduce the main quantities of interest. Finally, the most common aerodynamic phenomena and aeroelastic instabilities encountered in structure wind loading are briefly described.

### Contents

---

<b>2.1</b>	<b>Dimensional analysis</b>	<b>13</b>
2.1.1	Time	14
2.1.2	Frequency	14
2.1.3	Forces and moments	15
2.1.4	Reynolds number	16
<b>2.2</b>	<b>Streamlined and bluff bodies</b>	<b>19</b>
<b>2.3</b>	<b>Vortex shedding and lock-in</b>	<b>21</b>
<b>2.4</b>	<b>Torsional divergence</b>	<b>22</b>
<b>2.5</b>	<b>Buffeting</b>	<b>23</b>
<b>2.6</b>	<b>Galloping</b>	<b>24</b>
2.6.1	Other forms of galloping	26
<b>2.7</b>	<b>Flutter</b>	<b>26</b>
<b>2.8</b>	<b>General remarks on aeroelastic phenomena</b>	<b>28</b>

---

### 2.1 Dimensional analysis

Dimensional analysis has probably represented one of the most powerful analytical tool in the development of fluid dynamics and aeroelasticity. In this section, the quantities involved in external aerodynamics and aeroelasticity are introduced and dimensional analysis is used in order to identify the physically meaningful non-dimensional groups

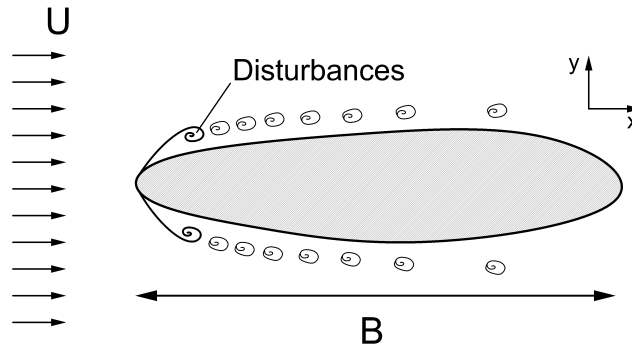


Figure 2.1: Main quantities and reference system presentation.

involved in commonly observed phenomena. Such a presentation choice is not insubstantial. Indeed, the physical insight given by the correct identification of the scales of the problem plays a crucial role in the definition of clearly readable and explicative relations and represents an indispensable background in order to be able to identify the dominant effects and study the influence of the problem parameters on the observed results.

Consider a body of characteristic dimension  $B$  immersed in a Newtonian incompressible fluid, flowing with uniform velocity  $U$ . The fluid has density  $\rho$  and viscosity  $\mu$ . Lets also consider that a periodic phenomenon is characterizing the system dynamics and that the period is defined by its frequency  $Fq$  (see Fig. 2.1).

### 2.1.1 Time

Lets now consider a disturbance that is created at the upper stream part of the body and that is transported by the flow downstream. If the disturbance is considered to move together with the flow, the time needed to move from the upper stream point to the extreme point downstream, indicated as  $S$ , can be calculated as:

$$S = B/U. \quad (2.1)$$

Such an amount of time can be considered as a characteristic time scale of the problem and can be assumed as an elementary time unit. Thanks to the previous considerations a non-dimensional time,  $s$ , can be defined as follows:

$$s = t/S = t \frac{U}{B}, \quad (2.2)$$

where  $t$  is the physical time. Such a non-dimensional time is representative of all the phenomena observed in the fluid flow that involve transport of information downstream.

### 2.1.2 Frequency

Once the non-dimensional time has been defined, the definition of a scale for frequencies is automatic. In fact, the dimensional frequency,  $Fq$ , can be transformed in the non-dimensional frequency,  $St$ , by calculating its equivalence in the non-dimensional time as

follows:

$$St = Fq \frac{B}{U}. \quad (2.3)$$

Such a non-dimensional frequency, especially when referred to the vortex shedding phenomenon, that will be later introduced, is known as Strouhal number after the physicist Vincent Strouhal.

When the frequency of the studied periodic phenomenon is imposed by external factors so that it is not directly related to the downstream transport of information in the fluid (which is the case of structures vibrating at their eigenfrequencies), the same approach can be adopted on dimensional ground. In this case, the time scale can be more closely related to the periodic event, so that a scale on the wind velocity is introduced, rather than a scale on the frequency:

$$U_{red} = \frac{U}{B \cdot Fq} = \frac{1}{St}, \quad (2.4)$$

where the non-dimensional velocity  $U_{red}$  takes the name of reduced velocity. In both cases it is of interest to define a non-dimensional angular velocity,  $k$ , as:

$$k = 2\pi St = 2\pi \frac{Fq \cdot B}{U}. \quad (2.5)$$

It is straightforward to verify that the following relation between  $U_{red}$  and  $k$  holds:

$$U_{red} = \frac{2\pi}{k}. \quad (2.6)$$

### 2.1.3 Forces and moments

It is common experience that a body immersed in a fluid flow experiences forces,  $F$ , which are called aerodynamic. On pure dimensional ground it is possible to state that:

$$F \propto \rho U^2 B^2, \quad (2.7)$$

so defining a scale for the measured forces.

Anticipating the result of the Bernoulli's theorem, the dimensional forces,  $F_j$ , can be written in terms of non-dimensional ones,  $C_j$ , as follows:

$$F_j = \frac{1}{2} \rho B^2 U^2 C_j, \quad (2.8)$$

where  $j = x, y, z$ . In the case of two dimensional flows, the forces per unit length read:

$$F_j = \frac{1}{2} \rho B U^2 C_j. \quad (2.9)$$

If moments are considered, analogous expressions can be found, that in the three-dimensional case, read:

$$M_j = \frac{1}{2} \rho B^3 U^2 C_j, \quad (2.10)$$

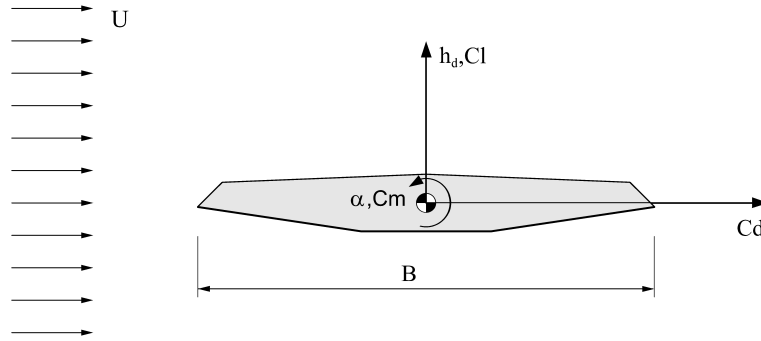


Figure 2.2: Reference system conventions.

while in two dimensions per unit length:

$$M_j = \frac{1}{2} \rho B^2 U^2 C_j. \quad (2.11)$$

In the following, if not differently specified, two dimensional cases will be considered and the following notation adopted:

$$D = \frac{1}{2} \rho B U^2 C_d, \quad L = \frac{1}{2} \rho B U^2 C_l, \quad M = \frac{1}{2} \rho B^2 U^2 C_m, \quad (2.12)$$

where, per unit length,  $D$  is the drag force,  $L$  the lift force and  $M$  the pitching moment while  $C_d$ ,  $C_l$  and  $C_m$  are the non-dimensional drag, lift and pitching moment coefficients, respectively. In the following such coefficients are assumed to be calculated in the global reference system (meaning that the reference system is not affected by the body motion) and  $D$  represents the force in the along flow direction while  $L$  represents the force in the cross flow direction as reported in Fig. 2.2.

In general, aerodynamic forces can be divided into four main contributions: time averaged values, vortex shedding induced contributions, aeroelastic effects, due to the body motion, and buffeting, due to incoming turbulence. It is already important to notice that, such distinction, is valid only if the aforementioned contributions are well decoupled in frequency so that their interaction can be neglected.

#### 2.1.4 Reynolds number

Up to this point the viscosity of the fluid, which is a constitutive parameter that relates the viscous stress,  $\tau$ , to the strain rate in the flow, has never been introduced in the described non-dimensional quantities. According to Fig. 2.3, for a Newtonian fluid, by definition, it is possible to write:

$$\tau = \mu \frac{\partial u}{\partial y}, \quad (2.13)$$

where  $u$  is the scalar velocity that, in this case, is oriented in the  $x$  direction. If the previously introduced reference length scale,  $B$ , and velocity scale,  $U$ , are introduced,

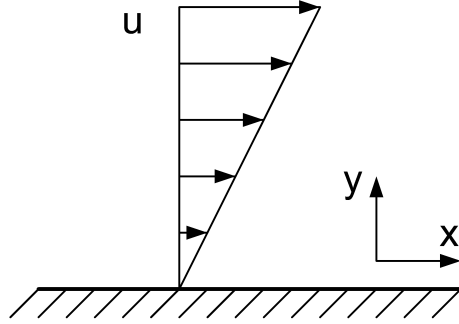


Figure 2.3: Simplified sketch of the flow velocity profile close to a solid wall.

on dimensional ground, it is obtained that:

$$\tau \propto \mu \frac{U}{B}. \quad (2.14)$$

It is of interest to calculate the relative importance of the inertial stresses,  $\sigma$ , with respect to the viscous ones. Still on dimensional ground, the inertial stresses can be assumed to be proportional to:

$$\sigma \propto \rho U^2, \quad (2.15)$$

so that it is possible to write their ratio, which is called Reynolds number,  $Re$ , as:

$$Re = \frac{\rho U B}{\mu}. \quad (2.16)$$

Such a ratio is of fundamental importance in fluid dynamics because the topology of the flow field is deeply affected by its value. In particular, let's consider a cylinder of diameter  $B$  immersed in a two dimensional flow.

For extremely low  $Re$  (see Fig. 2.4 (a)) the flow is regular. A steady-state solution is reached and the streamlines are smoothly deviated by the presence of the cylinder. Increasing the  $Re$  number, the streamlines detach from the rear of the cylinder and two vortices are formed downstream as depicted in Fig. 2.4 (b). When the  $Re$  number reaches approximately  $1.0E2$  the vortices are regularly shed and, while they are transported downstream, their shape is stretched by the velocity gradients present in the mean flow. If the  $Re$  number is further increased (Fig. 2.4 (d)), the wake becomes chaotic and narrower. The shed vortices are characterized by large and small scales distortions while the flow upstream the detachment point is still unaffected by the small scales. At some value in the range  $3.0E5 < Re < 3.5E6$  the transition to a chaotic flow is completed (see Fig. 2.4 (e)): the vortices in the wake assume a chaotic nature, high frequency oscillations of the flow field are observed also upstream the separation point and the drag force is reduced due to the migration of the separation point downstream. Further increasing the  $Re$  number (see Fig. 2.4 (f)), periodic shedding of medium size vortices is observed and the flow is mainly characterized by small scales with high frequency fluctuations.



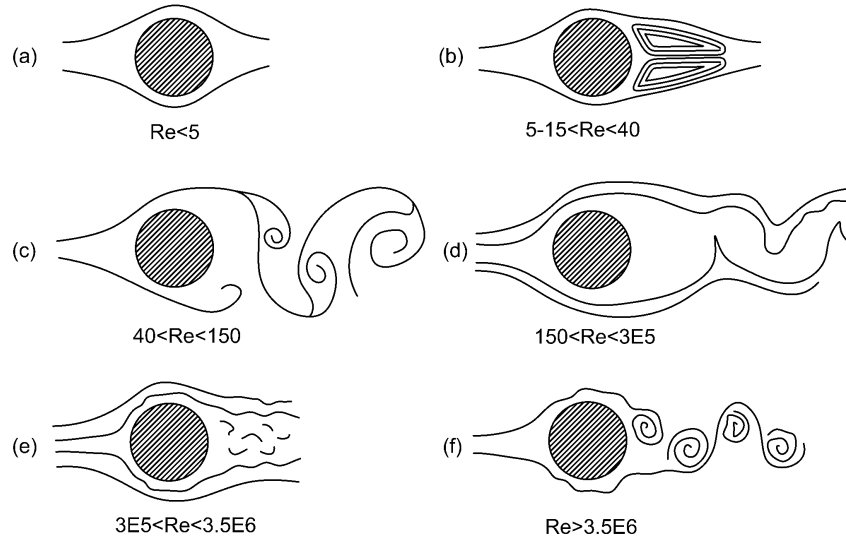


Figure 2.4: Evolution of the vortex shedding around a circular cylinder with the  $Re$  number.

Considering Fig. 2.4 and the graph presented in Fig. 2.5 (b), it is possible to link the topology of the flow to the evolution of the drag coefficient. In particular, Fig. 2.4 (a)-(c) are defined as subcritical conditions and in this  $Re$  range the drag coefficient can be assumed to be approximately constant. Sketch (d) is characteristic of the critical regime: a sharp decrease of the drag is observed which is known as *drag crisis*. As already stated, this condition is characterized by a downstream migration of the detachment point so that an increase in the pressure on the downstream part of the cylinder is observed. Then, a slow increase in the drag force is observed associated to flow fields of the type outlined in Fig. (e) and (f) which characterize the transcritical condition.

A detailed description of the vortex shedding phenomenon in the case of the cylinder is beyond the aim of this thesis (a comprehensive description of the phenomenon can be found in [3]) and is still an active research topic. In this context, it is sufficient to highlight that the  $Re$  number is a fundamental parameter in the characterization of the fluid flow and largely affects its organization.

In general, immersed bodies that do not present natural detachments points (sharp corners) show an accentuated variability of the flow topology with  $Re$ . This is because the detachment point is defined by the local stability of the boundary layer which is defined by the equilibrium between inertial forces, viscous forces and the generation of wall turbulence. Although the circular cylinder can be considered an extremely complex case, every shape undergoes the same evolution of the flow with respect to the  $Re$  number [4] even if the result might be not as apparent as the presented one and some

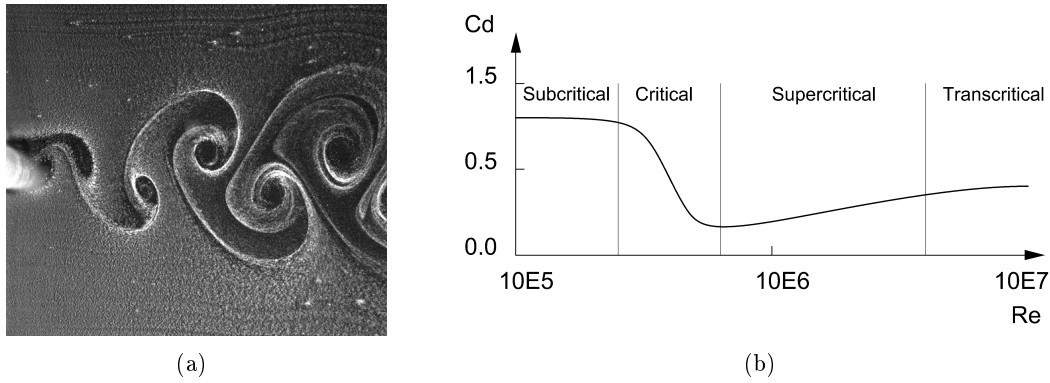


Figure 2.5: Laminar vortex shedding [1], (a), and drag evolution with  $Re$  number, (b).

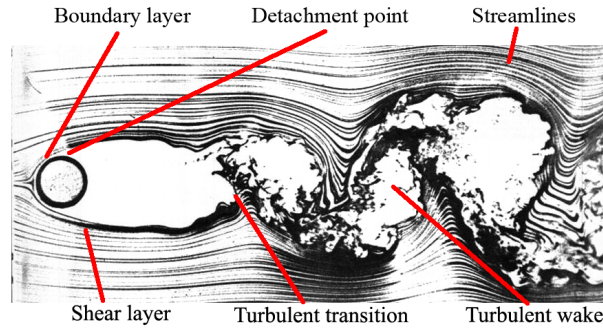


Figure 2.6: Structure of the flow field around a circular cylinder [2] ( $Re = 1.0E5$ ).

stages in the evolution might not occur.

At this point, it is useful to highlight a manifest contradiction in what has been presented until now: on the one hand it has been stated that for high  $Re$  numbers, which is always the case in applications encountered in structure aerodynamics, inertial forces are preponderant so that viscous forces can be disregarded. On the other side, it has been said that the flow topology is deeply affected by the  $Re$  number which has been derived as the ratio between inertial and viscous forces. The problem lies in the fact that, a zone of the flow exists in the immediate surroundings of the immersed body, where the length scales previously defined (based on the body dimensions), are not representative of the mechanisms that locally affect the flow. This zone is called boundary layer and will be introduced in Sec. 4.1. Right now, it is sufficient to recognize that, although globally the flow can be often considered as lead by inertial forces, locally this is often not the case and such local effects can deeply characterize the global topology of the flow.

## 2.2 Streamlined and bluff bodies

It is now important to introduce the distinction between streamlined and bluff bodies. As it can be seen in Fig. 2.7 (a), streamlined bodies are characterized by the fact that the

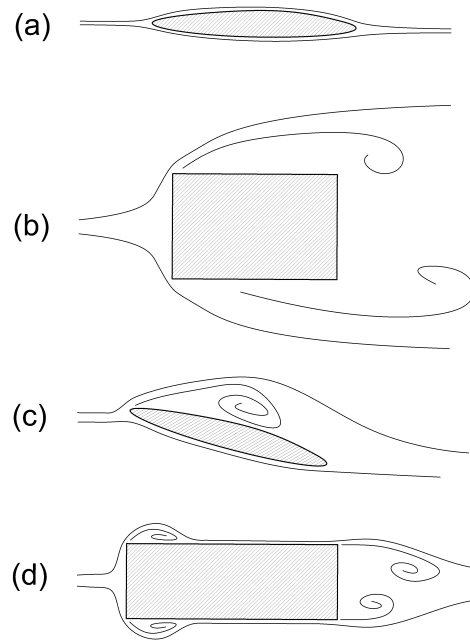


Figure 2.7: Streamlined body (a), bluff body (b), flow detachment due to the body orientation (c), reattached flow (d).

flow streamlines are adherent to the solid boundaries. If this is the case, the drag force is small and the presence of the body distorts the flow field only in its proximity. On the contrary, bluff bodies are characterized by large flow separations (Fig. 2.7 (b)). The drag force is considerable and the disturbances produced by the body are transported downstream in the wake. Although the distinction between the two is often apparent, it is important to remind that a streamlined body can easily behave as a bluff one if its angle of incidence with respect to the flow is changed. This is the case of wings when the stall angle is reached as depicted in Fig. 2.7 (c) (the stall angle also depends on the  $Re$  number). Finally, bodies that show multiple detachments and reattachments, whose position can be a function of  $Re$ , exist (see Fig. 2.7 (d)) and this is usually the case for modern bridge deck sections.

The presence of a well defined boundary layer is essential in order to derive analytical solutions able to describe the flow. As shown in subsequent chapters, when bluff bodies are considered, such analytical solutions still represent an extremely useful reference in order to interpret the fluid behaviour but their direct applicability is strongly limited by lack of correspondence between the observed flow fields and the introduced hypotheses. In this context, the importance of experiments in wind tunnel and numerical simulations assume a key role in the evaluation of empirical parameters used to describe the fluid

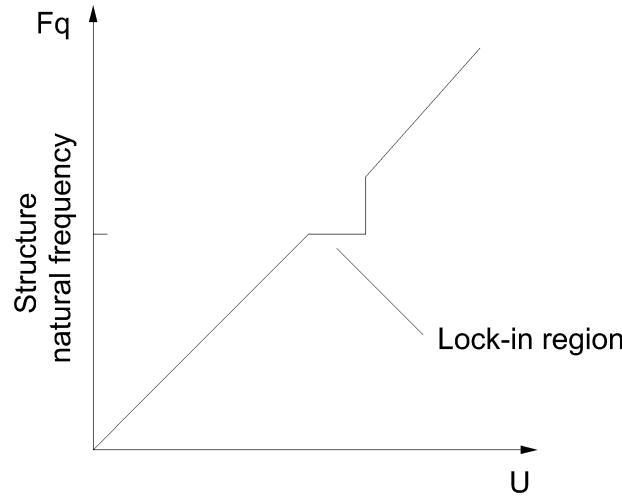


Figure 2.8: Evolution of shedding frequency with velocity and lock-in condition.

flow and its effect on immersed structures.

### 2.3 Vortex shedding and lock-in

As introduced in Sec. 2.1.4, when a body is immersed in a fluid flow, vortices are created in correspondence of solid boundaries and are regularly shed and transported downstream. The non-dimensional time is the appropriate time scale for such phenomenon so that the shedding frequency can be uniquely identified in the non-dimensional time taking the name of Strouhal number,  $St$ . Such a non-dimensional shedding frequency is a property of the immersed body shape and  $Re$ . If the dependence with  $Re$  is assumed to be negligible, which is often the case for shapes that present sharp corners or limiting the consideration to an appropriate range for  $Re$ , the following holds:

$$Fq = St \frac{U}{B}, \quad (2.17)$$

which states that the shedding frequency is proportional to the fluid velocity.

Lets now consider a structure with natural frequency close to the shedding one. A synchronization of the shedding cycle with the structure motion is observed together with a deviation from Eq. (2.17) (see Fig. 2.8). It can be observed that, given a structure with fixed natural frequency, a velocity range exists which causes the synchronization of the natural vibrations with the vortex shedding. The unstationary forces, produced by the vortex detachment, excite the structure in a resonant condition so that large oscillation amplitudes can be reached. In reality, such vibrations are limited by the structural damping and the damping induced by the presence of the fluid so that the motion does not diverge stabilizing to a limit cycle as shown in Fig. 2.9.

Although divergence does not occur, in the case of bridges, this condition can be reached for low velocities, often observed on site, so that its effect must be taken into account in order to prevent fatigue of materials and discomfort.

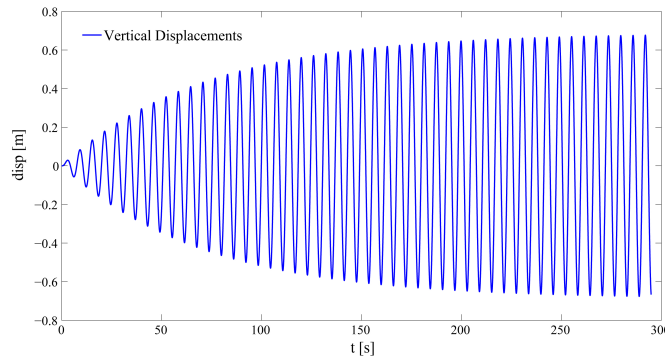


Figure 2.9: Limit cycle for lock-in condition: numerical simulation.

## 2.4 Torsional divergence

Torsional divergence is the easiest form of aeroelastic instability: dynamic effects are not present and the phenomenon can be studied as a limit equilibrium condition.

The aerodynamic pitching moment in the surrounding of the initial attack angle,  $\alpha_0$ , following a first order approximation, reads as:

$$M_\alpha = \frac{1}{2}\rho U^2 B^2 \left[ C_m(\alpha_0) + \left. \frac{dC_m}{d\alpha} \right|_{\alpha_0} \alpha \right]. \quad (2.18)$$

The equilibrium condition can be written as:

$$\frac{1}{2}\rho U^2 B^2 \left[ C_m(\alpha_0) + \left. \frac{dC_m}{d\alpha} \right|_{\alpha_0} \alpha \right] + k_\alpha \alpha = 0, \quad (2.19)$$

where  $k_\alpha$  is the structure torsional stiffness, leading to:

$$\alpha = \frac{\frac{1}{2}\rho U^2 B^2 C_m(\alpha_0)}{k_\alpha - \frac{1}{2}\rho U^2 B^2 \left. \frac{dC_m}{d\alpha} \right|_{\alpha_0}}. \quad (2.20)$$

The angle in equilibrium condition diverges when the following condition holds:

$$U_{cr} = \sqrt{\frac{2k_\alpha}{\rho B^2 \left. \frac{dC_m}{d\alpha} \right|_{\alpha_0}}}, \quad (2.21)$$

which identifies the incipient divergence condition being  $U_{cr}$  the critical divergence wind speed.

The instability is caused by the fact that an increase in the attack angle results in a corresponding increase of the aerodynamic moment which contributes to the system destabilization.

In reality the rotation does not diverge indefinitely and stabilizes due to the nonlinearities in the pitching moment variation around the stall angle. Such instability in bridges leads to extremely high critical speed which are often not of technical interest as other forms of instability might occur at lower speed. Nevertheless, such phenomenon must be carefully studied and might be observed in wind tunnel tests especially if sectional models are used.

## 2.5 Buffeting

Buffeting is the excitation of an immersed body due to turbulence present in the incoming flow. The problem of predicting the structure response to a random loading is a classical problem of stochastic mechanics which implies the evaluation of admittance functions that relates the velocity variations to the forces measured on the deck.

In the aeronautical field the problem has been solved by Sears and Küssner who studied the problem of a thin airfoil encountering a transverse sharp gust in the frequency and time domain, respectively.

As regards bridge decks, if the incoming velocity variations have characteristic period much higher than one non-dimensional time unit, dynamic effects in the organization of the fluid flow around the body can be disregarded and a quasi-steady approach can be used imposing a value equal to 1.0 to the admittance functions [5] (those concepts will be discussed in detail in Chapter 6). When such condition is not representative of the incoming flow the admittance functions can be evaluated on the basis of Sears function (see Fig. 2.10) or empirically evaluated in wind tunnel tests. According to the reference system conventions reported in Fig. 2.2, regardless of the particular choice on the evaluation of the system admittance, the general formulation reads:

$$D^b(Fq) = \frac{1}{2}\rho U^2 B \left\{ 2C_d(\alpha_0)\chi_d^u(Fq)\frac{\tilde{S}_u}{U} + \left. \frac{dC_d}{d\alpha} \right|_{\alpha_0} \chi_d^v(Fq)\frac{\tilde{S}_v}{U} \right\}, \quad (2.22)$$

$$L^b(Fq) = \frac{1}{2}\rho U^2 B \left\{ 2C_l(\alpha_0)\chi_l^u(Fq)\frac{\tilde{S}_u}{U} + \left. \frac{dC_l}{d\alpha} \right|_{\alpha_0} \chi_l^v(Fq)\frac{\tilde{S}_v}{U} \right\}, \quad (2.23)$$

$$M^b(Fq) = \frac{1}{2}\rho U^2 B^2 \left\{ 2C_m(\alpha_0)\chi_m^u(Fq)\frac{\tilde{S}_u}{U} + \left. \frac{dC_m}{d\alpha} \right|_{\alpha_0} \chi_m^v(Fq)\frac{\tilde{S}_v}{U} \right\}, \quad (2.24)$$

where the superscript  $b$  denotes the buffeting contribution, the functions  $\chi_i^j(Fq)$  (with  $i = d, l, m$  and  $j = u, v$ ) are the admittance functions which are expressed as functions of the frequency,  $Fq$ , and  $\tilde{S}_j$  is the wind spectral content for each velocity component. In order to highlight the structure of Eq. (2.24), it must be noticed that the contribution arising from  $\tilde{S}_u$  is multiplied by a factor 2 according to the following approximation:

$$(U + u)^2 = U^2 + 2Uu + u^2 \simeq U^2 + 2Uu, \quad (2.25)$$

which implies that the unsteady turbulent component  $u$  must be small enough if compared to the mean value  $U$ . Considering the contributions arising from  $\tilde{S}_v$  it must be noticed that the primary effect obtained by adding the component  $v$  is represented by a variation of the effective attack angle which is taken into account by the aerodynamic coefficient derivatives, once again assuming a first order approximation.

This formulation is widely used in practical cases but it strongly relies on the superposition principle (so invoking the linearity of the system) and, indeed, this can be considered to be adequate in a wide variety of cases (far from the main aerodynamic and aeroelastic instabilities). Nevertheless, its phenomenological form denounces the lack of insight shed on the physical phenomenon which is all condensed in the evaluation of the

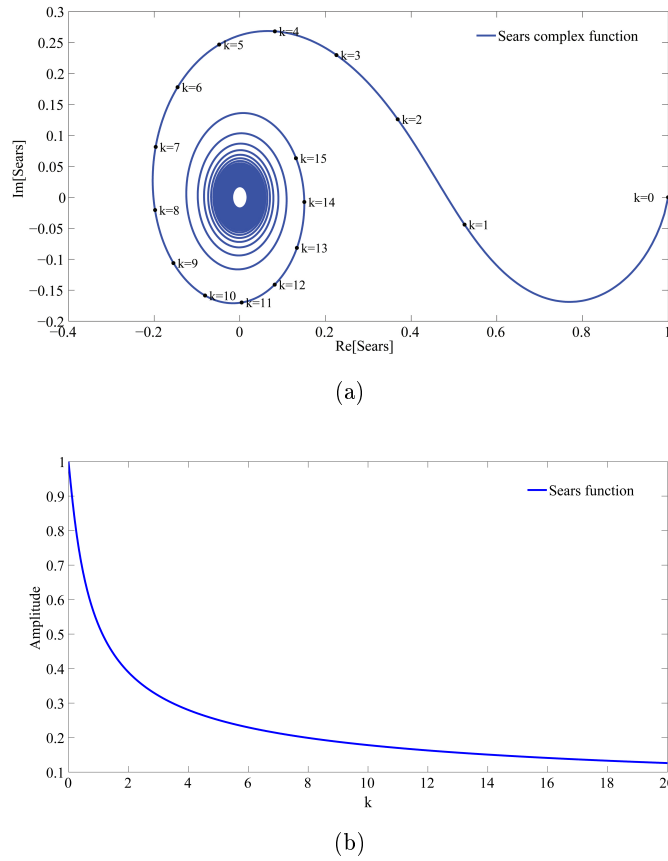


Figure 2.10: Sears complex function: (a), complex values, (b) amplitude.

admittance functions.

## 2.6 Galloping

Galloping is a typical aeroelastic instability encountered in slender flexible structures characterized by bluff sections (like cables). The bluff features of the cross section minimizes the role played by the flow memory effects, so that a quasi-steady approach can be used to describe the phenomenon.

The instability, in this case, is inherently dynamic and consists in the superposition of a negative aerodynamic damping to the positive structural one. Such superposition decreases the total damping acting on the structure and eventually leads to negative total values exposing the structure to theoretically unbounded growing oscillations.

In order to study the phenomenon, it is common practice to perform a first order approximation of the aerodynamic lifting force which, disregarding the static force in the initial condition, reads:

$$L(\alpha) = \frac{1}{2} \rho U^2 B C_l(\alpha). \quad (2.26)$$

It is then possible to write the motion equation as:

$$M \left[ \ddot{h}_d + 2\xi\Omega\dot{h}_d + \Omega^2 h_d \right] = L, \quad (2.27)$$

where  $M$  is the mass of the body per unit length,  $\xi$  is the structural damping and  $\Omega$  is the vibration natural frequency while  $h_d$  is the displacement in the  $y$  direction. The effective angle of attack can be calculated based on the average incoming wind speed and the first derivative of the structure heaving with respect to time. Considering once again a first order approximation, it is possible to write:

$$\alpha = \text{atan} \left( \frac{\dot{h}_d}{U} \right) \simeq \frac{\dot{h}_d}{U}, \quad (2.28)$$

while the effective wind speed  $U_{eff}$ , considering only the zero order terms, reads:

$$U_{eff} = \left( U^2 + \dot{h}_d^2 \right)^{\frac{1}{2}} \simeq U. \quad (2.29)$$

Under such hypotheses the motion equation reads:

$$M \left[ \ddot{h}_d + 2\xi\Omega\dot{h}_d + \Omega^2 h_d \right] = \frac{1}{2}\rho U^2 B \frac{dC_l}{d\alpha} \bigg|_{\alpha_0} \frac{\dot{h}_d}{U}. \quad (2.30)$$

Considering Eq. (2.30), the effective damping can be written as:

$$\xi_{eff} = \xi - \frac{\frac{1}{2}\rho U B \frac{dC_l}{d\alpha} \big|_{\alpha_0}}{M\Omega}, \quad (2.31)$$

and the critical galloping speed can be calculated as follows by imposing null total damping:

$$U_{cr} = \frac{2\xi M \omega}{\rho B \frac{dC_l}{d\alpha} \big|_{\alpha_0}}. \quad (2.32)$$

Considering that the structural damping is always positive, a sufficient condition to evaluate if a section is prone to galloping can be derived as:

$$\frac{dC_l}{d\alpha} \bigg|_{\alpha_0} > 0. \quad (2.33)$$

Such approach can be used to evaluate the galloping critical condition. More refined approaches consider a higher order approximation for  $C_l(\alpha)$  and are thus able to evaluate the limit cycles amplitude in the postcritical condition.

From the technical point of view, rather than explicitly calculate a critical speed, only a qualitative evaluation of the tendency of the body to gallop is often considered. In fact, it is possible to define the Scruton number,  $Sc$ , as:

$$Sc = \frac{M\xi}{\rho B^2}, \quad (2.34)$$



which is a measure of the relative importance between the structural and the aerodynamic damping. It is observed that for values  $Sc \simeq 5$  the vibrations are usually of small amplitude and a convenient design limit can be considered  $Sc > 10$ .

Considering Eq. (2.33), note that the effective damping coefficient cannot be modified by the fluid action if the derivative of  $C_l$  with respect to the attack angle is zero. Such observation implies that cables with circular cross section cannot be prone to galloping. Unfortunately, the presence of ice on cables can modify the geometry so leading to aeroelastic instability.

### 2.6.1 Other forms of galloping

It is beyond the goal of this thesis to analyse all the possible form of aeroelastic instabilities which can be grouped under the name of galloping and the reader is invited to refer to [6]. It is however important to say that galloping can develop in a variety of conditions and some of them are not well understood still today.

In particular, any dependence of the aeroelastic coefficients with respect to the position of the body and variation of the aerodynamic coefficients with the motion of the structure, can lead to instability of the equilibrium condition. Regarding this second case, it is interesting to notice that, in some situations, the body section can be influenced by the motion of the structure itself like in the case of bridge cables exposed to the rain (wind-rain induced vibrations). In this case, although the phenomenon is still an active research topic, the instability seems to be driven by the motion-induced migration of the water rivulets which induce dynamic modifications to the cable cross section and thus of its aerodynamic properties.

In order to roughly distinguish galloping from the flutter instability, that will be later introduced, we can say that galloping can develop in systems characterized by a single degree of freedom (heaving) and is observed in bluff sections whose aerodynamic properties, as a first approximation, can be studied in quasi-steady regime.

## 2.7 Flutter

In this section the flutter instability is qualitatively introduced while it will be extensively described in later sections. In analogy to galloping, the main feature that leads to the outbreak of instability can be identified in the variation of the aerodynamic coefficients driven by the body motion. Nevertheless, in this case, the body is usually characterized by an elongated cross section (like wings and bridge decks) so that memory effects of the fluid play a crucial role in the definition of the aerodynamic loads (see Chapter 6).

Flutter is usually divided in various subgroups on the base of its generative mechanism:

- Classical coupled flutter
- Torsional flutter (or one degree of freedom flutter)
- Stall flutter

The first one is characterized by the aerodynamic coupling of heaving and torsional modes which leads to the extraction, of energy from the fluid so developing unbounded

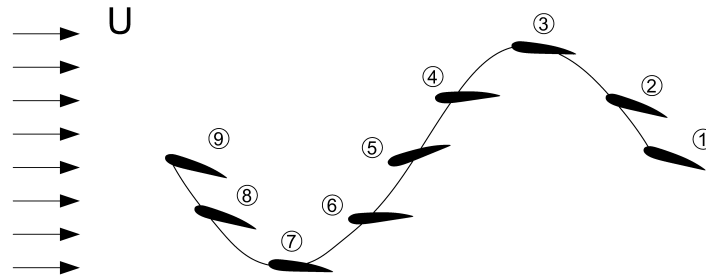


Figure 2.11: Mechanism of the coupled flutter.

growing oscillations of the body. The second, on the contrary, involves oscillations of the torsional degree of freedom only and it is caused by the development of a negative total damping due to the aerodynamic effects, in analogy to galloping. The third one is triggered by the non-linearity of the lift curve in the proximity of the stall angle.

Although the phenomenon is highly non-linear, especially for non-streamlined sections, from the technical point of view, the phenomenon has been successfully studied adopting audacious linearizations justified by the fact that the main practical interest is restricted to the identification of the limit stability condition.

The approach is based on the theoretical evaluation or, more commonly, the experimental extraction of frequency response functions that link the structure motion to the aerodynamic forces acting upon it, following the well known method proposed by Scanlan [6]. Such an approach consists in the definition of equivalent aerodynamic stiffness and damping coefficients as well as coupling terms which are linearly superimposed to the structural ones.

Such an approach has strong theoretical support in the case of well streamlined sections where flow detachments are absent or play a negligible role while it should be seen as a synthetic phenomenological approach when bluff sections are considered.

Flutter is without a doubt the most dangerous aeroelastic instability for wings and bridge decks and leads to the failure of the structure due to extremely large amplitude oscillations.

The mechanism which leads to the classical coupled flutter (which is characteristic of wings and well shaped decks) is qualitatively represented in Fig. 2.11. A direct experience of its effectiveness can be obtained by waving a hand outside a car window reproducing the mechanism depicted in Fig. 2.11. The heaving motion naturally synchronizes with the torsional motion and the energy extraction from the fluid tends to increase the amplitude of the oscillations extremely rapidly.

## 2.8 General remarks on aeroelastic phenomena

In the previous sections the most important aeroelastic phenomena have been briefly described. All the presented analytical developments should be considered as first approximations which can be used for reasonable predictions of the instability onset condition. Indeed, the main problem lies in the fact that the interactions between them cannot be accounted for in the proposed simplified approaches. In fact, their coupling usually involves highly non-linear mechanisms and their mutual dependence can lead to strong modification of the aerodynamic behaviour. Due to such interactions, the instability onset velocity can decrease dramatically and hysteresis and sudden jumps in the system state can be observed.

For example let's consider the buffeting of a bridge. As it has been briefly explained in Sec. 2.7, the presence of wind changes the effective stiffness and damping of the immersed structure due to aeroelastic effects. As a result buffeting should be studied considering the structure effective properties rather than the structural ones.

Furthermore, let's consider a body characterized by a bluff section vibrating in a smooth flow due to vortex shedding in the proximity of the lock-in condition. The critical galloping velocity is much higher than the lock-in one. In this case the two mechanisms are independent and the previously described approaches hold. If the Scruton number is reduced (for example by lowering the structural damping) the galloping critical speed decreases accordingly and the galloping speed approaches the lock-in one. In such conditions, it is observed that the onset of galloping, individuated by the insurgence of large amplitude vibrations, is considerably lowered and tends to coincide with the lock-in condition. Unfortunately, the interaction between the two phenomena can span over a surprisingly wide velocity range so that only experimental observation can clarify how wide such intervals should be considered.

Such simple examples highlight the difficulties encountered in the study of aeroelastic phenomena and, indeed, justify the need for experimental testing on the base of a case by case approach limiting the hope for the development of general reliable approaches.

An attractive prospective is represented by Computational Fluid Dynamics (CFD) simulations which, on theoretical ground, are able to fully reproduce complex aerodynamic phenomena and their interaction with the structure motion. Such approaches are gaining more and more attention in the scientific community and undoubtedly represent a significant step forward the modelling of aerodynamic and aeroelastic effects. Unfortunately, their effectiveness is strongly limited by the complications encountered in turbulence modelling which introduces a high level of unreliability in the simulations. It is the author's opinion that, beside the development of new turbulence models, the developments of coherent and validated frameworks, able to guide technicians in the interpretation of the results obtained with currently available standard models, is of fundamental importance in order to widen the diffusion of such modelling tools in practical cases.

# Chapter 3

## Inviscid flows

In this chapter the inviscid fluid model is analysed. Although the limitations of such a fluid description prevent its direct application to a wide range of cases of practical interest, it provided some fundamental concepts that led to the evolution of modern aeronautics. In the following, the fluid motion governing equations are deduced from basic physical concepts and specialized to the case of inviscid flows. Elementary flow field are deduced and, finally, the thin airfoil theory is introduced together with the theoretical background needed to understand limitations of its application to bridge decks.

### Contents

<b>3.1</b>	<b>Conservation laws</b>	<b>29</b>
<b>3.2</b>	<b>Mass conservation</b>	<b>30</b>
<b>3.3</b>	<b>Momentum conservation</b>	<b>31</b>
<b>3.4</b>	<b>Energy conservation</b>	<b>32</b>
<b>3.5</b>	<b>Inviscid flows</b>	<b>33</b>
3.5.1	Bernoulli's theorem	34
3.5.2	Potential flows	34
<b>3.6</b>	<b>The thin airfoil</b>	<b>40</b>
3.6.1	Static aerodynamic loads on the thin airfoil	43
3.6.2	Motion-induced loads on the thin airfoil	43

### 3.1 Conservation laws

Before deducing the governing equations for inviscid fluids, it is useful to introduce the general structure underlying all the equations that will be later considered. Such a structure is represented by the conservation law of physically meaningful quantities during the evolution of the flow and can be generally written as:

$$\frac{\partial(\rho q)}{\partial t} + \text{div}(\rho \mathbf{u} q) + \text{div}(\mathbf{f}_q) = S_q, \quad (3.1)$$

where  $\rho$  is the mass volumetric density,  $t$  is the time,  $\mathbf{u}$  is the velocity vector,  $q$  is a quantity that is conserved during the process,  $\mathbf{f}_q$  is the flux of the quantity  $q$  considered positive when exiting the considered control volume,  $S_q$  is a volumetric specific production term which is considered positive when it is a source [7].

The terms encountered in the aforementioned equation can be easily distinguished considering the role that they assume in the system dynamics. In particular, starting from the left hand side, the first one can be interpreted as the inertia of the system, the second one represents the convection due to the fluid motion, the third one represents the exchange of  $q$  through the external surface of the considered control volume while the right hand side includes the production of  $q$ , its destruction and its exchange with the external environment.

It is convenient to rewrite Eq. (3.1) expanding the second term as follows:

$$\text{div}(\rho \mathbf{u} q) = q \cdot \text{div}(\rho \mathbf{u}) + \rho \mathbf{u} \cdot \text{grad}(q). \quad (3.2)$$

Substituting Eq. (3.2) in (3.1), expanding and grouping terms:

$$\rho \left[ \frac{\partial q}{\partial t} + \mathbf{u} \cdot \text{grad}(q) \right] + q \left[ \frac{\partial \rho}{\partial t} + \text{div}(\rho \mathbf{u}) \right] = S_q - \text{div}(\mathbf{f}_q). \quad (3.3)$$

The second term on the left hand side of Eq. (3.3) can be demonstrated to be always equal to zero thanks to the mass conservation principle that will be demonstrated in the next paragraph, so that the general form of the conservation laws can be written as:

$$\rho \left[ \frac{\partial q}{\partial t} + \mathbf{u} \cdot \text{grad}(q) \right] = S_q - \text{div}(\mathbf{f}_q), \quad (3.4)$$

which, on the left hand side, is the substantive derivative of the considered fluid particle. Equations (3.1) and (3.4) are indeed the expression of a general conservation law from the Eulerian and the Lagrangian point of view, respectively. All the equations involved in fluid dynamics and a variety of other branches of physics can be expressed in such a form.

## 3.2 Mass conservation

The mass conservation law can be deduced from the general formulation presented in Sec. 3.1 by substituting the quantity  $q$  with the uniform scalar field of value 1.0. This is justified by the fact that the density per mass unit of the mass density is 1.0 by definition. Furthermore the fluxes  $\mathbf{f}_q$  are considered to be identically null as the elementary fluid volume is considered to be atomic in nature and the term  $S_q$  is assumed to be zero because no mass production or exchange with the external environment is permitted.

Specializing Eq. (3.1) accordingly, the following equation is obtained:

$$\frac{\partial \rho}{\partial t} + \text{div}(\rho \mathbf{u}) = 0, \quad (3.5)$$

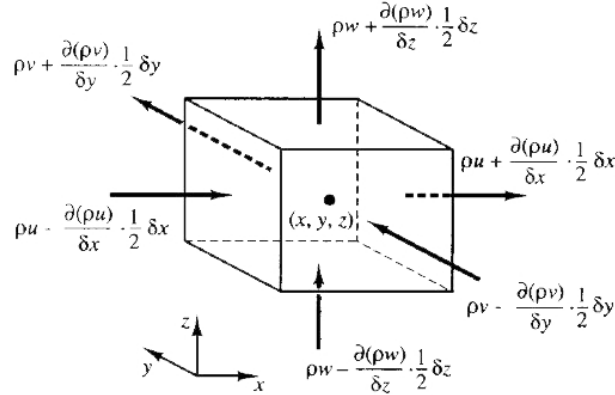


Figure 3.1: Mass balance of the elementary volume [8].

which states that the substantive derivative of the mass of the fluid particle is always equal to zero.

Equation (3.5) can be deduced in a more intuitive way considering Fig. 3.1. In that case, considering the mass balance of the elementary prismatic volume of dimensions  $\delta_x, \delta_y, \delta_z$ , and approximating fluxes to the first order, the following is obtained:

$$\frac{\partial \rho}{\partial t} + \frac{\partial(\rho u)}{\partial x} + \frac{\partial(\rho v)}{\partial y} + \frac{\partial(\rho w)}{\partial z} = 0, \quad (3.6)$$

where  $u, v, w$  are the components of the  $\mathbf{u}$  vector in the  $x, y, z$  directions, respectively. Such result is identical to Eq. (3.5). If the fluid is assumed to be incompressible the density  $\rho$  is a constant and Eq. (3.6) becomes:

$$\text{div}(\mathbf{u}) = 0. \quad (3.7)$$

### 3.3 Momentum conservation

The momentum conservation equation can be deduced following the same procedure described in the previous sections. In particular, Eq. (3.1) can be rewritten substituting to the quantity  $q$  the velocity  $u_i$ , component of the vector  $\mathbf{u}$  in the  $i$ -th direction, leading to:

$$\frac{\partial(\rho u_i)}{\partial t} + \text{div}(\rho \mathbf{u} u_i) + \text{div}(\mathbf{f}_{ui}) = S_{ui}. \quad (3.8)$$

The fluxes of the momentum components are represented by the stresses exchanged at the elementary fluid volume surface. Lets indicate the stress tensor at the considered point as  $\mathbf{T}$  and its components as  $\tau_{i,j}$  with  $i, j = x, y, z$ . Furthermore, the source term,

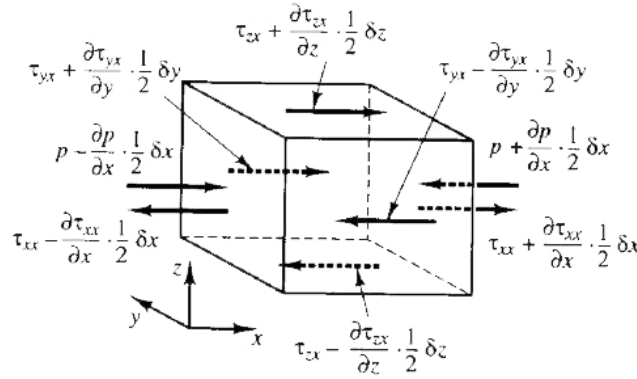


Figure 3.2: Momentum balance in the x-direction [8].

according to Newton's second law, can be identified as the volume force vector component in the  $i$ -th direction. Following such conventions, Eq. (3.8) can be rewritten as:

$$\frac{\partial(\rho u_i)}{\partial t} + \text{div}(\rho \mathbf{u} u_i) + \text{div}(-\mathbf{T}_{i,:}) = S_{ui}. \quad (3.9)$$

where the symbol  $:$  indicates to span along all the values of the index. The same equation can be deduced also considering the dynamic equilibrium of the elementary fluid volume as presented in Fig. 3.2.

It is important to remember that the application of Newton's second law, fulfilled imposing the balance between inertial and applied forces, follows inherently a Lagrangian point of view so that Eq. (3.2) can be more explicitly be rewritten as:

$$\frac{D(\rho u_i)}{Dt} + \text{div}(-\mathbf{T}_{i,:}) = S_{ui}, \quad (3.10)$$

highlighting the role played by the substantive derivative. Equations (3.5) and (3.9) are of general applicability and fully describe the kinematic and dynamic equilibrium condition of a fluid.

Different fluid models are obtained from the aforementioned equations by introducing different constitutive equations that link the stress tensor  $\mathbf{T}$  to the calculated velocity fields.

It is here reminded that if the volume forces are generated by an irrotational volumetric force field and if the moment of inertia of the fluid particle is negligible, the equations obtained imposing the conservation of the angular momentum of the elementary fluid volume impose that the stress tensor  $\mathbf{T}$  must be symmetric [9].

### 3.4 Energy conservation

Although not used in the following developments, the energy conservation equation is here briefly presented. The energy content of the elementary fluid particle is composed

of its internal energy,  $i_e$ , its kinetic energy and gravitational potential. In particular, the specific energy per mass unit can be written as:

$$e = i_e + \frac{1}{2} (u^2 + v^2 + w^2) + gz. \quad (3.11)$$

where  $g$  is the gravity acceleration. It is possible to introduce such quantity in the format presented in Eq. (3.1):

$$\frac{\partial(\rho e)}{\partial t} + \text{div}(\rho \mathbf{u} e) + \text{div}(\mathbf{f}_e) = S_e. \quad (3.12)$$

The fluxes of energy through the fluid element surface are represented by the mechanical power exchanged through the surface and the fluxes of internal energy. If we consider the latter to be of the form  $\mathbf{f}_{ie} = -k_{ie} \cdot \text{grad}(T)$ , where  $T$  is the temperature and  $k_{ie}$  is the thermal conductivity, it is possible to write:

$$\frac{\partial(\rho e)}{\partial t} + \text{div}(\rho \mathbf{u} e) + \text{div}(-\mathbf{T} \cdot \mathbf{u} - k_{ie} \cdot \text{grad}(T)) = S_e, \quad (3.13)$$

which describes the energy conservation in the fluid flow.

### 3.5 Inviscid flows

The governing equations for an inviscid fluid can be derived from Eqs. (3.5) and (3.8) by imposing  $\mathbf{T}$  of the form:

$$\mathbf{T} = -p \cdot \mathbf{I} \quad (3.14)$$

where  $p$  is the fluid pressure and  $\mathbf{I}$  is the identity matrix. This fluid description is known as ideal fluid or Euler's fluid and has been published for the first time in 1757.

Such an assumption is extremely strong and assumes that inertial forces are preponderant if compared to viscous ones which is to say that the Reynolds number is assumed to be infinite. Although this is indeed true for large parts of the fluid domain in a wide range of applications, unfortunately zones where this assumption does not hold exist (close to the solid boundaries and in shear layers) and although often limited in size, they play a crucial role in the definition of the fluid flow topology as shown in Sec. 2.1.4.

Lets now rewrite the governing equations in the simplified case of an incompressible fluid, hypothesis that will be always considered acceptable in the following developments (this is a very reasonable hypothesis when the Mach number is smaller than 0.3). In such a case, considering the density  $\rho$  as a constant, Eqs. (3.5) and (3.9) can be written as:

$$\text{div}(\mathbf{u}) = 0, \quad \rho \frac{D\mathbf{u}}{Dt} + \text{grad}(p) = \mathbf{S}_u. \quad (3.15)$$

As already stated the source term in the momentum conservation equation,  $\mathbf{S}_u$ , is represented by the volumetric forces acting on the elementary fluid particle.



### 3.5.1 Bernoulli's theorem

In many applications it is possible to assume that the volumetric forces are conservative so that it is possible to define their potential,  $\psi_f$ . Then, it is possible to write:

$$\rho \frac{D\mathbf{u}}{Dt} + \text{grad}(p) = \rho \cdot \text{grad}(\psi_f). \quad (3.16)$$

The equation can be multiplied by  $d\mathbf{u}$  and integrated along the fluid particle trajectory, leading to:

$$\int_{t_0}^{t_1} \left[ \rho \frac{D\mathbf{u}}{Dt} + \text{grad}(p) + \rho \cdot \text{grad}(\psi_f) \right] d\mathbf{u} = \text{const}, \quad (3.17)$$

which written in extended form, adopting Einstein's index summation convention and remembering that  $du_i = dx_i/dt$ , reads:

$$\int_{t_0}^{t_1} \rho \frac{Du_i}{Dt} du_i + \int_{t_0}^{t_1} \left[ \frac{\partial p}{\partial x_i} \frac{dx_i}{dt} + \rho \cdot \frac{\partial \psi_f}{\partial x_i} \frac{dx_i}{dt} \right] = \text{const}, \quad (3.18)$$

where  $\text{const}$  is a numerical constant. Then, after the integration the result is:

$$\frac{1}{2} \rho U^2 + p + \rho \psi_f = \text{const}, \quad (3.19)$$

where  $U$  is the velocity magnitude defined as  $U = \sum_i u_i^2$ . Equation (3.19) states that, for an ideal fluid, the sum of the kinetic energy, the pressure and the potential energy of the volumic forces is constant along any fluid streamline.

If the volumetric forces are considered to be small with respect to the inertial ones, Eq. (3.19) can be simply written as:

$$\frac{1}{2} \rho U^2 + p = p_0 + p_{dyn}, \quad (3.20)$$

where  $p_0$  is a reference pressure and  $p_{dyn}$  is the dynamic pressure.

### 3.5.2 Potential flows

Lets now assume that the velocity field is irrotational:

$$\text{curl}(\mathbf{u}) = \mathbf{0}, \quad (3.21)$$

which in extended notation can be written as:

$$\left( \frac{\partial v}{\partial x} - \frac{\partial u}{\partial y}, \quad \frac{\partial w}{\partial x} - \frac{\partial u}{\partial z}, \quad \frac{\partial u}{\partial z} - \frac{\partial w}{\partial x} \right) = \mathbf{0}. \quad (3.22)$$

Lets assume that a scalar function  $\psi_u$  exists such that:

$$\mathbf{u} = \text{grad}(\psi_u). \quad (3.23)$$

Such function  $\psi_u$  is called velocity potential and, by definition, it ensures that Eq. (3.21) is respected, in fact:

$$\frac{\partial u_i}{\partial x_j} = \frac{\partial^2 \psi_u}{\partial x_i \partial x_j} = \frac{\partial u_j}{\partial x_i}. \quad (3.24)$$

It is then possible to substitute Eq. (3.23), which is a definition, in the first of Eq. (3.15), obtaining:

$$\text{div}(\text{grad}(\psi_u)) = 0, \quad (3.25)$$

which is a Laplace equation. Then, the following procedure could be used to find a solution for an ideal irrotational fluid flow:

1. Eq. (3.25) is solved so that the velocity field is known
2. Eq. (3.19) is used to compute the pressure field
3. Pressures can be integrated in order to obtain the forces on immersed bodies

It must be noticed that Eq. (3.25) is linear so that it is possible to build complex solution by simply using the linear superposition principle. In the following, some two-dimensional basic solutions of interest are reported. The reader can find a complete description in [10].

### Uniform current

Lets consider a uniform current (Fig. 3.3 (a)) such that:

$$u = u_\infty, \quad v = w = 0, \quad (3.26)$$

it is trivial to identify the velocity potential as:

$$\psi_u = u_\infty x. \quad (3.27)$$

### Point source

Consider a radial flow diverging from a point source (Fig. 3.3 (b)) such that:

$$u_r \neq 0, \quad u_\alpha = 0, \quad (3.28)$$

where  $r$  denotes the radial direction diverging from the point source and  $\alpha$  indicates the direction orthogonal to the radius. It is possible to demonstrate that the velocity potential of such a flow, assuming volumetric flow rate  $Q$ , is:

$$\psi_u = \frac{Q}{2\pi} \ln(r) \quad (3.29)$$

Identical result, with opposite signs, can be obtained assuming a point sink instead of a source.

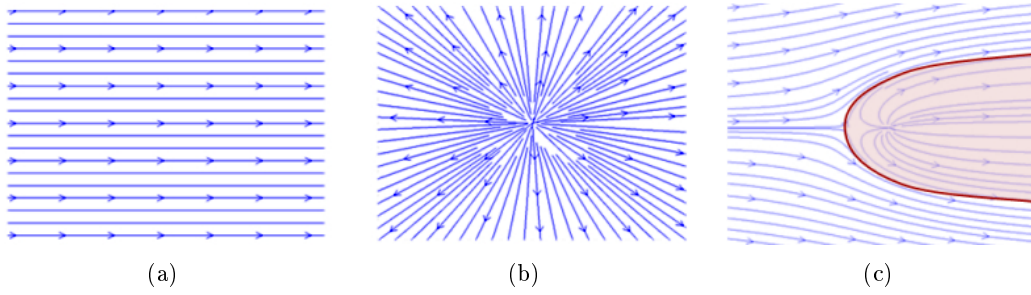


Figure 3.3: Elementary flow fields: (a) uniform current, (b) point source, (c) half-body. Images taken from [11]

### Half-body

It is possible to superimpose an uniform flow and a source in order to describe the flow field around a half indefinitely long body (Fig. 3.3 (c)). In particular, once the velocity field is calculated, it is theoretically possible to substitute any streamline with an impermeable boundary because the adjacent streamlines are not perturbed by such a substitution (thanks to the hypothesis of inviscid fluid).

### Cylinder

If an uniform flow is superimposed to the flow originated by a source and a sink of equal  $Q$  aligned to the uniform flow direction, a closed body can be obtained. In particular it is possible to observe that the streamlines generated in the flow far upwind the source are deviated in the source proximity and describe an open trajectory. The streamlines originated at the source are deviated by the uniform flow and are collected at the sink. The limiting case between the two is a closed loop streamline that describes a body of oval shape called Rankine oval. As already stated, such a streamline can be substituted with an impermeable boundary so originating a closed body which can be considered immersed in the flow.

If the distance  $d$  between source and sink is decreased tending to zero in such a way that:

$$Q \cdot d = \text{const}, \quad (3.30)$$

a doublet is obtained (Fig. 3.5 (b)). For such a flow, the velocity potential, if the source and the sink are aligned along the  $x$  axis, reads:

$$\psi_u = -\frac{Qdx}{r} = -\frac{Qd\cos(\alpha)}{r}, \quad (3.31)$$

where  $\alpha$  is the angular coordinate in a cylindrical reference system. If the doublet is immersed in an uniform current a cylinder of radius  $R$  is described as shown in Fig. 3.5 (c) (details can be found in [10]).

$$R = \sqrt{\frac{Qd}{u_\infty}}. \quad (3.32)$$

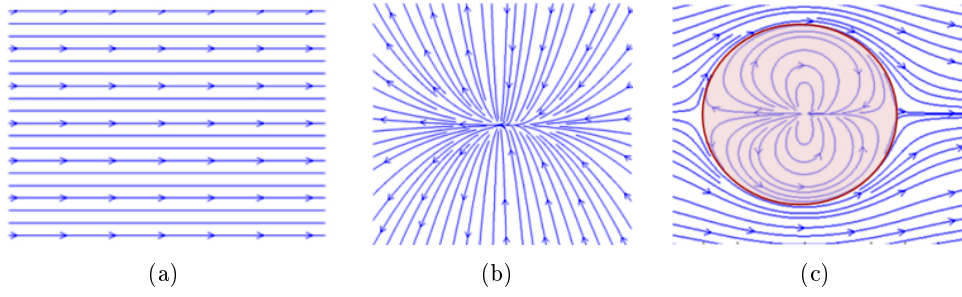


Figure 3.4: Elementary flow fields: (a) uniform current, (b) doublet, (c) cylinder. Images taken from [11]

Using such a method, it is possible to superimpose elementary flow fields in order to obtain complex geometries modelled as a distribution of sources and sinks.

### D’Alambert paradox

The potential flow model is able to provide physically sound solutions for flow fields around a variety of streamlined bodies. Nevertheless, D’Alambert was the first one to notice that, if the hypotheses of incompressible, inviscid, stationary and irrotational fluid flow are retained, no aerodynamic forces can arise on immersed bodies. Such a conclusion is in apparent contradiction with experimental results and highlights the deep shortcomings of the potential flow model.

It must be noted that as Eq. (3.25) is second order in space, only one boundary condition can be applied to the components of  $u$  at the solid boundaries, which is usually chosen as Neumann type so describing an impermeability condition. Experimental evidences prove that, in correspondence of solid boundaries, the velocity magnitude vanishes because also the velocity component tangential to the boundaries tends to zero due to viscosity when approaching the wall.

It can be proved that the condition that imposes aerodynamic forces to be null is Eq. (3.21) that states that the vorticity is null everywhere in the flow field. Then, it is of interest to study a flow field characterized by the fact that Eq. (3.21) is respected everywhere a part from a punctual singularity. Such elementary flow is called vortex.

### Vortex

Consider a velocity field describe by the following velocity potential:

$$\psi_u = \frac{\Gamma}{2\pi}\alpha, \quad (3.33)$$

where  $\Gamma$  is a constant. It is possible to demonstrate that the velocity field described by Eq. (3.33) is:

$$u_r = 0, \quad u_\alpha = \frac{\Gamma}{2\pi r}, \quad (3.34)$$

which is composed of concentric circular streamlines centered on the origin of the coordinate system. Lets now calculate the circulation of the velocity field along a streamline:

$$\oint_l \mathbf{u} \cdot \hat{\mathbf{t}} d\mathbf{l} = \int_{2\pi} \frac{\Gamma}{2\pi r} r d\alpha = \Gamma, \quad (3.35)$$

where  $\hat{\mathbf{t}}$  is the tangent versor in all the streamlines points. Equation (3.35) states that the circulation around a vortex streamline is independent of the particular streamline chosen. It must be noticed that the curl is null everywhere but the origin where the velocity is not defined because of the inconsistency arising from the derivation of a curling flow field from the potential theory.

Moving from the definition of the elementary vortex and Kelvin's circulation theorem, it is possible to define a vortical zone as a portion of the fluid flow where the curl of the velocity field is non null. In the following the curl of the velocity field will be indicated as vorticity.

An important result can be obtained calculating the time variation of the vorticity on a closed loop formed by a material line evolving in time. The result is known as Kelvin theorem and states that, in an ideal fluid, the vorticity calculated on a material close circuit is constant in time. This means that a vortex can be deformed but cannot vary its intensity.

Lets now define a vortical tube as a closed surface which is tangent in every point to the vorticity vector. It is possible to demonstrate that, moving along the vortical tube, the circulation along any close path is constant. Furthermore, it can be shown that a vortical tube cannot end in a fluid region and must extend to the boundary of the fluid zone or form a closed path. These two statements are known as the first and the second Helmholtz theorems. The third one is a consequence of the other two and states that considering an ideal fluid, if only irrotational external forces are present, an irrotational flow field cannot develop vorticity.

### Spinning cylinder

The flow field of a vortex can be superimposed to the one of a cylinder in order to simulate a spinning cylinder. In this statement it is already possible to recognize a contradiction that will be present in all the subsequent developments and that will deeply characterize the thin airfoil theory. In particular, it has been demonstrated that a solid boundary, following the potential flow theory, is modelled imposing a Neumann condition, whose physical meaning is to guarantee perfect impermeability of the solid boundary.

Under such condition, the motion of the boundary in the tangent direction cannot influence in any way the flow field around the body.

Nevertheless, experience shows that the motion of the boundary in the tangential direction deeply affects the flow field. This is caused by the fact that, in a viscous flow, the friction between the wall and the fluid does not allow slip between the fluid and the boundary.

From this point of view it is clear that, if we assume the fluid to be truly inviscid, there would be no difference between a still and a spinning cylinder. Nevertheless, in order to simulate a spinning cylinder in a viscous fluid, to a certain extent, we can still use the potential theory if we are able to correctly describe the flow field around the

body. The presence of the vortex, in this case, is used to impose a tangential velocity to the cylinder boundary in order to account for the no slip condition which cannot be directly described by the potential flow theory.

It is then clear that such an approach can be deemed valid only if the effects of viscosity are not negligible only in an extremely small part of the domain so that the flow field can be accurately described by the potential theory and the effects of viscosity are synthetically accounted for by using singularities.

The velocity potential for the spinning cylinder then reads:

$$\psi_u = u_\infty \left( r + \frac{R^2}{r} \right) \cos(\alpha) + \frac{\Gamma \alpha}{2\pi}, \quad (3.36)$$

the velocity field can be deduced deriving the velocity potential leading to:

$$u_r = u_\infty \left( 1 - \frac{R^2}{r^2} \right) \cos(\alpha), \quad u_\alpha = u_\infty \left( 1 - \frac{R^2}{r^2} \right) \sin(\alpha) + \frac{\Gamma}{2\pi r}. \quad (3.37)$$

On the cylinder surface ( $r = R$ ) the radial velocity is null and the tangential velocity is:

$$u_\alpha = 2u_\infty \sin(\alpha) + \frac{\Gamma}{2\pi R}. \quad (3.38)$$

Then, Bernoulli's theorem can be used to calculate the pressure distribution on the cylinder:

$$\begin{aligned} p &= p_\infty + \frac{1}{2}\rho(u_\infty^2 - u^2) = \\ &= p_\infty + \frac{1}{2}\rho u_\infty^2 - \frac{1}{2}\rho \frac{\Gamma^2}{4\pi^2 R^2} - 2\rho u_\infty^2 \sin^2(\alpha) + \rho \frac{u_\infty \Gamma}{\pi R} \sin(\alpha). \end{aligned} \quad (3.39)$$

The pressure distribution is symmetric with respect to the  $y$ -axis so that the drag is null. Considering the lift force:

$$L = - \int_0^{2\pi} p R \sin(\alpha) d\alpha, \quad (3.40)$$

excluding the constant terms and the ones in  $\sin^2$  which give no contribution, the applied lift force is:

$$L = - \frac{\rho u_\infty \Gamma}{\pi} \int_0^{2\pi} \sin^2(\alpha) d\alpha = -\rho u_\infty \Gamma, \quad (3.41)$$

which in vectorial form reads

$$L = -\rho \mathbf{u}_\infty \times \mathbf{\Gamma}, \quad (3.42)$$

where  $\times$  indicates the cross product.

Such a result is of general applicability, it is known as Kutta-Joukowski theorem and, in this case, the physical effect is known as Magnus effect.

The presented analytical developments highlight some important characteristic of aerodynamic forces. The first important result is that, if a potential flow is considered,

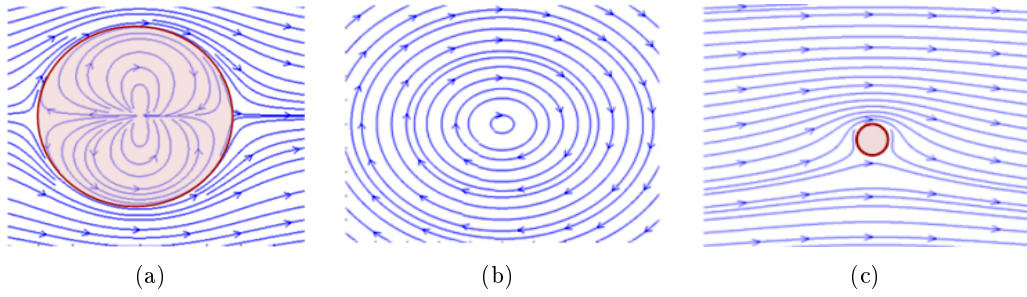


Figure 3.5: Elementary flow fields: (a) cylinder, (b) vortex, (c) rotating cylinder. Images taken from [11]

no aerodynamic forces can arise on an immersed body. Secondly, it is possible to explain the development of forces in the orthogonal direction with respect to the fluid flow by removing the hypothesis of irrotational flow. From the practical point of view, this can be done by introducing punctual singularities in a potential flow. The thin airfoil theory, which is described in the next section, strongly relies on these results.

Summing up, the importance of viscosity is recognized and its global effect is synthetically accounted for by introducing the concept of vorticity and linking it to the lifting forces. It must be noticed that, in the presented framework, no explanation has been found for drag forces in apparent contradiction with the experience. Such a contradiction is indeed related to the dissipative nature of the fluid motion due to viscous forces that, up to this point, has been considered as a conservative system.

### 3.6 The thin airfoil

It is beyond the aim of this thesis to describe in details the analytic developments that lead to the formulation of the airfoil theory. A detailed and comprehensive description of the concepts presented in the previous and in the following sections can be found in [12]. Briefly, it can be said that the results obtained for the still cylinder, thanks to conformal transformations, can be used to generate solutions around a variety of shapes of technical interest.

In particular, beside the description of wing cross sections, the method can be applied in order to predict the aerodynamic properties of a thin plate of vanishing thickness obtained by sending to zero the dimension of the cylinder axis oriented in the cross-flow direction. As already stated, if the irrotational flow model is considered, no aerodynamic forces can arise on the body even if it is inclined with respect to the main flow. This result is again in apparent contradiction with experience.

Furthermore, the conformal transformation shows singularities at the plate front and rear tips that result in an infinite velocity. Such points of high velocity and high velocity gradients cannot exist in real fluids as they introduce, due to viscous effects, localized high energy dissipation in the fluid flow so modifying the flow configuration. Let's now consider a flat plate which is rotated by a step-wise motion. The energy dissipated at the rear tip does not allow the fluid to flow around the tip itself in a stable configuration (Fig. 3.6 (a)). As a result, a vortex is created (Fig. 3.6 (b)) and then it is shed and

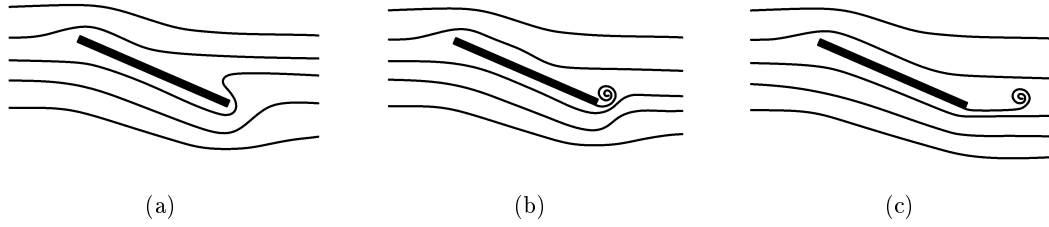


Figure 3.6: Starting vortex: (a) unstable recirculation, (b) starting vortex shedding, (c) transport downstream of the starting vortex.

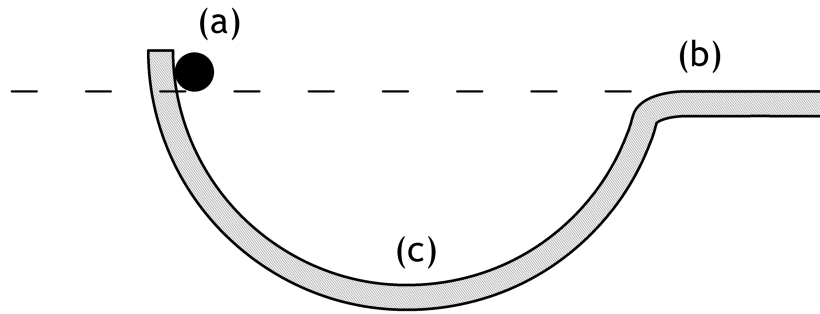


Figure 3.7: Starting vortex: (a) unstable recirculation, (b) shedding of the starting vortex, (c) transport downstream of the starting vortex.

transported downstream (Fig. 3.6 (c)). Such vortex is called starting vortex. In the new, stable, configuration the tip is a stagnation point as the velocity must there go to zero.

The mechanism is similar to the one that can be observed if a ball is released on a concave surface as pictured in Fig. 3.7. If no energy dissipation is considered, the ball rolls down from point (a) and reaches point (b) which is exactly at the same height. In the real world dissipation is always present and the ball cannot climb up the opposite side and finds its stable equilibrium position at point (c).

In the case of airfoils of finite thickness, characterized by an acute rear edge, the fact that the velocity must go to zero at the tip is confirmed also by the fact that, due to the impermeability condition, the velocity must be tangent to the airfoil profile in every point. As the tangent is not uniquely defined at the trailing edge, thus in that point the velocity must be zero so that the point is also defined as the rear stagnation point (see Fig 3.8).

As it has been already said, the solution for the thin airfoil is obtained from the one calculated for the cylinder through a conformal transformation. It can be observed that, if a concentrated vortex is added to the cylinder, producing a spinning cylinder, the position of the rear stagnation point can be controlled. Experience suggests that for



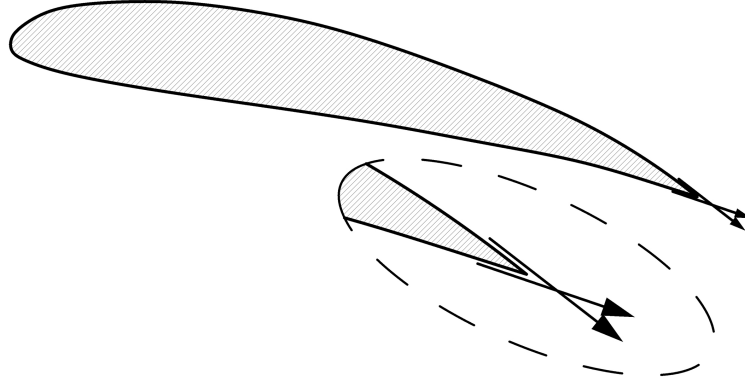


Figure 3.8: Rear stagnation point for airfoil: Kutta condition

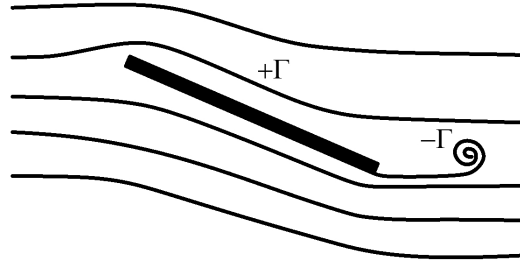


Figure 3.9: Vorticity of the airfoil and the starting vortex.

all attached flows around airfoils the rear stagnation point corresponds to the trailing edge so that the amount of vorticity needed to enforce such flow configuration can be calculated. Such condition is known as Kutta condition and states that the amount of vorticity produced by an airfoil can be calculated by imposing the position of the rear stagnation point in correspondence of the trailing edge.

It must be noticed that, similarly to the case of the spinning cylinder, vorticity cannot be produced by the body in a potential flow. Nevertheless, introducing singularities it is possible to take into account the overall effects of viscosity without directly introducing it in calculations.

It must be also noticed that, as a consequence of the third Helmholtz theorem (see Section 3.5.2), the total vorticity in the fluid must remain zero. This means that the vortex taking into account the effect of the wall viscosity must have the same intensity and opposite vorticity sign with respect to the starting vortex which is shed and transported downstream.

The applicability of the Kutta condition, which is indeed an empirical fact, is limited by the possibility of uniquely define a clear separation point *a priori*. In the case of bridge decks, this is never possible in practice so preventing the direct use of the thin airfoil theory. Nevertheless, the results obtained for mildly bluff bodies often show good

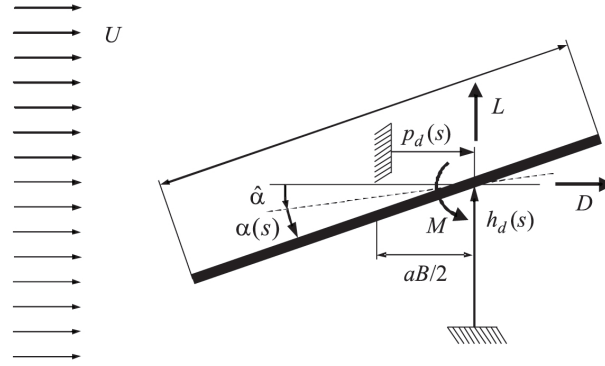


Figure 3.10: The sectional model: notation and conventions.

agreement (at least in the trends) with the results that can be calculated using such a framework.

### 3.6.1 Static aerodynamic loads on the thin airfoil

Consider a thin airfoil of chord length,  $B$ , with an infinite span length immersed in an inviscid smooth incompressible flow orthogonal to the body axis. With reference to Fig. 3.10, the body has three degrees of freedom, corresponding to horizontal,  $p_d$ , vertical,  $h_d$ , and angular,  $\alpha$ , displacements in the cross-sectional plane,  $p = p_d/B$  and  $h = h_d/B$  denoting the dimensionless displacement components. Rotation is assumed to be about a chord point distant  $aB/2$  from the chord midpoint (with  $a > 0$  for a downstream rotation center). Moreover, let the reference configuration of the body be defined by the angle of attack  $\hat{\alpha}$  between the mean wind direction and the cross-section chord.

In the framework of a linearized approach about the reference configuration, sectional loads can be represented as the linear superposition of steady mean loads in the reference configuration (described by functions  $\hat{C}_j(\hat{\alpha})$ ) and motion-induced (self-excited or aeroelastic) loads.

The fundamental theoretical reference for describing flow-induced loads in such a problem is represented by the closed-form approaches developed in the early decades of the past century.

As a result of the potential flow theory [13], flow-induced pressure distribution on a fixed thin airfoil under a small incidence  $\hat{\alpha}$  reduces in a zero drag force, a downward (negative) lift with  $\hat{C}_l = -2\pi\hat{\alpha}$ , and an anti-clockwise (positive) pitching moment with  $\hat{C}_m = \pi(1/2 + a)\hat{\alpha} = -\hat{C}_l(1/2 + a)/2$ . Accordingly, static aerodynamic forces are equivalent to the lift force applied at the upstream quarter-chord point, namely the aerodynamic center, and they vanish for  $\hat{\alpha} = 0$ .

### 3.6.2 Motion-induced loads on the thin airfoil

The problem related to the characterization of the aerodynamic forces acting on the thin airfoil harmonically oscillating in the flow about  $\hat{\alpha} = 0$  was solved by Theodorsen

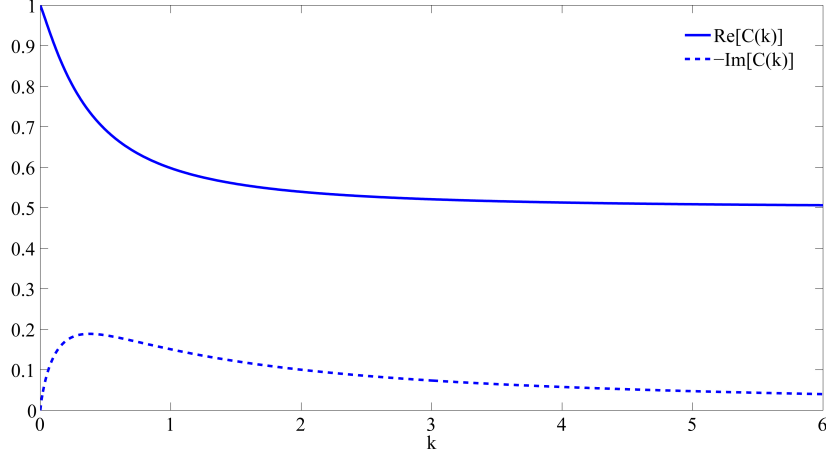


Figure 3.11: Theodorsen circulation function.

[14]. He described the generalized self-excited loads per unit length as the superposition of circulatory ( $c$ , depending on the frequency of oscillations and accounting for flow unsteady effects) and non-circulatory ( $nc$ , frequency-independent and including inertial effects due to the moved fluid mass) contributions. In dimensionless form they result in

$$C_l^{nc}(s) = \frac{C_{l,\alpha}}{4} \left( \alpha' + h'' - \frac{a}{2} \alpha'' \right), \quad (3.43)$$

$$C_m^{nc}(s) = -\frac{C_{m,\alpha}}{2 \left( \frac{1}{2} + a \right)} \left[ \frac{1}{2} \left( \frac{1}{2} - a \right) \alpha' + \frac{1}{4} \left( \frac{1}{8} + a^2 \right) \alpha'' - \frac{a}{2} h'' \right], \quad (3.44)$$

$$C_l^c(k, s) = C_{l,\alpha} \mathcal{C}(k) \left[ \alpha + h' + \frac{1}{2} \left( \frac{1}{2} - a \right) \alpha' \right], \quad (3.45)$$

$$C_m^c(k, s) = C_{m,\alpha} \mathcal{C}(k) \left[ \alpha + h' + \frac{1}{2} \left( \frac{1}{2} - a \right) \alpha' \right] = -\frac{1}{2} \left( \frac{1}{2} + a \right) C_l^c(k, s), \quad (3.46)$$

where  $s = Ut/B$  is the dimensionless time,  $k = B\Omega/U$  is the reduced frequency of oscillation,  $C_{j,\alpha} = \partial \hat{C}_j / \partial \hat{\alpha}$ , and  $f'$  denotes the first derivative of  $f$  with respect to  $s$ , so that the first dimensional time derivative is  $\dot{f} = U f' / B$ . The frequency-dependent function  $\mathcal{C}(k) = \mathcal{F}(k) + i\mathcal{G}(k)$  introduced in Eqs. (3.45) and (3.46) is the Theodorsen's complex circulatory function (see Fig. 3.11), defined by Hankel functions of the second kind [13]. For low frequency regimes (namely, quasi-stationary motions) the imaginary part  $\mathcal{G}(k) = \text{Im}[\mathcal{C}]$  vanishes and the real part  $\mathcal{F}(k) = \text{Re}[\mathcal{C}]$  tends to the unity, so that the circulatory terms reduce to the static aerodynamic loads.

It is worth pointing out that circulatory contributions to lift and moment are expressed by a mixed time-frequency formulation and they both depend on the downwash dimensionless velocity at the three-quarter chord point (namely, the rear neutral point), equal to

$$w_{3/4}(s) = h' + \alpha + \frac{1}{2} \left( \frac{1}{2} - a \right) \alpha'. \quad (3.47)$$

The aerodynamic loads induced by an arbitrary motion of the thin airfoil in a po-

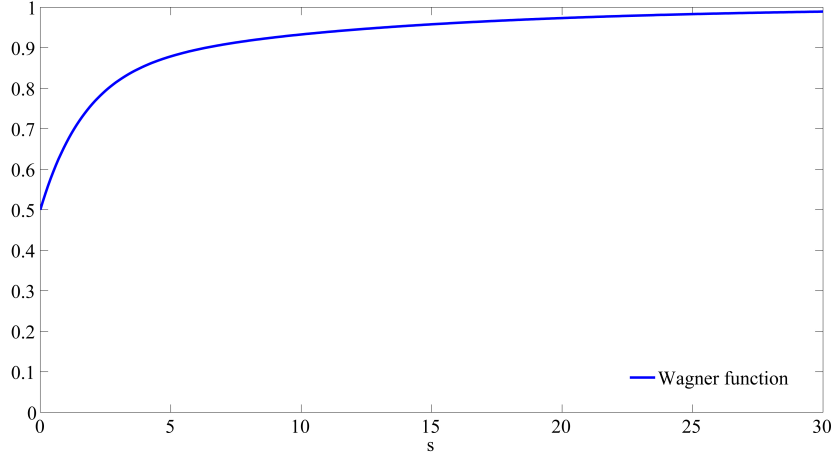


Figure 3.12: Wagner function.

tential flow can be expressed moving from the results proposed by Wagner [15], who solved the problem of an abrupt change of the attack angle from  $\alpha = 0$ . He described the transient evolution of the lift force up to its static value by introducing an indicial lift-growth function  $\phi(s)$ , characterized by  $\phi(0) = 0.5$  and by  $\phi(s)$  tending to 1.0 for  $s$  approaching infinity as depicted in Fig. 3.12.

Due to the special simplicity of the thin airfoil theory, the downwash function  $w_{3/4}(s)$  and the Wagner's indicial function  $\phi(s)$  suffice to define both lift and moment induced by an arbitrary motion that involves also the vertical displacement  $h$ . In this case, invoking the linear superposition principle and assuming that the airfoil moves from the rest at  $s = 0$ , circulatory terms in the time domain are expressed by the following Duhamel's convolution integrals [16]:

$$\begin{aligned}
 C_l^c(s) &= C_{l,\alpha} \int_{-\infty}^s \phi(s-\sigma) w'_{3/4}(\sigma) d\sigma, \\
 &= C_{l,\alpha} \left[ \phi(s) w_{3/4}(0) + \int_0^s \phi(s-\sigma) w'_{3/4}(\sigma) d\sigma \right], \\
 &= C_{l,\alpha} \left[ \phi(0) w_{3/4}(s) + \int_0^s \phi'(\sigma) w_{3/4}(s-\sigma) d\sigma \right], \tag{3.48}
 \end{aligned}$$

$$C_m^c(s) = C_{m,\alpha} \int_{-\infty}^s \phi(s-\sigma) w'_{3/4}(\sigma) d\sigma = -\frac{1}{2} \left( \frac{1}{2} + a \right) C_l^c(s), \tag{3.49}$$

where  $\phi(s)$  is assumed to be null for  $s < 0$ .

By using the Fourier synthesis, a strong duality was proven by Garrick [17] between time-domain and frequency-domain descriptions, resulting in the following relationships among the Theodorsen's circulatory function  $\mathcal{C}(k)$  and the Wagner's indicial function  $\phi(s)$ :

$$\phi(s) = \frac{1}{2\pi i} \int_{-\infty}^{\infty} \frac{\mathcal{C}(k)}{k} e^{iks} dk, \quad \mathcal{C}(k) = ik \int_0^{\infty} \phi(\sigma) e^{-ik\sigma} d\sigma, \tag{3.50}$$

$i$  being the imaginary unit.

The Wagner and Theodorsen approaches are extremely elegant yet powerful as they allows the description of aerodynamic loads generated by any motion history of the immersed airfoil thanks to Eq. (3.49) and during vibrations, respectively. Unfortunately, although the thin airfoil theory has proved to describe with sufficient accuracy the loads measured on real airfoils far from the stall angle, they are in no way directly applicable to bridge decks which are characterized by a more complex aerodynamic behaviour due to the boundary layer detachments and the consequent formation of shear layers.

## Chapter 4

# Viscous and turbulent flows

In the previous chapter the conservation laws governing inviscid flows have been presented and the potential flow theory has been used in order to derive analytic solutions for simple flow fields. It has been stated that, in order to model the development of aerodynamic forces, the introduction of singularities where vorticity is concentrated plays a crucial role and, indeed, it is justified by empirical observations (leading in simple cases to the application of the Kutta-Jourawsky condition). In this chapter the role played by viscosity is highlighted and turbulence introduced completing the physical background needed to rationally justify the subsequent developments.

Turbulence is the main source of prediction errors in Computational Fluid Dynamics. Despite the great interest of the scientific and the industrial community, its intrinsic complexity and chaotic nature remains one of the most challenging field for numerical modelling and it has prevented, until now, the development of simple reliable models which can be deemed to be universally reliable.

In the following, viscosity is introduced in the fluid flow governing equations and its effect on the fluid motion discussed. Then, turbulence is introduced and the available techniques used for its modelling presented.

### Contents

---

<b>4.1</b>	<b>Boundary layer</b>	<b>48</b>
<b>4.2</b>	<b>Viscosity</b>	<b>50</b>
<b>4.3</b>	<b>Momentum conservation for viscous fluids</b>	<b>51</b>
4.3.1	Origin of the boundary layer	52
<b>4.4</b>	<b>Origin of turbulence</b>	<b>53</b>
<b>4.5</b>	<b>Turbulent flows</b>	<b>54</b>
<b>4.6</b>	<b>Kolmogorov's energy spectrum</b>	<b>56</b>
<b>4.7</b>	<b>Time-averaged Navier-Stokes equations</b>	<b>57</b>
4.7.1	Scalar transport equation	58
<b>4.8</b>	<b>Turbulence modelling using RANS models</b>	<b>59</b>
4.8.1	Prandtl's mixing length	59
4.8.2	Two equation models	61

4.8.3 Reynolds Stress Models . . . . .	67
4.9 Large Eddies Simulations . . . . .	68
4.10 Scale-Resolving Simulations . . . . .	69

## 4.1 Boundary layer

It has been noticed in Sec. 3.5.2 that the governing equations for inviscid flows do not allow the fulfilment of suitable boundary conditions near solid walls. In particular, the impermeability condition has been there imposed in order to take into account the effect of solid walls but this appears to be a drastic simplification of the observed flow fields which, in reality, show vanishing tangential relative velocity between the boundary and the fluid as well. This is a major shortcoming of the inviscid flow model and leads to the remarkable inconsistencies that we observed between real and inviscid flows like the D’Alambert paradox.

In reality, the problem lies in the fact that, close to solid boundaries, viscous stresses become important and dominate the behaviour of the fluid which is forced to adhere to the solid boundaries so being delayed with respect to the mean flow. The extent of such zone decreases with increasing  $Re$  number and can be extremely small if compared to the characteristic dimension of the immersed body. There is no unique way to individuate the limits of such flow structure and usually its thickness is defined as the distance from the wall where the velocity reaches 99% of the free stream velocity and it is indicated as boundary layer.

It has been said that viscosity is responsible for the development of the boundary layer. Although the effect of viscosity is surely the cause of the boundary layer development, turbulence, that will be later introduced, plays a crucial role in its structure definition so that, in this section, its description is presented mainly on a qualitative base and in the limit of a morphological description rather than a physical interpretation.

Based on a wide selection of experimental observations of wall bounded flows, it has been demonstrated that, despite the peculiar structure of the free flow field, boundary layers show a universal structure (Fig. 4.1). In the *sublayer*, viscous effects are dominant so that a linear increment of the velocity is observed. Based on dimensional analysis it is possible to write:

$$\mu \frac{\partial u}{\partial y} = \tau_w = \rho u_\tau^2, \quad (4.1)$$

where  $\mu$  is the fluid viscosity,  $\tau_w$  is the constant shear stress observed in the *sublayer* while  $u_\tau$ , from the dimensional point of view, is a velocity which is usually indicated as friction velocity. Rearranging Eq. (4.1), it is possible to write:

$$u_\tau = \sqrt{\tau_w / \rho}. \quad (4.2)$$

Based on the friction velocity, it is possible to define a non-dimensional velocity,  $U^+$ , and a non-dimensional wall distance,  $y^+$ , which are the proper scales to be used in the description of the boundary layer:

$$U^+ = u / u_\tau, \quad (4.3)$$

$$y^+ = y u_\tau \rho / \mu. \quad (4.4)$$

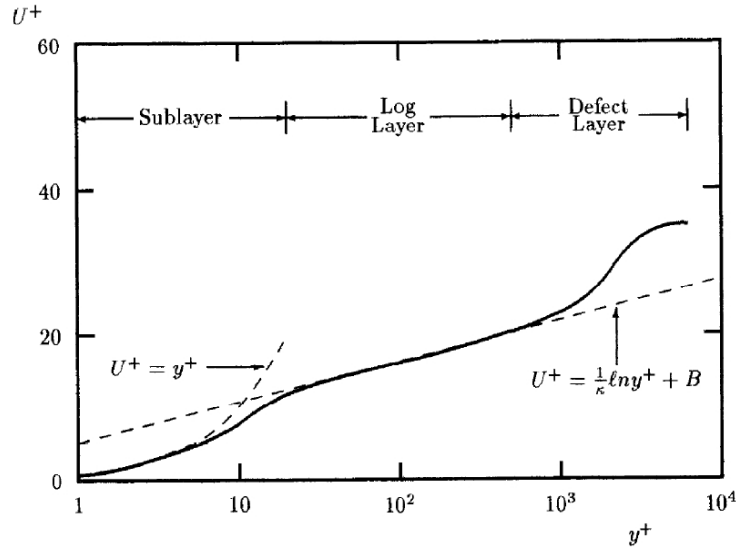


Figure 4.1: Law of the wall [18].

Based on the introduced scales, the well known *law of the wall* depicted in Fig. 4.1, represents the universal velocity distribution observed in boundary layers. It should be noticed that the definition of  $y^+$  is formally equivalent to the definition of a  $Re$  number based on the quantities which are found to be dominant in the boundary layer. Indeed, this is more than a pure formal similarity so that the non-dimensional distance from the wall actually quantifies the relative importance between viscous and inertial forces at the boundary layer scale for any given distance from the wall.

It can be noticed that the proportionality between  $y^+$  and  $U^+$  observed in the viscous sublayer is lost for  $y^+$  higher than 5–10 where a transition is observed to a logarithmic law which dominates the velocity distribution in the *log layer*. This transition is due to the development of turbulence, that will be later introduced, so that the log layer is often referred as the *fully turbulent wall layer* because turbulence effects are dominant in such flow region. The law of the wall in such zone can be expressed as:

$$U^+ = \frac{1}{\kappa} \ln(y^+) + B, \quad (4.5)$$

where  $\kappa \simeq 0.41$  is the universal Von Kármán constant which represents the ratio between the characteristic size of turbulence and the distance from the wall while  $B \simeq 5.0$ . At this point such a law can be considered as an experimental evidence but, later on, a deeper insight will be provided.

Proceeding further away from the wall, for  $y^+ \simeq 1000$ , the velocity profile deviates from the logarithmic law so indicating the transition to the *defect layer* where inertial forces become dominant and the flow distribution is more widely affected by the free stream flow structures.

Right now it is not possible to describe in greater details the observed behaviour. Nevertheless, it must be considered that the structure of the boundary layer played a crucial role in the comprehension of the effects of turbulence on the mean flow and



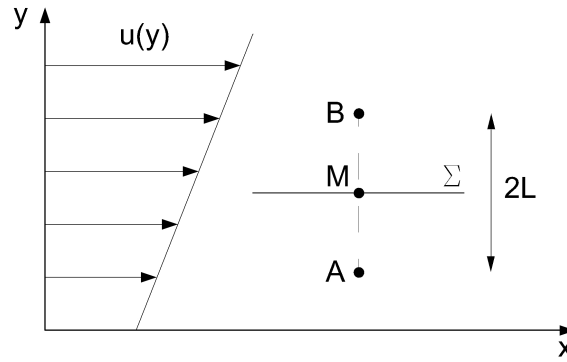


Figure 4.2: Simplified sketch of the mean velocity profile.

the ability of turbulence models in reproducing such universal velocity distribution is considered a fundamental step in their validation process.

## 4.2 Viscosity

It is of interest to clarify what viscosity is before proceeding any further. Although its intuitive concept is familiar to everybody, based on its practical effects, its origin is of fundamental importance as it will be later widely adopted to tackle turbulence modelling.

Consider a shear smooth flow characterized by the velocity profile represented in Fig. 4.2. As already stated, by definition, it is possible to write:

$$\tau = \mu \frac{du}{dy}, \quad (4.6)$$

where  $u = u(y)$  is the velocity component oriented in the  $x$  direction and  $\mu$  is the viscosity constant. The tangential stress,  $\tau$ , represents the momentum flux exchanged between adjacent fluid fillets.

Lets not consider the phenomenon at the molecular scale. Brownian random motions, whose average velocity is the thermal velocity  $u_{th}$ , characterizes the particles motion. We now want to calculate the momentum flux,  $dP$ , originated by such random motion through the unit surface  $\Sigma$ . The random motion is isotropic so that particles move in every direction with equal probability. Under this assumption, only half of the particles move in the  $y$  positive direction so actively contributing to the flux. Furthermore, their average vertical component is  $u_{th} \cos \phi$  where  $\phi$  is the angle from the vertical, leading to an average vertical speed  $u_{th}/2$ . Then, the average number of molecules contributing to the momentum flux is  $nu_{th}/4$ , with  $n$  number of molecules per unit volume. Assuming that molecules have mass  $m$  and that, on average, they have the same velocity of the fluid region they come from, the momentum flux oriented from A to B through the unit surface  $\Sigma$  is:

$$dP_{AB} = nm [u(M) - u(A)] \simeq \frac{1}{4} \rho u_{th} L \frac{du}{dy}. \quad (4.7)$$

Analogously, considering the flux crossing  $\Sigma$  oriented from B to A:

$$dP_{BA} \simeq \frac{1}{4} \rho u_{th} L \frac{du}{dy}, \quad (4.8)$$

so that the total flux is:

$$dP \simeq \frac{1}{2} \rho u_{th} L \frac{du}{dy}. \quad (4.9)$$

It is then possible to write:

$$\tau = \mu \frac{du}{dy} = \frac{1}{2} \rho u_{th} L \frac{du}{dy}, \quad (4.10)$$

which leads to the identification of the viscosity as:

$$\mu = \frac{1}{2} \rho u_{th} L. \quad (4.11)$$

In this framework  $L$  can be identified as the *mean free path* of the particle. This result of the Gas Kinetic Theory is of crucial importance and can be used to accurately describe the viscosity of gases. One immediate consequence of such a model is that viscosity must increase with temperature because it increases the thermal velocity while cryogenic fluids must exhibit extremely low viscosity as they are close to the absolute zero temperature which implies absence of molecular random motion. Both predictions are confirmed by experiments.

For what it concerns us, it is now clear that viscosity represents the diffusion of the momentum in the flow due to molecular random motions, in analogy to energy and species diffusion.

### 4.3 Momentum conservation for viscous fluids

The momentum conservation law, expressed in Eq. (3.9), is of general applicability and the only modification needed in order to take into account the effect of viscosity is the form adopted for  $\mathbf{T}$ . The equation is here reported for the reader convenience:

$$\frac{\partial(\rho u_i)}{\partial t} + \text{div}(\rho \mathbf{u} u_i) + \text{div}(-\mathbf{T}_{i,:}) = S_{ui}. \quad (4.12)$$

In this case the form for  $\mathbf{T}$  is chosen, according to the results described in the previous section, as:

$$\mathbf{T} = -p \cdot \mathbf{I} + 2\mu \cdot \mathbf{S}, \quad (4.13)$$

where  $\mathbf{S}$  is the strain rate tensor defined as:

$$\mathbf{S} = \frac{1}{2} (\text{grad}(\mathbf{u}) + \text{grad}(\mathbf{u})^T), \quad (4.14)$$

so accounting for the viscosity effects and leading to additional second order terms. It must be noticed that, the new choice of the stress tensor radically changes the nature of the equations as they become second order in space allowing the adoption of physically sound boundary conditions.

This system, coupled with the mass conservation equation, is known as Navier-Stokes system and it is the standard model for the description of Newtonian fluids. It is here important to stress that, from the theoretical point of view, such equations contain all the physics needed to model the flow and are able to predict extremely complex phenomena such as laminar to turbulence transition, turbulence development and decay.

From the practical point of view, the problem lies in the fact the solution of this system often leads to extremely complex flow fields, characterized by a wide spectrum of length and time scales interacting with each other, whose description is far beyond the computational power of modern computers.

The direct integration of the Navier-Stokes system is indicated as Direct Numerical Simulations (DNS). Such kind of simulations are used in the research field to provide insight in the mechanisms involved in the turbulence development and require extremely large computational facilities even for extremely simple flows.

The problem is exquisitely technological but, considering that even modern HCP supercomputers are unable to solve the system for cases of technical interests with sufficient accuracy at high  $Re$  number, the DNS approach is not sustainable in practice and this fact is unlikely to change in the near future.

### 4.3.1 Origin of the boundary layer

In this section a mathematical insight in the reasons for the development of the boundary layer is quickly analysed. A useful, detailed and more comprehensive explanation of this matter can be found in [18].

It is observed that the Navier-Stokes equations for viscous fluids can be written in non-dimensional form by substituting Eq. (4.13) in Eq. (4.12) and dividing terms by the appropriate reference scales. In such a way it is found that the terms representing viscous effects are multiplied by the inverse of the  $Re$  number. When the  $Re$  number is high, these terms tends asymptotically to zero becoming a small number  $\delta$  and thus making the equations approach the case obtained for the inviscid fluid.

The Navier-Stokes equations, specialized for inviscid fluids, have been already described and it has been already noticed that, in that case, it was not possible to respect the no-slip condition for solid boundaries. Indeed, such observation is coherent with the fact that the equations are second order in space if viscosity is considered but become first order when its contribution is discarded so decreasing the requirements that can be fulfilled at the domain boundaries.

Such problem is common to all differential equations that show vanishing coefficients multiplying the highest order derivatives and useful information regarding their asymptotic behaviour can be obtained by using perturbation methods.

In order to provide a simple example showing the same characteristics of the Navier-Stokes system, the following equation is considered in [18]:

$$\delta \frac{d^2 F}{ds^2} + \frac{dF}{ds} + F = 0 \quad 0 \leq s \leq 1, \quad (4.15)$$

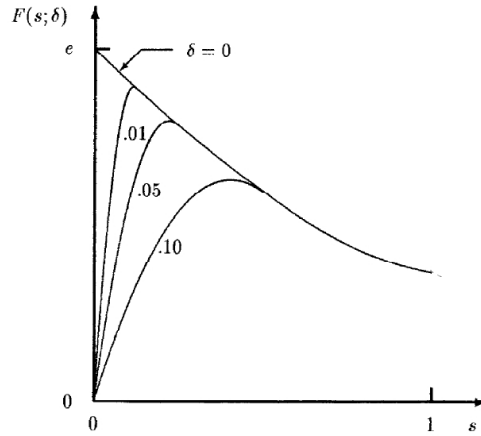


Figure 4.3: Solution of Eq. (4.15) and boundary conditions (4.16) with varying  $\delta$ . [18].

where  $F$ , in this case, is a generic variable that can be assimilated to the velocity in the Navier-Stokes system. The following boundary conditions are considered:

$$F(0) = 0, \quad F(1) = 1. \quad (4.16)$$

which are analogous to a solid wall and a free stream condition. When  $\delta = 0$  the equation is first order only and it is not possible to respect both boundary conditions (only the second one is then imposed which leads to a non-trivial solution). When  $\delta$  is increased it is possible to fulfil both conditions but a boundary layer (inner layer) is created which blends the newly imposed boundary condition to the solution obtained for  $\delta = 0$  (which is known as outer layer). The thickness of such zone vanishes with vanishing  $\delta$  so that the length scale of the inner layer tends to collapse with respect to the scales of the outer layer (see Fig. 4.3).

The described problem is one of the main complications encountered in the solution of the Navier-Stokes equations from both the analytical and the numerical point of view and greatly differentiate the behaviour of fluid systems at low and high  $Re$  numbers.

## 4.4 Origin of turbulence

It has been stated in Sec. 4.3 that the Navier-Stokes equations often leads to extremely complex solutions. It is here important to focus the attention on the source of such complexity. When velocity gradients exist between two regions, even for inviscid fluids, small disturbances of the velocity profiles can be amplified or damped out. This is the matter of Linear Hydrodynamic Stability Theory [19] which gives a precious insight in the mechanisms involved in the transition from laminar to turbulent flow.

The mechanisms that tend to amplify such small disturbances are a source of instability and, before proceeding any further, an example will help to clarify their importance in the definition of the flow field. Figure 4.4 shows the development of the Kelvin-Helmholtz instability. Consider two layers of fluid moving at different speed. This situation is typical of the shear layers encountered in real flows such as jets and

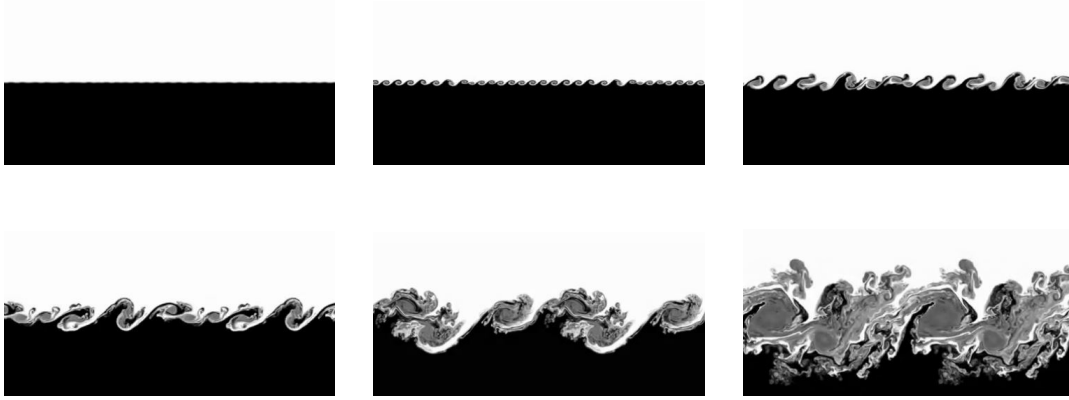


Figure 4.4: Numerical simulation of the Kelvin-Helmholtz instability [20].

flow detachments around bluff bodies. In this case, small perturbations are introduced at the interface between the two layers of fluid and the system is allowed to evolve. The disturbances are rapidly amplified and the system quickly moves from a highly organized state to a chaotic one characterized by a fractal isotropic distribution of vortical structures.

The Kelvin-Helmholtz instability is two-dimensional but in real flows a great number of similar mechanisms exist which inevitably lead to full three-dimensionality of the turbulent structures. The viscous forces usually act as a stabilizing contribution in such mechanisms even if this statement is not of general applicability and cases exist which show opposite behaviour.

Despite the particular mechanism involved in the transition to turbulence, the stability of these mechanisms is a function of the  $Re$  number so, with no surprise, such parameter strongly influences the flow topology.

## 4.5 Turbulent flows

Once the transition from laminar to turbulent flow is completed, the flow is defined as fully turbulent and the origin of the transition is no longer recognizable. Indeed, it seems that, whatever the triggering mechanisms is, turbulence tends to assume a universal form and it superimposes and interacts with the mean flow which, on the contrary, is completely case dependent. As already stated, the flow always appears to be fully three-dimensional even when the mean flow is two-dimensional. A visual representation of a turbulent flow is reported in Fig. 4.5 (a) in order to allow visual inspection of the described phenomenon.

Let us now consider a fully turbulent flow, whose mean velocity  $U$  is oriented in the  $x$  direction and suppose to measure the three components of the velocity vector  $\mathbf{u} = (u, v, w)$  in one point. An example of the recorded time histories can be observed in Fig. 4.5 (b).

As already stated, the flow is characterized by a fractal distribution of vortical structures interacting with each other and with the mean flow. A wide range of length

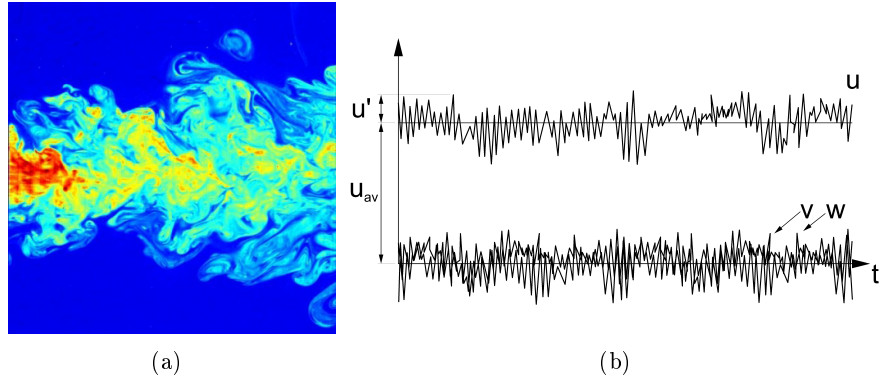


Figure 4.5: Turbulent flow: (a) image of a turbulent flow [20], (b) time history of velocity.

and time scales are present in the flow which appears chaotic, isotropic and three-dimensional. Large vortical structures (eddies) are transported downstream by the mean flow and are characterized by its velocity scale. It is possible to define a  $Re$  number for such eddies as follows:

$$Re_e = \frac{\rho U_e l_e}{\mu}, \quad (4.17)$$

where  $Re_e$  is the eddy  $Re$  number,  $U_e$  is the typical eddy velocity,  $l_e$  is the typical eddy length scale. The large eddies are characterized by high  $Re_e$  indicating that viscous effects are negligible so they behave as conservative structures. Such large vortical structures mainly interact with the mean flow which tends to stretch them due to gradients in the mean velocity distribution. When the eddies are stretched they become unstable and eventually brake transferring energy to smaller length scales.

The smaller structures are only marginally deformed by the mean flow but they strongly interact with the large vortical structures which provide the energy needed for the vortex stretching.

Such mechanism is reproduced at every length scale leading to what is usually called *energy cascade* which is to say that energy is continuously transferred from the mean flow to the large vortical structures and down to the small ones.

Once the energy has been transferred to smaller and smaller structures, typically for length and time scales comparable to  $1/10 - 1/100 \text{ mm}$  and  $1/10000 \text{ sec.}$ , respectively, viscosity becomes important and energy is dissipated into heat.

The level of isotropy of the eddies is indeed not uniform. In fact, large eddies, which strongly interact with the mean flow, are usually not isotropic. Nevertheless, a strong tendency to isotropy is observed in the energy cascade so that smaller scales tend to quickly lose information about the mean flow orientation.

From the experimental point of view, it is observed that the evolution of the flow field does not follow a deterministic dynamic (two experiments do not lead to identical results) and only statistical properties can be used to describe the flow which should be thus regarded as a stochastic process. For later convenience, following such an approach, the velocity field is decomposed into a slowly time dependent contribution,  $u_{av}$ , and a zero mean fluctuating contribution,  $u'$ , as depicted in Fig. 4.5 (b). Analogous

decomposition is applied to all the quantities involved in the flow.

For later convenience the turbulent kinetic energy,  $k$ , is here introduced as follows:

$$k = \frac{1}{2} \left( \overline{u'^2} + \overline{v'^2} + \overline{w'^2} \right), \quad (4.18)$$

where the overbar indicates the time averaging operation. In the following attention should be paid in order to avoid confusion between the reduced frequency and the turbulent kinetic energy here introduced (the symbol is overloaded in order to match standard notations).

## 4.6 Kolmogorov's energy spectrum

It is beyond the aim of this thesis to fully develop the theory underlying the study of turbulence and the reader can refer to [18] for details. Nevertheless, in order to understand the hypotheses embedded in turbulence modelling, some additional details are here presented.

We already introduced the concept of *energy cascade* and discussed that medium and small scales show a universal structure independently from the large scales that contributed to their development. Furthermore, it has been said that energy is extracted by the large scales from the mean flow and transferred to smaller scales. If we assume that turbulence is in equilibrium, meaning that its statistical properties are time invariant, all the energy extracted by the large scales must be transferred to the smaller ones and finally dissipated without accumulation at specific scales. In such a process the relevant parameters are the turbulent kinetic energy,  $k$ , its rate of dissipation,  $\epsilon$ , and the fluid viscosity,  $\mu$ . Considering that both  $k$  and  $\epsilon$  are defined per mass unit, the kinematic viscosity,  $\nu$ , will be used in the following developments. At this point, from the dimensional point of view, we have:

$$[k] = \frac{m^2}{s^2}, \quad [\epsilon] = \frac{m^2}{s^3}, \quad [\nu] = \frac{m^2}{s}, \quad (4.19)$$

on the basis of such quantities Kolmogorov in 1941 defined the following length, velocity and time scales:

$$\eta_{kol} = \left( \frac{\nu^3}{\epsilon} \right)^{\frac{1}{4}}, \quad v_{kol} = (\nu\epsilon)^{\frac{1}{4}}, \quad t_{kol} = \left( \frac{\nu}{\epsilon} \right)^{\frac{1}{2}}. \quad (4.20)$$

Lets now consider the Fourier transformation of  $k(t)$ ,  $E(\kappa)$ , where  $\kappa$  is the wavenumber (whose physical dimensions are  $1/m$ ). The following identity holds:

$$k \equiv \frac{1}{2} \overline{u_i'^2} = \int_0^\infty E(\kappa) d\kappa. \quad (4.21)$$

The physical dimensions of  $E(\kappa)$  are:

$$[E(\kappa)] = \frac{m^3}{s^2}. \quad (4.22)$$

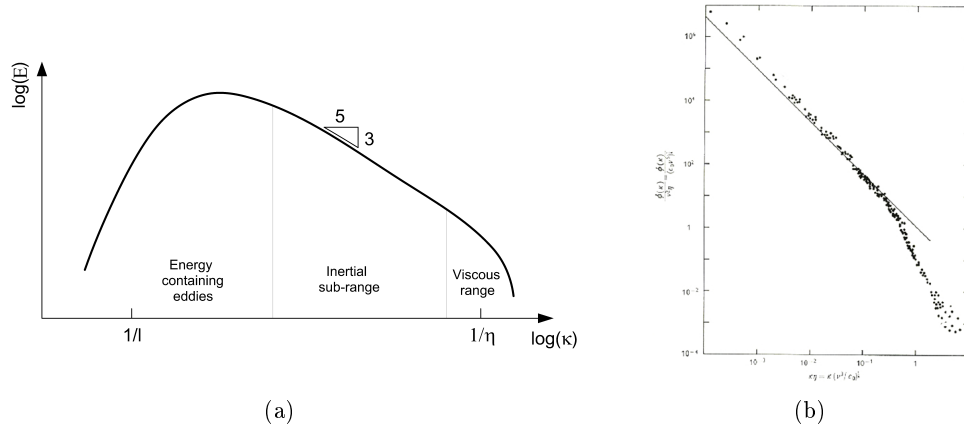


Figure 4.6: Kolmogorov spectrum: (a) theoretical spectral energy distribution, (b) experimental results. [22]

Under such assumptions, the physical dimensions of  $E(\kappa)$  are:

$$E(\kappa) = C_k \epsilon^{2/3} \kappa^{-5/3} \quad \frac{1}{l} \ll \kappa \ll \frac{1}{\eta} \quad (4.23)$$

where  $l$  and  $\eta$  are the characteristic length scale of the large inertial eddies and the small dissipative ones, respectively. Such behaviour has been observed both experimentally and in numerical simulations which employ scale resolving approaches to turbulence modelling (see Sec. 4.6). Indeed, this result is so well established that "theoretical or numerical predictions are regarded with scepticism if they fail to reproduce it" [21].

## 4.7 Time-averaged Navier-Stokes equations

The direct solution of the Navier-Stokes equations, although theoretically possible, is not feasible for flows of technical interest. The size of the mesh and time step should be defined based on the smallest scales while the extent of the computational domain is defined by the problem macroscopic scale. The problem is so severe that, even with modern supercomputers, an accurate solution might take millions of years to be obtained. This is particularly true when high  $Re$  number are considered. In fact, while the large scales are  $Re$ -independent the small ones decrease in size when  $Re$  is increased so widening the length and time scales range.

In order to overcome such problem, it is possible to rewrite the Navier-Stokes equations introducing a time averaging filter which has the effect of smoothing out the high frequency components of the spectrum.

The governing equations for the time averaged quantities can be deduced as follows. Consider the scalar time varying quantity  $q(t)$  and its time average,  $q_{av}$ , calculated over a short but significant amount of time. Its evolution in time, according to Fig. 4.5, can be decomposed as:

$$q(t) = q_{av}(t) + q'(t), \quad (4.24)$$



where  $q'(t)$  is the high frequency containing contribution while  $q_{av}$  can be defined as follows:

$$\overline{q(t)} = q_{av}(t) = \frac{1}{\Delta t} \int_t^{t+\Delta t} q(\tau) d\tau, \quad (4.25)$$

being  $\bar{\cdot}$  the time averaging operation. Let's now consider, in analogy to  $q(t)$ , another variable  $f(t)$ . It can be demonstrated that the following relations hold:

$$\begin{aligned} \overline{q'} &= \overline{f'} = 0, & \overline{q_{av}} &= q_{av}, & \frac{\partial \overline{q}}{\partial t} &= \frac{\partial q_{av}}{\partial t}, \\ \overline{\int q dt} &= \int q_{av} dt, & \overline{q + f} &= q_{av} + f_{av}, & \overline{qf} &= q_{av} f_{av} + \overline{q' f'}, \\ \overline{q f_{av}} &= q_{av} f_{av}, & \overline{q' f_{av}} &= 0. \end{aligned} \quad (4.26)$$

If a fluctuating vector,  $\mathbf{r}$ , is considered the following holds:

$$\begin{aligned} \overline{div(\mathbf{r})} &= div(\mathbf{r}_{av}), & \overline{div(grad(q))} &= div(grad(q_{av})), \\ \overline{div(q\mathbf{r})} &= div(\overline{q\mathbf{r}}) = div(q_{av}\mathbf{r}_{av}) + div(q'\mathbf{r}'). \end{aligned} \quad (4.27)$$

If the Navier-Stokes equations are rewritten introducing the averaged and the fluctuating quantities, the resulting equations look like:

$$\frac{\partial(\rho u_i)}{\partial t} + div(\rho \mathbf{u} u_i) + \frac{\partial p}{\partial x_i} - div(2\mu \cdot \mathbf{S}_{i,:}) + div(\overline{\rho u'_i \mathbf{u}'}) = S_{ui}, \quad (4.28)$$

where the subscript  $av$  has been dropped for the sake of notation clearness so that all the quantities should be regarded as time averaged ones with the exception of the ones marked with  $'$ . In the averaging process the mass conservation law does not modify, from the formal point of view, and it is not here rewritten.

The time averaging process introduced new terms which represent the momentum diffusion due to the fluctuating nature of the flow field. Unfortunately such terms, which are covariances between the fluctuating quantities, are not known so that the process introduced extra unknowns without introducing the extra equations needed to solve the system. This is universally known as the *closure* problem and it is the core of turbulence modelling.

From the physical point of view, such covariances represent momentum fluxes and are usually indicated as Reynolds stresses.

#### 4.7.1 Scalar transport equation

For later convenience the conservation law for scalar quantities is here introduced as it is extensively used in turbulence modelling. Such equation corresponds to Eq. 3.1.

If we consider a scalar quantity which diffuses and it is convected by the flow, the following conservation equation holds:

$$\frac{\partial(\rho q_{av})}{\partial t} + div(\rho q_{av} \mathbf{u}) - div(\Gamma_q \cdot grad(q_{av})) + div(\overline{\rho q' \mathbf{u}'}) = S_q, \quad (4.29)$$

where  $\Gamma_q$  represent the diffusion of the scalar quantity given by molecular random motion while the terms implying correlations of the fluctuating components can be interpreted as diffusion due to turbulence.

## 4.8 Turbulence modelling using RANS models

In the previous section the time averaged Navier-Stokes equations have been introduced. The process led to the introduction of additional unknowns in the system without providing any additional equation. From the theoretical point of view, it is possible to find exact equations for such terms but this strategy does not solve the problem as it systematically introduces more unknowns than new equations.

In order to solve the system these unknown terms must be modelled so that their effect on the mean flow mimics the behaviour of the exact ones. Additionally, they should be modelled using the mean flow quantities, for which the governing equations are known, or using additional quantities and writing for them additional conservation laws.

Many attempts have been made to develop such models but none of them can be claimed to be robust, accurate and universally applicable. The approach to the flow field solution described up to this point is usually indicated as RANS (Reynolds-averaged Navier-Stokes) and must be coupled with a turbulence model which provides a reasonable description of the terms introduced in the time-averaging filtering.

### 4.8.1 Prandtl's mixing length

This is the simplest available turbulence model but it already contains some of the most important concepts that will be further developed when more complicated models will be introduced.

In particular, Boussinesq in 1887 was the first one to propose a simple but reasonable way to account for the effect of turbulence on the mean flow. The idea stemmed from the fact that turbulence promotes diffusion in the fluid similarly to the Brownian random motion. Furthermore, turbulence often shows an isotropic pattern so that no information about directionality is preserved in many fully turbulent flows. From this point of view it makes sense to model the effect of turbulence as an additional viscosity which is usually indicated as *turbulent viscosity* to be superimposed to the one provided by the particle random motion.

On dimensional ground, according to what has been obtained for viscosity in Eq. (4.11), it is possible to state that:

$$\mu_t = C\rho U_t L_t, \quad (4.30)$$

where  $C$  is a constant while  $U_t$  and  $L_t$  are turbulence velocity and length scales, respectively. If we keep in mind the velocity profile represented in Fig. 4.2, it makes sense to state that:

$$U_t \propto L_t \left| \frac{\partial u}{\partial y} \right|. \quad (4.31)$$

Substituting Eq. (4.31) into (4.32) the following is obtained:

$$\mu_t = C\rho L_t^2 \left| \frac{\partial u}{\partial y} \right|. \quad (4.32)$$

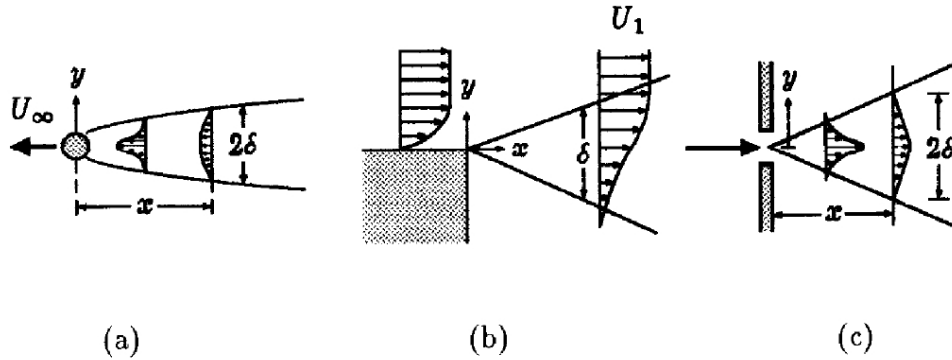


Figure 4.7: Self similar flows: (a) wake, (b) mixing layer, (c) jet [18].

In this way, assuming that we are able to estimate a value for  $L_t$ , the Reynolds-averaged Navier-Stokes equations can be solved.

Indeed, the problem now is to estimate  $L_t$ . Such parameter represents an effective mixing length thus the model is assuming that, with respect to the mean flow, a "typical" eddy exists, that is able to represent the mixing effect of the real eddies distribution. There are few, yet relevant, examples of simple flows that are well captured by this modelling framework. Those flows are usually free shear flows and are characterized by self similarity [7, 18] like jets, mixing layers and boundary layers (see Fig.4.7). In such conditions, the length scale can be expressed as a constant fraction of the flow transverse dimension,  $\delta$ , so allowing the solution of the system (see Fig. 4.7).

Unfortunately, nothing exists like a general rule able to provide  $L_t$ , which is usually a function of space, for all flows of technical interest.

For self similar flows, simple rules can be used to map  $L_t$  and, if well calibrated, results can be surprisingly accurate. Nevertheless, the major shortcoming of the mixing length model lies essentially in the need to provide a distribution for  $L_t$  as an input data of the analysis.

### Von Kármán constant and boundary layer

The mixing length model has limited applicability to flows of technical interest, nevertheless it is now possible to shed light on the structure of the boundary layer that has been presented in Sec. 4.1. Lets consider the case of a boundary layer produced by a surface orthogonal to the  $y$  direction. The  $x$ -oriented momentum conservation law written for a two-dimensional flow reads:

$$\rho \frac{\partial u}{\partial t} + \rho u \frac{\partial u}{\partial x} + \rho v \frac{\partial u}{\partial y} + \frac{\partial p}{\partial x} - \frac{\partial}{\partial y} \left[ \mu \frac{\partial u}{\partial y} + \tau_{xy}^{Re} \right] = 0, \quad (4.33)$$

where  $\tau_{xy}^{Re}$  is the Reynolds stress. Considering a steady state solution and that in such a boundary layer the terms

$$\frac{\partial \cdot}{\partial x} \ll \frac{\partial \cdot}{\partial y}, \quad (4.34)$$

and that convective terms are negligible, the equation simplifies as follows:

$$\frac{\partial}{\partial y} \left[ \mu \frac{\partial u}{\partial y} + \tau_{xy}^{Re} \right] = 0, \quad (4.35)$$

implying that the sum of the viscous stress and the Reynolds stress is constant throughout the viscous sublayer and the log layer. Following the mixing length approach and considering that in the log layer the Reynolds stresses dominate the viscous ones, it is possible to write:

$$L_t^2 \left( \frac{\partial u}{\partial y} \right)^2 \simeq u_\tau^2. \quad (4.36)$$

Remembering the physical meaning of  $L_t$ , it is reasonable to assume that the mixing length is in some way proportional to the distance from the wall, so that:

$$L_t = \varkappa y, \quad (4.37)$$

where  $\varkappa$  is the already introduced Von Kármán constant. The straightforward integration of such equation leads to:

$$u(y) \simeq \frac{u_\tau}{\varkappa} \ln(y) + B, \quad (4.38)$$

which is in agreement with the law of the wall and the experimental results.

#### 4.8.2 Two equation models

In the mixing length model, the turbulence length scale is an external parameter to be provided based on experimental results and empirical laws. Using such an approach, it is possible to study only simple flows, which are already well known and that allow a simple description of the turbulence length scale distribution. If we want to avoid such shortcoming, we must develop a turbulence model which do not require such specific input.

According to Boussinesq hypothesis, we assumed that we can mimic turbulence by introducing a turbulent viscosity. The definition of such quantity is linked to the punctual identification of a length and a velocity scale representing the turbulence scales that contribute the most to the flow mixing.

Going back to the Kolmogorov spectrum, it is possible to notice that two quantities, the turbulent kinetic energy and its dissipation rate,  $k$  and  $\epsilon$ , have been introduced assuming that they would suffice to characterize the energy cascade of isotropic turbulence in equilibrium condition.

Dimensional analysis in this case provided an invaluable insight in the phenomenon. In fact, on dimensional ground, these two quantities suffice to provide the two scales needed to define an equivalent turbulent viscosity, so bridging the gap between the complex physical phenomenon and the relatively simple approach we are building to model it. In fact, it is possible to write:

$$U_t = k^{1/2}, \quad L_t = \frac{k^{3/2}}{\epsilon}, \quad (4.39)$$

so that the turbulent viscosity can be defined as:

$$\mu_t = \rho C_\mu \frac{k^2}{\epsilon}, \quad (4.40)$$

where  $C_\mu$  is a model constant to be calibrated. The problem now lies in the fact that  $k$  and  $\epsilon$  are two scalar field which are not known *a priori*. At this point, from the conceptual point of view, we can follow two approaches which lead to identical results.

The first one is to derive from the Navier-Stokes equations the conservation laws for  $k$  and  $\epsilon$ . The process is not here reported and it can be found in [18]. Unfortunately the result are two conservation laws involving triple and higher correlations between fluctuating quantities and a definition for  $\epsilon$  involving correlations between their spatial derivatives. Such new unknown terms can be modelled one by one using quantities related to the mean flow and empirical constants, based on our best knowledge of the phenomenon.

As suggested by Wilcox [18] "This process is by no mean rigorous. The closure approximations are no better than the turbulence data upon which they are based" and he defined the term by term modelling as drastic surgery on the governing equations.

Fortunately, looking at such complicated high order correlations, it can be seen that the physical meaning of such terms can be identified and matched with the standard phenomena observed in fluid flows like diffusion, diffusion due to turbulence, convection, production and destruction. This is to say that it is possible to write a conservation law for  $k$  and  $\epsilon$ , on the model of Eq. (4.29), and calibrate its coefficients based on experimental evidences with the attention to divide in the source terms the creation,  $C_q$ , and the destruction,  $D_q$ , as follows:

$$S_q = C_q + D_q. \quad (4.41)$$

Such approach leads to the definition of some of the most commonly adopted turbulence models and it is one of the simplest way to create a model which can be deemed to be complete, meaning that the closure coefficients can be calibrated on standard experiments (for example free isotropic turbulence decay and similar cases) and directly adopted in other cases of industrial interest.

At this point, before proceeding any further, it is important to critically review the hypotheses that have been introduced. The first step, common to every approach to Computational Fluid Dynamics that involves turbulence modelling, has been to filter the Navier-Stokes equations. In our case we used time averaging but space averaging can be used instead, leading to another family of turbulence models that will be later introduced.

Independently from the particular filtering choice adopted, this operation inevitably leads to the introduction of additional unknowns in the equations which are not compensated by the definition of additional conservation laws. Such terms, which from the dimensional point of view are momentum fluxes due to turbulence, must be modelled according to our best knowledge of their effect on the flow.

Inspired by the analogy between turbulence and Brownian random motion (Kinetic Theory of gasses), Boussinesq modelled such terms as an additional viscosity strongly relying on dimensional analysis. In this way, our problem is reduced to the punctual

identification of a turbulent length and velocity scale which, in our framework, should represent the whole turbulence spectrum mixing effect. Such scales have been finally defined writing two additional conservation laws for the turbulent kinetic energy and its dissipation rate once again mainly relying on dimensional analysis. This is, with a certain degree of simplification and ignoring some technical details, the framework which led to the definition of the universally famous  $k - \epsilon$  turbulence model.

It is now clear that there is not a restriction *a priori* on the quantities that should be used to define the turbulent viscosity, provided that a length and a velocity scale can be defined through their combination and that a conservation law can be written to model their evolution in the flow. Turbulence models derived adopting the described framework are known as two-equation models.

Additionally, some clarifications are needed. Firstly, the effort in developing a universally valid turbulence model does not match in general with its accuracy. For example, considering simple flows, if the mixing length model is well calibrated, results might be more accurate than any two-equation model. Secondly, in between the proposed approaches many other have been proposed which, in terms of complexity and physical insight, can be considered hybrid between the described ones.

### The $k - \epsilon$ turbulence model

This model is still today probably the most commonly used in industrial applications. The two quantities employed for the characterization of turbulence, as already stated, are  $k$  and  $\epsilon$ . Their transport equations can be written as follows:

$$\frac{\partial(\rho k)}{\partial t} + \text{div}(\rho k \mathbf{u}) - \text{div} \left( \left( \mu + \frac{\mu_t}{\sigma_k} \right) \cdot \text{grad}(k) \right) = \mathbf{T}_{Re} : \text{grad}(\mathbf{u}) - \rho \epsilon, \quad (4.42)$$

$$\frac{\partial(\rho \epsilon)}{\partial t} + \text{div}(\rho \epsilon \mathbf{u}) - \text{div} \left( \left( \mu + \frac{\mu_t}{\sigma_\epsilon} \right) \cdot \text{grad}(\epsilon) \right) = C_{1\epsilon} \frac{\epsilon}{k} \mathbf{T}_{Re} : \text{grad}(\mathbf{u}) - C_{2\epsilon} \rho \frac{\epsilon^2}{k} \quad (4.43)$$

where  $\mathbf{T}_{Re}$  is the Reynolds stress tensor that will be later introduced, the operator  $:$  denotes the Frobenius product while the diffusion due to turbulence is modelled based on  $\mu_t/\sigma_q$  ( $q = \mu, \epsilon$ ) where  $\mu_t$  is the already introduced turbulent viscosity and  $\sigma_q$  is a ratio which characterizes the efficiency of the diffusion of the quantity  $q$  with respect to the momentum. The terms on the right hand side of the equations represent production and destruction of the transported quantity, respectively. Considering the peculiar mechanism of turbulent mixing, which involves mass transport due to eddies, the value of the coefficient  $\sigma_q$  is usually close to one.

The Reynolds stress tensor can be modelled as follows:

$$\mathbf{T}_{Re} = 2\mu_t \cdot \mathbf{S} - \frac{2}{3}\rho k \mathbf{I} \quad (4.44)$$

where  $\mathbf{I}$  is the identity matrix. The second term ensures that the trace of  $\mathbf{T}_{Re}$  is consistent with the definition of turbulent kinetic energy provided in Eq. (4.18). The total stress tensor will be build by adding the Reynolds stress tensor to the viscous stresses tensor.

The equations must be closed by adding to the Navier-Stokes system and the two

additional transport equations, the following constitutive relationships:

$$\begin{aligned} \mu_t &= \rho C_\mu \frac{k^2}{\epsilon}, \\ C_\mu &= 0.09, \quad \sigma_k = 1.00, \quad \sigma_\epsilon = 1.30, \quad C_{1\epsilon} = 1.44, \quad C_{2\epsilon} = 1.92. \end{aligned} \quad (4.45)$$

Such system of equations, algebraic relations and constant is known as standard  $k - \epsilon$  model.

Suitable boundary conditions must be provided to allow the solution of the system. Indeed, this task, especially at the inlet and in correspondence to solid walls is not trivial and represents itself a great source of uncertainty and complication. To what it concerns us, it must be said that the  $k - \epsilon$  model is not reliable close to solid walls so that *ad hoc* techniques have been developed in order to overcome such shortcomings as presented in the next section.

Another well known problem of the  $k - \epsilon$  model is that it tends to overestimate the production of  $k$  in stagnation points so including excessive dissipation in their surroundings. Nevertheless, it is a relatively inexpensive and robust approach to turbulence modelling and proved to behave reasonably well in fully turbulent internal flows.

### The $k - \omega$ turbulence model

The two major shortcomings of the  $k - \epsilon$  model have been described in Sec. 4.8.2. Trying to find a solution for them, Wilcox [18] created a model, inspired by early works of Kolmogorov, that instead of being based on the specific dissipation rate per mass unit,  $\epsilon$ , is based on the specific dissipation rate per mass and turbulent kinetic energy unit,  $\omega = \epsilon/k$ . The resulting model reads:

$$\frac{\partial(\rho k)}{\partial t} + \text{div}(\rho k \mathbf{u}) - \text{div}((\mu + \sigma^* \mu_t) \cdot \text{grad}(k)) = \mathbf{T}_{Re} : \text{grad}(\mathbf{u}) - \beta^* \rho k \omega, \quad (4.46)$$

$$\frac{\partial(\rho \omega)}{\partial t} + \text{div}(\rho \omega \mathbf{u}) - \text{div}((\mu + \sigma \mu_t) \cdot \text{grad}(\omega)) = \alpha \frac{\omega}{k} \mathbf{T}_{Re} : \text{grad}(\mathbf{u}) - \beta \rho \omega^2. \quad (4.47)$$

Auxiliary equations and the model constants are:

$$\mu_t = \rho k / \omega, \quad \alpha = 5/9, \quad \beta = 3/40, \quad \beta^* = 9/100, \quad \sigma = \sigma^* = 1/2. \quad (4.48)$$

The resulting model has proved to lead to good results, especially because the resulting equations can be integrated through the boundary layer. Unfortunately, the model is extremely sensitive to the value of the turbulence-related boundary conditions which is often problematic as we do not have good estimates for them. Furthermore, in RANS models the meaning of such boundary values for turbulence should not be overestimated. They often represent no more than parameters governing the model dissipation rather than measurable physical quantities.

### The $k - \omega$ *sst* turbulence model

This model, which is one of the most used in the industrial practice nowadays, tries to combine together qualities of the two aforementioned models. It has been developed

by Menter [23, 24] and it consists in a blending between the two presented models. In particular, the  $k - \epsilon$  model is used far from the solid walls so taking advantage of its robustness and relatively small boundary condition dependence while the  $k - \omega$  is used close to the solid walls so allowing direct integration through the boundary layer.

The blending between the two models is obtained by rewriting the  $k - \omega$  in terms of  $k$  and  $\epsilon$  and weighting the two models using smooth functions which depend on the non-dimensional wall distance.

The result is a robust model which provides good, physically sound, results for a variety of problems even when the hypotheses implicit in RANS approach are not strictly respected.

### Wall functions

It has been stated in Sec. 4.8.2 that the  $k - \epsilon$  model does not provide good results when integrated through the boundary layer. It must be noticed that integrating the filtered Navier-Stokes equation through the boundary layer is considerably expensive as the characteristic size,  $\delta$ , of such structure is proportional to  $Re^{-0.5}$ . This means that, for high  $Re$ , an extremely fine grid is needed in the boundary layer to capture the velocity gradients so greatly increasing the calculation time.

It is then convenient to implement the boundary condition for solid walls in such a way that the law of the wall is incorporated in the solution and taken as the boundary condition for the cells close to the wall.

Such an approach is known as wall-function approach and represents the standard wall treatment when the  $k - \epsilon$  turbulence model is used. From the practical point of view, in its standard form, it consists in imposing the law of the wall in the last cell in proximity to the solid boundary in such a way that the logarithmic law is respected for  $y^+ \geq 10$  while the linear approximation, characteristic of the viscous sublayer, is imposed for smaller values of  $y^+$ .

Such an approach strongly relies on the assumption that the boundary layer can be universally described by the law of the wall and this is actually the case in a relatively wide selection of flows of technical interest at least within an acceptable degree of accuracy. Unfortunately, when adverse pressure gradients are present and boundary layer detachment occurs, such assumption is no longer acceptable and models able provide a reasonable solution when integrated in the proximity of the wall are needed.

A number of variants of the wall-function approach have been developed in order to take into account adverse pressure gradients, streamlines curvature, surface roughness, temperature gradients and so on. Here, the discussion is limited to the fact that wall functions can be used to correct inaccurate predictions of the turbulence model in the boundary layer so that the law of the wall (or same more sophisticated version taking into account other physical aspects) is respected. In other cases, like in the  $k - \omega$  based models, the wall function approach is alternative to the direct integration throughout the boundary layer and, although less reliable, it leads to a great reduction of the computational effort.



### Conclusions about two-equations models

The structure of the most widely used two-equations models have been presented and further details can be found in [25]. Their actual implementation in CFD codes is somehow more complex than what has been presented because of the complications arising from the imposition of boundary conditions especially if wall functions are used. Whatever particular model is considered, it must be always reminded that a great number of hypotheses have been introduced to arrive to such a simple formulation. Dimensional analysis played a crucial role in the definition of the two equations approach denouncing the lack of physical insight in the phenomena.

Some of the introduced hypotheses are particularly strong. We assumed that turbulent mixing is an isotropic process. This is the core of the Boussinesq hypothesis and led to the definition of the turbulent viscosity as a constant instead of a tensor, greatly simplifying our modelling effort.

Turbulence has been assumed to be in an equilibrium while this is often not the case and its unsteadiness plays a significant role in a number of flows of practical interest.

Going back to Kolmogorov spectrum, we focused on the fine scales aiming at modelling the behaviour of the large and medium non-isotropic scales as we know that they are the ones that contribute the most to the flow mixing. In addition to that, the models have been calibrated on simple flows like free turbulent decay and boundary layers.

From the aforementioned arguments one might be persuaded that there are more reasons for two-equations models for failing than being accurate and probably this is quite true.

A number of model exists which are variants of the presented ones or introduce new evolving variables trying to add some feature to turbulence. This includes anisotropy, models for transition and a variety of corrections attempting to remove each of the introduced hypotheses. All these corrections and variations might be effective for certain categories of flows but none of them is able to overcome the major shortcomings of the RANS approach based on two-equations models.

One point is of particular interest and will be later further investigated. Turbulence is assumed to be an isotropic stochastic process. Although this is true for small scales, it is completely wrong for big ones that usually show an high level of organization both in space and time. Such large scales, which do not contribute to dissipation and whose characteristics are not universal at all, should be regarded as vortical structures rather than turbulence. The problem is that a clear distinction between the two do not exists so that the results can be evaluated only based on the model predictions. In one sentence, we defined the averaged quantities separating a slowly varying component and a quickly varying one but the cutoff between the two is not easily recognizable in practice.

In our approach, we always thought turbulence as a stochastic process fixed in an equilibrium state and this is the original version of the RANS approach which where conceived for boundary layers, pipe flows, jets and similar ones that can be actually regarded as in equilibrium.

The extension of such models to unsteadiness, although trivial from the practical point of view (this is the version we already presented in the models equations in previous sections), led to the URANS (Unsteady-RANS) approach and indeed to an even more intricate and delicate distinction between vortical structures and turbulence.

### 4.8.3 Reynolds Stress Models

The two-equations models, although showing limited accuracy and robustness, especially in strongly unsteady flows, provided a precious insight in the mechanisms underlying the effects of turbulence. We introduced the Boussinesq hypothesis by observing that turbulence, when medium and small scales are considered, is an isotropic random process so that no information about the directionality of the flow mixing can be observed. Such approach is not always physically sound and in some cases, when the anisotropy of Reynolds stresses plays a crucial role in the definition of the flow field, can lead to non realistic results. This is often observed when secondary or swirling flows are studied and in such cases, the hypothesis of isotropic turbulence is not acceptable.

The Boussinesq hypothesis led to the definition of the turbulent viscosity so bridging the gap between turbulence related quantities and mean flow velocity components. One way of avoiding the definition of the turbulent viscosity and, thus, the isotropy of the simulated turbulence, is to write a transport equation for each Reynolds stress on the model of Eq. 4.7.1. Indeed, writing a transport equation for each Reynolds stress might sound non rigorous. Also in this case, as it was for the turbulent kinetic energy, it is possible to derive the transport equation for each Reynolds stress from the time averaged Navier-Stokes equations. With no surprise we conclude that such equations include high-order correlations between fluctuating quantities so that, once gain, a good amount of drastic surgery and dimensional analysis is needed in order to model the unknown quantities on the base of the available ones, so closing the system. Fortunately, once again, despite the complexity of the analytical expression, the mechanisms observed in Eq. 4.7.1 can be recognized so that the equation can be formally written in the presented standard form.

Usually, the time averaged Navier-Stokes system is solved together with the transport equations for each Reynolds stress and the equations for  $k$  and a quantity related to the kinetic energy dissipation like  $\epsilon$  or  $\omega$ .

This approach is extremely intense from the computational point of view as it introduces new equations (three in two-dimensions or six in three-dimensions) and leads to a stiff formulation with strong coupling between the momentum conservation equations and the Reynolds stress transport ones.

A number of combinations can be built involving the Reynolds stress transport equations, the available two-equation models and different wall treatments showing strengths and weaknesses of each modelling strategy.

The usage of such models, due to the complications they introduce (especially with respect to the stiffness of the resulting system that implies long calculation time and long simulation time before a converged solution is reached), is usually limited to cases for which secondary flows or high level of swirling are observed. In other cases (between these bluff bodies should be included as well), it is not possible to uniquely individuate the advantage in using such an approach. Some simulation approaches lead to more accurate results if compared to two equations models while other combinations might perform in similar or less satisfying ways indicating that the major shortcomings cannot be related to the Boussinesq hypothesis.

## 4.9 Large Eddies Simulations

In the previous sections the RANS approach has been described. The strategy moves from the time-averaging of the Navier-Stokes equations and the definition of suitable closure strategies for the unknown correlations.

Another approach can be obtained by applying a spatial filter to the original equations leading to a family of turbulence models which is usually indicated as Large Eddy Simulations (LES). Such a strategy has the advantage over the previously described one that, if the filter amplitude is locally set according to the mesh size, a procedure able to produce a variable smoothing of the resolved flow field can be built leading to optimal usage of the provided computational grid.

The experimental evidence that turbulence quickly tends to isotropy, while decaying according to the energy cascade, supports the idea that such approach might lead to much more accurate results provided that the computational grid is able to describe the large energy containing scales leaving to the turbulence model the role of simulating the effect of the highly isotropic small eddies only.

The result of the filtering operation leads to the appearance of unknown terms that must be modelled in analogy to what has been described for the RANS approach. The physical interpretation of these unknowns has been presented by Leonard [26] and includes the interactions among the large scales, the modelled scales and their crossed contribution. Such terms are usually modelled all together similarly to what has been done in the RANS approaches by defining a sub-grid model which takes into account the effects of the non-simulated scales. Some of the basic ideas underlying such models can be closely related to what has been described for RANS with the difference that a reasonable length scale can be readily provided by the mesh size weakening the interest for equations providing a length scale.

The simplest model of this kind is the one proposed by Smagorisky which reads:

$$\mathbf{T}_{sgs} = 2\mu_{sgs} \cdot \mathbf{S} \quad (4.49)$$

$$\mu_{sgs} = \rho(C_s \Delta)^2 \sqrt{2\mathbf{S} : \mathbf{S}} \quad (4.50)$$

where  $C_s$  is the Smagorisky constant and  $\Delta$  is usually defined as the cubic root of the cell volume. In addition to such terms, corrections to the pressure terms must be added in order to take into account the diagonal terms which has been linked to the turbulence kinetic energy in the case of the RANS models.

The analogy between such model and the mixing length presented in Sec. 4.8.1 is apparent and the definition of the equivalent viscosity according to the Boussinesq approximation is a framework which should sound familiar at this point. The constant  $C_s$  is not universal and values ranging between 0.10 and 0.24 have been used.

Extensions of such model have been proposed including an additional scalar transport equation describing the sub-grid kinetic energy thus providing a velocity scale decreasing the case by case variability of  $C_s$ .

The importance of the sub-grid model in the decay of homogeneous isotropic turbulence has been deeply investigated by Ferziger [27]. In that case the dissipation due to

the sub-grid model has been found to represent 29% of the total for a mesh composed of  $16^3$  points while it has been estimated to represent 20% of the total when the simulation is performed on a bisected grid counting  $32^3$  points, so highlighting the importance of the sub-grid model.

In conclusion, the LES approach has proved to be much more reliable than the RANS approach for a wide range of cases including bluff bodies. Indeed, this is coherent with the observation that small eddies show a more universal structure if compared to large ones and the sub-grid model selectively simulates the first ones on the base of the calculation grid resolution. Unfortunately, the computational effort required by LES is much higher than the one required by RANS so that this latter approach still represent the most utilized way of tackling turbulence in industrial CFD calculations.

## 4.10 Scale-Resolving Simulations

In the previous sections the most widely adopted turbulence simulation strategies have been synthetically presented. The results obtained simulating a jet flow using the RANS and LES approaches are reported in Fig. 4.8.

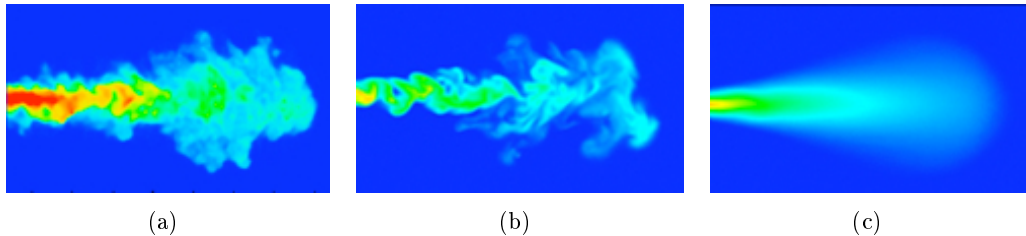


Figure 4.8: Comparison between experimental (a), LES simulated (b) and RANS simulated (c) turbulent structures [28].

The distinction between RANS and LES simulated flows, as it has been presented until now (which is the classical way), is in some way misleading. In fact, there are no physical arguments that can be adduced to justify the differences in the simulated flow field based on the choice of averaging the flow in the spatial or the temporal dimension. The problem is that RANS models are often identified as the two-equation models because historically they have been the most successful members of the the RANS family.

Two articles, providing great insight in the very nature of turbulence modelling, has been published by Ergorov, Menter at al. [29, 30]. In these papers it is demonstrated that the main difference between turbulence models should be set between scale-resolving and non scale-resolving ones. Such distinction is related to the actual behaviour of the models when they are applied rather than to the specific filtering operation used to derive them or the quantities used to define the simulated turbulence length and velocity scales.

In fact, it can be seen that two-equation RANS models ususally tend to unnaturally damp the unstable mechanisms which are the main sources of large vortical structures that, through the energy cascade, lead to turbulence. Such stabilization is actually performed by increasing the effective viscosity which in turns exasperates the momentum

diffusion so taking into account the effect of the turbulence which was suppressed. Obviously, large scales, which have size comparable to the immersed bodies, are able to deform the mean flow significantly so that in no way diffusion can recover their effect.

The LES approach usually has better performance and shows Scale-Resolving capabilities because it produces a limited amount of turbulent viscosity so that the stability conditions of the main flow features (especially shear-layers for bluff bodies) are respected with a much higher accuracy. In such conditions, the large eddies are produced and the energy cascade is simulated up to the scales which are damped out by the turbulent viscosity.

A similar behaviour can be obtained starting from the RANS formulation by modifying the equations for the turbulence related parameters. With no surprise it is found that, while the equation for  $k$  is virtually not modified, the equation for  $\epsilon$ , which was modelled almost completely using a term by term approach, requires some revision. Following such an approach, the development of an effective RANS model showing Scale-Resolving capabilities is shown in [29].

The most interesting feature of the model (called *KSKL*) is that it is able to automatically detect the scale of the resolved turbulence and adjust the length scale according to it so automatically switching between a classical two-equation RANS and a LES model (the model is implemented so that a minimum for the turbulent viscosity is provided by an underlying LES model). Figure 4.9 shows the vortical structures around a circular cylinder simulated using a  $k - \omega$  *sst* and the *KSKL* model. The ratio between the turbulent viscosity and the fluid viscosity is more than one order of magnitude higher in the first case.

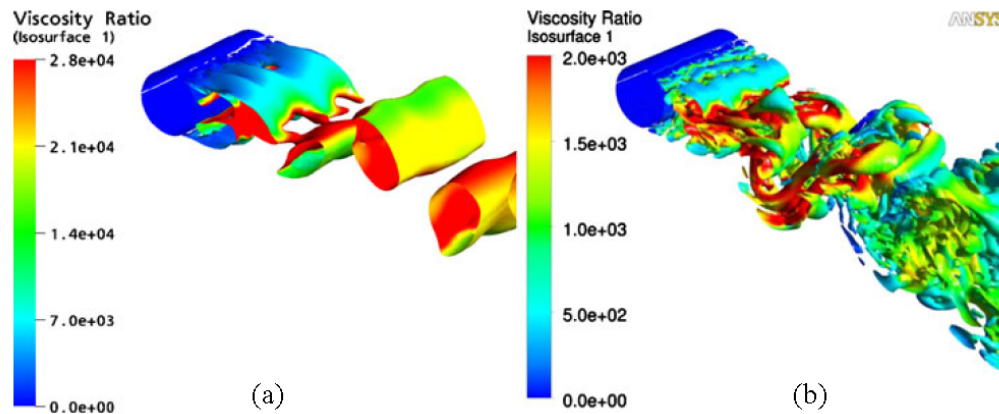


Figure 4.9: Vortical structures around a circular cylinder: (a)  $k - \omega$  *sst*, (b) *KSKL* [29].

A number of models with Scale-Resolving capabilities have been developed which are not here discussed. The main idea underlying them all is to take advantage of the RANS two-equation formulation near solid walls and to use the LES scale resolving capabilities in zones characterized by strong unsteady behaviour. Such approaches are called Detached Eddy Simulations (DES) and are another example of scale-resolving model not completely based on LES.

At this point, it is interesting to have a closer look to Fig. 4.9. Looking at the flow

field produced by the  $k - \omega$  *sst* model, obviously the two-equations URANS models, show some limited Scale Resolving capability.

It is hard to tell if this can be really claimed to be an advantage or not because, on one side, it proves that even this approach can provide an unsteady description of the flow field but, on the other, it encourages CFD users to believe that two-equations URANS models can be used to study some delicate unsteady aspects of the flow which is indeed not true. The matter is complicated by the fact that, in some cases, parameters related to the unsteady behaviour of the flow can be predicted by two-equations models with reasonable accuracy so that individuating their limit of applicability is not straightforward (this is typically the case of the Strouhal number).

To what it concerns the simulations outputs, when RANS turbulence models are applied to flows which show strong global instability (which is often the case in bluff bodies aerodynamics), the model is not able to converge to a steady solution and often returns a single vortex shedding frequency. Such frequency might be not so far from the real main shedding frequency because the global mechanisms are only marginally influenced by the local stability conditions of the shear layers (conditions which are completely lost with two-equations models). The situation is even more problematic than this. In zones protected by obstacles, in some cases vortical structures form which appear to be extremely stable due to the turbulent viscosity. Such structures are able to deform the average flow field in a remarkable way so that the simulations might be compromised.

Only one thing can be stated with a certain confidence: although two-equations URANS simulations are able to reproduce some of the main dynamic behaviour of the flow field around bluff bodies, the insurgence of such unsteady phenomena mainly indicates that the applicability of non scale-resolving approaches reached its validity limit and results should be interpreted with caution. A comprehensive comparative study of the performance of RANS, LES and DES models in predicting flows around bluff bodies can be found in [31].



# Chapter 5

## Flutter derivatives

In this chapter, the well known Scanlan loading model, based on flutter derivatives is discussed. Such model is extremely effective in describing the overall bridge deck behaviour with respect to vibrations and it is used in standard procedures used to evaluate the flutter critical wind speed. The model is formally based on the Theodorsen theory but such similarity should not be overestimated. In fact, the synthetic nature of the Scanlan model allows to incorporate some non-linearities in the system response and should be regarded as a punctual evaluation of the bridge deck aerodynamic response functions (for given frequency and amplitude) rather than the extension of the Theodorsen formulation to mildly bluff bodies. Such capability is a great advantage of the model which appears to be at the same time simple and robust. Nevertheless, sometimes, its applicability might be overestimated and carefulness should be used when non-linearities are relevant.

### Contents

<b>5.1</b>	<b>Introduction</b>	<b>74</b>
<b>5.2</b>	<b>Scanlan formulation</b>	<b>74</b>
<b>5.3</b>	<b>Flutter derivative estimation</b>	<b>76</b>
5.3.1	Forced vibration method	77
5.3.2	The free vibration method	78
<b>5.4</b>	<b>Computational fluid dynamics estimation</b>	<b>82</b>
5.4.1	Combined forced vibration method	86
<b>5.5</b>	<b>Critical flutter speed evaluation</b>	<b>88</b>
5.5.1	Flutter determinant	89
5.5.2	Iterative eigenvalue analysis	91
5.5.3	Motion equations integration	92
<b>5.6</b>	<b>Fully coupled simulations</b>	<b>93</b>



## 5.1 Introduction

Scanlan was the first one to extend the results obtained by Theodorsen for the thin airfoil to bridge decks. The formal similarity between the two approaches is at the same time the result of a mimicking procedure with respect to the analytical solution and an effort towards a simple approach based on strong physical reasoning.

When unstreamlined bodies are considered, possible large flow separations, reattachments, recirculation zones and vortex shedding can occur, inducing significant unsteady effects, that prevent the identification of a thin and well defined boundary layer. Thereby, in these cases, the hypothesis of inviscid and fully attached flow, generally acceptable for streamlined bodies immersed in a flow with a small angle of attack, must be often rejected. Accordingly, the description of the motion-induced loads on cylindrical bodies with a bluff sectional geometry, such as typical bridge decks, can not be directly obtained by using the thin airfoil theory.

In this context, Scanlan [32, 33, 34, 6, 35] profitably exported some features of the Theodorsen results, describing the wind loads induced by sectional harmonic motions by means of a linearized format, based on experimentally-evaluated frequency-dependent filter functions (namely, the flutter derivatives), that supplied the lack of closed-form analytical formulations.

The mixed time-frequency formulation, in the case of the flutter derivatives, can lead to misleading interpretations. The deck displacements and their first derivatives are in no way independent and the formulation is valid strictly under the hypothesis of harmonic motions as it was for the Theodorsen formulation. Thus, the approach can be considered as mixed only with respect to its standard representation format but its applicability is restricted to the frequency domain.

Another critical point in the usage of the flutter derivatives is the validity of the superposition principle. As it will be explained in the subsequent sections, commonly used identification procedures allow to estimate the flutter derivatives without invoking any system linearity. Nevertheless, in order to evaluate the critical flutter speed, the combination of vertical and rotational motions is studied so that the linear superposition principle, although not directly invoked to evaluate the flutter derivatives, is of primary importance in their practical application. The system linearity, which in principle can be regarded as a first order approximation, has proved to be accurate in the majority of the cases when small displacements are considered so explaining the large success of the method in predicting the incipient instability condition.

## 5.2 Scanlan formulation

Consider two harmonic motions of the deck, one rotational around the elastic axis and one vertical, of angular velocity  $\Omega$  and amplitude  $\alpha_0$  and  $h_{d0}$ , respectively (see Fig. 5.1):

$$\begin{aligned}\alpha(t) &= \alpha_0 e^{i\Omega t}, \\ h_d(t) &= h_{d0} e^{i\Omega t}.\end{aligned}\tag{5.1}$$

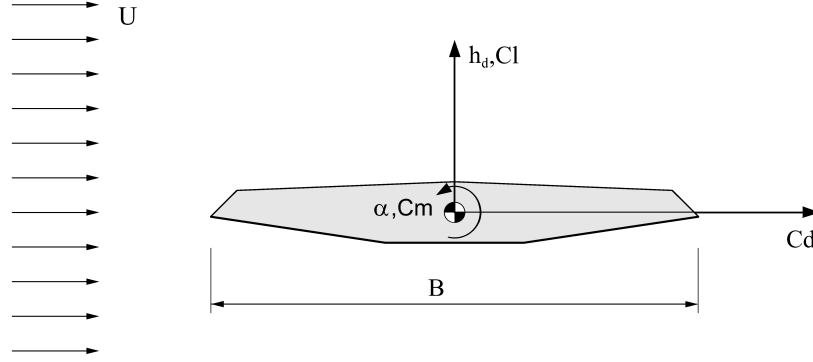


Figure 5.1: Bridge deck, reference system and degrees of freedom.

The two motions can be written in non-dimensional form as follows:

$$\begin{aligned}\alpha(s) &= \alpha_0 e^{iks}, \\ h(s) &= h_0 e^{iks},\end{aligned}\tag{5.2}$$

being  $h$  the non-dimensional form of  $h_d$  defined as  $h = h_d/B$ . Simple calculations can demonstrate that  $k = \Omega B/U$  and that  $\Omega t = ks$ .

Following the model proposed by Scanlan, the aeroelastic forces acting on the deck can be written in a mixed frequency-time domain form as:

$$\begin{aligned}L(t, k) &= \frac{1}{2} \rho U^2 B \left( k H_1^* \frac{\dot{h}_d}{U} + k H_2^* \frac{B \dot{\alpha}}{U} + k^2 H_3^* \alpha + k^2 H_4^* \frac{h_d}{B} \right), \\ M(t, k) &= \frac{1}{2} \rho U^2 B^2 \left( k A_1^* \frac{\dot{h}_d}{U} + k A_2^* \frac{B \dot{\alpha}}{U} + k^2 A_3^* \alpha + k^2 A_4^* \frac{h_d}{B} \right),\end{aligned}\tag{5.3}$$

being  $H_i^* = H_i^*(k)$  and  $A_i^* = A_i^*(k)$  the flutter derivatives.

These expressions can be written in non-dimensional form as follows:

$$\begin{aligned}C_l(s, k) &= k H_1^* h' + k H_2^* \alpha' + k^2 H_3^* \alpha + k^2 H_4^* h, \\ C_m(s, k) &= k A_1^* h' + k A_2^* \alpha' + k^2 A_3^* \alpha + k^2 A_4^* h,\end{aligned}\tag{5.4}$$

where the operator  $'$  denotes the derivative with respect to the non-dimensional time  $s$ . Expanding such derivatives, it is possible to write:

$$\begin{aligned}C_l(s, k) &= k^2 \{ [H_4^* + i H_1^*] h(s) + [H_2^* + i H_3^*] \alpha(s) \}, \\ C_m(s, k) &= k^2 \{ [A_4^* + i A_1^*] h(s) + [A_2^* + i A_3^*] \alpha(s) \}.\end{aligned}\tag{5.5}$$

Equations (5.5) allow to easily estimate the flutter derivatives from experimental results.

On the one hand, the model can be merely seen as the evaluation of frequency response functions linking the deck motion to the recorded forces. On the other hand, it is possible to notice the formal similarity between the Scanlan model and the Theodorsen

formulation reported in Sec. 3.6.2. In fact, the Theodorsen formulation can be easily rearranged in order to match the format of Eqs. (5.4) so leading to:

$$\begin{aligned}
 H_1^* &= -2\pi \frac{\mathcal{F}}{k}, & H_4^* &= \pi \left[ \frac{1}{2} + 2\frac{\mathcal{G}}{k} \right], \\
 H_2^* &= -\pi \left[ \frac{1}{2k} + \frac{\mathcal{F}}{k} \left( \frac{1}{2} - a \right) + 2\frac{\mathcal{G}}{k^2} \right], \\
 H_3^* &= -\pi \left[ \frac{a}{4} + 2\frac{\mathcal{F}}{k^2} - \frac{\mathcal{G}}{k} \left( \frac{1}{2} - a \right) \right], \\
 A_1^* &= \pi \left( \frac{1}{2} + a \right) \frac{\mathcal{F}}{k}, & A_4^* &= -\pi \left[ \frac{a}{4} + \frac{\mathcal{G}}{k} \left( \frac{1}{2} + a \right) \right], \\
 A_2^* &= \pi \left[ -\frac{1}{4k} \left( \frac{1}{2} - a \right) + \frac{\mathcal{F}}{2k} \left( \frac{1}{4} - a^2 \right) + \frac{\mathcal{G}}{k^2} \left( \frac{1}{2} + a \right) \right], \\
 A_3^* &= \pi \left[ \frac{1}{8} \left( \frac{1}{8} + a^2 \right) + \frac{\mathcal{F}}{k^2} \left( \frac{1}{2} + a \right) - \frac{\mathcal{G}}{2k} \left( \frac{1}{4} - a^2 \right) \right],
 \end{aligned} \tag{5.6}$$

where  $a$ ,  $\mathcal{F}(k)$  and  $\mathcal{G}(k)$  are defined accordingly to Sec. 3.6.2 thus justifying the introduction of the Scanlan model on the base of the Theodorsen results. The functions  $H_i^*(k)$  and  $A_i^*(k)$  are reported in Fig. 5.4 where the dependence with  $k$  has been changed, as usually done in the context of bridge deck aeroelasticity, to a dependence with  $U_{red} = 2\pi/k$  in agreement with Eq. (2.6).

The strong hypotheses embedded in the definition of such closed form solution for the aeroelastic coefficients have been already presented. Although inadequate for a detailed study, the critical flutter speed calculated using Theodorsen's flutter derivatives can provide a good first quantification of the structure sensitivity to aeroelastic coupling. In particular, if we define  $\beta = U_{cr}/U_{cr}^{Theo}$  where  $U_{cr}$  is the real critical flutter speed and  $U_{cr}^{Theo}$  is the one obtained for the same structure using the thin airfoil flutter derivatives, the approximate estimations reported in Fig. 5.3 are proposed by Dyrbye [5].

### 5.3 Flutter derivative estimation

In the following sections, the most widely adopted methods, currently used to extract the flutter derivatives, are described. Roughly speaking, the available techniques can be grouped in two main families: the first one is the *forced vibration method* which consists in directly evaluating the flutter derivatives by measuring the frequency response functions to imposed forced vibrations of constant amplitude. The second one is the *free vibration method* which infers the deck aeroelastic coefficients from the variation of the system response with respect to the zero wind condition. While the first methodology requires the usage of an *ad hoc* experimental apparatus, able to move the sectional deck model and measure the resulting forces, the second one only requires the suspension of the deck sectional model with springs and the measurement of displacements.

From the practical point of view, it can be said that while the first method tackles the identification difficulties by requiring the use of a complex experimental apparatus, the second one deals with it by increasing the complexity of the identification procedure. The two methods are described in the following sections.

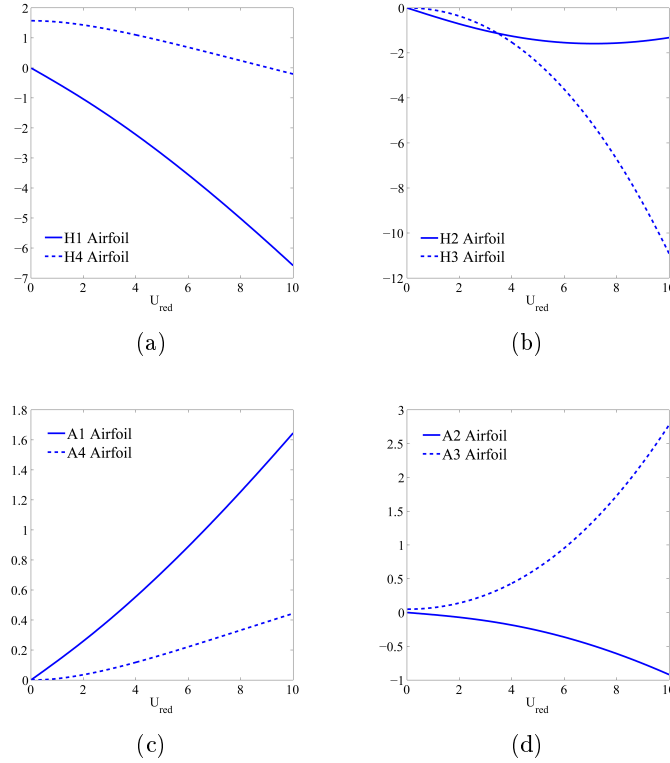


Figure 5.2: Thin airfoil flutter derivatives

### 5.3.1 Forced vibration method

The forced vibration method (f.v.m in the following) is probably the simplest and most reliable method for extracting flutter derivatives.

A vertical or torsional harmonic motion of non-dimensional circular frequency  $k$  is imposed and the aerodynamic unsteady forces acting on the body are recorded.

This is achieved by means of hydraulic actuators which must be able to impose torsional and heaving motions, separately. The forces acting on the body can be estimated both by integrating pressures recorded on the deck surface or by using balances. In the first case, some difficulties might arise from the presence of barriers and wind screens as it is not possible to integrate pressures accurately on those elements. On the con-


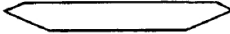

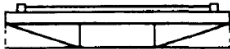
Bridge-deck section		$\beta$
Flat plate		1
Streamlined box-girder section		approximately 0.8–0.9
Non-streamlined box-girder section		approximately 0.4–0.6
Truss-stiffened girder		approximately 0.6–0.8

Figure 5.3: Approximate critical flutter speed with respect to thin airfoil [5].

trary, when balances are used, the recorded forces must be separated in the contribution provided by the fluid action and the one originated by the inertia of the model. Such operation is usually accomplished by measuring the forces at zero wind speed thus inferring the model inertial properties. A comparative study between the two possibilities can be found in [36].

Once the displacements and the forces are recorded, by a least square fitting method, the stabilized unsteady  $C_l(s)$  and  $C_m(s)$  profiles are fitted obtaining their amplitudes  $(C_L, C_M)$  and their phases  $(\psi_L, \psi_M)$  with respect to the imposed motion. Considering Eqs. (5.5), the flutter derivatives can be written in the following form:

$$\frac{C_L e^{i\psi_L}}{k^2 h_0} = H_4^* + iH_1^*, \quad \frac{C_M e^{i\psi_M}}{k^2 h_0} = A_4^* + iA_1^*, \quad (5.7)$$

for the imposed harmonic vertical motion of non-dimensional amplitude  $h_0$  and

$$\frac{C_L e^{i\psi_L}}{k^2 \alpha_0} = H_3^* + iH_2^*, \quad \frac{C_M e^{i\psi_M}}{k^2 \alpha_0} = A_3^* + iA_2^*, \quad (5.8)$$

for the imposed harmonic torsional motion of amplitude  $\alpha_0$ .

Flutter derivatives, grouped as shown in Eqs. (5.7) and (5.8), explicitly show their role of transfer functions between the applied motion and the resulting forces thus describing the aeroelastic effects only in terms of amplification and phase shifting with respect to the applied displacements.

The described procedure allows to completely separate the structure characteristics from its aerodynamic behaviour so allowing to study the dependence of the aeroelastic coefficients with the imposed motion amplitude.

The results obtained from forced vibration tests are usually characterized by low scatter and good reproducibility. This is the most convenient technique for the estimation of flutter derivatives and it is the most appropriate for comparison with numerical results.

### 5.3.2 The free vibration method

The free vibration method consists in comparing the structure free vibration response with and without the presence of wind. The motion equation of the deck immersed in the fluid flow, considered as a two degrees of freedom system, can be written as:

$$\mathbf{M}^{st} \ddot{\boldsymbol{\vartheta}} + \mathbf{C}^{st} \dot{\boldsymbol{\vartheta}} + \mathbf{K}^{st} \boldsymbol{\vartheta} = \mathbf{F}^{ae}, \quad (5.9)$$

where  $\mathbf{M}^{st}$  is the mass matrix,  $\mathbf{C}^{st}$  is the damping matrix,  $\mathbf{K}^{st}$  is the stiffness matrix and  $\boldsymbol{\vartheta}$  is the vector grouping the system degrees of freedom  $\boldsymbol{\vartheta} = \boldsymbol{\vartheta}(t) = [h_d(t), \alpha(t)]^T$ .  $\mathbf{F}^{ae}$  is the vector of the aeroelastic self-excited forces.

Following Scanlan approach, thanks to Eqs. (6.1),  $\mathbf{F}^{ae}$  can be represented as a correction over the system damping and stiffness matrices induced by aeroelastic effects, namely the aeroelastic damping and stiffness matrices  $\mathbf{C}^{ae}$  and  $\mathbf{K}^{ae}$ :

$$\mathbf{C}^{ae} = \frac{1}{2} \rho U^2 B k^2 \begin{bmatrix} H_1^*/U & H_2^*B/U \\ A_1^*B/U & A_2^*B^2/U \end{bmatrix}, \quad (5.10)$$

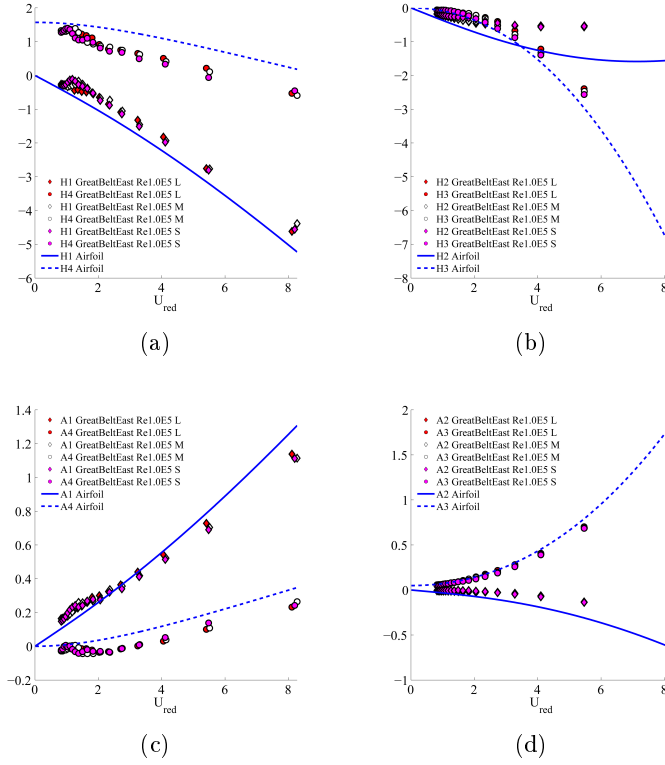


Figure 5.4: Flutter derivatives of the Great Belt East Bridge obtained with forced vibration method using large (L), medium (M) and small (S) vibration amplitudes. Data taken from [37].

$$\mathbf{K}^{ae} = \frac{1}{2} \rho U^2 B k^2 \begin{bmatrix} H_4^*/B & H_3^* \\ A_4^* & A_3^* B \end{bmatrix}. \quad (5.11)$$

It is then possible to rewrite the equations of motion as:

$$\mathbf{M}^{st} \ddot{\boldsymbol{\vartheta}} + (\mathbf{C}^{st} - \mathbf{C}^{ae}) \dot{\boldsymbol{\vartheta}} + (\mathbf{K}^{st} - \mathbf{K}^{ae}) \boldsymbol{\vartheta} = \mathbf{0}. \quad (5.12)$$

For later convenience, let's define:

$$\begin{aligned} \bar{\mathbf{C}}^{st} &= \mathbf{M}^{st^{-1}} \mathbf{C}^{st}, & \bar{\mathbf{K}}^{st} &= \mathbf{M}^{st^{-1}} \mathbf{K}^{st}, \\ \bar{\mathbf{C}} &= \mathbf{M}^{st^{-1}} (\mathbf{C}^{st} - \mathbf{C}^{ae}), & \bar{\mathbf{K}} &= \mathbf{M}^{st^{-1}} (\mathbf{K}^{st} - \mathbf{K}^{ae}). \end{aligned} \quad (5.13)$$

Rewriting the system in standard form and grouping the structural and the aeroelastic matrices:

$$\ddot{\boldsymbol{\vartheta}} + \bar{\mathbf{C}} \dot{\boldsymbol{\vartheta}} + \bar{\mathbf{K}} \boldsymbol{\vartheta} = \mathbf{0}. \quad (5.14)$$

From this equation, assuming to know the total stiffness and damping matrices with

and without the presence of wind, the flutter derivatives can be evaluated as follows [38]:

$$\begin{aligned}
H_1^* &= -\frac{M}{\rho B^2 \Omega} (\bar{C}_{11} - \bar{C}_{11}^{st}), & H_2^* &= -\frac{M}{\rho B^3 \Omega} (\bar{C}_{12} - \bar{C}_{12}^{st}), \\
H_3^* &= -\frac{M}{\rho B^3 \Omega^2} (\bar{K}_{12} - \bar{K}_{12}^{st}), & H_4^* &= -\frac{M}{\rho B^2 \Omega^2} (\bar{K}_{21} - \bar{K}_{21}^{st}), \\
A_1^* &= -\frac{I}{\rho B^3 \Omega} (\bar{C}_{21} - \bar{C}_{21}^{st}), & A_2^* &= -\frac{I}{\rho B^4 \Omega} (\bar{C}_{22} - \bar{C}_{22}^{st}), \\
A_3^* &= -\frac{I}{\rho B^4 \Omega^2} (\bar{K}_{22} - \bar{K}_{22}^{st}), & A_4^* &= -\frac{I}{\rho B^3 \Omega^2} (\bar{K}_{21} - \bar{K}_{21}^{st}).
\end{aligned} \tag{5.15}$$

which are valid assuming  $\mathbf{M}$  to be a diagonal matrix with  $\mathbf{M}_{11} = M$  the mass and  $\mathbf{M}_{22} = I$  the inertia of the sectional model per unit length.

### Direct estimation

The direct terms (which lies the diagonal) can be estimated as follows: the model is suspended on eight calibrated springs (four for each side) so that heaving and the torsional frequencies can be adjusted separately. Damping can be adjusted by adding some neoprene strips linking the model suspension system to the fixed part of the suspension frame in order to reach approximately 0.3% damping ratio. Then, one degree of freedom is restrained and the model free vibrations measured without wind.

The wind speed is increased and the free vibrations measured at increasing velocities. Analysing the system frequency and its total damping, it is possible to evaluate the flutter derivatives using Eqs. (5.15). Finally, the procedure is repeated changing the constrained degree of freedom.

In the procedure proposed by Scanlan and discussed in details in [33], once the direct terms are evaluated from pure vertical and torsional free vibrations, coupled motions are used to evaluate the cross terms.

The methodology is extremely simple and results easily obtained for low wind speeds when the total damping is small. On the contrary, when the speed is increased and the damping increases significantly, the recorded time histories might be extremely short (sometimes just a couple of oscillations) so that the evaluation of the system properties might be inaccurate (see Fig. 5.5). Such problem might be mitigated by varying the system mechanical properties but this is surely one major shortcoming of the free vibration method and explains the large scatter observed at high reduced velocities. It must be also noticed that, on theoretical ground, the whole formulation, when the amplitude of the oscillations decreases rapidly, is not consistent with Theodorsen results. In fact, the analytical solution is derived through the Duhamel's convolution integral on the assumption of constant amplitude harmonic oscillations.

From a practical viewpoint, it must be considered that the time required to change the model setup is significant and since many degrees of freedom combinations must be explored, the time needed for the flutter derivative evaluation might be relevant.

### Simultaneous identification

The described procedure is simple but cumbersome and not very efficient. It is possible to avoid the need of multiple setups by using identification procedures which are

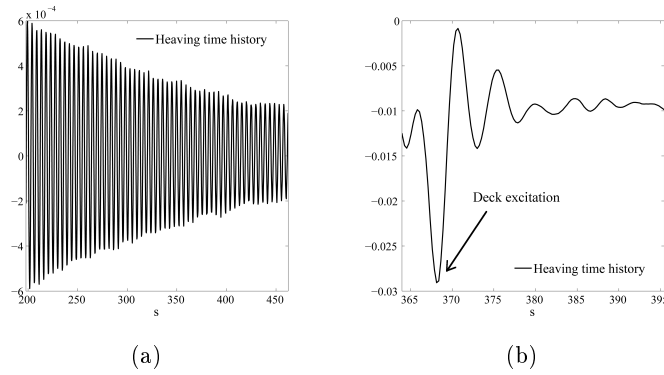


Figure 5.5: Examples of recorded time histories: (a) without wind, (b) with strong wind.

able to identify all the system parameters at the same time from coupled vibrations. A variety of techniques have been proposed in literature with varying degree of accuracy and robustness. Such identification techniques, starting from the knowledge of the degrees of freedom time histories and a scale for the system mechanical properties (which is usually fixed providing the mass matrix), are able to identify the eight coefficients which characterize the stiffness and damping matrices. Again, by comparison with the system properties at zero wind speed, it is possible to evaluate the complete set of flutter derivatives. It is important to remark that such procedures are usually performed in smooth flow and that the deck motion is triggered by external excitation.

Detailed descriptions of available techniques are reported in [39, 40, 41, 42] and a review is provided in [43]. Such methods share the same problem that has been highlighted for the direct method, which is to say that, when the aerodynamic damping is high, the recorded time histories might be extremely short compromising the identification accuracy.

### The stochastic subspace identification techniques

A family of methods exists, based on stochastic subspace identification techniques, which are able to identify the system from its response when excited by Gaussian noise [44, 45, 46]. Such methods are extremely robust and they can be applied even if the vibration of the deck is triggered by the turbulence of the approaching flow (buffeting). Such methods are extremely convenient for two main reasons: the first one is that the effects of buffeting are particularly remarkable in the velocity range in which aerodynamic damping becomes relevant so overcoming the difficulty highlighted for the other methods. The second reason is that the identification procedure is extremely straightforward because the system response is recorded in turbulent approaching flow and, without major modifications in the setup, a large velocity range can be analysed. After the model has been positioned in the wind tunnel, it is sufficient to record the heaving and rotation time histories at constant incoming speed for the velocity range that has to be analysed (see Fig. 5.8 (b)).

Such methods might produce extremely inaccurate results for low wind speeds, when buffeting forces are small, but are able to identify the system with reasonable accuracy



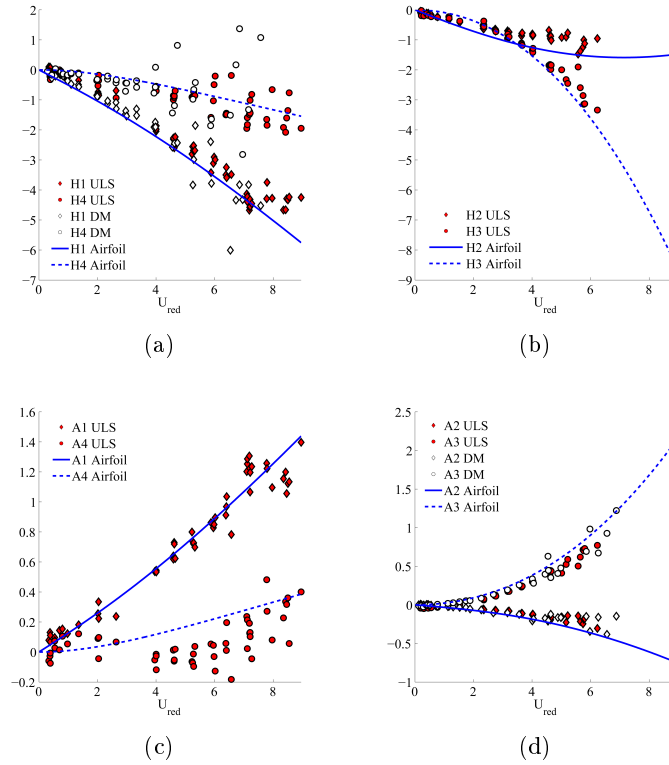


Figure 5.6: Example of flutter derivatives obtained with free vibration method: DM indicates the direct estimation of diagonal terms and ULS indicates the Unified Least Square approach.

for high speeds. The length of the considered time histories is crucial for the accuracy of the identification and typically some hundreds (five to ten) of oscillations should be used (based on the heaving motion that usually shows the lower frequency).

As a concluding remark it is noticed that the frequency ratio of the scaled model in the wind tunnel should be chosen so that the deck reaches the flutter critical speed for higher reduced velocities if compared to the full scale structure. In this way the flutter derivatives are available in the range of interest for the critical flutter speed evaluation.

## 5.4 Computational fluid dynamics estimation

A reliable procedure able to evaluate flutter derivatives using computational techniques is still a research matter [47, 36, 48]. The shortcomings encountered in turbulence modelling introduce a considerable amount of uncertainties in the flutter derivative estimation and in literature there is still no agreement about the best strategies to be adopted for the aeroelastic coefficient determination, their limit of applicability and the way results should be interpreted.

From the practical point of view it is possible to follow both forced and free vibrations methods but the first one is surely the most convenient technique to extract the flutter

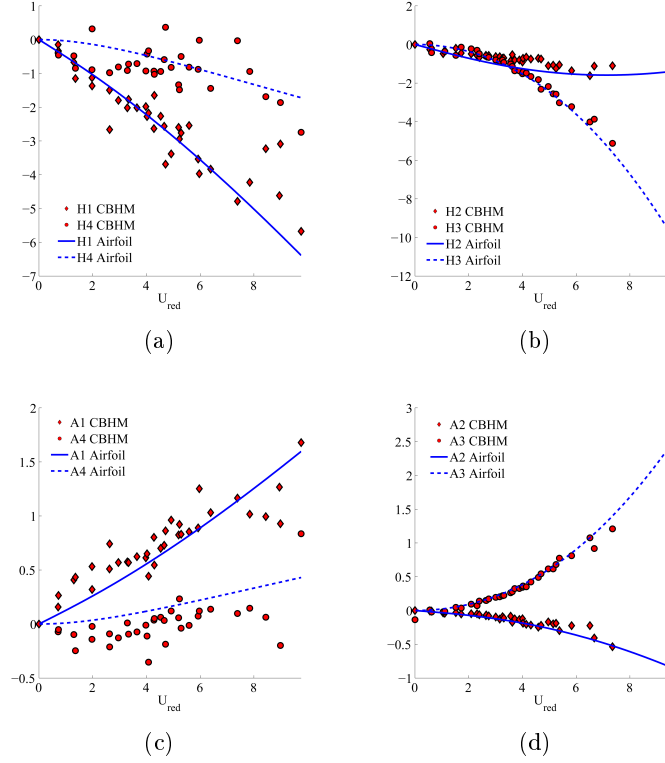


Figure 5.7: Example of flutter derivatives obtained with stochastic subspace identification techniques: CBHM indicates the Covariance Hankel Block Matrix approach [43].

derivatives with numerical simulations. This reflects what is observed in experimental results where forced vibrations are more conveniently used for the flutter derivative extraction while free vibrations are more conveniently used for the evaluation of the flutter critical speed for a given configuration.

From the numerical point of view the complexity of the two approaches is similar but it should be considered that the degree of coupling between the equations of the fluid and the structure is different. In particular, forced vibrations require a one way coupling because the motion is imposed *a priori* while free vibrations require a full two ways coupling between the fluid and the structure. It is in no way convenient to simulate free vibrations tests to evaluate flutter derivatives and, in fact, the simulation of forced vibration tests is well established in the literature. Free vibrations instead can be used to reproduce the effect of the vortex shedding excitation (possibly using Scale Resolving Simulations because RANS models are not adequate for such a problem) and the near instability condition calculated on the basis of the aeroelastic coefficients extracted with forced vibrations tests.

The extraction of the flutter derivatives follows the same framework presented for wind tunnel tests. The deck degrees of freedom are studied separately and the flutter derivatives estimated using Eqs. (5.7) and (5.8).

In order to tackle the imposed movement of the deck section, it is common practice to

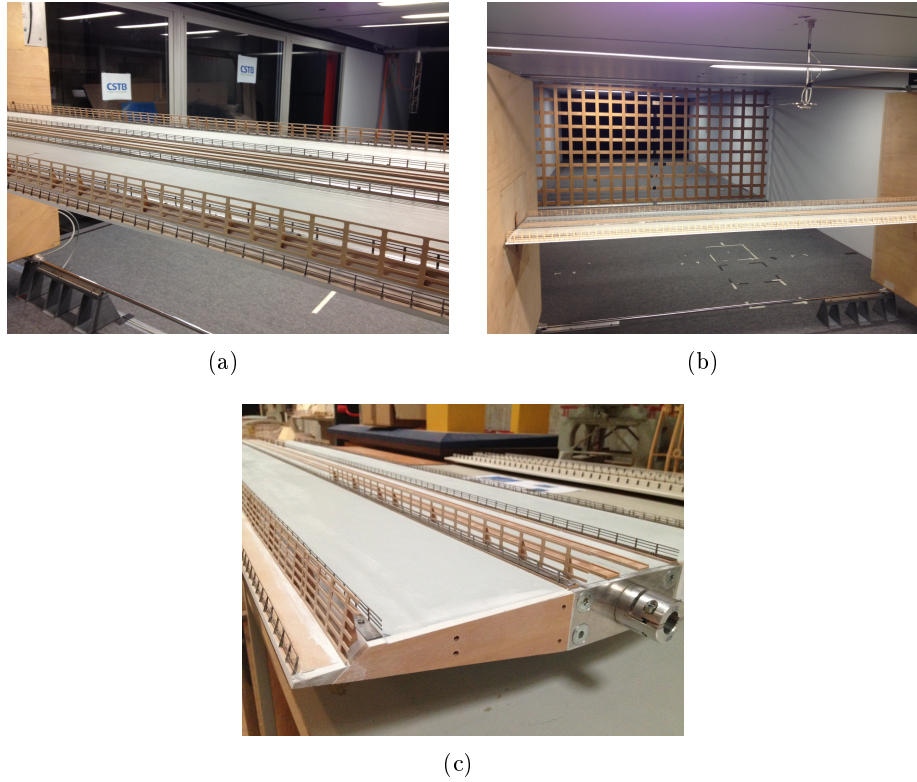


Figure 5.8: Experimental setup for free vibration test at CSTB Nantes: (a) bridge deck positioned in the wind tunnel, (b) particular of the grid used as turbulence generator for the identification performed with the CBHM method, (c) particular of the deck model.

adopt the Arbitrary Lagrangian Eulerian approach (ALE) which is already implemented in numerous CFD softwares like Fluent, Code\_Saturne and OpenFOAM. This method consists in a hybrid description of the fluid motion which combines the Lagrangian and the Eulerian description writing the fluid motion governing equation in a reference system coherent with the mesh motion.

On the basis of the author's experience [49] and practices presented in other papers [50], to accommodate the mesh motion and deformation, the computational domain is split into three parts (Fig. 5.9): a rigid motion zone, a deforming zone and an undeforming zone. The rigid motion zone is directly connected to the bridge profile (considered as rigid), therefore the vertical/torsional motion applied to the cross-section is identically applied to all the mesh nodes into the rigid motion zone. The undeforming zone is not deformed by the bridge-section motion, while the deforming zone is the only mesh region deformed by the bridge motion at each time step. Adopting this strategy, the initial mesh quality assured in the boundary layer region (rigid motion zone) at the beginning of the simulation is not reduced by the cross-section motion.

The mesh stretching affecting the deforming zone can be handled using two algorithms: spring-based smoothing algorithm and remeshing algorithm [51]. During the simulation, at each time step, the mesh internal nodes placed between the rigid motion

zone and the static zone are repositioned according to the bridge displacements. After the node displacements, each cell is checked by quality parameters based on the cell dimension and skewness. Cells which do not satisfy the quality criteria are marked and remeshed before updating the solution to the next time step.

Figure 5.10 shows typical time history for lift and pitching moment obtained for a reduced velocity equal to 11 for an harmonic vertical motion. Using these time histories, the  $(H_1^*, H_4^*)$  and  $(A_1^*, A_4^*)$  values are extracted according to Eqs. (5.7) and (5.8).

As a remark about the comparison between experimental and numerically extracted flutter derivatives, when  $H_4^*$  and (less visibly)  $A_3^*$  are considered, a shift in the measured values is observed as a consequence of most experimental procedure used to experimentally evaluate the flutter derivatives. In particular, when reduced velocities equal to zero are considered, the flutter derivatives represent the effects of a still fluid on a vibrating body while, for higher values of  $U_{red}$ , they take into account also the effects induced by the presence of wind.

If the free vibration method is used to evaluate the flutter derivatives, these changes in the system properties are commonly evaluated by comparing the system frequencies and damping ratios at different reduced velocities to the one measured at zero wind speed. Considering that the initial system identification is always performed in still air, as a result the value of the experimentally obtained flutter derivatives is always zero for  $U_{red} = 0$ .

If the forced vibration method is used, two cases are possible. On the one hand, if forces are measured using balances, the model inertial contributions have to be subtracted from the measured forces. Typically, such forces are evaluated analysing the model vibrations at zero wind speed so that, also in this case,  $H_4^*$  is null at zero reduced velocity. On the other hand, if forces are estimated integrating pressure measurements, the forces measured in still air show a finite value for  $H_4^*$  and  $A_3^*$  even at  $U_{red} = 0$ . The thin airfoil theory [14] often provides a good reference for the starting value of  $H_4^*$  for well streamlined decks that is approximately equal to  $\pi/2$ .

In the following, the thin airfoil reference solution is plotted adjusting the origin point coherently with the method used to extract the flutter derivatives but in some cases, when different extraction methods are compared (see Fig. 5.11), the shift might be visible. Such differences might be avoided if the model inertial properties are computed in still air and the test is performed in water [37]. However, it should be noticed that this terms have very little effects on the critical flutter speed (in the first Scanlan formulation they were even disregarded) so that such differences should be considered when comparison is made between data extracted with different methods but they are not relevant for applications.

Moreover, when flutter derivatives are estimated using the free vibration method, data are sometimes represented defining the reduced velocity on the base of the initial vibration frequency at zero wind speed. Considering that, with increasing wind speed, the natural vibration frequencies are changed by both the aerodynamic stiffness and damping, this can cause a shift in the data representation that, for typical bridge decks section model, can reach 30% for high  $U_{red}$  so that the reduced velocity definition should be carefully checked before comparison.

### 5.4.1 Combined forced vibration method

The method here proposed is a simple extension of the well established forced vibration method. Taking full advantage of the linear superposition principle always embedded in the flutter derivative analysis, it consists in imposing on the bridge deck a linear combination of harmonic motions instead of a single one.

When the recorded forces are post-processed, the frequencies are separated and they

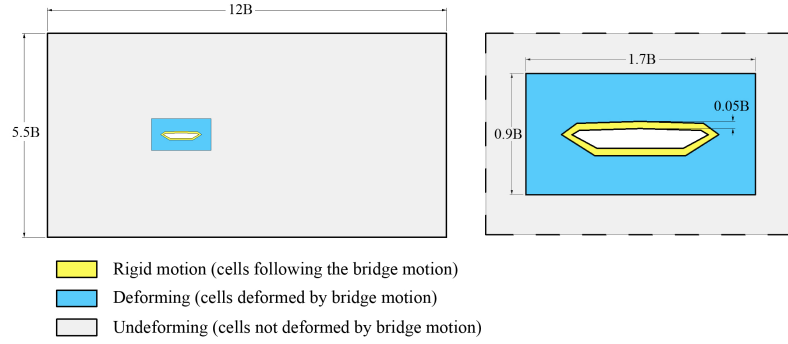
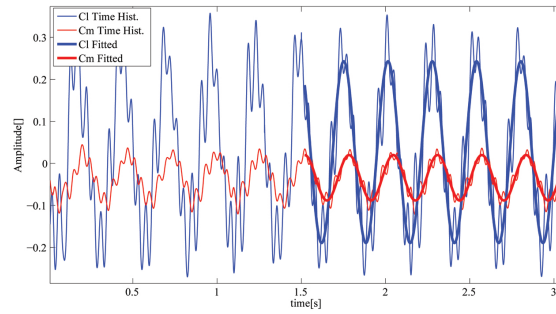
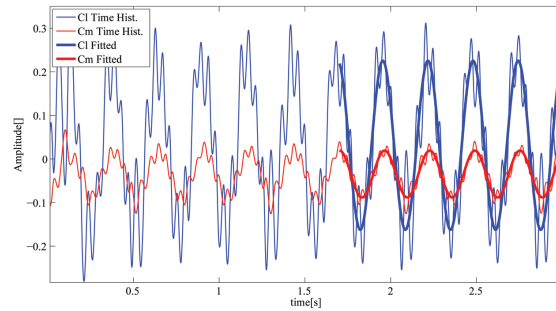


Figure 5.9: Computational domain subdivision adopted to manage the mesh motion.



(a)



(b)

Figure 5.10: Typical time histories recorded for  $U_{red}$  equal to 3.0: (a) rotational and (b) vertical motions.

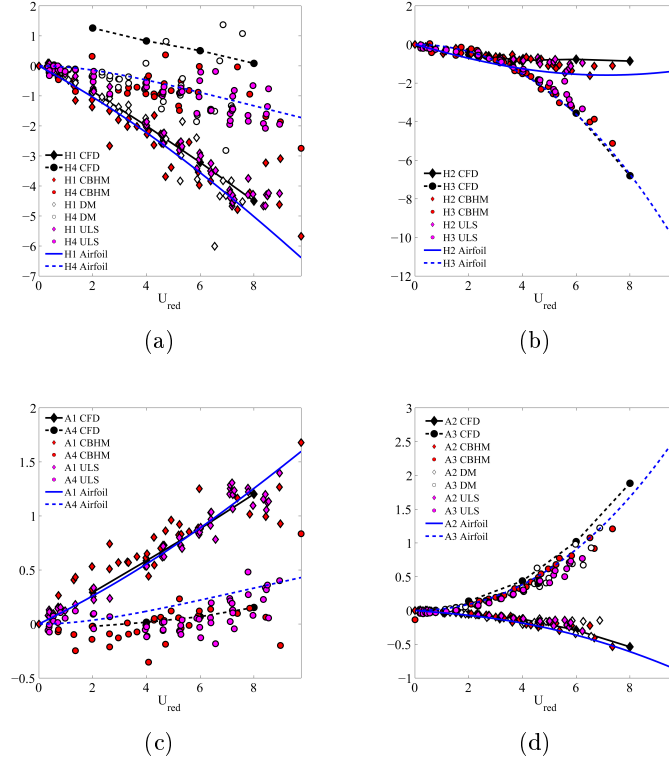


Figure 5.11: Example of Comparison of the flutter derivatives estimated with various methods and comparison with CFD estimation: the shift in the value of  $H_4^*$  can be clearly observed.

are studied independently like in standard procedures.

On one side, from the experimental point of view, this method would notably complicate the experimental apparatus needed to run the test in the wind tunnel without providing relevant time saving. On the other hand, from the computational point of view, the complications introduced by the combined vibrations are negligible while the computational time saving is considerable as only two simulations (one for rotational motions and one for the heaving ones) are strictly needed to evaluate the full set of flutter derivatives.

The limit of applicability of the method are clearly related to the system linearity and to the possibility of accurately separate the response to different motion frequencies. In this example, in order to accurately separate the frequencies, a procedure based on the response signal non-linear fitting, using a least square method has been used.

In this case, the considered bridge deck is well streamlined and barriers were not considered so explaining the similarity to the Theodorsen solution and the almost perfect linearity of the system response.

Unfortunately, when bridge decks are characterized by strong bluff features, neither linearity is observed nor it is possible to easily and accurately separate the contributions of different frequencies because the response itself is not so clearly sinusoidal.

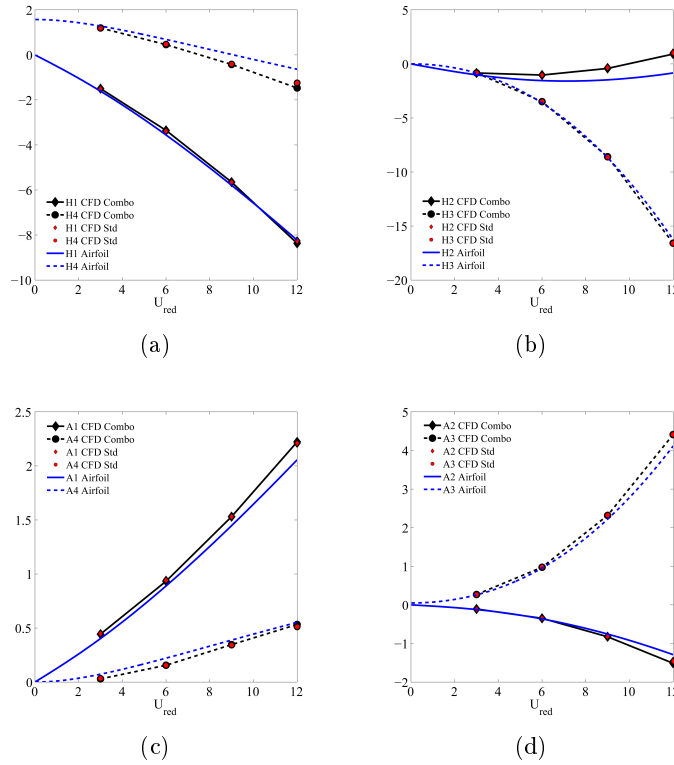


Figure 5.12: Comparison of flutter derivatives obtained with the standard forced vibration test and the combined one.

## 5.5 Critical flutter speed evaluation

Once the complete set of flutter derivatives is known and the structural properties defined, it is possible to evaluate the flutter critical speed. In the following, for simplicity, the bimodal approach will be followed because it has been proved to be reliable enough for the majority of practical applications and it is representative of the tests performed on sectional models, which are the topic of this thesis. A complete description of multi-modal approaches, more suitable for full bridge studies, can be found in [52, 53].

When real bridges, characterized by a set of flexural and torsional modes are considered, if the bimodal approach is used, it is necessary to individuate the pairs of modes that might lead to coupling and run the stability analysis for each couple. The critical speed will be the lowest between the identified ones.

Lets indicate the mode shapes as  $\psi_j$  with  $j = h, \alpha$  for the flexural and the torsional mode, respectively. The mode shapes are scaled so that:

$$\int_{\mathcal{L}} \psi_j^2 = 1, \quad (5.16)$$

where  $\mathcal{L}$  is the bridge length.

The coupling factor between the considered flexural and torsional modes is defined as:

$$Q_{h\alpha} = \int_{\mathcal{L}} \psi_h \psi_{\alpha}, \quad (5.17)$$

so that the modal coupling matrix can be written as:

$$\mathbf{Q} = \begin{bmatrix} 1 & Q_{h\alpha} \\ Q_{h\alpha} & 1 \end{bmatrix}. \quad (5.18)$$

The system motion equations can be written according to Eq. (5.12) as:

$$\mathbf{M}^{st} \ddot{\boldsymbol{\vartheta}} + (\mathbf{C}^{st} - \mathbf{Q} \circ \mathbf{C}^{ae}) \dot{\boldsymbol{\vartheta}} + (\mathbf{K}^{st} - \mathbf{Q} \circ \mathbf{K}^{ae}) \boldsymbol{\vartheta} = \mathbf{0}, \quad (5.19)$$

where the operator  $\circ$  represents the element-wise product (Hadamard product). The structural mass, damping and stiffness matrices can be obtained, once the bridge or model vibration modes are known, as:

$$\mathbf{M}^{st} = \begin{bmatrix} M & 0 \\ 0 & I \end{bmatrix}, \quad \mathbf{C}^{st} = \begin{bmatrix} 2\xi_h \Omega_h M & 0 \\ 0 & 2\xi_{\alpha} \Omega_{\alpha} I \end{bmatrix}, \quad \mathbf{K}^{st} = \begin{bmatrix} \Omega_h^2 M & 0 \\ 0 & \Omega_{\alpha}^2 I \end{bmatrix}, \quad (5.20)$$

where  $\xi_j$  are modes damping ratios,  $\Omega_j$  are mode frequencies and  $M, I$  are the deck mass and inertia per unit length. The system can be written in non-dimensional form as:

$$\ddot{\boldsymbol{\vartheta}} + (\bar{\mathbf{C}}^{st} - \mathbf{Q} \circ \bar{\mathbf{C}}^{ae}) \dot{\boldsymbol{\vartheta}} + (\bar{\mathbf{K}}^{st} - \mathbf{Q} \circ \bar{\mathbf{K}}^{ae}) \boldsymbol{\vartheta} = \mathbf{0}, \quad (5.21)$$

which is an extension of Eq. (5.12). In the following the notation  $\bar{\mathbf{C}}$  and  $\bar{\mathbf{K}}$  will be used according to Eq. (5.14) intending that the matrix  $\mathbf{Q}$  has been embedded in the formulation according to Eq. (5.21).

When real bridges are considered, such modes are evaluated by solving the structure in static condition including geometrical non-linearities and the modal analysis is performed by linearising the system in the surrounding of such static equilibrium condition.

It must be noticed that, in the critical flutter speed evaluation, the aerodynamic damping and stiffness matrices depend on the system eigenvalues which in turns are affected by such matrices leading to a non-linear problem. Two well known approaches to calculate the critical flutter speed are reported in the following.

### 5.5.1 Flutter determinant

The method consists in individuating the wind speed that makes the system described by Eq. (5.12) become singular [5]. The method starts by observing that, in flutter condition, heaving and torsional motions are characterized by the same angular velocity,  $\Omega^{cr}$ , and by the same reduced velocity,  $U_{red}^{cr}$ .

The determinant of the characteristic equation of the system is written at each reduced velocity leaving the system angular velocity unknown. This leads to two equations, one for the real part and another for the imaginary part of the determinant. Such equations are set equal to zero and solved providing a vector of angular velocities. The critical condition is reached when a reduced velocity is found where the same angular velocity makes both the real and the imaginary part of the determinant equal to zero.



In particular, assuming the system in critical condition, by substituting harmonic solutions in the motion equations of the form:

$$\boldsymbol{\vartheta} = \{h_d^c \quad \alpha^c\}^T e^{\Omega^{cr}t}, \quad (5.22)$$

where  $h_d^c$  and  $\alpha^c$  are complex amplitudes and  $\Omega^{cr}$  is the angular velocity in critical condition, Eq. (5.19) can be written in extended form as:

$$\left[ -\Omega^2 + 2i\xi_h\Omega + 1 - \frac{\Omega}{2\gamma_M}(H_4^* + iH_1^*) \right] \frac{h_d^c}{B} - \left[ \frac{Q_{h\alpha}\Omega^2}{2\gamma_M}(H_3^* + iH_2^*) \right] \alpha^c = 0, \quad (5.23)$$

$$\left[ -\frac{Q_{h\alpha}\Omega^2}{2\gamma_I}(A_4^* + iA_1^*) \right] \frac{h_d^c}{B} + \left[ -\Omega^2 + 2i\xi_\alpha\gamma_\Omega\Omega + \gamma_\Omega^2 - \frac{\Omega}{2\gamma_I}(A_3^* + iA_2^*) \right] \alpha^c = 0. \quad (5.24)$$

where:

$$\Omega = \frac{\Omega^{cr}}{\Omega_h}, \quad \gamma_\Omega = \frac{\Omega_\alpha}{\Omega_h}, \quad \gamma_M = \frac{M}{\rho B^2}, \quad \gamma_I = \frac{I}{\rho B^4}. \quad (5.25)$$

If the determinant of the coefficient matrix of the system defined by Eqs. (5.23) and (5.24) is set to zero and real and imaginary parts are separated, the following is obtained:

$$R_4\Omega^4 + R_3\Omega^3 + R_2\Omega^2 + R_1\Omega + \gamma_\Omega = 0, \quad (5.26)$$

$$I_3\Omega^3 + I_2\Omega^2 + I_1\Omega + [2\xi_h\gamma_\Omega^2 + 2\xi_\alpha\gamma_\Omega] = 0, \quad (5.27)$$

where the equations coefficients are:

$$R_1 = 0,$$

$$R_2 = -\gamma_\Omega^2 - 4\xi_\alpha\xi_h\gamma_\Omega - 1 - A_3^*/(2\gamma_I) - \gamma_\Omega^2 H_4^*/(2\gamma_M),$$

$$R_3 = \xi_\alpha\gamma_\Omega H_1^*/\gamma_M + \xi_h A_2^*/\gamma_I,$$

$$R_4 = 1 + H_4^*/(2\gamma_M) + A_3^*/(2\gamma_I) + \frac{Q_{h\alpha}^2 A_1^* H_2^* - A_2^* H_1^* + H_4^* A_3^* - Q_{h\alpha}^2 A_4^* H_3^*}{4\gamma_M\gamma_I}, \quad (5.28)$$

$$I_1 = -\gamma_\Omega^2 H_1^*/(2\gamma_M) - A_2^*/(2\gamma_I),$$

$$I_2 = -2\xi_\alpha\gamma_\Omega - 2\xi_h - \xi_\alpha\gamma_\Omega H_4^*/\gamma_M - \xi_h A_3^*/\gamma_I,$$

$$I_3 = H_1^*/(2\gamma_M) + A_2^*/(2\gamma_I) + \frac{H_4^* A_2^* + H_1^* A_3^* - Q_{h\alpha}^2 H_3^* A_1^* - Q_{h\alpha}^2 H_2^* A_4^*}{4\gamma_M\gamma_I}.$$

Finally, the critical flutter speed is obtained by plotting the roots of such equations for varying  $U_{red}$  and individuating the minimum reduced velocity for which the two equations have one coincident root (see Fig 5.13).

Such method is quite simple but it does not provide insight in the evolution of the structure properties with increasing wind speed because the form of the solution substituted in the motion differential equations is not representative of the system responses in non-critical conditions.

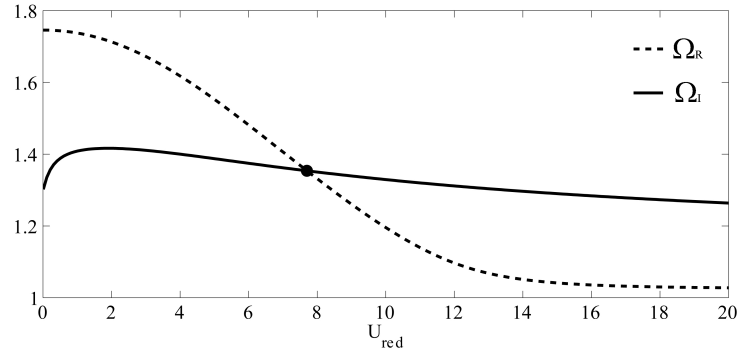


Figure 5.13: Example of critical flutter speed evaluation using the flutter determinant.

### 5.5.2 Iterative eigenvalue analysis

This procedure is more cumbersome than the one based on the flutter determinant but it has the advantage to allow the study of the structure properties evolution with increasing wind speed. A detailed description of such procedure is reported in [52].

The linear second order equations presented in Eq. (5.19) are converted into a linear first order system in the state space. Then, considering harmonic motions of the form:

$$\boldsymbol{\vartheta} = \{h_{d0} \quad \alpha_0\}^T e^{\lambda t} = \mathbf{w} e^{\lambda t}, \quad (5.29)$$

where  $\lambda$  is a complex eigenvalue and, this time,  $h_{d0}$  and  $\alpha_0$  are real amplitudes. When the solution is substituted in the first order system of equations, it leads to:

$$\left( \begin{bmatrix} \mathbf{I} & \mathbf{0} \\ \mathbf{0} & \mathbf{I} \end{bmatrix} \begin{bmatrix} \lambda^2 \mathbf{w} \\ \lambda \mathbf{w} \end{bmatrix} + \begin{bmatrix} \bar{\mathbf{C}} & \bar{\mathbf{K}} \\ -\mathbf{I} & \mathbf{0} \end{bmatrix} \begin{bmatrix} \lambda \mathbf{w} \\ \mathbf{w} \end{bmatrix} \right) e^{\lambda t} = \mathbf{0}, \quad (5.30)$$

where  $\mathbf{I}$  is the identity matrix. If we define:

$$\mathbf{w}_\lambda = \begin{bmatrix} \lambda \mathbf{w} \\ \mathbf{w} \end{bmatrix}, \quad \mathbf{A} = \begin{bmatrix} \bar{\mathbf{C}} & \bar{\mathbf{K}} \\ -\mathbf{I} & \mathbf{0} \end{bmatrix}, \quad (5.31)$$

it is possible to rewrite Eq. (5.30) as:

$$(\mathbf{A} - \lambda \mathbf{I}) \mathbf{w}_\lambda e^{\lambda t} = \mathbf{0}. \quad (5.32)$$

The system has  $2n$  degrees of freedom where  $n$  is the number of modes considered (in our case  $n = 2$ ). When an eigenvalue is found, its complex conjugate is an eigenvalue as well so defining, together with the corresponding eigenvectors, an oscillation mode. Such system, must be solved iteratively as the matrix  $\mathbf{A}$  depends on the eigenvalue  $\lambda$ . In particular, once an eigenvalue  $\lambda_j$  (with  $j = 1 \dots 2n$ ) is found, it can be demonstrated that:

$$\Omega_j = \text{Im}[\lambda_j] \quad (5.33)$$

$$\xi_j = -\text{Re}[\lambda_j] / \text{Mod}[\lambda_j] \quad (5.34)$$

where  $\text{Im}[\cdot]$  and  $\text{Re}[\cdot]$  indicate the imaginary and real part, respectively and  $\text{Mod}[\cdot]$  indicates the modulus.

The procedure can be implemented as follows:

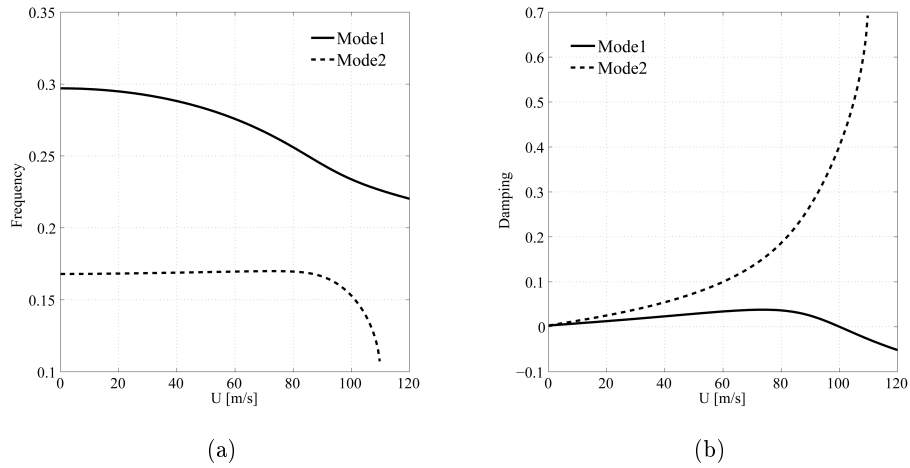


Figure 5.14: Example of critical flutter speed evaluation using the iterative eigenvalue analysis: evolution with the wind speed of (a) modes frequencies, (b) modes damping.

1. The eigenvalues  $\lambda_{j0}$  are extracted at zero wind speed.
2. The velocity is increased of some meters per second and the eigenvalue problem described in Eq. (5.32) is solved  $n$  times building the  $\mathbf{A}_{\lambda_j}$  (with  $j = 1, 2, \dots, n$ ) matrix using  $\Omega_{j0}$  extracted using the eigenvalue  $\lambda_{j0}$ .
3. The new eigenvalue obtained in the previous step is used to calculate an updated  $\mathbf{A}_{\lambda_j}$  matrix, one for each  $\lambda_j$ . The system is solved iteratively, for each eigenvalue, until the  $\mathbf{A}_{\lambda_j}$  matrix stabilises and a converged solution is reached. In such iterative procedure it is always necessary to work with the eigenvalue that minimizes the distance between  $\Omega_j^{(i)}$  and  $\Omega_j^{(i+1)}$  where  $i$  is the iteration counter.
4. The wind velocity is increased and the initial guess on  $\Omega_j$ , used to calculate the  $\mathbf{A}_{\lambda_j}$  matrix at the subsequent wind speed, can be extracted by linear extrapolation from previous steps.
5. Points 3-4 are repeated increasing the velocity so scanning the range of interest.

At each main iteration (iteration that provides the increase in wind speed) the frequency and damping ratio are recorded for each eigenvalue. Flutter instability occurs when one mode is found to become negatively damped.

### 5.5.3 Motion equations integration

Such method is here presented on one side in order to introduce the matter of Chapter 6 and on the other side because, although not rigorous, it sometimes provides good results, even if compared to more rigorous approaches as the ones proposed in previous sections.

The flutter derivatives are defined in the frequency domain so that it is in no way rigorous to proceed to the integration of the equation of motion starting from Eq. (5.19)

which is unknown because the aeroelastic contributions are not defined until the vibration frequency has been found.

Nevertheless, it must be noticed that the structure motion is usually characterized by harmonic oscillations (both considering instability and vortex shedding) so that, if an estimate for such motion frequency is available, the system can be identified and resolved.

Two situations can be encountered that might be used to obtain meaningful results:

1. The system is studied in lock-in condition. In such circumstance the frequency of oscillation and the wind velocity are defined *a priori*. The system vibrates at a single frequency (both heaving and torsion) so defining a unique reduced velocity used to evaluate the aeroelastic contributions.
2. The system is studied in free vibrations at a predefined velocity. Although not rigorous, it is possible to perform an iterative eigenvalue analysis neglecting the aeroelastic coupling terms so approximately evaluating the structure properties at such velocity. In such a way the two modes remain decoupled defining a frequency for torsion and one for heaving. The aeroelastic contributions are evaluated separately, including the coupling terms, each one considering the appropriate frequency.

The previously described approaches are not rigorous and their accuracy depends on the validity of the assumptions regarding the final oscillation frequency. The integration of the equations can be performed using a Runge-Kutta integration scheme and the solution should be considered physically based only when the harmonic motion is fully established (see Fig. 5.15).

The previously described approaches cannot be claimed to be developed in the time-domain because the information on the aeroelastic response is still completely provided by a frequency-based approach. In fact, in order to define a real time-domain approach it is necessary to consider the so called indicial functions (extensions of the Wagner function) described in Chapter 6.

## 5.6 Fully coupled simulations

In this section, fully coupled simulations are addressed. Such simulations require the full coupling between the structure and the fluid providing a direct estimation of the critical flutter wind speed. There is no advantage in proceeding in such a way for flutter analyses but it might be of interest to have a visual inspection of the coupling mechanism in order to individuate the feature which lead to instability. Noticed that, on theoretical ground, the estimation of the critical flutter speed obtained in such a way includes the fluid non-linearities so, at a first sight, it should lead to more precise results if compared to the procedures described in Sec. 5.5.1 and Sec. 5.5.2. In practice, simulations involving highly non-linear fluid behaviours might be inaccurate if RANS turbulence models are used and their reliability should be evaluated case by case based on the operator experience. In general, the vortex shedding intensity, the stall angle and the development of large vortical structures might be inaccurate if RANS models are used and caution should be used if such mechanisms and conditions are developed

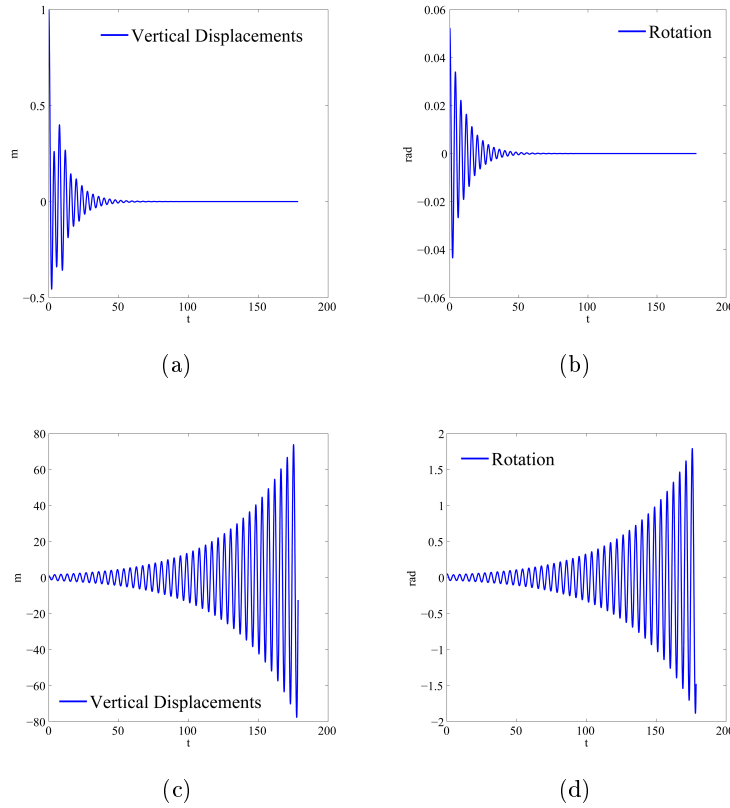


Figure 5.15: Example of free vibration time histories calculated with initial displacements: (a) and (b)  $U = 0.8U_{cr}$ , (c) and (d)  $U = 1.1U_{cr}$ .

(in Chapters 7 and 8 a wide selection of cases is analysed).

The settings regarding the mesh organization are identical to what has been described for forced vibration tests while the analysis settings are described in details in Chapters 7 and 8.

Lets now consider difficulties peculiar to fully coupled analysis. Once the simulation  $Re$  number is chosen (in Chapter 8 the problem is addressed in detail) the mesh sizing should be fixed according to the wall treatment that we want to use (wall functions or integration through the boundary layer). In order to keep the simulation strategy constant while exploring the velocity range of interest, it is convenient to keep the mesh and the inlet velocity constant and modify the structure properties in order to simulate a velocity increase. Furthermore, it is often preferable to build the deck geometry considering  $B = 1$  and scale the structure properties accordingly.

When the numerical model is built with  $B_{num} = 1$  and the inlet velocity,  $U_{num}$ , fixed on the base of the selected target  $Re$  number, it is possible to define a length and a velocity scale between the numerical simulation and the real structure as:

$$U_{real} = U_{scale}U_{num}, \quad B_{real} = B_{scale}B_{num}. \quad (5.35)$$

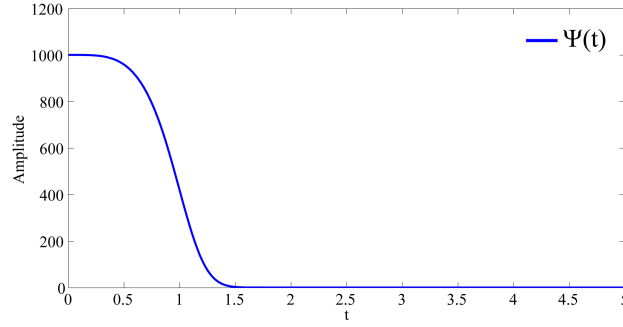


Figure 5.16: Ramp function used to scale the structure stiffness and damping after initialization ( $Fq = 1.0$ ).

It is then possible to scale the structure properties as follows:

$$\begin{aligned} M_{num} &= M_{real}/B_{scale}^2, & I_{num} &= I_{real}/B_{scale}^4, \\ Fq_{num} &= Fq_{real} \frac{B_{scale}}{U_{scale}}, & \xi_{num} &= \xi_{real}. \end{aligned} \quad (5.36)$$

Coupling between the structure and the fluid can be obtained following an explicit scheme greatly decreasing the computational cost. This is justified by the fact that typical reduced velocities for the flutter mechanism of bridge decks are higher than  $U_{red} = 4$ . If we assume that one non-dimensional time  $S$  is discretized at least with 500 time steps, each cycle of the structure motion is divided in 2000 time steps and the explicit scheme is justified.

Another problem is the initialization of the flow field. It is convenient to start the simulation fixing the structure and arrive to a converged solution (stable shedding mechanism and time averaged aerodynamic coefficients). The structure is then gradually released so avoiding shocks due to impulsive loading. This is achieved by amplifying the structure stiffness and damping so that they have extremely high value in the beginning of the simulation and reach their final value within 2-3 deck oscillation periods.

The ramp used to amplify the structure parameters,  $\Psi(t)$  ( $t$  is the simulation time), should be such that  $\Psi(0) \simeq 1.0E3$  and  $\Psi(T_s) = 1.0$  with extremely good accuracy for  $T_s = 2/Fq$ . The following form is here proposed:

$$\Psi(t) = 1.0 + 2.0E3 \left( \frac{1}{2} - \frac{1}{2} \tanh((t \cdot Fq/1.5)^4) \right), \quad (5.37)$$

whose graph is reported in Fig. 5.16 for  $Fq = 1.0$ . In order to accelerate the insurgence of instability, which might be sometimes quite slow, it is possible to trigger it by artificially inducing a small shock after the structure is released.

Typical outputs, obtained for the Chongqing bridge are reported in Fig. 5.17. The simulation refers to Str. 1, as defined in Chapter 8, with  $U_{scale}$  selected so that the inlet velocity is  $1.1U_{cr}$ .

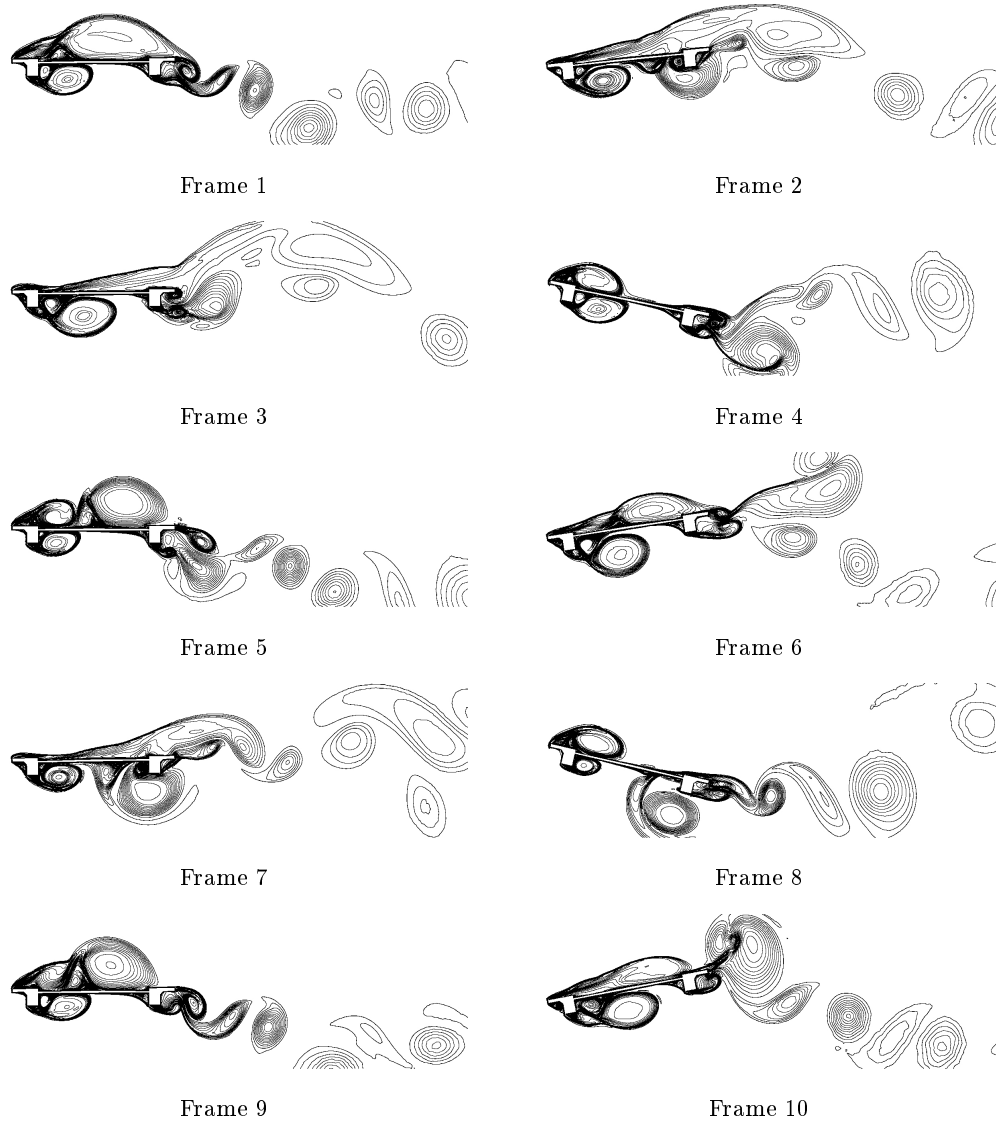


Figure 5.17: Fully coupled simulation: vorticity contours showing flutter instability for Chongqing bridge ( $Re = 1.5E5$ ). Full details about the geometry of the deck and the simulation settings are provided in Chapter 8.

## Chapter 6

# The thin airfoil theory and its generalization

In this chapter the thin airfoil theory is described according to Wagner and Theodorsen models in the time and the frequency domain, respectively. The strong duality between the two approaches, the embedded hypotheses and their limitations are highlighted and discussed in detail. A generalization of the model and a procedure able to identify its parameters with a minimum number of numerical simulations, is proposed. The aim is to provide a coherent framework to the modelling of self-induced aeroelastic loads and explore the applicability of linearised approaches when mildly bluff bodies are considered.

### Contents

---

<b>6.1</b>	<b>Introduction</b>	<b>98</b>
6.1.1	Motion-induced loads on bridge deck sections	100
<b>6.2</b>	<b>A consistent time-domain description</b>	<b>102</b>
6.2.1	Time-frequency duality	103
<b>6.3</b>	<b>Identification of model parameters</b>	<b>105</b>
6.3.1	Asymptotic regimes	105
6.3.2	Response to quasi-step motions	106
6.3.3	Response to an angular harmonic motion	108
<b>6.4</b>	<b>A numerical approach</b>	<b>109</b>
6.4.1	The numerical model	109
6.4.2	Aerodynamic data evaluation procedure	110
6.4.3	Response to vertical motions	112
<b>6.5</b>	<b>Numerical results: the FTP case</b>	<b>113</b>
6.5.1	Harmonic motions	113
6.5.2	Quasi-step motion	113
6.5.3	Application of the identification procedure	114
<b>6.6</b>	<b>Numerical results: the CBS case</b>	<b>116</b>

---



## 6.1 Introduction

The problem of evaluating the forces acting on a moving cylindrical body immersed in a low-speed flow is of great importance in many industrial and structural applications, ranging from aeronautics to mechanical and civil engineering. The case of the airfoil moving within an inviscid two-dimensional flow was solved by Wagner [15] and Theodorsen [14] under the assumption of a zero-thick profile (namely, the thin airfoil) approached by the flow with a small angle of incidence. The time-domain formulation based on the Wagner indicial approach, and the mixed frequency-time description developed by Theodorsen were reorganized and further developed by many authors [13, 16, 54, 32, 55], revealing the main theoretical background needed to systematically explain some complex fluid-structure interaction phenomena, such as the flutter instability.

Nevertheless, when unstreamlined bodies are considered, possible large flow separation, reattachment, recirculation zones and vortex shedding can occur, inducing significant unsteady effects and preventing to identify a thin and well defined boundary layer. Thereby, in these cases the hypothesis of inviscid and fully attached flow, generally acceptable for streamlined bodies immersed in a flow with a small angle of attack, must be often rejected. Accordingly, the description of the motion-induced loads on cylindrical bodies with a bluff sectional geometry, such as typical bridge decks, can not be directly obtained by using the thin airfoil theory.

In order to overcome such a drawback several theoretical and computational approaches have been developed, based on both frequency-domain and time-domain descriptions. In the context of bridge aerodynamics, motion-induced forces are synthetically described by distinguishing in-phase and out-of-phase components with respect to the time evolution of the motion, instead of the distinction between circulatory and non-circulatory effects as for the thin airfoil [56]. As a matter of fact, if proper circulatory and non-circulatory terms appear as clearly recognizable in the thin airfoil theory, in the case of bluff sections a certain distinction can be made only referring to flow memory-dependent (pseudo circulatory) and independent (pseudo non-circulatory) contributions.

As reported in Chapter 5, Scanlan [33, 34, 6, 32, 57, 35] profitably exported some features of the Theodorsen results, describing the wind loads induced by sectional harmonic motions by means of a linearized format based on experimentally-evaluated frequency-dependent filter functions (namely, the flutter derivatives), that supplied the lack of closed-form analytical formulations.

Time-domain approaches, generally established by introducing more than one indicial function, did not develop as much as the frequency-based models, due to the difficulties arising in the direct experimental evaluation of the response to step-wise motions. In the context of the bridge aerodynamics and following the classical results for the airfoil by Garrick [17] and Jones [58], Scanlan and coworkers [54, 59] were the first to combine Fourier synthesis and rational approximation techniques for analytically extracting the indicial functions from the experimentally-derived flutter derivatives. Starting from more refined formulations of the indicial response and considering generalized rational approximation procedures, similar approaches were recently developed in [56, 60, 61]. Nevertheless, indicial responses indirectly estimated from the flutter derivatives include implicitly non-circulatory contributions associated with the exper-

imental procedures employed to determine flutter derivatives themselves. Therefore, when memory-independent effects are not negligible, the corresponding estimates of the indicial functions can not be generally considered as fully consistent with the Wagner theory, that formally describes circulatory effects only (a consistent approach has been proposed in [62]).

As a matter of fact, the relative importance of non-circulatory contributions with respect to circulatory ones can be considered as problem dependent. For example, pseudo non-circulatory effects can be generally considered a priori of secondary importance for a truss deck with large openings and grillages, or when the flow regime and the sectional geometry induces wide bluff features characterized by large vortex structures. Nevertheless, many modern long-span bridges exhibit almost elongated and streamlined cross-sections characterized by mildly bluff performances. As a consequence, this occurrence on one hand does not allow to apply directly the ideal thin airfoil model but, on the other hand, can lead to non-circulatory effects generally not completely negligible with respect to the circulatory ones [63]. This matter can be more evident when eccentricity between the elastic axis and the gravity axis, and/or small values of the reduced velocity (or equivalently high values of the reduced frequency) are considered.

In this context, a general theoretical framework based on the main formal structure of the classical results of Theodorsen and Wagner, and developed without introducing simplifications a priori, would contribute to overcome some consistency problems with respect to the thin airfoil model. In this way, the mutual role played by memory-independent terms and pseudo-circulatory downwash effects could be highlighted, opening also to the possibility of drawing some insights on issues to which the thin airfoil theory does not provide suitable indications (e.g., drag force components).

In order to directly identify indicial responses on bridge decks, allowing also the indirect extraction of flutter derivatives, very few successful experimental techniques can be found in literature [64, 65]. This lack is mainly due to the drawbacks associated with the experimental replicability of an exact step function, as well as with the controllability of a suitable quasi-step description. As an alternative and/or support to the experimental methodologies, different computational approaches have been recently proposed, aiming to furnish direct estimates of aerodynamic indicial responses. Referring to two-dimensional grid-based methods, two different strategies are generally employed. The first considers a motionless solid region immersed in the fluid domain, simulating the step-response by suitable flow boundary conditions. The second directly simulates the motion of the solid domain within the flow, prescribing a smoothed-ramp motion of the section during a finite time in order to overcome the computational problems involved by the exact step-wise condition [66, 67]. The first attempt to directly determine indicial functions by using computational fluid dynamics (CFD) was made by Brar and coworkers [68] and was based on the first type of strategy; but, as highlighted in [67], some questionable aspects can be traced due to the adopted boundary conditions. Addressing aeronautical and industrial applications, more effective numerical formulations were recently developed, modeling step-wise body motions by the field velocity approach [69, 70, 71]. As regards the second class of numerical methods, mention is herein made to formulations based on an Arbitrary Lagrangian Eulerian (ALE) description of the fluid problem [47, 72, 73, 74, 67, 49, 48], allowing to account in a direct and consistent way for the motion of the solid domain within the fluid one. In this case, suitable mesh

morphing and/or remeshing algorithms have to be employed in order to accomplish the grid adaptation during the time-marching computation.

All the previous approaches have been successfully applied to streamlined geometries, for which the well-posed theoretical background drives the identification procedure of well-defined quantities. On the other hand, when unstreamlined bodies are considered, a fundamental task in time-domain formulations is the choice of the indicial responses to be considered in the loading description, and their relationships with downwash effects induced by the body motion. Partially borrowing the structure of the thin airfoil theory, available time-domain formulations have been generally developed by postulating the type of the indicial functions and the downwash contributions to which they combine by convolution. As a result, such an axiomatic approach has led to different formulations, that often are not directly comparable each other and that can suffer from some consistency and/or effectiveness lack. In particular, addressing the case of bridge deck sections, downwash contributions given by the pitch rate are usually neglected, and this choice is justified by invoking the bluff character of the section. Nevertheless, it is the author opinion that, in the majority of cases, modern bridge sections are neither streamlined enough to simply apply the airfoil theory nor bluff enough to justify such an assumption.

This chapter, moving from the available time-domain formulations and generalizing the thin airfoil theory within a unified dimensionless approach, attempts to furnish, without introducing simplifications a priori, a simple and consistent description of the motion-induced wind loads on elongated bridge sections, preserving the main features of the classical Theodorsen and Wagner theories. Both the time-domain and the frequency-domain representations are fully developed, aiming at providing a seamless framework that allows to identify meaningful and direct relationships between proper Wagner-like indicial functions and flutter derivatives. Consistency conditions based on the aerodynamic response in asymptotic regimes and simplified strategies involving a minimal amount of experiments or simulations suffice to completely define the model parameters.

### 6.1.1 Motion-induced loads on bridge deck sections

In the context of the bridge aerodynamics, moving from the Scanlan formulation [32, 6, 35], lift and moment induced by small-amplitude harmonic motions with reduced frequency  $k$  can be expressed in dimensionless form according to Eqs. (5.4):

$$C_l(s, k) = \hat{C}_l + kH_1^*h' + kH_2^*\alpha' + k^2H_3^*\alpha + k^2H_4^*h, \quad (6.1)$$

$$C_m(s, k) = \hat{C}_m + kA_1^*h' + kA_2^*\alpha' + k^2A_3^*\alpha + k^2A_4^*h, \quad (6.2)$$

where quantities  $\hat{C}_j$  are the mean generalized dimensionless forces associated with  $\hat{\alpha}$ , and  $A_i^*(\hat{\alpha}, k)$ ,  $H_i^*(\hat{\alpha}, k)$  ( $i = 1, \dots, 4$ ) are the flutter derivatives. They are dimensionless real functions generally depending on the section shape, on the steady part of the angle of attack (namely,  $\hat{\alpha}$ ), and on the reduced frequency  $k$ . Accordingly, considering for instance an harmonic rotation  $\alpha(s) = \alpha_0 e^{iks}$  about  $\hat{\alpha}$ , the dimensionless motion-induced generalized forces result in:

$$C_l(s, k) - \hat{C}_l = k^2(iH_2^* + H_3^*)\alpha_0 e^{iks} = \mathcal{H}_{l\alpha}(k) \alpha(s), \quad (6.3)$$

$$C_m(s, k) - \hat{C}_m = k^2(iA_2^* + A_3^*)\alpha_0 e^{iks} = \mathcal{H}_{m\alpha}(k) \alpha(s), \quad (6.4)$$

where the square moduli of the complex functions  $\mathcal{H}_{j\alpha}(k)$  have the meaning of aerodynamic frequency-response functions. Moreover, since forces themselves can be postulated as harmonic in time with reduced frequency  $k$ , the following equations hold

$$\frac{C_L e^{i\psi_L}}{\alpha_0} = \mathcal{H}_{l\alpha}(k), \quad \frac{C_M e^{i\psi_M}}{\alpha_0} = \mathcal{H}_{m\alpha}(k), \quad (6.5)$$

where  $C_J$  (with  $J = L, M$ ) denotes the amplitude of the harmonic function  $C_j(s) - \hat{C}_j$  ( $j = l, m$ ), and  $\psi_J$  is its phase shift with respect to the motion. Relationships similar to Eqs. (6.3)-(6.5) and involving the frequency-response functions  $\mathcal{H}_{jh}(k)$  are obtained by considering harmonic vertical motions  $h(s) = h_0 e^{iks}$ . In this way, by measuring values of quantities  $C_J$  and  $\Psi_J$  for different values of  $k$ , the eight flutter derivatives defining the Scanlan frequency-domain description can be extracted in agreement with the well-known forced vibration method [32], widely employed in both experimental [33, 75, 76, 77, 78] and computational approaches [47, 79, 80].

In agreement with the Wagner indicial approach, available time-domain descriptions of the aeroelastic loads on bridge sections are generally formulated moving from the basic rationale that the body motion can be regarded as an infinite series of infinitesimal step-wise increments. Thereby, assuming that flow memory effects are linearly superposable and considering small-amplitude motions, self-excited wind load are represented by Duhamel's convolution integrals, involving time-dependent dimensionless functions (often improperly indicated as Wagner-like indicial functions) that describe the transient evolution of the aerodynamic forces induced by step-wise changes of specific body displacement or velocity components. Therefore, several indicial responses are usually considered, depending on motion and force components. This occurrence represents a significant difference with respect to the thin airfoil theory, and arises from the attempt to account for possible unsteady effects induced by the sectional bluntness. In fact, when unstreamlined geometries are considered, a fixed rear neutral point which is common for different motions and forces, as it occurs for the thin airfoil, can not be identified, and the mean position of the aerodynamic center varies depending on the motion type. Attempts were made to describe motion-induced wind loads by postulating that downwash effects related to step-wise motions along different degrees of freedom are characterized by the same transient evolution, and differently affect lift and moment [13, 54]. This corresponds to consider relationships similar to Eqs. (3.48) and (3.49) where different indicial functions are introduced for describing  $C_l$  and  $C_m$ . Nevertheless, although such an approach can be successfully applied in the case of almost streamlined profiles (such as real wings or some modern bridge deck sections), it usually fails for bluffer bodies. In these cases, it is likely to assume that the indicial responses associated to the various downwash contributions are different.

Disregarding for drag and horizontal effects, available time-domain formulations are mostly based on two indicial functions for each generalized force. They are combined by convolution with downwash terms described by the displacement functions  $\alpha(s)$  and  $h(s)$  [81, 82], or by  $\alpha(s)$  and  $h'(s)$  [32, 56, 34, 60, 83]. Therefore, downwash contributions related to the pitch rate  $\alpha'(s)$  are not explicitly described, unlike the thin airfoil theory. Moreover, inertial effects are usually neglected or are at most intended to be implicitly incorporated within the indicial response. In fact, the adopted indicial functions are generally obtained by rational approximation techniques from the

experimentally-determined flutter derivatives, so preventing to formally distinguish between circulatory and non-circulatory terms. As a consequence, when inertial effects are not negligible, indirectly-extracted indicial functions for bluff sections have no direct correspondence with the Wagner's one (that instead describes circulatory effects only), because they include inertial contributions related to the identification procedure of the flutter derivatives. Such a consistency violation can be significant in the description of the first transient stage of the aerodynamic response to step-wise motions (i.e., for very small values of  $s$ ) and tends to disappear for high values of  $s$  (namely, when the response tends to be steady), inertial effects tending there to vanish.

It is worth pointing out that, as highlighted by [34], a convenient normalization of the indicial responses should ensure that dimensionless indicial functions tend to the unit when the time tends to infinity. Moreover, a consistency condition, verified for the thin airfoil, is that the time-domain formulation should be able to recover, as an asymptotic behavior, the quasi-stationary description of the aeroelastic loads.

## 6.2 A consistent time-domain description

Moving from the thin airfoil theory, self-excited loads on elongated sections with a mildly bluff character are herein described as the superposition of mean aerodynamic forces (described by  $\hat{C}_j(\hat{\alpha})$ ), pseudo-non-circulatory forces ( $C_j^{mc}$ ) and pseudo-circulatory ones ( $C_j^c$ ). It is worth pointing out that, addressing real sections, the distinction between circulatory and non-circulatory effects cannot be rigorously introduced as in the case of the ideal thin airfoil. Nevertheless, in the case of sectional geometries with a moderate bluff aerodynamic response, a certain distinction can be postulated in terms of measurable effects between contributions depending or not on the history of the body motion. Accordingly, pseudo-non-circulatory contributions should be regarded as independent on the motion history, whereas pseudo-circulatory ones as memory-dependent downwash-related terms. In the framework of a time-domain approach, non-circulatory loads are described as linearly depending on the first and the second time derivatives of the displacement functions  $h(s)$  and  $\alpha(s)$ :

$$C_j^{mc}(s) = C_{j,\alpha} [I_{j\alpha 1}\alpha' + I_{j\alpha 2}\alpha'' + I_{jh 1}h' + I_{jh 2}h''], \quad (6.6)$$

where the eight dimensionless quantities  $I_{jgi}$  (with  $i = 1, 2$ ) are model parameters and, as a rule,  $C_{j,\alpha} = \partial \hat{C}_j / \partial \hat{\alpha}$ .

The circulatory contributions are represented by combining via convolution four indicial functions (two for each generalized force) with downwash terms. These latter are assumed to be different for each force and for each displacement component, and are described as linear combinations of displacements and their first time derivatives, then including also effects related to the pitch rate  $\alpha'(s)$ . Thereby, circulatory terms read as

$$C_j^c(s) = C_{j,\alpha} \int_{-\infty}^s [\phi_{j\alpha}(s-\sigma) w'_{j\alpha}(\sigma) + \phi_{jh}(s-\sigma) w'_{jh}(\sigma)] d\sigma, \quad (6.7)$$

where the following four downwash functions have been introduced

$$w_{j\alpha}(s) = D_{j\alpha 0}\alpha(s) + D_{j\alpha 1}\alpha'(s), \quad (6.8)$$

$$w_{jh}(s) = D_{jh 0}h(s) + D_{jh 1}h'(s), \quad (6.9)$$

the eight dimensionless quantities  $D_{jgi}$  (with  $i = 0, 1$ ) being other model parameters, and where  $\phi_{jg}(s)$  are proper Wagner-like indicial functions, assumed to be zero for  $s < 0$  and generally depending on  $\hat{\alpha}$ . They describe the transient aerodynamic response in terms of the generalized force  $j$  when a step-wise change in the downwash function  $w_{jg}(s)$  from zero to the final value  $\tilde{w}_{jg}$  occurs at  $s = 0$ . If  $D_{jg0} \neq 0$  such a step-wise change is achieved by an abrupt change in the function  $g(s)$  (with  $g = \alpha, h$ ), that is by considering  $g(s) = \Theta(s)\tilde{g}$  where  $\Theta(s)$  is the Heaviside function; otherwise, if  $D_{jg0} = 0$ , by considering  $g'(s) = \Theta(s)\tilde{g}'$ . In both cases it results  $w'_{jg}(s) = 0$  for  $s > 0$ . The final value  $\tilde{g}$  (respectively  $\tilde{g}'$ ) is assumed to be small so that the first-order approximation of all physical quantities can be consistently applied.

As a consistency condition, Wagner-like indicial functions are assumed to be normalized in such a way that they tend to the unit when the time tends to infinity.

In the case of the thin airfoil and considering  $\hat{\alpha} = 0$  the four indicial functions consistently reduce to the Wagner's one, i.e.  $\phi_{j\alpha}(s) = \phi_{jh}(s) = \phi(s)$ , and  $w_{j\alpha}(s) + w_{jh}(s) = w_{3/4}(s)$ . Moreover, the introduced parameters result in:

$$I_{l\alpha 1} = \frac{1}{4}, \quad I_{l\alpha 2} = -\frac{a}{8}, \quad I_{lh1} = I_{mh1} = 0, \quad I_{lh2} = \frac{1}{4}, \quad (6.10)$$

$$I_{m\alpha 1} = -\frac{1}{4} \frac{(\frac{1}{2} - a)}{(\frac{1}{2} + a)}, \quad I_{m\alpha 2} = -\frac{1}{8} \frac{(\frac{1}{8} + a^2)}{(\frac{1}{2} + a)}, \quad I_{mh2} = \frac{a}{4(\frac{1}{2} + a)}, \quad (6.11)$$

$$D_{j\alpha 0} = D_{jh1} = 1, \quad D_{j\alpha 1} = \frac{1}{2} \left( \frac{1}{2} - a \right), \quad D_{jh0} = 0. \quad (6.12)$$

### 6.2.1 Time-frequency duality

As for the thin airfoil, the Fourier synthesis allows to establish duality between time-domain and frequency-domain descriptions. By equating Fourier transforms of motion-dependent loads described via the Scanlan formulation Eqs. (6.1) and (6.2) and through Eqs. (6.6) and (6.7), the following four ( $j = l, m$  and  $g = \alpha, h$ ) complex relationships hold:

$$C_{j,\alpha} [ikI_{jg1} - k^2I_{jg2} + C_{jg}(k)(D_{jg0} + ikD_{jg1})] = \mathcal{H}_{jg}(k), \quad (6.13)$$

where the frequency-response functions  $\mathcal{H}_{jg}(k)$  are defined as in Eqs. (6.3) and (6.4), and the following four Theodorsen-like complex circulatory functions are introduced:

$$C_{jg}(k) = \mathcal{F}_{jg}(k) + i\mathcal{G}_{jg}(k) = ik \int_0^\infty \phi_{jg}(\sigma) e^{-ik\sigma} d\sigma = \phi_{jg}^0 + \overline{\phi'_{jg}}(k), \quad (6.14)$$

so that

$$\phi_{jg}(s) = \frac{1}{2\pi i} \int_{-\infty}^\infty \frac{C_{jg}(k)}{k} e^{iks} dk = \frac{2}{\pi} \int_0^\infty \frac{\mathcal{F}_{jg}(k)}{k} \sin ks dk, \quad (6.15)$$

$\mathcal{F}_{jg} = \text{Re}[C_{jg}]$  and  $\mathcal{G}_{jg} = \text{Im}[C_{jg}]$  being the real and imaginary parts of  $C_{jg}(k)$ , respectively,  $\phi_{jg}^0 = \phi_{jg}(0)$ , and where the frequency-dependent quantity  $\bar{f}(k) = \int_{-\infty}^\infty f(s) e^{-iks} ds$  denotes the Fourier transform of the time-dependent function  $f(s)$ .

Collecting real and imaginary contributions in Eq. (6.13), the following eight frequency-based equations hold:

$$k^2 H_1^*(k) = C_{l,\alpha} [k I_{lh1} + \mathcal{G}_{lh}(k) D_{lh0} + k \mathcal{F}_{lh}(k) D_{lh1}], \quad (6.16)$$

$$k^2 H_2^*(k) = C_{l,\alpha} [k I_{l\alpha1} + \mathcal{G}_{l\alpha}(k) D_{l\alpha0} + k \mathcal{F}_{l\alpha}(k) D_{l\alpha1}], \quad (6.17)$$

$$k^2 H_3^*(k) = C_{l,\alpha} [-k^2 I_{l\alpha2} + \mathcal{F}_{l\alpha}(k) D_{l\alpha0} - k \mathcal{G}_{l\alpha}(k) D_{l\alpha1}], \quad (6.18)$$

$$k^2 H_4^*(k) = C_{l,\alpha} [-k^2 I_{lh2} + \mathcal{F}_{lh}(k) D_{lh0} - k \mathcal{G}_{lh}(k) D_{lh1}], \quad (6.19)$$

$$k^2 A_1^*(k) = C_{m,\alpha} [k I_{mh1} + \mathcal{G}_{mh}(k) D_{mh0} + k \mathcal{F}_{mh}(k) D_{mh1}], \quad (6.20)$$

$$k^2 A_2^*(k) = C_{m,\alpha} [k I_{m\alpha1} + \mathcal{G}_{m\alpha}(k) D_{m\alpha0} + k \mathcal{F}_{m\alpha}(k) D_{m\alpha1}], \quad (6.21)$$

$$k^2 A_3^*(k) = C_{m,\alpha} [-k^2 I_{m\alpha2} + \mathcal{F}_{m\alpha}(k) D_{m\alpha0} - k \mathcal{G}_{m\alpha}(k) D_{m\alpha1}], \quad (6.22)$$

$$k^2 A_4^*(k) = C_{m,\alpha} [-k^2 I_{mh2} + \mathcal{F}_{mh}(k) D_{mh0} - k \mathcal{G}_{mh}(k) D_{mh1}]. \quad (6.23)$$

Previous equations identify closed-form relationships between flutter derivatives and Theodorsen-like circulatory functions, and allow to clearly distinguish between pseudo-circulatory contributions and pseudo-non-circulatory ones within the classical Scanlan formulation.

With the aim to contribute to define a simple procedure for identifying model parameters, based on very few experiments or numerical simulations, the following decomposition of the Wagner-like indicial functions will be useful in what follows:

$$\phi_{jg}(s) = \phi_{jg}^0 \Theta(s) + \phi_{jg}^*(s). \quad (6.24)$$

Thereby, the Theodorsen-like circulatory functions can be conveniently decomposed as (see Eq. (6.14)):

$$\mathcal{C}_{jg}(k) = \phi_{jg}^0 + \mathcal{C}_{jg}^*(k), \quad (6.25)$$

where

$$\mathcal{C}_{jg}^*(k) = \mathcal{F}_{jg}^*(k) + i \mathcal{G}_{jg}^*(k) = \overline{\phi_{jg}'(k)} = ik \int_0^\infty \phi_{jg}^*(\sigma) e^{-ik\sigma} d\sigma. \quad (6.26)$$

Accordingly, Eq. (6.13) can be rearranged as

$$\frac{\mathcal{H}_{jg}(k)}{C_{j,\alpha}} = [\phi_{jg}^0 + \mathcal{C}_{jg}^*(k)] + ik \{ I_{jg1} + [\phi_{jg}^0 + \mathcal{C}_{jg}^*(k)] D_{jg1} \} - k^2 I_{jg2}. \quad (6.27)$$

In the case of the thin airfoil, since Eqs. (6.10) to (6.12), relationships (6.16) to (6.23) reduce to Eqs. (5.6) recovering, for  $a = 0$ , Eq. (5.6) proposed by Scanlan [6]. It is worth noting that non-circulatory contributions for the thin airfoil (that is contributions that do not depend on  $\mathcal{F}$  or  $\mathcal{G}$ ) appear in flutter derivatives  $H_i^*$ ,  $A_i^*$  with  $i = 2, 3, 4$ ; they are of order  $(1/k)^1$  for  $i = 2$ , and of order  $(1/k)^0$  for  $i = 3, 4$ . When high frequency regimes are considered (that is, when  $1/k$  tends to zero)  $\mathcal{F}$  tends to  $\phi(0) = 0.5$  and  $\mathcal{G}$  tends to zero [13]. Accordingly, flutter derivatives of type 1 and 2 tend to vanish, whereas those with indexes 3 and 4 tend to values different from zero because of inertial effects.

### 6.3 Identification of model parameters

In theory, if experimental, theoretical and/or numerical approaches are properly established in order to successfully estimate the complex functions  $\mathcal{C}_{jg}(k)$  (accounting for circulatory effects only and related to Wagner-like indicial functions  $\phi_{jg}(s)$  via Eq. (6.14), the sixteen parameters (postulated to be frequency-independent) that define the proposed loading description could be identified by using Eqs. (6.16)-(6.23), and analysing the frequency-domain system response at only two different finite value of  $k$ . Nevertheless, as previously recalled, the identification of the indicial responses for bridge deck sections is nowadays generally based on rational approximations from flutter derivatives, including both circulatory and non-circulatory effects. Therefore, the evaluation of proper Wagner-like indicial functions, accounting only for circulatory contributions, could be considered as a possible drawback of the proposed approach, preventing the practical applicability of Eqs. (6.16) to (6.23) for estimating the model parameters.

In the following, asymptotic relationships and simplified strategies will be traced for attempting to overcome such a limitation, showing that few experimental or computational tests can suffice to consistently describe the motion-induced wind loads on elongated sectional geometries with a mildly bluff character. In detail, in these cases the identification of the aerodynamic response to two quasi-step motions (one for each degree of freedom) and to an angular harmonic motion, combined with consistency conditions arising from the asymptotic behavior in quasi-stationary regimes, allow to give an estimate of the complete set of parameters needed to apply the proposed loading model.

#### 6.3.1 Asymptotic regimes

As a consistency condition, for quasi-stationary body motions, that is for very low frequency regimes, the unsteady wind load description has to recover the steady aerodynamic response. Therefore, in agreement with the quasi-stationary theory [84, 85] and neglecting drag effects, the following relationships hold in the limit of vanishing  $k$ :

$$\begin{aligned} \lim_{k \rightarrow 0^+} k H_1^* &= \lim_{k \rightarrow 0^+} k^2 H_3^* = C_{l,\alpha}, \\ \lim_{k \rightarrow 0^+} k A_1^* &= \lim_{k \rightarrow 0^+} k^2 A_3^* = C_{m,\alpha}, \\ \lim_{k \rightarrow 0^+} k^2 H_4^* &= \lim_{k \rightarrow 0^+} k^2 A_4^* = 0. \end{aligned} \quad (6.28)$$

Due to the normalization employed in Eq. (6.7), the asymptotic response for low frequency values of the Theodorsen-like circulatory functions  $\mathcal{C}_{jg}(k)$  can be postulated to be such that

$$\lim_{k \rightarrow 0^+} \mathcal{F}_{jg}(k) = 1, \quad \lim_{k \rightarrow 0^+} \mathcal{G}_{jg}(k) = 0. \quad (6.29)$$

Accordingly, by combining Eq. (6.28) with Eqs. (6.16), (6.18), (6.19), and with Eqs. (6.20), (6.22), (6.23), six independent conditions among eight model parameters are obtained ( $j = l, m$ ):

$$D_{j\alpha_0} = 1, \quad D_{jh0} = 0, \quad I_{jh1} + D_{jh1} = 1, \quad (6.30)$$



previous relationships being consistent with the thin airfoil theory (see Eqs. (6.10) to (6.12)). Since the aerodynamic response in the steady regime is not affected by inertial contributions, it has to be recovered as the limit of circulatory effects only, as it occurs in the case of the thin airfoil. Accordingly, the third equation in Eq. (6.30) is satisfied by assuming that  $I_{jh1} = 0$  and  $D_{jh1} = 1$ . As a matter of fact, the choice  $D_{jh0} = 0$  sounds as physically consistent with the condition that a step-wise change in vertical body configuration (i.e., that affects solely the displacement along the direction orthogonal to the approaching flow) is not expected to induce memory-dependent contributions. As a consequence, since the position (6.8), the indicial function  $\phi_{jh}(s)$  can be reasonably associated to a step-wise change in function  $h'(s)$  only. Under this assumption, the analysis of Eq. (6.7) in the case of a step-wise change in  $\alpha(s)$  or in  $h'(s)$ , indicates that the further choices  $D_{j\alpha0} = D_{jh1} = 1$  correspond only to a scale normalization of indicial response functions  $\phi_{jg}(s)$ , and then they do not affect the force model.

In view of these considerations, although in some cases with a high bluntness character the quasi-stationary prediction can be found inaccurate even at high values of reduced velocities, and although quasi-stationary limit conditions are not necessarily observable in experiments due to possible experimental limitations, previous theoretical consistency requirements can be considered as physically-driven and acceptable in many practical cases characterized by moderate bluntness levels.

It is worth pointing out that Eqs. (6.17) and (6.21) do not allow to obtain useful indications in the quasi-stationary limit since, for vanishing  $k$ , the flutter derivatives  $H_2^*$  and  $A_2^*$  tend to functions of the characteristic aerodynamic radius of the section [85, 86], which is a priori unknown.

Further relationships can be obtained by considering the asymptotic response for an high frequency regime. In this case, non-trivial conditions are obtained from Eqs. (6.18), (6.19), (6.22) and (6.23):

$$C_{l,\alpha} I_{l\alpha2} = - \lim_{k \rightarrow +\infty} H_3^*(k), \quad C_{l,\alpha} I_{lh2} = - \lim_{k \rightarrow +\infty} H_4^*(k), \quad (6.31)$$

$$C_{m,\alpha} I_{m\alpha2} = - \lim_{k \rightarrow +\infty} A_3^*(k), \quad C_{m,\alpha} I_{mh2} = - \lim_{k \rightarrow +\infty} A_4^*(k). \quad (6.32)$$

As it is customary, experimental results for bridge deck sections are presented by showing that flutter derivatives at very high values of  $k$ , namely for vanishing reduced velocity  $U_{\text{red}} = 2\pi/k$ , are zero. Nevertheless, due to inertial effects, this occurrence could be not generally satisfied. This is the case of the thin airfoil, as well as, for instance, of the original deck cross-section of the Lions Gate Bridge in Vancouver, that experienced a value of  $A_4^*$  significantly different from zero at  $U_{\text{red}} = 0$  [63].

On the other hand, since flutter derivatives of type 3 and 4 at  $U_{\text{red}} = 0$  and including inertial contributions are generally not available a priori, Eqs. (6.32) can not be useful for estimating parameters  $I_{jg2}$ .

### 6.3.2 Response to quasi-step motions

A quasi-step motion is herein introduced as the fast (but formally not step-wise) smooth evolution of the downwash function  $w_{jg}(s)$  from zero to the final value  $\tilde{w}_{jg}$ . Let such a quasi-abrupt change be achieved in the short dimensionless time interval  $(0, s_{g\epsilon})$ , with  $s_{g\epsilon} \ll 1$ , so that  $w'_{jg}(s) = 0$  for  $s \geq s_{g\epsilon}$ . Accordingly, in the first motion stage, i.e. for

$0 < s < s_{g\epsilon}$ , inertial contributions are dominant, whereas for  $s > s_{g\epsilon}$  circulatory ones develop and prevail. Since the smallness of  $s_{g\epsilon}$ , at the first transient stage the Wagner-like indicial functions can be approximated by their initial values, that is  $\phi_{jg}(s) \cong \phi_{jg}^0(0) = \phi_{jg}^0$  for  $s \in (0, s_{g\epsilon})$ . As a result, combining Eqs. (6.6), (6.9) with Eq. (6.30), the response to quasi-step motions can be conveniently described as

$$\frac{C_j(s) - \hat{C}_j}{C_{j,\alpha}} = \begin{cases} \phi_{j\alpha}^0 \alpha(s) + [I_{j\alpha 1} + \phi_{j\alpha}^0 D_{j\alpha 1}] \alpha'(s) + I_{j\alpha 2} \alpha''(s) & s \in (0, s_{\alpha\epsilon}) \\ \phi_{j\alpha}(s) \tilde{\alpha} & s \geq s_{\alpha\epsilon} \end{cases}, \quad (6.33)$$

in the case of the angular degree of freedom, and as

$$\frac{C_j(s) - \hat{C}_j}{C_{j,\alpha}} = \begin{cases} \phi_{jh}^0 h'(s) + I_{jh 2} h''(s) & s \in (0, s_{h\epsilon}) \\ \phi_{jh}(s) \tilde{h}' & s \geq s_{h\epsilon} \end{cases}. \quad (6.34)$$

for the vertical one.

It is worth noting that Eq. (6.33) for  $0 < s < s_{\alpha\epsilon}$ , that identifies the initial response to an angular quasi-step motion, is formally equivalent to Eq. (6.27) describing the response to harmonic motions, the only difference being the term  $\phi_{j\alpha}^0$  instead of  $\phi_{j\alpha}^0 + \mathcal{C}_{j\alpha}^*(k)$ .

The response detected for very large values of  $s$  in the case of an angular quasi-step motion allows to assess the quantities  $C_{j,\alpha}$  (with  $j = l, m$ ) as

$$C_{j,\alpha} = \frac{C_j^\infty - \hat{C}_j}{\tilde{\alpha}}, \quad (6.35)$$

where  $C_j^\infty$  denotes the time average of the function  $C_j(s)$  in the interval  $(s_\infty, s_\infty + \Delta s)$ , extracted from experimental or numerical results by choosing  $s_\infty \gg s_{\alpha\epsilon}$  and  $\Delta s$  large enough with respect to the time scales characterizing possible unsteady effects observed at large values of  $s$ .

Starting from the assessment of the aerodynamic response during the smoothed-ramp motion (i.e., for  $0 < s < s_{g\epsilon}$ ), and by using a standard least square fitting procedure, estimates for coefficients multiplying the known (once the quasi-step motion is assigned) functions  $\alpha(s)$ ,  $\alpha'(s)$ , and  $\alpha''(s)$  in Eq. (6.33) (respectively,  $h'(s)$  and  $h''(s)$  in Eq. (6.34)) can be obtained. It has to be remarked that the assessment of the quantities  $\phi_{jg}^0$ , (multiplying  $\alpha(s)$  and  $h'(s)$ ) by such a fitting procedure might be unreliable or not effective, because of during the smoothed-ramp motion it results  $|\alpha(s)| \ll |\alpha'(s)|$ ,  $|\alpha(s)| \ll |\alpha''(s)|$ , and  $|h'(s)| \ll |h''(s)|$ . Nevertheless, the measure for  $s > s_{g\epsilon}$  of the dimensionless forces  $C_j(s)$  induced by a  $g$ -type quasi-step motion allows to estimate (by Eq. (6.33) or (6.34)) the Wagner-like indicial functions  $\phi_{jg}(s)$  (with  $g = \alpha, h$ ). Thereby, since the smallness of  $s_{g\epsilon}$ , suitable values of  $\phi_{jg}^0$  can be extrapolated by continuity.

Therefore, after the fitting and the extrapolation process based on the responses to two assigned quasi-step motions (one for each degree of freedom), indicial functions  $\phi_{jg}(s)$ , their initial values  $\phi_{jg}^0$ , parameters  $I_{jg 2}$  and the quantity

$$\mathcal{O}_{j1} = I_{j\alpha 1} + \phi_{j\alpha}^0 D_{j\alpha 1}, \quad (6.36)$$

are completely estimated. Moreover, Eqs. (6.14) and (6.25) allow to deduce an estimate of the complex functions  $\mathcal{C}_{j\alpha}(k)$  and  $\mathcal{C}_{j\alpha}^*(k)$ .

It is worth pointing out that, the proposed identification procedure is not affected by limit conditions (6.30) and it has a general character. Accordingly, if consistency requirements (6.30) are not enforced a priori, then Eqs. (6.33) and (6.34) can be simply generalized, and the corresponding coefficients can be estimated by an analogous fitting and extrapolation process based on the system response to quasi-step motions.

### 6.3.3 Response to an angular harmonic motion

In order to measure parameters  $D_{j\alpha 1}$  the response to an angular harmonic motion with a fixed value  $\tilde{k}$  of the reduced frequency is considered.

Since Eqs. (6.3) to (6.5) and following the procedure described in Section 6.1.1, the values of flutter derivatives  $A_i^*$  and  $H_i^*$ , with  $i = 2, 3$ , at  $\tilde{k}$  can be measured. As a result, the values of the aerodynamic frequency-response functions  $\mathcal{H}_{j\alpha}$  at  $\tilde{k}$  are known, and a complete estimate for the complex quantity

$$\mathcal{O}_{j2}(\tilde{k}) = \frac{\mathcal{H}_{j\alpha}(\tilde{k}) + C_{j,\alpha} \left\{ \tilde{k}^2 I_{j\alpha 2} - [\phi_{j\alpha}^0 + C_{j\alpha}^*(\tilde{k})] \right\}}{i\tilde{k}C_{j,\alpha}}, \quad (6.37)$$

can be obtained. Due to Eq. (6.27) specialized to the case  $g = \alpha$ , and accounting for Eq. (6.36), the following relationship holds

$$\mathcal{O}_{j2}(k) = \mathcal{O}_{j1} + C_{j\alpha}^*(k)D_{j\alpha 1}. \quad (6.38)$$

Accordingly, two independent indications for  $D_{j\alpha 1}$  can be deduced:

$$D_{j\alpha 1}^{(\Re)} = \frac{\text{Re}[\mathcal{O}_{j2}(\tilde{k})] - \mathcal{O}_{j1}}{\mathcal{F}_{j\alpha}^*(\tilde{k})}, \quad D_{j\alpha 1}^{(\Im)} = \frac{\text{Im}[\mathcal{O}_{j2}(\tilde{k})]}{\mathcal{G}_{j\alpha}^*(\tilde{k})}. \quad (6.39)$$

In particular, the first estimate,  $D_{j\alpha 1}^{(\Re)}$ , ensures that the measured values of  $H_2^*(\tilde{k})$  (for  $j = h$ ) and  $A_2^*(\tilde{k})$  (for  $j = \alpha$ ) are respected, while the second one,  $D_{j\alpha 1}^{(\Im)}$ , ensures the respect of the measured  $H_3^*(\tilde{k})$  and  $A_3^*(\tilde{k})$  (for  $j = h, \alpha$ , respectively). In order to guarantee the approximate fulfillment of both conditions, the average between the two estimates can be used to identify  $D_{j\alpha 1}$ . Otherwise, a more refined approach could involve a weighted averaging, corresponding to a least square procedure, in order to minimize the distance between the measured and estimated (via Eqs. (6.16) to (6.23)) flutter derivatives. As a further refinement, angular harmonic motions at different frequencies could be considered, extracting a suitable estimate for  $D_{j\alpha 1}$  by a least square procedure on data associated with different values of  $k$ . It is worth remarking that, in such a procedure, values of the reduced frequency  $k$  have to be neither too small nor too large in order to emphasize the role played by circulatory effects.

In the following, for the sake of simplicity, the proposed identification procedure will be applied considering only one value of  $k$  and adopting the average value between those computed by Eqs. (6.39) as an estimate for  $D_{j\alpha 1}$ .

## 6.4 A numerical approach

The identification procedure previously described has been implemented through a numerical approach based on the simulation of the fluid dynamics characterizing the two-dimensional flow problem under investigation. In the context of the presented theoretical framework and for the sake of compactness, reference will be made only to sectional angular motions and considering sectional geometries characterized by  $B = 1$  m,  $a = 0$ , and immersed in an air flow with  $\rho = 1.225$  kg/m<sup>3</sup>. Numerical analyses have been carried out on the model of a flat thin plate (denoted in the foregoing as FTP), and on the model of a closed box section (denoted as CBS, Fig. 3.10 and 6.1) similar to the bare deck cross-section of the Great Belt East Bridge [47, 87].

### 6.4.1 The numerical model

The aerodynamic response to quasi-step and harmonic motions has been simulated by employing the commercial software Ansys Fluent (release 14) [51]. It allows the analysis of a rigid solid domain moving within the fluid domain by means of a grid-based ALE formulation, based on a finite-volume approach. Well-established and high-performance algorithms of smoothing and remeshing are available in the adopted numerical tool, enabling to efficiently manage the mesh morphing during the computation.

For the FTP case and with the aim to reproduce the theoretical results obtained by Wagner and Theodorsen, an inviscid and incompressible two-dimensional fluid model has been adopted. In the CBS case the fluid has been modelled as viscous and incompressible, by employing as turbulence model the two-equation eddy-viscosity shear-stress-transport model  $k - \omega$  *sst* [51, 18], combined with an enhanced wall treatment, that is with a near-wall modeling method that integrates a two-layer model with enhanced wall functions [51]. The approaching flow has been assumed to be characterized by  $U = 1$  m/s for the FTP case, and by a Reynolds number  $Re = UB/\nu$  equal to  $1.1E5$  for the CBS, the air kinematic viscosity  $\nu$  being assumed equal to  $1.54E-5$  m<sup>2</sup>/sec.

In order to accurately simulate the dynamics of an external flow acting on the flat plate without unphysical boundary effects, the computational domain is assumed to be  $30B$  long in the mean flow direction and  $15B$  long in the cross-flow direction (Fig. 6.2). Moreover, the section chord midpoint is assumed to be fixed, vertically centered, and distant  $8B$  from the inlet boundary. In the FTP case the solid domain has been modelled by a zero-thick geometry, by considering two adjacent topological solid walls at a zero distance. At the inlet boundary a velocity-based Dirichlet condition is prescribed; at the outlet boundary a zero relative pressure is assigned, enforcing a continuative outflow regime; at the solid walls the impenetrability condition is assumed (prescribing also the free-slip requirement for the FTP model); finally, symmetry conditions are assigned on the other boundaries.

As a result of a convergence analysis, the domain partition consists in about 160 000 cells and 135 000 nodes for the FTP model, and in about 130 000 cells and 110 000 nodes for the CBS model. Furthermore, in order to minimize the computational effort associated with the mesh morphing, four different computational subregions have been defined, in agreement with [67, 47]. With reference to Fig. 6.2, during the time-marching computation the mesh in the deforming zone only undergoes to smoothing and remeshing

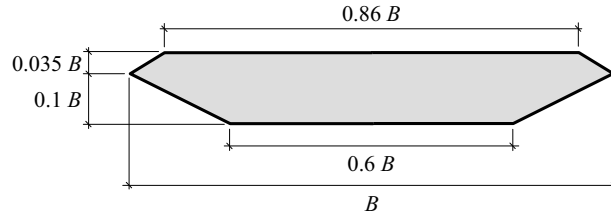


Figure 6.1: Geometry of the closed box section (CBS) analysed in the present study.

treatments, whereas the cells in the far-field zone are kept fixed, and those in both coarsening and fine zones follow rigidly the prescribed motion of the section. In the fine zone, closed to the solid domain, a structured mesh based on quadrilateral cells has been adopted (Fig. 7.1), with a mesh size equal to  $3.0E-4 B$  for the FTP model, and equal to  $1.0E-3 B$  for the CBS case. These choices should ensure low levels of numerical viscosity and a suitable resolution to represent unsteady effects at the solid boundaries. In fact, in the case of the CBS model, the non-dimensional wall distance  $y^+$  has been computed to be always lower than 5.0, confirming the good resolution of the boundary layer. In the coarsening zone, the discretization has been performed by recurring to an unstructured topology based on triangular cells, whose size is increased up to the mesh size in the deforming zone. There, the triangular unstructured mesh has been obtained by considering a size as constant as possible, so that smoothing and remeshing algorithms can be used without compromising the mesh quality (Fig. 7.1). Finally, the far-field region has been discretized by a quadrilateral structured grid, with the element size progressively increased up to the outer fluid domain boundaries.

The discretized problem has been numerically solved by adopting a PISO (Pressure Implicit solution by Split Operator method, [47]) pressure-velocity coupling algorithm. Green-Gauss node-based approximation for spatial gradients has been employed, coupled with a second order scheme for pressure, and with a second order upwind scheme for velocities and turbulence related quantities (in the CBS analyses), in order to ensure numerical accuracy and stability [46, 48]. The time discretization has been performed by a first order implicit scheme. As a result of an optimization analysis aiming to guarantee a good approximation of transient regimes, especially in the case of a quasi-step motion, the dimensionless time-step has been set equal to  $2.0E-4$  for the FTP case, and equal to  $5.0E-4$  for the CBS, ensuring that the Courant number was well below 1.0, except for very few cells wherein it was at most equal to 5.0.

#### 6.4.2 Aerodynamic data evaluation procedure

The time traces of the aerodynamic forces acting on the solid domain are obtained by numerically integrating for each computational time-step the pressure distribution (and the wall shear stresses also, in the case of the CBS model) computed at the solid boundary.

In the framework of the identification procedure previously discussed, the aerodynamic frequency-response functions  $\mathcal{H}_{j\alpha}(k)$  are computed by using the forced vibration method. In detail, angular harmonic motions of amplitude  $\alpha_0 = 1$  degree for FTP and

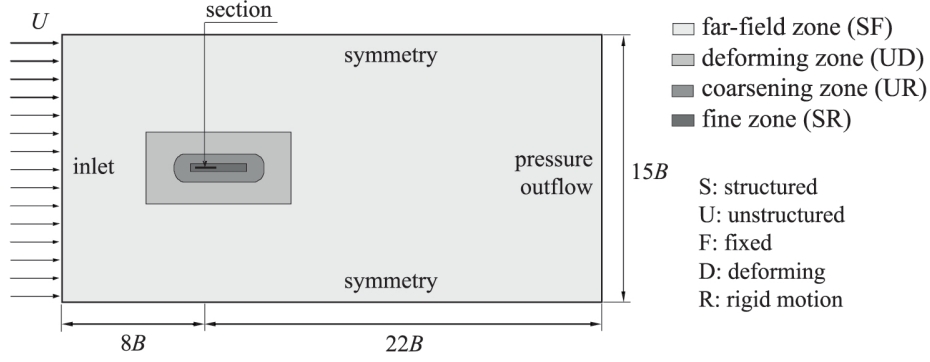


Figure 6.2: Outline of the computational domain.

$\alpha_0 = 3$  degrees for CBS have been imposed to the solid domain and the time traces of the dimensionless lift and pitching moment have been recorded. In agreement with [47], the computed data have been fitted by using a sinusoidal function and the flutter derivatives have been extracted according to Eqs. (6.5).

As regards the indicial response, a crucial aspect of the whole procedure is the choice of the smoothed-ramp function  $\alpha(s)$  that describes the quasi-step motion. It has to be a regular growing function, that allows to ensure a rapid, but smooth, transition from zero to the final value  $\tilde{\alpha}$ . Moreover, it has to be zero for  $s < 0$  and its shape should be adjustable, in order to modulate the speed of the transition, by operating on few parameters. As a good compromise between these requirements, a log-normal function has been herein selected, ensuring the highest class of continuity (Fig. 6.4)

$$\alpha(s) = \frac{\tilde{\alpha}}{2} \left\{ 1 + \operatorname{erf} \left[ \ln \left( \frac{s}{R} \right) \right] \right\} \Rightarrow \alpha'(s) = \frac{\tilde{\alpha}}{s\sqrt{\pi}} e^{-\ln^2(s/R)}, \quad (6.40)$$

where  $\operatorname{erf}[\cdot]$  denotes the error function and  $R$  is a parameter used to arrange the function shape. The peak value of the function  $\alpha'(s)$  is achieved for  $s_{\alpha'_{\max}} = R/\sqrt{e}$  and it is equal to  $\alpha'_{\max} = \tilde{\alpha} e^{1/4}/(R\sqrt{\pi})$ . Moreover, the value  $\alpha_P = P\tilde{\alpha}$  (with  $P < 1$ ) of the function  $\alpha(s)$  is achieved at the dimensionless time  $s_P = R e^{\operatorname{erf}^{-1}[2P-1]^2}$ . Numerical results proposed in what follows have been obtained by assuming  $\tilde{\alpha} = 1$  degree for FTP-based analyses and  $\tilde{\alpha} = 6$  degrees in the CBS case. Moreover, in order to guarantee a fast smoothed-ramp motion and a suitable numerical stability,  $R$  is set equal to 0.02 and  $s_{\alpha\epsilon}$  is associated to  $P = 0.99$ . Thereby, it results  $s_{\alpha\epsilon} = s_P|_{P=0.99} \simeq 0.1$ , which is a reasonably small dimensionless time value if compared with the time scale characterizing the evolution of the Wagner indicial function.

Once the indicial response has been measured by using the procedure introduced in Section 6.3.2, the effective assessment of the model parameters needs the circulatory functions  $C_{j\alpha}(k)$  to be numerically estimated. To this aim, assuming that at the large dimensionless time  $s_{\text{end}} \gg s_{\alpha\epsilon}$  the indicial functions can be approximated by their asymptotic values (i.e., the unit), Eq. (6.14) can be conveniently arranged in the form:

$$C_{j\alpha}(k) = ik \int_0^{s_{\text{end}}} \phi_{j\alpha}(\sigma) e^{-ik\sigma} d\sigma + e^{-iks_{\text{end}}}, \quad (6.41)$$

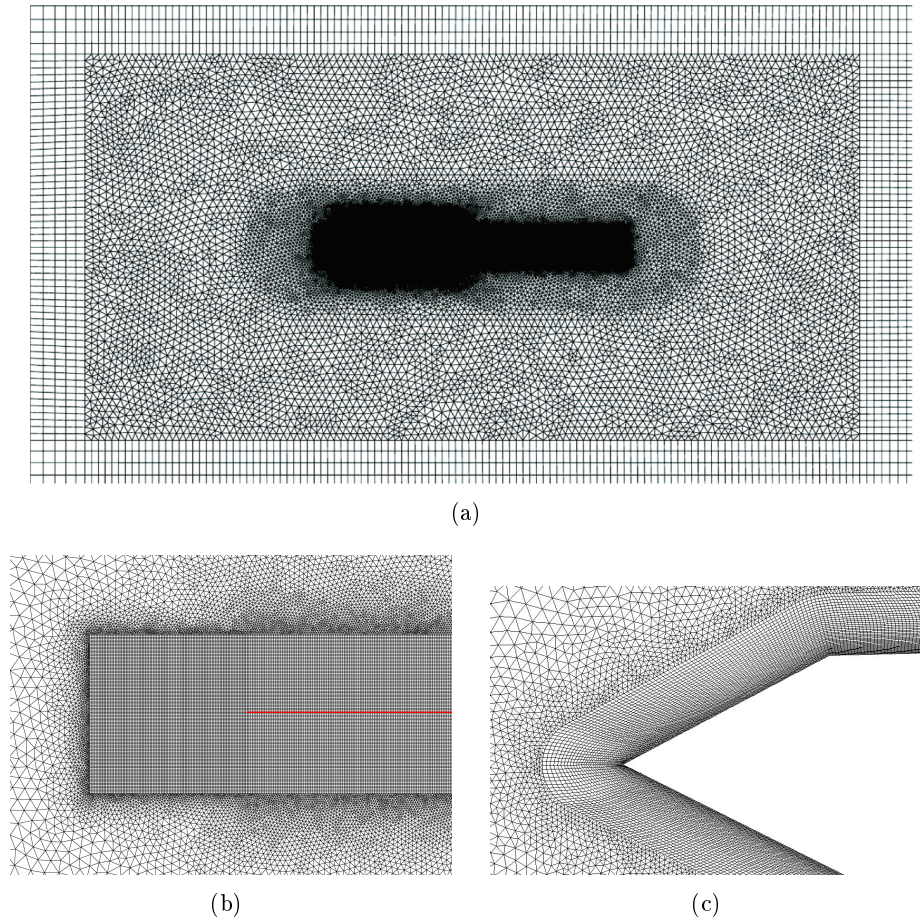


Figure 6.3: Computational mesh employed for numerical analyses. (a) Overview of deforming, coarsening and fine zones. Details of the topological transition between coarsening and fine zones for (b) the flat thin plate model (FTP) and for (c) the model of the closed box section (CBS).

where the integral contribution can be numerically evaluated through a standard Fast Fourier Transform algorithm.

### 6.4.3 Response to vertical motions

The numerical approach previously described can be applied also to the case of vertical body motions. In detail, forced small-amplitude harmonic oscillations can be numerically treated by directly simulating the motions of the solid domain within the flow. Therefore, no special indication is necessary with respect to the case of harmonic angular motions. On the other hand, a different implementation strategy could be considered for simulating the indicial response associated with a step change in the vertical motion rate. From a computational point of view, this can be more conveniently achieved by using the field velocity approach [69, 70, 71]. It allows to simulate step changes in body configuration by means of an apparent grid movement, described by suitable flow boundary

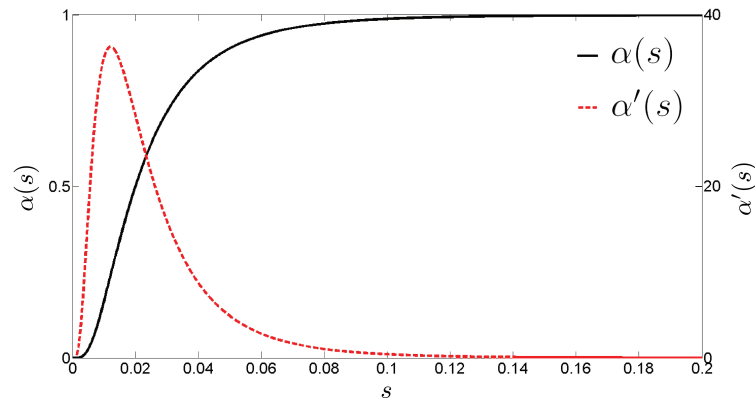


Figure 6.4: Log-normal smoothed-ramp function adopted for simulating the aerodynamic response to an angular quasi-step motion ( $\tilde{\alpha} = 1$  degree,  $R = 0.02$ ,  $P = 0.99$ ,  $s_{\alpha\epsilon} = 0.1$ ).

conditions. Accordingly, the effects induced by step-wise body motions are described by superposing a velocity field equivalent to the impulsive change over the free-stream conditions. This superposed velocity field is modeled by the suitable modification of the grid time metrics, without any distortion or movement of the computational mesh, ensuring accuracy and computational efficiency [69].

## 6.5 Numerical results: the FTP case

In what follows, data obtained by numerical simulations in the case of the flat thin plate (FTP) model are presented and compared with the available theoretical results.

### 6.5.1 Harmonic motions

In order to validate the numerical approach previously described, the aerodynamic response of a flat thin plate harmonically moving under an approaching flow has been simulated for different values of the reduced frequency  $k$ . Accordingly, starting from the recorded time traces of lift and moment coefficients, the flutter derivatives  $H_i^*$  and  $A_i^*$  with  $i = 2, 3$  have been extracted. Figure 6.5 depicts the time-traces  $C_l(s)$  and  $C_m(s)$ , simulated by considering a sinusoidal forced angular motion at the reduced velocity  $U_{\text{red}} = 6$ . As it is expected, these output signals are harmonic in time, and isofrequency but shifted with respect to the input motion signal. The flutter derivatives numerically computed are showed in Fig. 6.6, and are compared with the theoretical ones, consistently deduced from the Theodorsen theory [6]. The comparison highlights an excellent agreement.

### 6.5.2 Quasi-step motion

The analysis of the time-dependent pressure field computed by the simulation of an angular quasi-step motion highlights that upstream vortex regions arise during the early transient stage. Afterwards, these starting vortexes are transported downstream by the



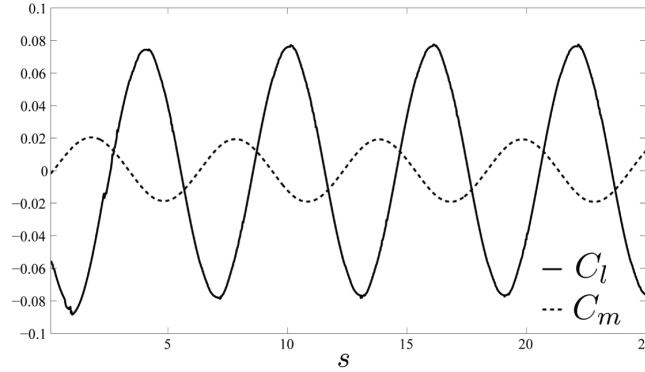


Figure 6.5: Time traces of the dimensionless aerodynamic coefficients  $C_l$  and  $C_m$  in the case of the flat thin plate model, numerically computed for an angular sinusoidal forced motion at  $U_{\text{red}} = 6$ .

approaching flow, leading to a state that tends to be steady. This occurrence is clearly showed in Fig. 6.7, where the patterns of the pressure coefficient around the airfoil are reported for different values of the dimensionless time  $s$ .

Figure 6.8 shows the time traces of lift and moment coefficients during the quasi-step motion, revealing that the unsteady character induced by the fast transient motion practically disappears within the time interval  $(0, s_{\alpha\epsilon})$  when pressure integral measures on the section are considered. The aerodynamic response recorded for  $s \geq s_{\alpha\epsilon} = 0.1$  has been used to extract the indicial functions  $\phi_{l\alpha}(s)$  and  $\phi_{m\alpha}(s)$ . The corresponding measured values for  $s \geq s_{\alpha\epsilon}$  are compared in Fig. 6.9 to the Wagner function, revealing an excellent agreement between theoretical and numerical results. It is worth noting that the peak observed between  $s = 1$  and  $s = 2$  is induced by the shedding of the starting vortex originated during the quasi-step motion at the plate front tip. This peak has been filtered before using the indicial functions in later calculations, even though this is not expected to lead to considerable discrepancies with respect to the theoretical results.

### 6.5.3 Application of the identification procedure

The identification procedure introduced in Section 6.3 has been numerically applied to the FTP model. Since the streamlined features of the sectional geometry, the quasi-stationary asymptotic relationships (6.30) are enforced and reference is made to the numerically observed response under an harmonic angular forced oscillation at  $U_{\text{red}} = 9$ , corresponding to  $\tilde{k} \simeq 0.7$ . Estimates of the model parameters extracted by the proposed procedure are summarized in Table 6.1, where they are compared with the available theoretical data.

Some differences between theoretical and numerical values can be observed. Nevertheless, as the following results highlight, these estimates lead to a good representation of the overall motion-induced aerodynamic response, suggesting a compensative effect when their combined influence is taken into account. In fact, it can be noticed that the largest differences with respect to the theoretical values have been computed for

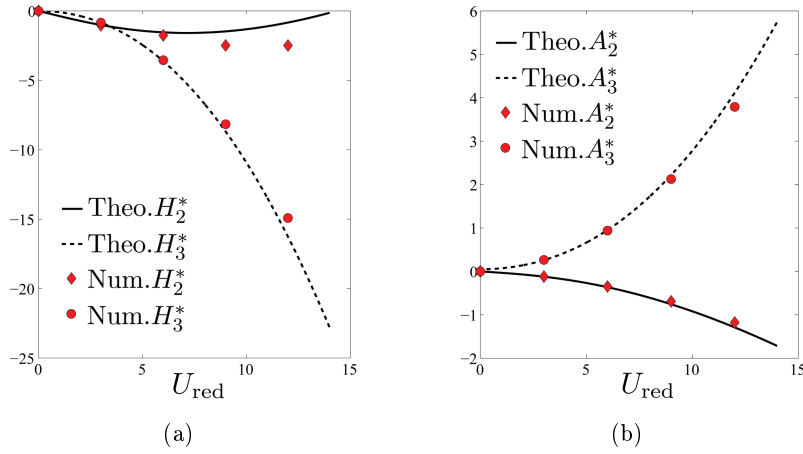


Figure 6.6: Comparison between theoretical and numerically-extracted (via the forced-vibration method) flutter derivatives as functions of the reduced velocity  $U_{\text{red}} = 2\pi/k$ , in the case of the flat thin plate model. (a)  $H_2^*$  and  $H_3^*$ . (b)  $A_2^*$  and  $A_3^*$ .

Table 6.1: Values of the dimensionless model parameters computed via the proposed identification procedure in the case of the flat thin plate model and comparison with the corresponding theoretical results.

	$C_{l,\alpha}$	$\phi_{l\alpha}^0$	$I_{l\alpha 1}$	$I_{l\alpha 2}$	$D_{l\alpha 1}$	$C_{m,\alpha}$	$\phi_{m\alpha}^0$	$I_{m\alpha 1}$	$I_{m\alpha 2}$	$D_{m\alpha 1}$
Num.	-6.18	0.60	0.22	0.00	0.25	1.53	0.61	-0.21	-0.03	0.33
Theo.	-6.28	0.50	0.25	0.00	0.25	1.57	0.50	-0.25	-0.03	0.25

parameters  $I_{m\alpha 1}$  (about 20 %) and  $D_{m\alpha 1}$  (about 30 %), that mainly affect the torsional aerodynamic damping in terms of inertial ( $I_{m\alpha 1}$ ) and pseudo-circulatory ( $D_{m\alpha 1}$ ) effects. Nevertheless, in usual ranges of the reduced velocity these effects are almost comparable and, although they are not simply separable, the corresponding deviations from the expected theoretical values are opposite in sign. As a consequence, by combining the previous parameter assessment (based on the frequency value  $\tilde{k}$  only) with the Theodorsen-like circulatory functions numerically identified by the computed indicial functions (see Eq. (6.41)), the flutter derivatives can be accurately reconstructed by means of Eqs. (6.16)-(6.23), as functions of  $k = 2\pi/U_{\text{red}}$ . Figure 6.10 shows the excellent agreement between this indirect assessment of the flutter derivatives and the theoretical results. In this figure, the values of the flutter derivatives directly computed at  $\tilde{k}$  by using the forced-vibration method are also shown. It is worth pointing out that, in order to obtain more accurate and effective results, the fundamental averaging process proposed in Section 6.3.3 between different estimates of  $D_{j\alpha 1}$  and based on real and imaginary parts of  $\mathcal{H}_{j\alpha}(k)$  and  $\mathcal{C}_{j\alpha}^*(k)$  (see Eq. (6.39)), may be enhanced by computing the system response for different values of the reduced frequency.

Finally, Fig. 6.11 shows the circulatory functions  $\mathcal{C}_{j\alpha}(k)$  (namely, their real and imaginary parts), numerically deduced from the extracted indicial functions  $\phi_{j\alpha}(s)$ , and Fig. 6.12 depicts the aerodynamic frequency-response functions  $\mathcal{H}_{j\alpha}(k)$  computed by Eq.

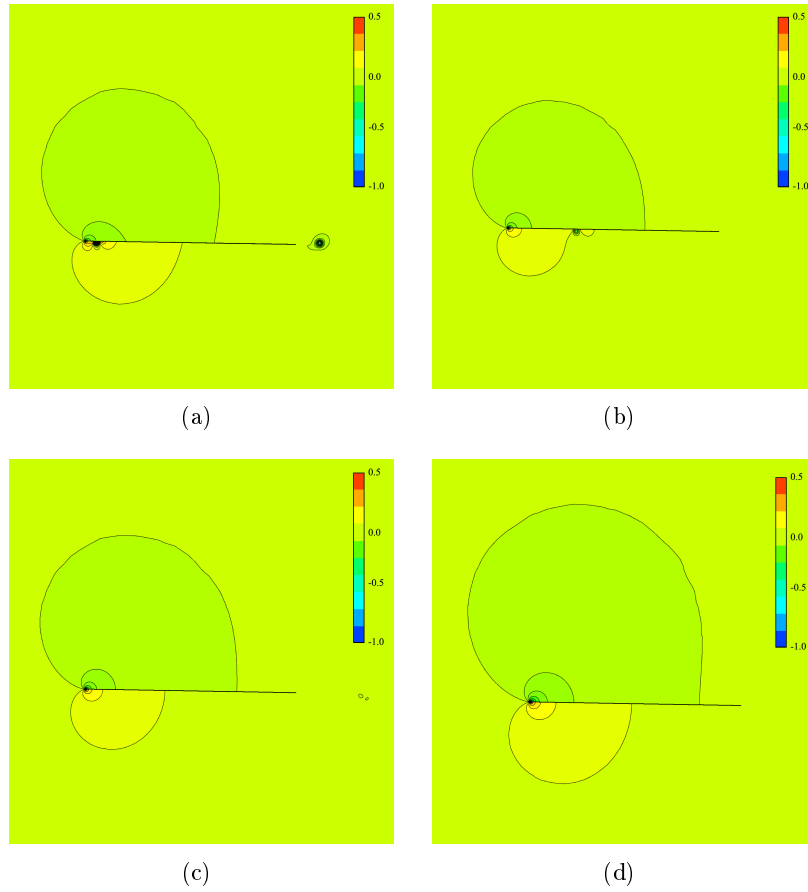


Figure 6.7: Pressure coefficient distribution around the flat thin plate for different values of the dimensionless time and in the case of a quasi-step angular motion. (a)  $s = 0.1$ , (b)  $s = 0.5$ , (c)  $s = 2$ , (d)  $s = 10$ .

(6.13). Comparisons with the Theodorsen circulatory function  $\mathcal{C}(k)$  and with available theoretical results are presented, highlighting soundness and accuracy of the proposed approach.

Proposed results indicate that the present technique allows an accurate estimate of the flutter derivatives in a wide range of  $U_{\text{red}}$ , by means of a reduced number of real and/or in-silico experiments, in comparison with the application of a classical procedure based on the forced vibration method. From a computational point of view and referring specifically to the FTP results herein discussed, the computational cost associated to the proposed identification strategy was 1:3 with respect to that necessary for extracting angular-motion-based flutter derivatives at four different values of the reduced velocity.

## 6.6 Numerical results: the CBS case

In order to highlight soundness and effectiveness of the proposed identification procedure in the case of a sectional geometry typical for decks of long-span bridges, the closed box

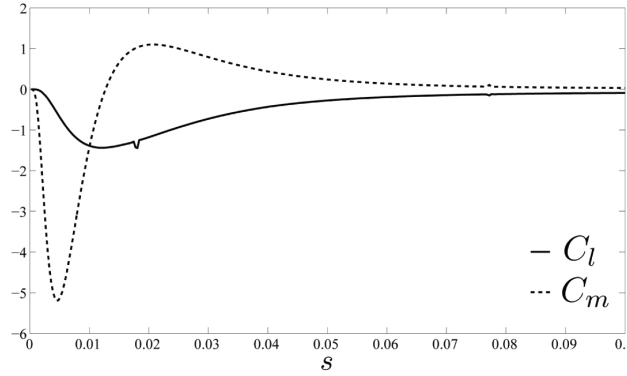


Figure 6.8: Time traces of dimensionless coefficients  $C_l$  and  $C_m$  during the smoothed-ramp angular motion ( $s_{\alpha\epsilon} = 0.1$ ) in the case of the flat thin plate model.

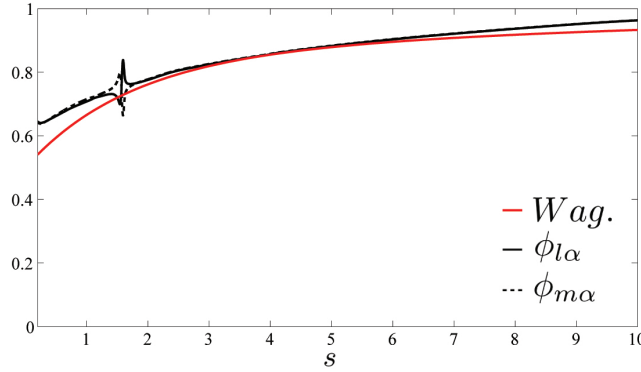


Figure 6.9: Comparison, within the dimensionless time interval  $s = s_{\alpha\epsilon} = 0.1$  to  $s = 10$ , between the theoretical Wagner function (red line) and the indicial functions  $\phi_{l\alpha}$  and  $\phi_{m\alpha}$  (continuous and dashed black lines) computed by numerical simulations in the case of the flat thin plate model. Simulation results have not been numerically filtered.

section (CBS) introduced in Fig. 6.1 has been analysed. Identification results, in terms of flutter derivatives and obtained by simulating the system aerodynamic response to one quasi-step motion and to one harmonic motion only, are compared in the following with corresponding consistent results computed by adopting a classical forced-vibration-method approach.

Since the bluff character of the section, vortex shedding effects appear. This occurrence is clearly highlighted by analysing Fig. 6.13, wherein the time traces of the dimensionless aerodynamic coefficients  $C_l$  and  $C_m$  are depicted, numerically computed by considering the section as fixed under a zero angle of incidence (i.e.,  $\hat{\alpha} = 0$ ). In particular, a quasi-periodic behaviour appears, characterized by root-mean-square-based mean values (respectively, amplitudes) for  $C_l$  and  $C_m$  equal to 0.7 and 0.035 (resp., 0.15 and 0.025), and by a Strouhal number (based on the cross-flow section dimension) of about 0.25. As a consequence, when a quasi-step motion is considered, these shedding effects

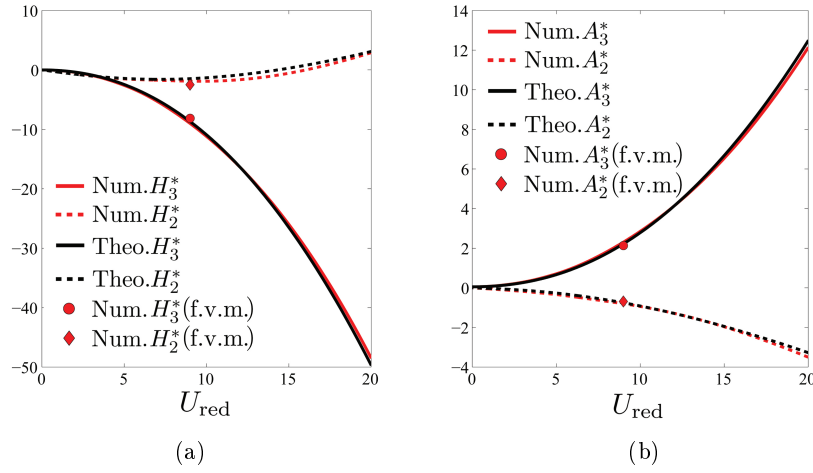


Figure 6.10: Flutter derivatives indirectly reconstructed by using parameter estimates and numerically-extracted indicial functions. Comparison between theoretical and numerical results in the case of the flat thin plate model. (a)  $H_2^*$  and  $H_3^*$ . (b)  $A_2^*$  and  $A_3^*$ . The values of the flutter derivatives (at  $U_{red} = 9$ ) used to assess model parameters and evaluated by the forced vibration method are also indicated (denoted as f.v.m.).

superimpose, and generally couple, with the corresponding aerodynamic response, preventing the direct estimation of the Wagner-like indicial functions. These effects are in agreement with the experimental results obtained by [56], wherein such a difficulty of a standard indicial function approach in replicating the time-dependent (lift) force for bridge-like sections was highlighted. Therefore, in the limit of a linear approach, vortex shedding contributions should be suitably filtered. Referring to angular motions, a possible strategy for attempting to distinguish vortex-shedding effects from the indicial ones is based on the use of values of  $\tilde{\alpha}$  large enough to induce mean values of the aerodynamic coefficients greater than their oscillation amplitudes [56]. Nevertheless, values of  $\tilde{\alpha}$  too large can lead to estimates of the indicial functions that are not suitable for deducing good descriptions of the flutter derivatives, because of possible high coupling non-linearities. By employing the assumption (consistent within a linear framework) that a small change in  $\tilde{\alpha}$  does not affect indicial functions  $\phi_{j\alpha}(s)$ , numerical analyses carried out on the CBS model have shown that the choice  $\hat{\alpha} = -3$  degrees and  $\tilde{\alpha} = 6$  degrees can be retained a good compromise among the previous counteracting requirements. In particular, numerical results obtained on the CBS model revealed that this choice contributes to compensate, in a neighborhood of the zero incidence condition, the small aerodynamic asymmetries induced by incidence configurations opposite in sign, as well as that the choice  $\hat{\alpha} = -3$  degrees tends to mitigate vortex shedding contributions, in agreement also with the numerical evidence proposed in [24]. Similarly, although the shedding frequency is well decoupled from the frequency range employed for extracting flutter derivatives, harmonic motion amplitudes should be such as to ensure that motion-induced and wake effects are distinguishable. Accordingly, numerical results associated to harmonic motions have been obtained considering  $\alpha_0 = 3$  degrees.

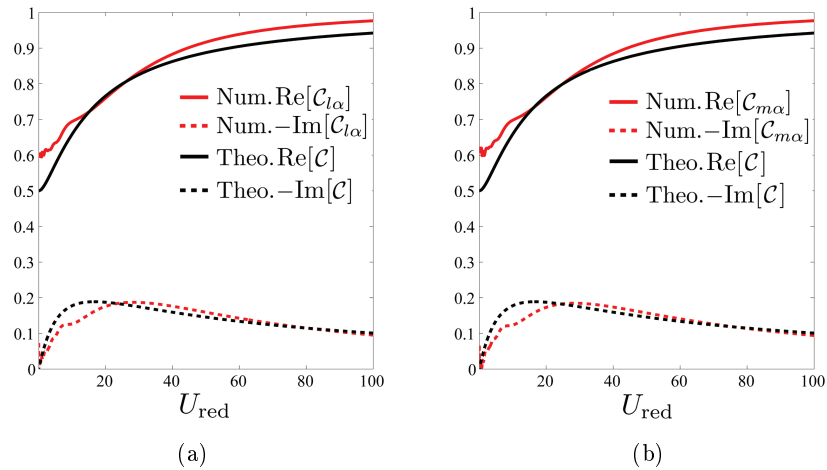


Figure 6.11: Complex circulatory functions (a)  $C_{l\alpha}(k)$  and (b)  $C_{m\alpha}(k)$  numerically extracted in the case of the flat thin plate model. Comparison with the Theodorsen circulatory function  $C(k)$ .

Results computed under these conditions in terms of angular-based indicial response are shown in Fig. 6.14, wherein the comparison with the Wagner function is also proposed. In particular, the similarity with the Wagner response and the absence of peaks over unity confirm the good aerodynamic performance of this sectional geometry.

The proposed identification procedure has been applied by enforcing asymptotic relationships Eqs. (6.30) and by simulating the aerodynamic response under an harmonic angular forced oscillation at  $U_{\text{red}} = 6$  (corresponding to  $\tilde{k} \simeq 1$ ). It is worth remarking that the oscillations experienced in functions  $\phi_{j\alpha}(s)$  have a spectral content well separated from the frequency range usually considered for describing flutter derivatives. Therefore, for simplicity, the identification procedure has been carried out without filtering data computed as response to the quasi-step motion. Estimates of the model parameters extracted by the proposed procedure are summarized in Table 6.2. As regards parameters  $D_{j\alpha 1}$ , they have been estimated via Eqs. (6.39) as a result of an iterative approach that minimizes the differences (in the least square sense) between flutter derivatives computed via the forced-vibration method and those extracted via the proposed identification procedure. It turns out that the estimated value of  $D_{m\alpha 1}$  is significantly lower than  $D_{l\alpha 1}$ , confirming the different aerodynamic behavior with respect to the thin airfoil. This evidence indicates also that, although a certain bluff character of the section, contributions associated to  $\alpha'(s)$  can not be generally considered as fully negligible. Moreover, the analysis of  $I$ -type coefficients in Tab. 2 confirms that, although the section is bluff, inertial (namely pseudo-non-circulatory) effects can be not fully negligible, remaining in some contributions of the same order as in the case of the thin airfoil (e.g.,  $I_{m\alpha 1}$ ).

By combining the previous parameter assessment with the numerical estimate of the indicial functions at  $\tilde{k}$ , flutter derivatives have been reconstructed by using Eqs. (6.16)-(6.23). Figure 15 shows the corresponding results, highlighting the good agree-

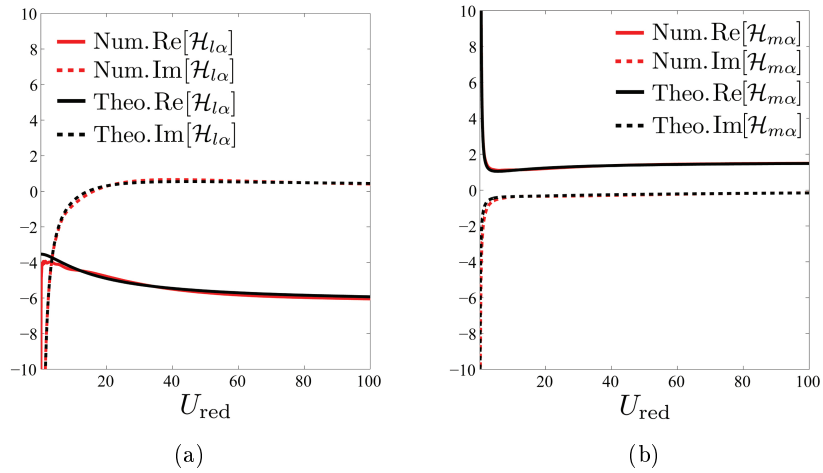


Figure 6.12: Complex aerodynamic frequency-response functions (a)  $\mathcal{H}_{l\alpha}(k)$  and (b)  $\mathcal{H}_{m\alpha}(k)$  numerically computed in the case of the flat thin plate model. Comparison with the Theodorsen-based theoretical results.

	$C_{l,\alpha}$	$\phi_{l\alpha}^0$	$I_{l\alpha 1}$	$I_{l\alpha 2}$	$D_{l\alpha 1}$	$C_{m,\alpha}$	$\phi_{m\alpha}^0$	$I_{m\alpha 1}$	$I_{m\alpha 2}$	$D_{m\alpha 1}$
CBS	-5.39	0.65	0.06	0.00	0.26	1.36	0.65	-0.11	-0.03	0.05

Table 6.2: Values of the dimensionless model parameters computed via the proposed identification procedure for the CBS model.

ment between the flutter derivatives computed by present identification procedure and those numerically estimated via the forced vibration method. The main differences in values are experienced only for  $H_2^*$  at  $U_{\text{red}} > 11$ , but the different trend with respect to the thin airfoil is well described.

As far as it concerns the limitations of the proposed approach, it must be noticed that the step motion might induce shear layers instabilities (those are clearly visible in RANS simulations). If the strength of the vortices originated by such mechanism is preponderant, the indicial function might be compromised because the response to the finite amplitude downwash variation is not representative of the impulse response function convoluted in the Duhamel integral. Such mechanisms are probably at the origin of the difficulties encountered in [65] where an extremely bluff body was considered. An example of shear layer roll-up due to impulsive motion for the Tacoma bridge deck observed in numerical simulations is reported in Fig. 6.16. Indeed, this limits the applicability of the proposed method to mildly bluff bodies with small detachments.

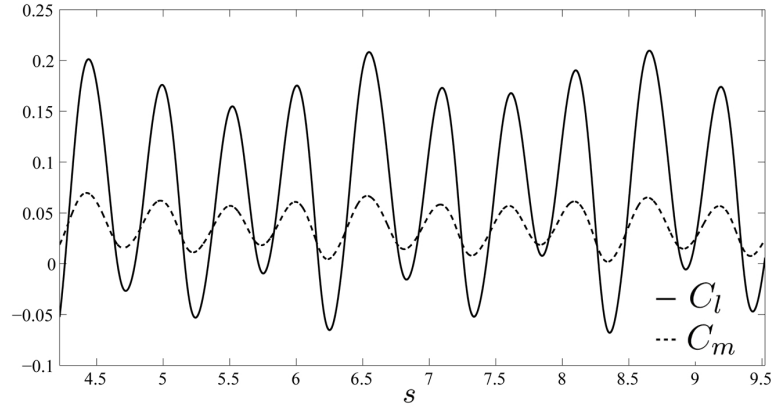


Figure 6.13: Time traces of dimensionless coefficients  $C_l$  and  $C_m$ , numerically computed for the closed box section in Fig. 6.1, by considering the section as fixed under a zero angle of incidence (i.e.,  $\hat{\alpha} = 0$ ).

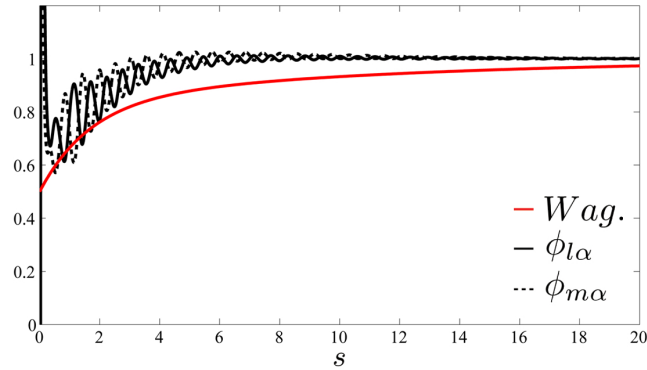


Figure 6.14: Comparison between the theoretical Wagner function (red line) and the indicial functions  $\phi_{l\alpha}(s)$  and  $\phi_{m\alpha}(s)$  computed by numerical simulations for CBS.



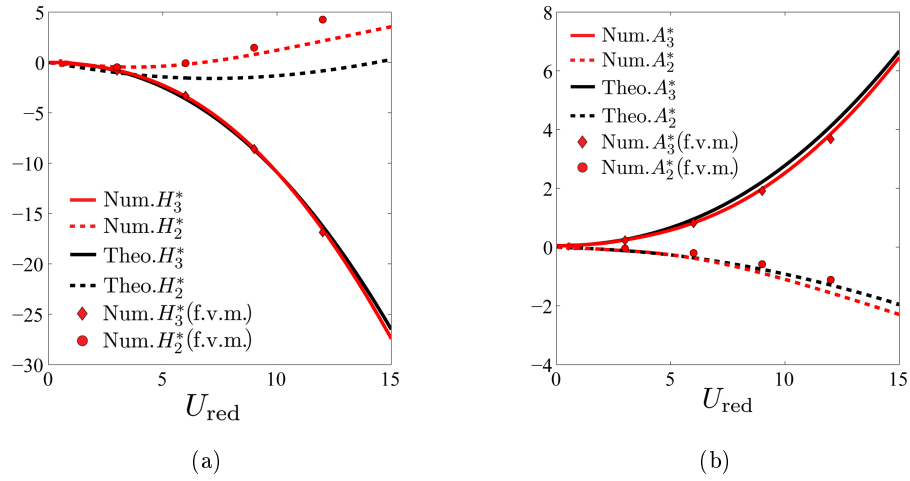


Figure 6.15: Flutter derivatives indirectly reconstructed by using model parameter estimates and numerically-extracted indicial functions. Comparison with numerical results obtained via the forced-vibration method and Theodorsen flutter derivatives for CBS.

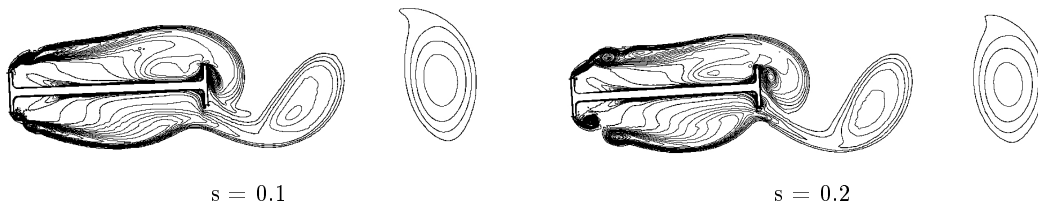


Figure 6.16: Shear layer roll-up due to impulsive motion for Tacoma bridge ( $Re = 1.5E5$ ). Simulation settings are given in Chapter 8.

## Chapter 7

# Flutter derivatives extraction: rectangular prisms

Although in many occasions the computational techniques have been found to be reliable enough for the aerodynamic characterization of a wide range of geometries, ranging from streamlined to bluff sections, it is often problematic to define the level of confidence that can be put in such simulations. This is caused by the fact that numerous mechanisms are involved in the definition of the aerodynamic properties and their relative importance strongly depends on the geometry of the body. The ability of available simulation technologies in reproducing such mechanisms is indeed not uniform so that their prediction can range from a mere qualitative level to an accurate quantitative one.

In this chapter, the forced vibration experimental tests performed by Matsumoto on a wide selection of rectangular prisms, have been simulated using both the standard  $k-\omega$  and the  $k-\omega$  *sst* turbulence models in order to highlight their limit of applicability and settle guidelines useful to engineers approaching the flutter derivatives estimation using CFD. The results are presented together with a wide collection of experimental and numerical data obtained by other authors emphasizing the limitations of the tested two-equations RANS models.

### Contents

---

<b>7.1</b>	<b>Introduction</b>	<b>124</b>
<b>7.2</b>	<b>Some comments on aeroelastic forces</b>	<b>125</b>
<b>7.3</b>	<b>Simulation approach</b>	<b>126</b>
7.3.1	Numerical setup	127
<b>7.4</b>	<b>Preliminary numerical analysis</b>	<b>128</b>
7.4.1	Comparison of turbulence models on <i>R4</i>	128
7.4.2	Calibration of the standard $k-\omega$ on <i>R4</i>	129
<b>7.5</b>	<b>Numerical results</b>	<b>131</b>
7.5.1	<i>R2</i>	131
7.5.2	<i>R3</i>	133
7.5.3	<i>R4</i>	140

---

7.5.4	<i>R5, R8 and R10</i>	144
7.5.5	<i>R12p5, R15 and R20</i>	150
7.5.6	Critical flutter wind speed evaluation	150
7.6	Conclusions on rectangular prisms	151

---

## 7.1 Introduction

Despite the progresses in turbulence modelling and the increase in computers power, wind tunnel tests still represent a fundamental step in the evaluation of bridge deck stability with respect to wind loading. In the technical practice, the major concern is surely represented by the insurgence of the flutter instability which, in case of unfavourable aerodynamic properties of the deck, can lead to unbounded growing oscillations even at relatively mild wind speed.

Due to their cost and the relevant time needed in their setup, wind tunnel tests are often performed in the late part of the design process and are often used only as a verification of the technical choices that have been already adopted. Numerical quantification of the aerodynamic performance of bridge decks in the early stages of the project development would allow early comparison of multiple options and the optimization of the design choices, so discarding *a priori* unfavorable solutions.

Evaluations of the flutter derivatives of bridge deck sections using numerical approaches can be found in [79, 47, 88, 49, 48] often showing reasonable agreement with experimental results. Nevertheless, in such cases the numerical model is tested only on a few geometries and the role of *a posteriori* model calibration on the basis of available experimental results is difficult to be evaluated. Furthermore, some extensively tested bridge decks are characterized by well profiled sections and exhibit aeroelastic coefficients extremely similar to the thin airfoil ones. In such cases the ability of the model to capture the dynamic behaviour of separation bubbles and other mechanisms involved in the definition of the aeroelastic response is not tested.

The case of rectangular cylinders, with varying aspect ratio, is of technical interest because it is representative of flows characterized by strong detachments at the leading edges, formation of shear layers and eventual reattachments (a detailed review of the mechanisms involved in the definitions of the flow around such shapes can be found in [89] and free vibration LES simulations on a few aspect ratios in [90]). The presence of such flow features is known to lead to unfavourable aerodynamic behaviour and it is often encountered in bridge decks with modest aerodynamic performance. For this reasons a deep numerical investigation of such flows is a matter of technical interest.

In the following, the forced vibration experimental tests performed by Matsumoto on rectangular prisms of varying aspect ratio and published in [75] are numerically reproduced. The performances of the standard  $k - \omega$  [18] and  $k - \omega_{sst}$  [23] turbulence models are compared.

Although the limitations of two-equations RANS turbulence models in the evaluation of strongly separated flows have been already presented in Chapter 4 as the benefits of LES models (see also [31, 91]), the chapter is focused on RANS models as the simulation time needed for the LES approach is still considerably too high for extensive use

in practical cases (typically some orders of magnitude larger than the time required for RANS models [92]). This is particularly true for motion induced wind loading which, in the case of very flexible structures is a slow phenomenon from the aerodynamic point of view. Moreover, it should be also considered that, in order to take full advantage from the LES formulation, the simulations should be three-dimensional so greatly increasing the computational time. For all these reasons, investigating the capabilities of RANS models using a two-dimensional approach is of technical interest still today.

Regarding the applicability of RANS models to the proposed application, it should be noticed that the wide spectral gap, often observed between turbulent structures and the structure motion, might suggest that the time averaging process embedded in the RANS approach is more physically sound in the calculation of self-excited forces if compared to the prediction of the vortex shedding phenomenon, which is notoriously inaccurate when RANS turbulence models are used.

In the following, both global aeroelastic coefficients and pressure distributions are presented in order to allow systematic interpretation of the results and build a database, useful for future investigations, aiming at setting guidelines for engineers approaching this kind of simulations. In addition, in order to allow direct visual inspection of the flow field, videos representing the vorticity magnitude contours are provided.

## 7.2 Some comments on aeroelastic forces

In order to highlight the limitations of the aeroelastic forces description based on the flutter derivatives, it is here important to notice that, as already stated, the independence of the flutter derivatives from the system motion amplitude, in the case of bluff bodies, is not in general guaranteed and Eqs. (6.1) can be in some way misleading. In fact, the form assumed for the aeroelastic forces and expressed in Eqs. (6.1), directly descends from the application of the Kutta condition to the thin airfoil, so assuming that the aerodynamic forces are generated by the vorticity production at the body boundaries. This contribution to the aerodynamic forces can be considered to be largely dominant in many aeronautic application far from the stalling angle, but the same considerations cannot be generally adopted for bluff shapes. Nevertheless, well streamlined bodies, like many bare modern aerodynamic decks, show large separations only at the trailing edge and, as a consequence, the aforementioned hypotheses can be still deemed to hold. This condition is normally characterized by a linear variation of the lift coefficient with the angle of attack, small drag coefficients and formation of vortical structures with characteristic dimension considerably smaller than the body length scale  $B$ .

In other cases, for bluffer sections, the flow exhibits small to medium size detachments, formation of shear layers and reattachments. In such conditions the definition of flutter derivatives still holds as the system response, although highly non-linear in nature, can be linearised in the surrounding of a small angle of attack. The superposition of effects can be applied (which is always the case in the calculation of critical speed for coupled flutter) and considered as a first order approximation of the system dynamic response. In such cases, the aeroelastic forces are generated by both the production of vorticity at the solid boundaries (and its transport downstream) and the dynamic response of the shear layers and separation bubbles. In such conditions, the generation of

large vortices, which are shed and transported downstream, is still limited to fractions of the characteristic body length  $B$  and their shedding mechanism must be well decoupled in frequency with respect to the considered body motions.

When detachments are comparable to the body dimension, the system response to forced motions is largely dominated by the shear layers dynamics and instability and by the creation of large vortical structures. In such conditions, nor the flutter derivatives are representative of the system aeroelastic response neither the superposition principle holds. The system is often dominated by locking of the vortex shedding at harmonics of the applied motion in a wide range of reduced velocities and by shear layer instabilities. In such conditions, the applied motion, rather than the generating mechanisms of aeroelastic forces, can be considered as a triggering single frequency disturbance affecting highly non-linear mechanisms governed by the flow instability.

### 7.3 Simulation approach

The numerical simulations have been performed on rectangular prisms of nine aspect ratios. In the following, such parameter will be used to distinguish the test cases indicating the tested rectangles as  $R$  followed by their aspect ratio. The results will be shown for  $R2$ ,  $R3$ ,  $R4$ ,  $R5$ ,  $R8$ ,  $R10$ ,  $R12p5$ ,  $R15$ ,  $R20$ .

In order to reproduce the conditions normally encountered in wind tunnel tests, the Reynold number,  $Re$ , is set equal to  $1.4E5$  based on the along wind dimension  $B$ . It must be noticed that the definition of the  $Re$  number, when RANS turbulence models are used, can be in some way questionable because the effective viscosity at the inlet is defined by the turbulence related inlet parameters. Although remarkable, in the following, such effect is not taken into account as the idea itself of turbulence viscosity is a radical simplification of the turbulence nature operated by the RANS approach, which can be hardly related to any measurable quantity.

Regarding the choice of modelling the flow in a two-dimensional framework, it is a commonly accepted practice when RANS turbulence models are used, justified by the huge decrease in the computational effort and the reasonable results obtained by some authors under such assumption. Nevertheless, such choice is definitely not obvious even for constant cross-section cylinders as demonstrated in [91, 93] and by comparing the results obtained in [94, 95]. In [93] the role of three-dimensionality is found to be not negligible even for mildly bluff sections as an airfoil at the stall angle and, most remarkably, RANS models show to be able to qualitatively capture such aspects of the flow organization when used in fully three-dimensional cases.

When RANS models are used, so suppressing medium and small turbulence scales, the three-dimensionality of the flow is largely negligible when the aerodynamic behaviour is led by the vorticity production in fully attached flows but might play a crucial role when large separation occurs. Indeed, in the literature no agreement can be found on the subject [96], probably because the importance of such effects is problem dependent. The results of a Proper Orthogonal Decomposition (POD) analysis on the pressure distribution calculated with a three-dimensional LES simulation of  $R5$  are reported in [91]. In that case, marked effects of three-dimensionality have been found already in the third mode. The role of such effects on aeroelastic loads is not well understood and further

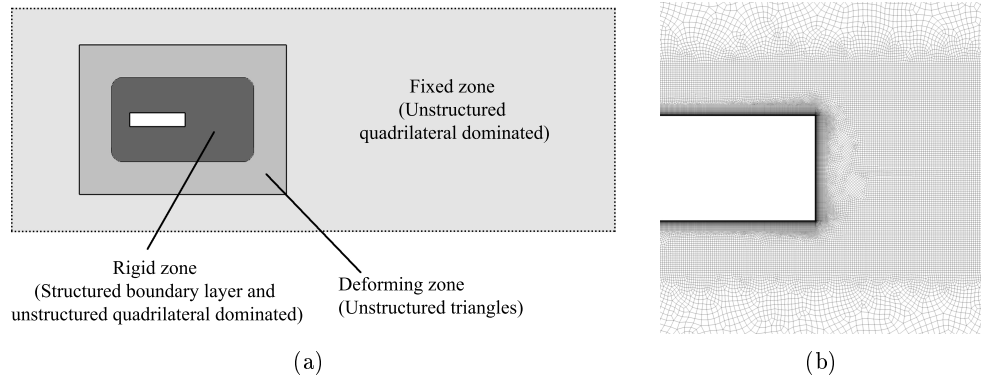


Figure 7.1: Computational domain subdivision (a) and close up of the computational mesh in the rigid zone (b).

research is needed on the subject.

### 7.3.1 Numerical setup

The mesh organization follows the same guidelines described in [48]: in particular a rigid body motion is defined close to the immersed body in order to avoid degradation of the mesh in critical zones. A deforming zone, meshed with triangular elements, is used to allow the mesh movement and it is deformed, smoothed and remeshed during the calculation. A fixed zone is then used to mesh the rest of the computational domain (see Fig. 7.1).

Second order schemes are selected for all quantities and upwinding enabled for convected ones. Node based gradient approximation is chosen and a PISO scheme used for velocity-pressure coupling. Time advancement is first-order implicit. Calculations have been performed using Fluent 14 [51] and Code\_Saturne 3.0 [97] where specified.

For all the cases, the mesh is structured in the proximity of the boundaries and unstructured quadrilateral dominated outside the boundary layer. The mesh height close to the solid boundaries is equal to  $5.0E-4 B$ , resulting in a  $y^+ \simeq 1$  [8] almost everywhere and  $y^+ < 6$  close to the rectangle corners. The mesh size close to the boundaries, in the along wind direction, is  $2.0E-3 B$  and, outside the boundary layer, it is coarsened until the size  $1.0E-2 B$  is reached. Such sizing is kept constant in the body proximity and it is coarsened until the domain boundaries. In the wake the mesh sizing is limited to  $2.5E-2 B$  for a distance equal to  $5.0 B$  and then it is slowly coarsened. All the meshes are constituted of 100-120k elements and are capable of resolving all the fine flow structures which are not suppressed by the turbulence model.

The time step is chosen to be  $1/500$  of the non-dimensional time unit,  $S$ , defined as  $S = B/U$ . Such choice is expected to lead to accurate description of the unsteady fluid behaviour and limits the Courant number,  $Co$ , to a maximum of 6 in extremely small areas close to the corners and well below 1 everywhere else.

The mesh and time step independence have been verified on  $R4$  at zero angle of attack using a standard  $k - \omega$  turbulence model. The boundary layer has been refined so that  $y_{max}^+ \simeq 1$ , the time step reduced so that the maximum  $Co_{max} \simeq 1$  and global forces

and pressure distributions compared to the previously described case. No meaningful discrepancies between the fine and the coarse case were observed.

Although the aim of this chapter is to assess the performance of the standard  $k - \omega$  [18] and the  $k - \omega_{sst}$  [23] turbulence models, comparisons are provided also for  $k - \epsilon$  [8],  $v2 - f$  [98] and LES [99] using both two- and three-dimensional approaches.

## 7.4 Preliminary numerical analysis

Preliminary numerical simulations on fixed bodies have been used to explore the differences between various turbulence models and the influence of the turbulence related inlet parameters. The analyses are organized as follows

1. The case *R4* is solved at 0.0 angle of attack with various turbulence models assuming very low incoming turbulence.
2. The case *R4* is used to calibrate the inlet conditions of the standard  $k - \omega$  turbulence model according to the LES results obtained by Yu et al. [95].

In particular, *R4* is chosen to compare different RANS turbulence models and for the model calibration because it exhibits large flow separations and reattachment so that it can be considered representative of the flow patterns encountered in the other cases, which range from fully detached to mainly reattached.

The results are compared to the data obtained by Yu et al. [94, 95] with a 2D and 3D LES approach, respectively, Bruno et al. [91] with 3D LES analysis and Shimada et al. [100] with a two-layer  $k - \epsilon$  model with a modified  $k$ -production term.

The LES results are also used for the calibration of the standard  $k - \omega$  turbulence model used in the following analysis. In fact, such results can be considered of good quality, based on the good performance experienced with three-dimensional LES analysis when highly separated flows around bluff bodies are considered when the detachment points are geometrically defined.

### 7.4.1 Comparison of turbulence models on *R4*

In order to verify the ability of tested turbulence models to predict the flow field around the rectangle *R4*, the case has been solved using four popular RANS models and measuring the time averaged pressure coefficient,  $C_p$ , distribution and its *rms* along the upper side of the rectangle. Extremely weak incoming turbulence is imposed by assuming in all cases an incoming turbulence intensity,  $I$ , of 0.5% and a turbulent viscosity ratio,  $TVR$ , of 2.0 (with  $TVR = \mu_t/\mu$  where  $\mu_t$  is the turbulent viscosity). The analysis using the  $v2 - f$  turbulence model has been performed in Code\_Saturne by keeping the same analysis settings or equivalent.

As depicted in Fig. 7.2, in this case, the realizable  $k - \epsilon$  and the  $k - \omega_{sst}$  behave very similarly, being the most relevant difference between the two models the near wall treatment that is not expected to be of primary importance in this case, as the flow is mainly characterized by shear layers. All the models appear to underestimate the suction after the leading separation point and the  $\epsilon$ -based models ( $k - \omega_{sst}$  included) underestimate the strength of the unstable vortex which is periodically formed and shed

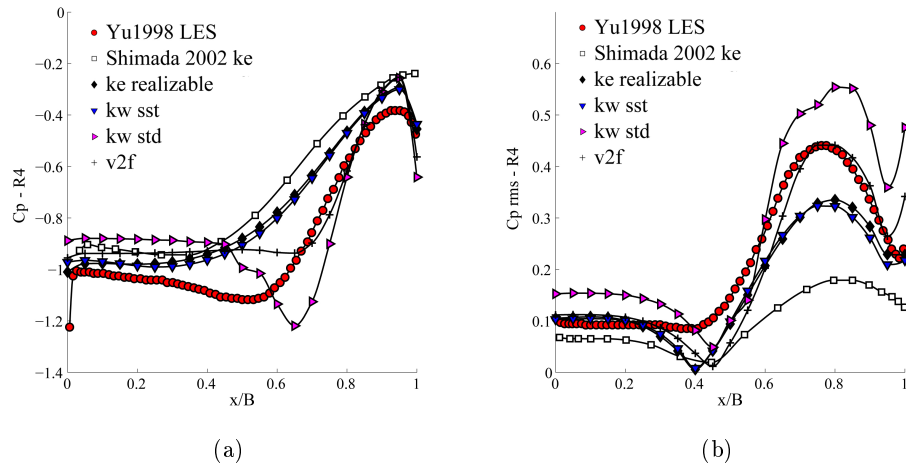


Figure 7.2: Pressure coefficient distribution along the upper side of  $R4$ . Comparison of the results obtained with different turbulence models assuming low turbulence: (a) time averaged, (b) *rms*.

from the second half of the side. The  $v2 - f$  model appears to lead to an improvement of the pressure distribution (especially in the *rms*), but, like the other models, it underestimates the suction after the separation point. The standard  $k - \omega$  model suffers from the same drawbacks but it overestimates the *rms* on the second half of the side if compared to the LES solution.

As expected the  $v2 - f$  model seems to lead to slightly better predictions and the  $k - \epsilon$  appears to be the least accurate but, at this stage, it is not possible to assess if one model is remarkably superior to the others.

#### 7.4.2 Calibration of the standard $k - \omega$ on $R4$

It is well known that the major drawback of the standard  $k - \omega$  turbulence model is its over dependence on the inlet parameters related to turbulence. Such parameters should not be directly related to measurable quantities characterizing the experimental inlet conditions and should be rather seen as a control over the turbulence model dissipation especially when unsteady and separated flows are considered. This can be highly problematic if no useful information is available to calibrate the model when the numerical analysis is performed.

With the aim of testing the robustness of the CFD, RANS based, evaluation of flutter derivatives when no reference data are available, the calibration procedure has been based on the pressure distribution at zero angle of attack on  $R4$ . In fact, such distribution is representative of the flow topology for that case but it is not directly related to the estimation of the flutter derivatives. In this way, only a minimum amount of information is extracted from the available results (especially considering that the calibrated inlet conditions are used for all the studied aspect ratios). Similarly to the comparison between various commonly available turbulence models discussed in Sec. 7.4.1, the case is calibrated based on the data obtained by Yu et al. [95].



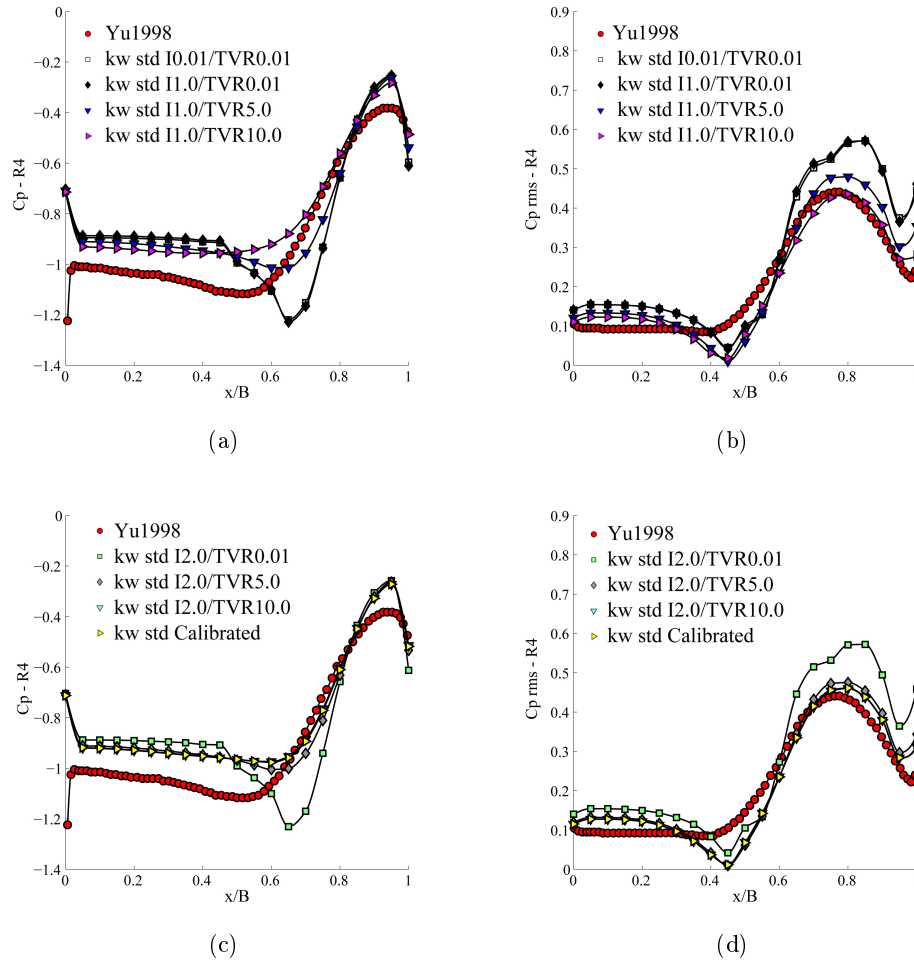


Figure 7.3: Pressure coefficient distribution along the upper side of  $R4$ . Comparison of the results obtained with different inlet conditions for the standard  $k - \omega$  model: (a) and (c) time averaged, (b) and (d)  $rms$ .

It must be noted that such a procedure might be applied even systematically when no experimental data are available. In fact it is possible to evaluate the pressure distribution around the bridge deck at zero incidence using a LES approach and then use such results to calibrate the RANS model. The advantage of such procedure is that the computationally expensive LES analysis is limited to a fixed case while the time consuming dynamic analysis are still performed using a RANS approach.

The dependence of the results on the inlet parameters can be clearly observed in Fig. 7.3. Based on the aforementioned considerations and the predicted results, the calibrated inlet parameters have been set to  $I = 1\%$  and  $TVR = 7.0$  and indicated as Calibrated in Figs. 7.3 (c) and (d).

The same procedure was followed for the  $k - \omega$  *sst* model but, as expected, no dependence on the turbulence related inlet parameters was observed [101] so confirming the model stability with respect to the inlet conditions.

As a concluding remark, it is noticed that, for this application, the model calibration, if experimental data are available, should be preferably based on the lift and moment coefficient derivative with respect to the angle of attack because such quantities are directly involved in the definition of the flutter derivatives.

## 7.5 Numerical results

In the following, the numerical results obtained during the investigation are presented. In particular, for each analysed case, the variation of the aerodynamic coefficients with the angle of attack, the topology of the flow field and the numerically evaluated flutter derivatives are reported.

In order to allow direct visual inspection to the obtained numerical results, videos of all the simulations are available at the Youtube channel *LAMC Rectangles*. Such videos are representative only of the converged solution and show the evolution of the vorticity magnitude in the non-dimensional time.

As a general convention, the length scale is represented by the along wind dimension,  $B$ , but  $C_d$ , its *rms* and the Strouhal number,  $St$ , are calculated with respect to the cross wind dimension  $H$ . The time averaged and the instantaneous vorticity contours are presented in order to visually describe the flow field organization and can be compared to the ones reported in [100]. In the following, the instantaneous vorticity contours are shown in correspondence of the peak of the lift coefficient if not differently specified.

The evaluation of the flutter derivatives is performed by applying to the body a harmonic rotational motion of amplitude 3.0 degrees and a vertical heaving motion of amplitude  $0.05 B$ , unless differently specified. The flutter derivatives are extracted from global forces while the motion-induced pressure distributions are calculated by fitting the recorded signal with a sinusoidal function of appropriate amplitude and then calculating its relative amplitude and phase shift with respect to the applied motion. Both elaborations are accomplished by using a non-linear fitting procedure. The resultant graphs can be compared to the one obtained experimentally by Matsumoto [75], a part from a sign swap caused by different sign conventions.

It must be noticed that such graphs are representative of the contribution of the local pressures to the aeroelastic forces but their shape is often far from being sinusoidal, as shown in Fig. 7.4, especially at the trailing edge. As a consequence, the definition of their amplitude and phase shift might be misleading if interpreted as a consistent representation of the recorded pressures.

### 7.5.1 $R2$

The numerically evaluated pressure coefficient distribution on the rectangle  $R2$ , obtained at zero angle of attack, is shown in Fig. 7.5. The time averaged pressure coefficient distribution is better described by the standard  $k-\omega$  model, while the pressure coefficient *rms* distribution appears to be barycentric with respect to the two tested turbulence models, taking as reference the 3D LES results [95] while the results based on the  $k-\omega$  *sst* model reveal more close to both experimental data by Ohtsuki in [102] and by Miyazaki and Miyata in [103]. The two models predict different vortex shedding topology as depicted in Fig. 7.6, with the  $k-\omega$  *sst* being unnatural because the shear

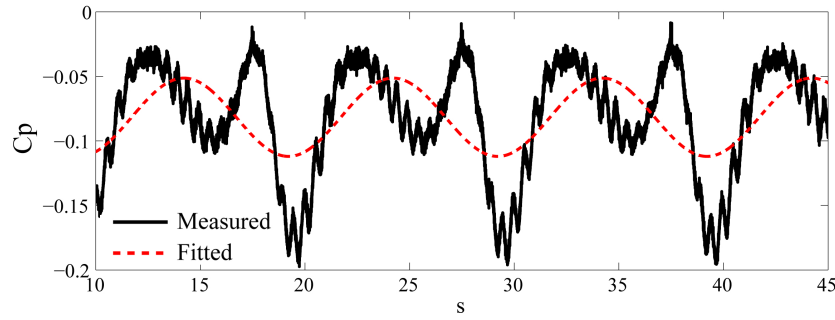


Figure 7.4: Fitting of the pressure coefficient used to evaluate amplitude and phase for  $R15$  at  $U_{red} = 10$  and  $x/B = 0.6$  using the  $k - \omega$  *sst*.

layers do not reattach on the downstream side. This leads to remarkable differences also for the integral flow quantities as reported in Table 7.1. Such circumstance is particularly obvious if the drag coefficient is analysed: in the case of the  $k - \omega$  *sst* the missed reattachment increases the base pressure so that the drag is underestimated while the standard  $k - \omega$  yields to good results.

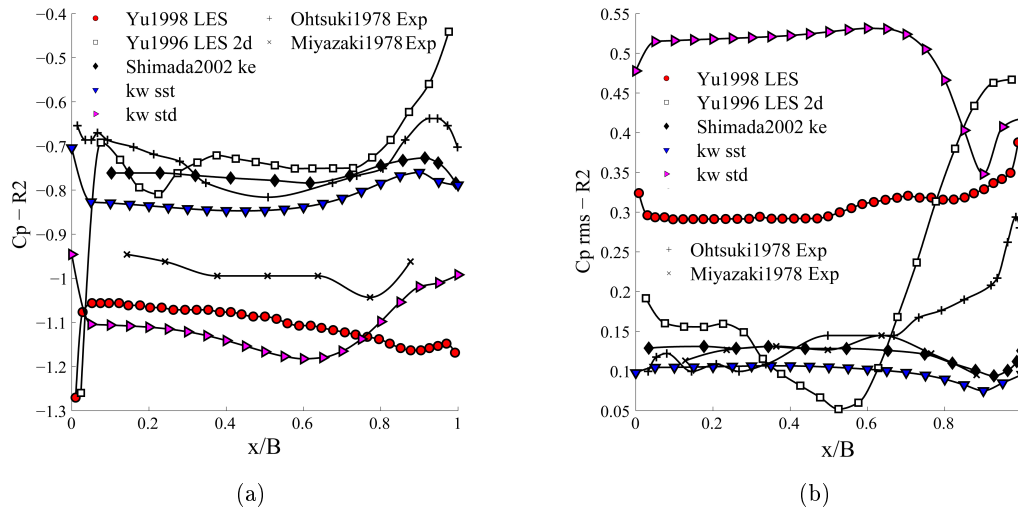
Figure 7.7 shows the variation of  $C_l$  and  $C_m$  with respect to the angle of attack. The aerodynamic coefficients derivatives with respect to the attack angle (at zero incidence)  $C_{l,\alpha}$  and  $C_{m,\alpha}$  appear to be greatly influenced by the turbulence model and remarkable differences in the evaluation of the flutter derivatives can be already expected at this stage.

According to what has been stated in Sec. 7.2, the definition of the flutter derivatives for a fully separated flow is at least questionable. For a wide range of reduced velocities the aeroelastic behaviour of the body is characterized by a lock-in condition between the von Kármán vortex shedding and the body motion, as reported in [75] and revealed by the peaks of the flutter derivatives values in Fig. 7.8. In such conditions, the flutter derivatives are not representative of the body aeroelastic behaviour meaning that they are not suitable for critical flutter speed assessments. Both models are able to predict such condition, but it is hard to assess if one is superior compared the other.

The static pressure distributions and the global aerodynamic parameters seem to indicate a better performance of the standard  $k - \omega$  model, which predicts a flow topology much closer to the LES results in compared with the  $k - \omega$  *sst* while the flutter derivatives seems to be better captured by the  $k - \omega$  *sst*. It is also interesting to notice that the flow topology in the lock-in condition at  $U_{red} = 10$  is the same for both models as it can be seen in the videos.

In conclusion, it can be said that the tested models are able to reproduce the flow field mainly on a qualitative base and although the instability originated by the shear layers interaction is captured, its strength is not well reproduced. Considering the flutter derivatives, some trends appear to be in agreement with the experimental data but overall the agreement is mainly qualitative.

$R2$	$C_d$ avg	$C_d$ rms	$C_l$ rms	St	$C_{l,\alpha}$	$C_{m,\alpha}$
$k - \omega$ sst	1.46	6.4E-3	0.2	0.079	0.06	-4.8E-3
$k - \omega$ std	1.66	0.38	0.95	0.0625	0.014	-8.3E-3
Yu et al. 2D [94]	1.62	0.14	-	0.18	-	-
Yu et al. 3D [95]	1.69	0.18	0.61	0.088	-	-
Exp.	1.65 [104]	-	-	0.08 [105]	-	-

Table 7.1: Global aerodynamic coefficients for  $R2$ Figure 7.5: Pressure coefficient distribution along the upper side of  $R2$  at zero angle of attack: (a) time averaged, (b)  $rms$ .

### 7.5.2 $R3$

The numerically evaluated pressure coefficient distribution and its  $rms$  on the rectangle  $R3$ , obtained at zero angle of attack, are shown in Fig. 7.9. All the tested models are in reasonable agreement with the LES results and only the  $k - \epsilon$  results reported in [100] appear to be clearly over damped.

The obtained global aerodynamic coefficients are shown in Table 7.2 together with other numerical solutions and experimental measurements. Overall good agreement is found between experimental and numerical results and the two investigated turbulence models are in fair agreement.

In this case, the aspect ratio is higher than the critical one 2.8 [100] and the flow is reattached at zero angle of attack. When the rectangle is inclined, even at small attack angles, the flow detaches on one side leading to complex shedding mechanisms which often are not well captured by a RANS two-dimensional approach. If the  $k - \omega$  sst is used, secondary low frequency mechanisms are involved at sub harmonics of the main shedding frequency that are not observed using the  $k - \omega$  sst.

It must be also noticed that all two-dimensional simulations (LES included) predict an apparent minimum in the  $C_p$   $rms$  (located between  $x/B = 0.4$  and  $0.5$  for  $R3$ ), which

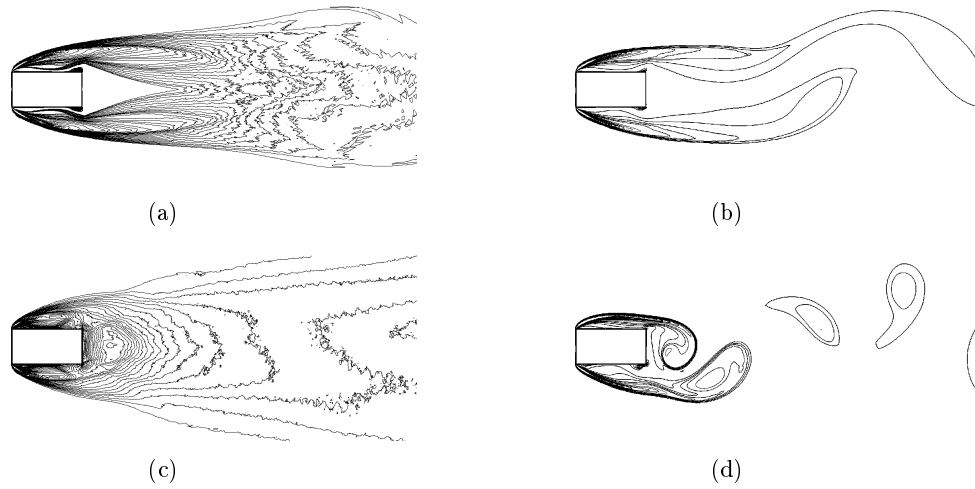


Figure 7.6: Vorticity contours for  $R2$ : (a) time averaged  $k - \omega$  sst, (b) instantaneous  $k - \omega$  sst, (c) time averaged standard  $k - \omega$ , (d) instantaneous standard  $k - \omega$ .

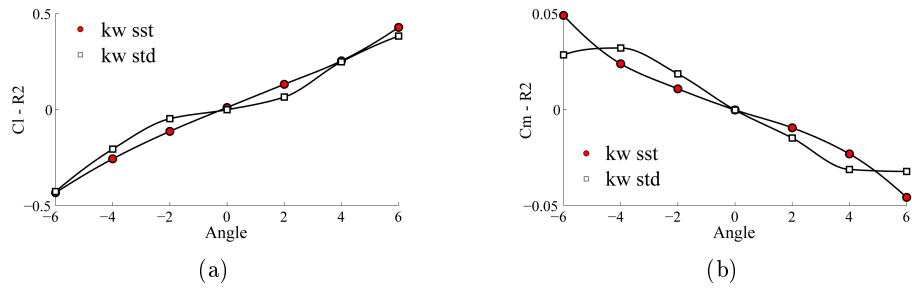


Figure 7.7: Variation of the aerodynamic coefficients with the angle of attack for  $R2$ : (a)  $C_l$ , (b)  $C_m$ .

is sensibly less apparent for three-dimensional LES, probably indicating that some three-dimensional flow features are disregarded. Notably, such characteristic is observed also for higher aspect ratios ( $R4$  and  $R5$ ).

In addition to that, two-dimensional simulations predict weaker suction at the leading edge if compared to three-dimensional LES. Such discrepancy is present in all the results presented in [95] ( $R3$  and  $R4$ ), but is not observed in [91] for  $R5$  so that it can not be generalized.

Despite the good description of the pressure distribution around the body, the flutter derivatives are predicted only qualitatively. The two turbulence models are in fairly good agreement with each other, but the experimental results are not well captured especially for the trend of  $H_2^*$ .

Looking at the motion induced pressure fields reported in Fig. 7.13, remarkable differences between the two turbulence models can be observed. The peak amplitude motion-induced pressures are located in the downstream half of the sides, in agreement with experimental results, but the peaks are too sharp compared to [75] especially if the

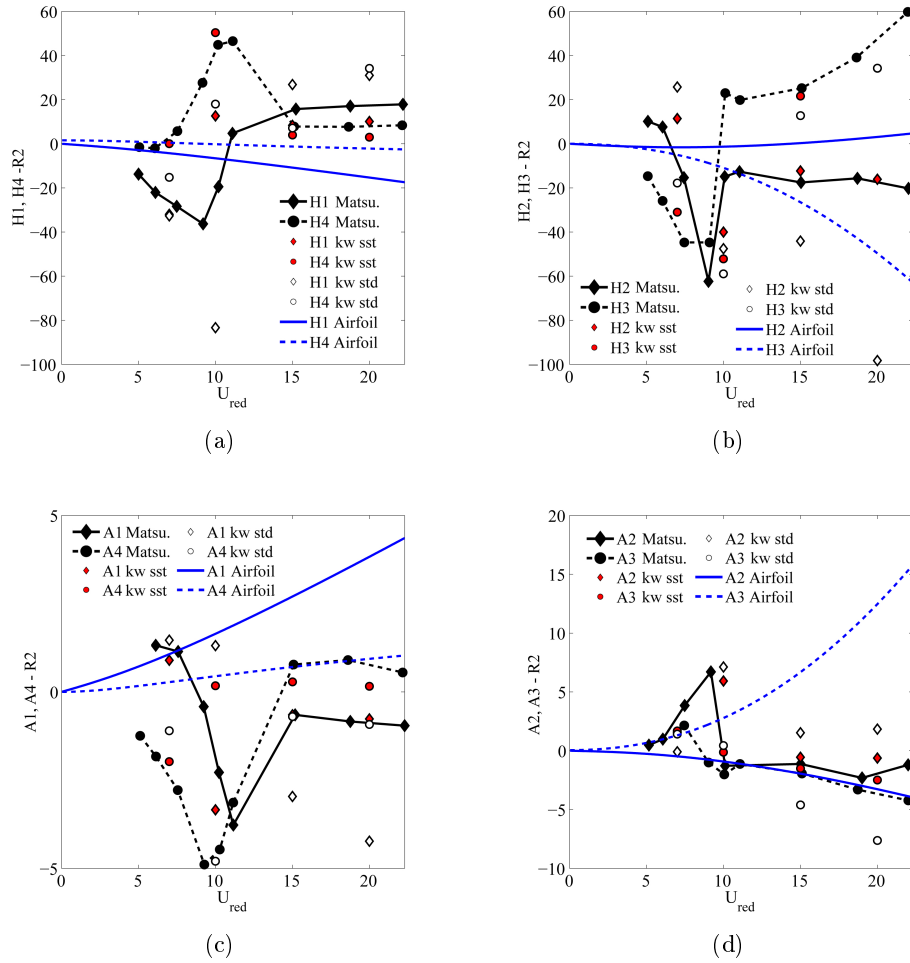
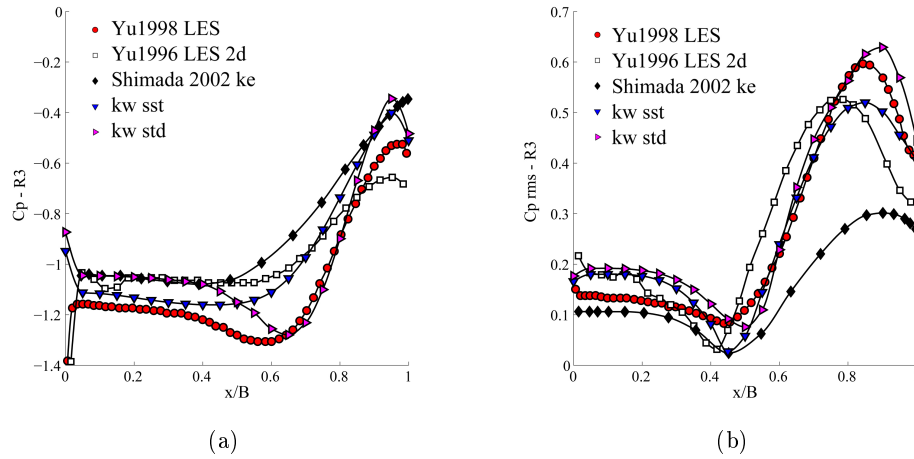


Figure 7.8: Comparison between numerically obtained flutter derivatives and experimental results for  $R2$ .

$R3$	$C_d$ avg	$C_d$ rms	$C_l$ rms	St	$C_{l,\alpha}$	$C_{m,\alpha}$
$k - \omega$ sst	1.35	0.025	0.42	0.16	-0.21	-0.027
$k - \omega$ std	1.37	0.063	0.47	0.16	-0.22	-0.020
Yu et al. 2D [94]	1.56	0.0927	-	0.17	-	-
Yu et al. 3D [95]	1.3	0.14	0.34	0.186	-	-
Exp.	1.4 [106]	-	-	0.17 [105]	-	-

Table 7.2: Global aerodynamic coefficients for  $R3$ .Figure 7.9: Pressure coefficient distribution along the upper side of  $R3$  at zero angle of attack: (a) time averaged, (b) *rms*.

standard  $k - \omega$  is considered.

Inspecting the video of the vorticity magnitude contours during the motion, the aeroelastic behaviour seems to be governed by the shear layer dynamics, which is characterized by non-linearities (as confirmed also by the lift and moment variation with the angle of attack, in Fig. 7.11) which might not be well reproduced by the adopted RANS approach.

In conclusion, this case shows that a reasonable representation of the pressure field in static conditions does not necessary lead to a correct representation of the flow behaviour in dynamic conditions even for slow and small motions. The obtained flutter derivatives are again mainly qualitative and different RANS models often tend to bias the results in similar ways.

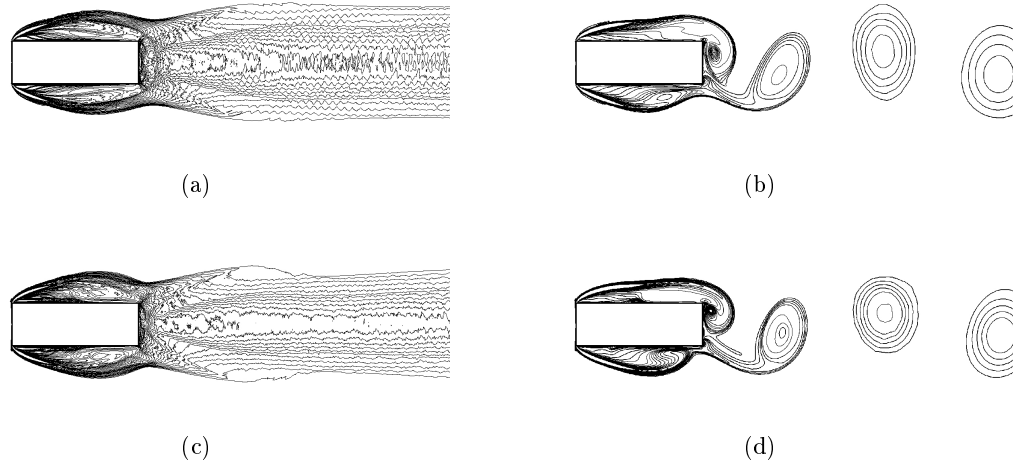


Figure 7.10: Vorticity contours for  $R3$ : (a) time averaged  $k - \omega$  sst, (b) instantaneous  $k - \omega$  sst, (c) time averaged standard  $k - \omega$ , (d) instantaneous standard  $k - \omega$ .

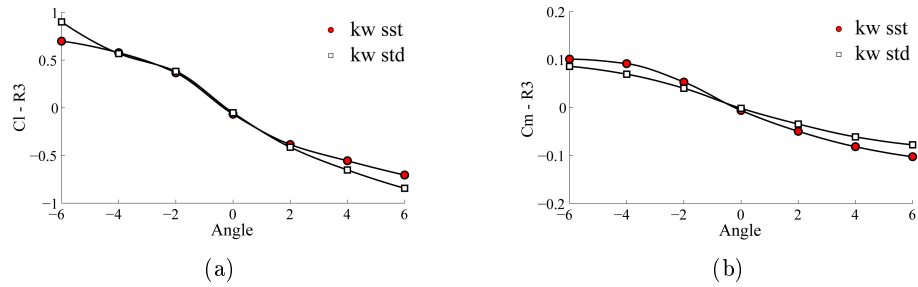
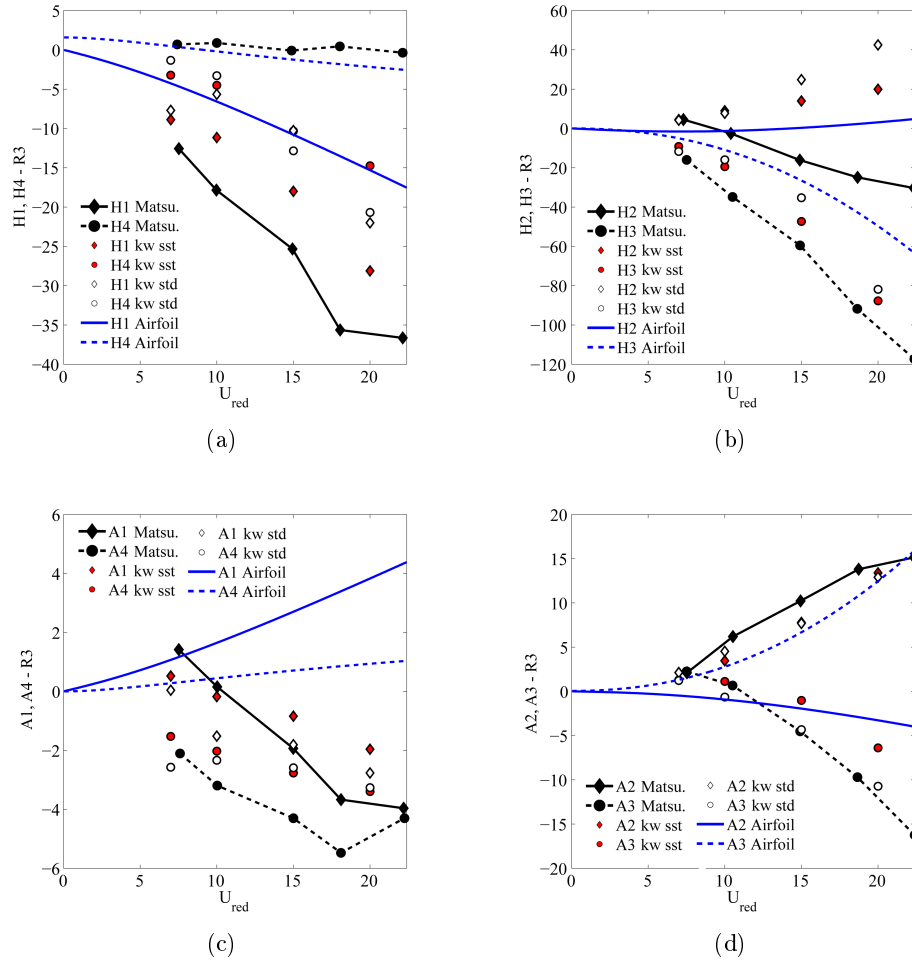


Figure 7.11: Variation of the aerodynamic coefficients with the angle of attack for  $R3$ : (a)  $C_l$ , (b)  $C_m$ .



Figure 7.12: Comparison between numerical and experimental flutter derivatives for  $R3$ .

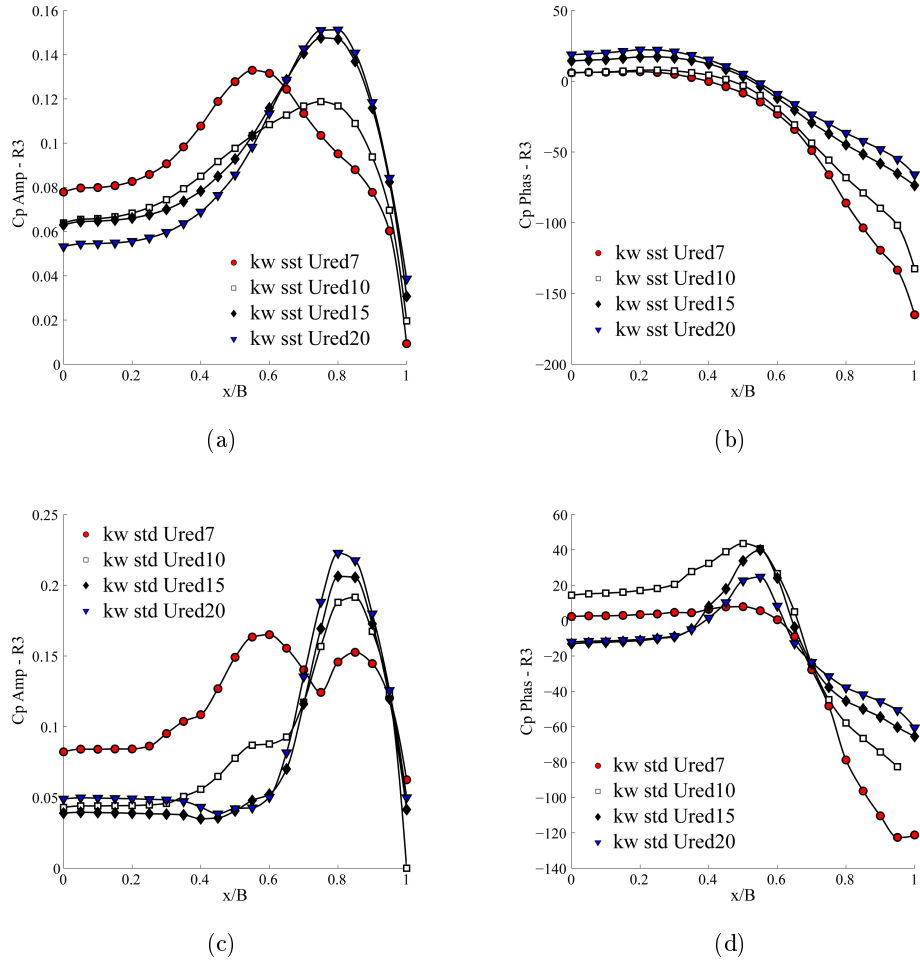


Figure 7.13: Rotational motion induced pressure coefficient distribution for  $k - \omega$  sst and standard  $k - \omega$  model for  $R3$ : (a) and (c) amplitude of pressure coefficient for 1.0 degree harmonic motion, (b) and (d) its phase shift with respect to the applied motion.

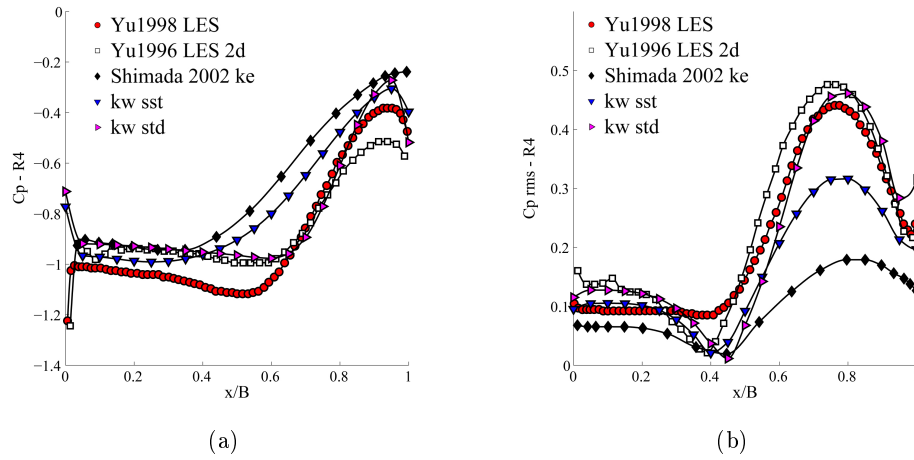


Figure 7.14: Pressure coefficient distribution along the upper side of  $R4$  at zero angle of attack: (a) time averaged, (b)  $rms$ .

### 7.5.3 $R4$

The pressure coefficient distribution and its  $rms$  for  $R4$  have been widely discussed in Sec. 7.4.1. Here, the results are reported only for the selected turbulence models and comparison is provided between two- and three-dimensional cases with the LES approach (see Fig. 7.14).

Figure 7.15 reports the flow topology for all the tested turbulence models and shows a good agreement among them. Nevertheless, the models predict different positions for the reattachment point so affecting the resultant global forces.

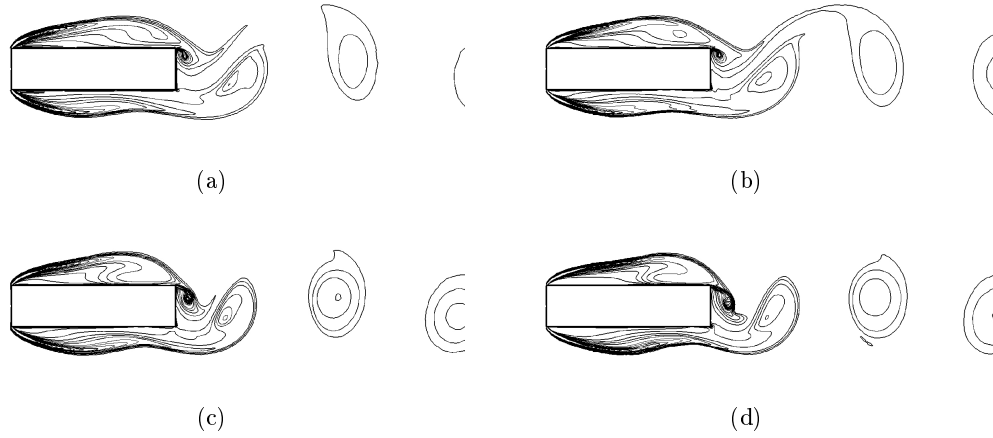
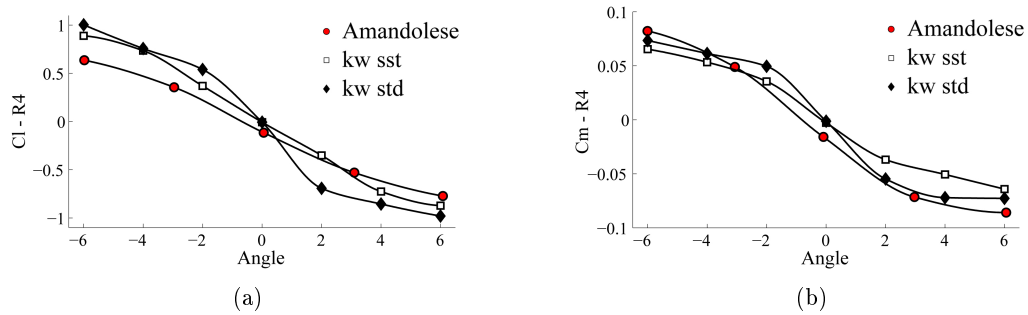
The variation of  $C_l$  and  $C_m$  with the attack angle is given in Fig. 7.16 and it is compared to the experimental data provided in [107]. It can be seen that the two considered turbulence models predict different variation of the aerodynamic coefficients with the angle of attack. The  $k-\omega$  *sst* seems to be able to better capture their variation for small angles, so returning a much better prediction of the punctually evaluated lift and pitching moment derivative at zero incidence.

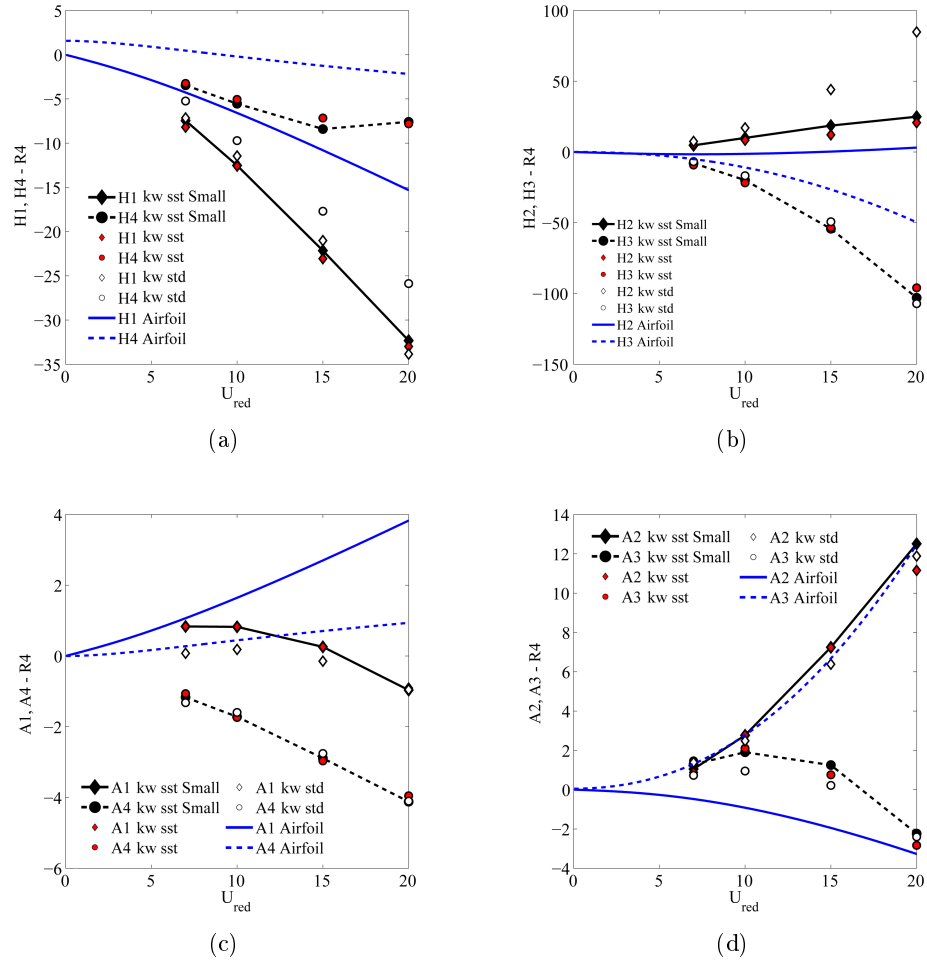
In general, it seems that the  $k-\omega$  model over-amplifies the shear layer sensitivity to the attack angle while the  $k-\omega$  *sst* damps it excessively, nevertheless leading to more acceptable results.

Flutter derivatives and motion-induced pressure distributions are here reported for completeness in Figs. 7.17 and 7.18, although no experimental data is available in [75] for this case.

In addition to the results presented for the other test cases, here a comparison is carried out between the values of the flutter derivatives obtained for the standard applied motion amplitudes (3 degrees for rotational motions and  $0.05B$  for vertical ones) and half of such values (indicated by Small in the figure) in the case of the  $k-\omega$  *sst* model. No significant change is experienced in the recorded values so confirming that, at least in the performed numerical simulations, the flutter derivatives are well defined and representative of the body aeroelastic properties.

$R4$	$C_d$ avg	$C_d$ rms	$C_l$ rms	St	$C_{l,\alpha}$	$C_{m,\alpha}$
$k - \omega$ sst	1.19	0.01	0.26	0.137	-0.17	-0.02
$k - \omega$ std	1.35	0.067	0.33	0.14	-0.36	-0.03
Yu et al. 2D [94]	1.43	0.168	-	0.15	-	-
Yu et al. 3D [95]	1.3	0.14	0.25	0.156	-	-
Exp.	1.4 [106]	-	-	0.135 [105]	-0.16 [107]	-0.022 [107]

Table 7.3: Global aerodynamic coefficients for  $R4$ .Figure 7.15: Instantaneous vorticity contours for  $R4$ : (a)  $k-\epsilon$ , (b)  $k-\omega$  sst, (c) standard  $k-\omega$ , (d)  $v2-f$ .Figure 7.16: Variation of the aerodynamic coefficients with the angle of attack for  $R4$ : (a)  $C_l$ , (b)  $C_m$ .

Figure 7.17: Flutter derivatives numerically obtained for  $R4$ .

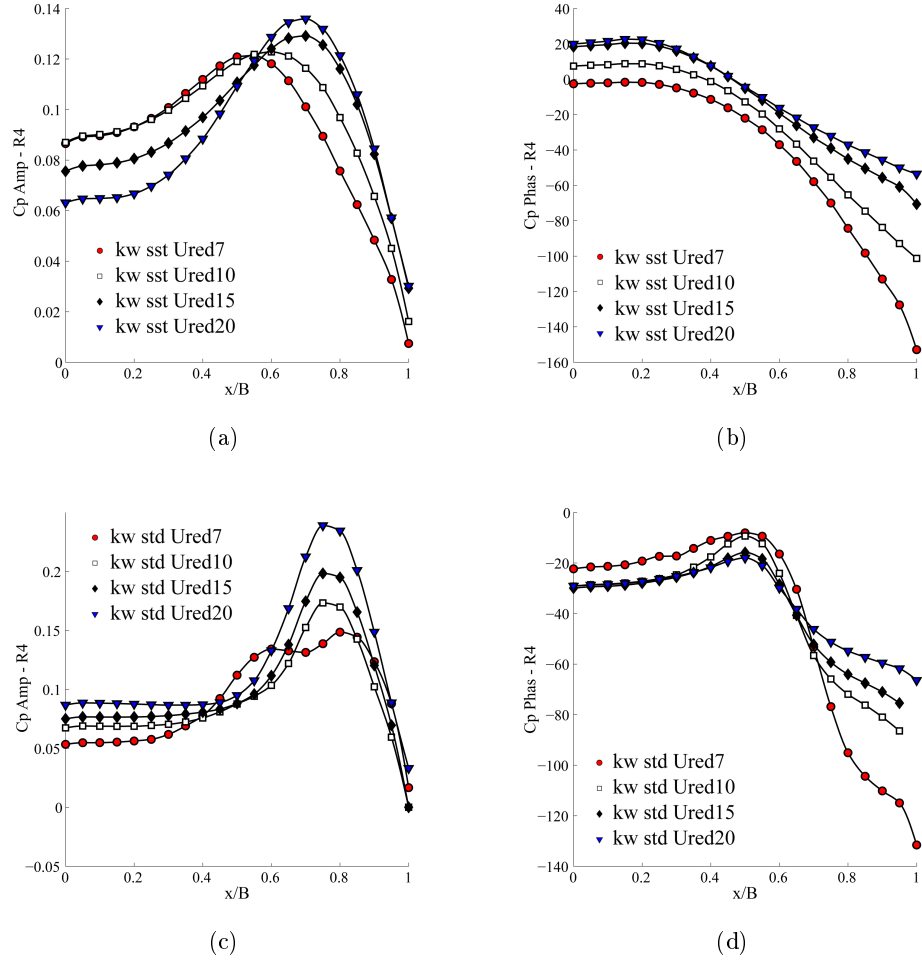


Figure 7.18: Rotational motion induced pressure coefficient distribution for  $k - \omega$  sst and standard  $k - \omega$  model for  $R4$ : (a) and (c) amplitude of pressure coefficient for 1.0 degree harmonic motion, (b) and (d) its phase shift with respect to the applied motion.

		$C_d$ avg	$C_d$ rms	$C_l$ rms	St	$C_{l,\alpha}$	$C_{m,\alpha}$
<i>R5</i>	$k - \omega$ <i>sst</i>	1.07	0.01	0.16	0.11	-0.11	-0.018
	$k - \omega$ <i>std</i>	1.15	0.05	0.23	0.11	-0.30	-0.029
<i>R8</i>	<i>Exp.</i> [107]	-	-	-	-	-0.186	-
	$k - \omega$ <i>sst</i>	0.93	1.2E-3	3.4E-3	0.114	-0.156	-2.3E-3
	$k - \omega$ <i>std</i>	1.18	1.4E-2	0.10	0.149	-0.174	-1.63E-2
<i>R10</i>	$k - \omega$ <i>sst</i>	1.04	7.7E-3	0.034	0.131	-0.196	-1.28E-2
	$k - \omega$ <i>std</i>	1.02	5.6E-3	0.025	0.126	-0.27	4.8E-4

Table 7.4: Global aerodynamic coefficients for *R5*, *R8* and *R10*.

#### 7.5.4 *R5*, *R8* and *R10*

The numerically evaluated pressure coefficient distributions on the rectangles *R5*, *R8* and *R10*, at zero attack angle, are shown in Fig. 7.19. Comparison is here made with the results obtained in [91, 100] in the case of *R5*. *R8* and *R10* are grouped together for brevity and no comparison with other results is provided.

The pattern observed in the other cases is mainly confirmed. The pressure recovery after the separation point is quicker for  $\epsilon$ -based models for all aspect ratios and for *R5* the  $C_p$  rms appears to be over damped if compared to the available LES results.

Figure 7.21 shows that *R8* produces a particularly stable flow when the  $k - \omega$  *sst* model is used. This occurrence seems non-physical but it is in agreement with the results presented in [100] for *R6* and *R7* obtained with a  $k - \epsilon$  model. Supplementary analyses, which are not here reported, confirm that such non-physical condition is found also when the *Re* number is doubled, but does not occur using the standard  $k - \omega$  model which predicts a much more unstable flow, as it can be seen in Fig. 7.21 (h).

The results clearly show that, despite the differences in the shedding intensity, all the models are able to correctly predict the change in flow topology between *R5* and ratios higher than 6 [100].

The global flow parameters are collected in Table 7.4 and the flow topology indicates that the aerodynamic behaviour is still largely affected by the shear layers dynamics rather than the vorticity production at the solid boundaries, as observed from Fig. 7.21.

The derivatives of the aerodynamic coefficients show an accentuated sensitivity to the turbulence model and, in particular, for *R10* the two turbulence models predict opposite sign for  $C_{m,\alpha}$  (see Fig. 7.20) so indicating that the aerodynamic centre is almost barycentric. Analogous condition is observed in the data presented in [107], which are not here reported for  $C_m$ , which show that opposite signs for  $C_{m,\alpha}$  were recorded on *R8* by considering global forces measured with a balance and those obtained by pressure integration.

Indeed, the fact that the aspect ratio that leads to a symmetric aerodynamic centre occurs, in two-dimensional RANS simulations, for a higher ratio if compared to the experimental data is a useful result as it indicates that the simulations are overestimating the role played by the shear layer in the definition of the aerodynamic behaviour. Such result is expected as the vorticity contour (Fig. 7.21) indicates the presence of a non-physical sharp coherent shear layer.

As regards the prediction of the aeroelastic coefficients (given in Fig. 7.22), good

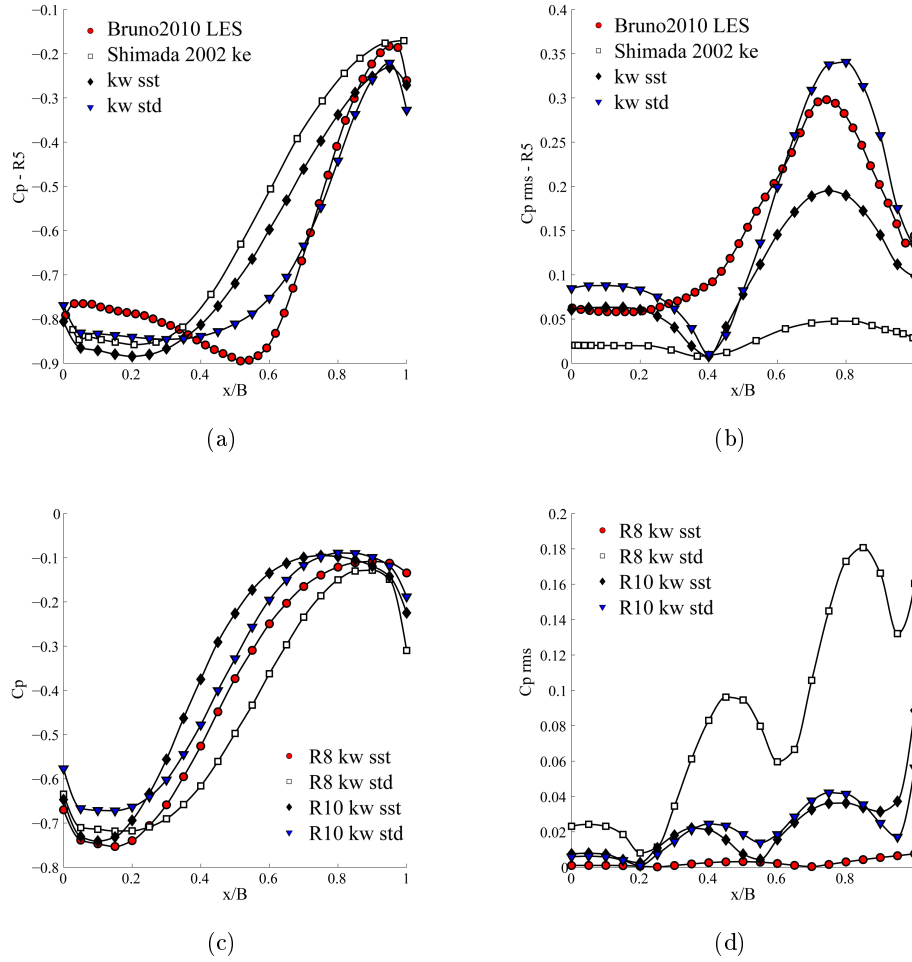


Figure 7.19: Pressure coefficient distribution along the upper side of  $R5$ ,  $R8$  and  $R10$  at zero angle of attack: (a)  $R5$  time averaged, (b)  $R5$  rms, (c)  $R8$  and  $R10$  time averaged, (d)  $R8$  and  $R10$  rms.

agreement is observed for  $R5$  when torsional motions are considered, but a deterioration of the prediction is observed for higher ratios, probably due to the change in the flow topology.

In the case of  $R8$ , the experimental data reported in [75] have been compared to the ones independently obtained and available in [37] (not here reported). The comparison shows good agreement between them, little sensitivity to the  $Re$  number and to the amplitude of the motion used for flutter derivatives extraction.

The prediction of the flutter derivatives, although some of them are in good agreement with the experimental results, is still mainly qualitative but useful information can be extracted. In particular, the  $k - \omega$  sst model correctly reproduces the trends observed in experimental results, although the corresponding values often appear to be moderately or rather amplified. In this cases it can be stated that reasonable agreement is observed.



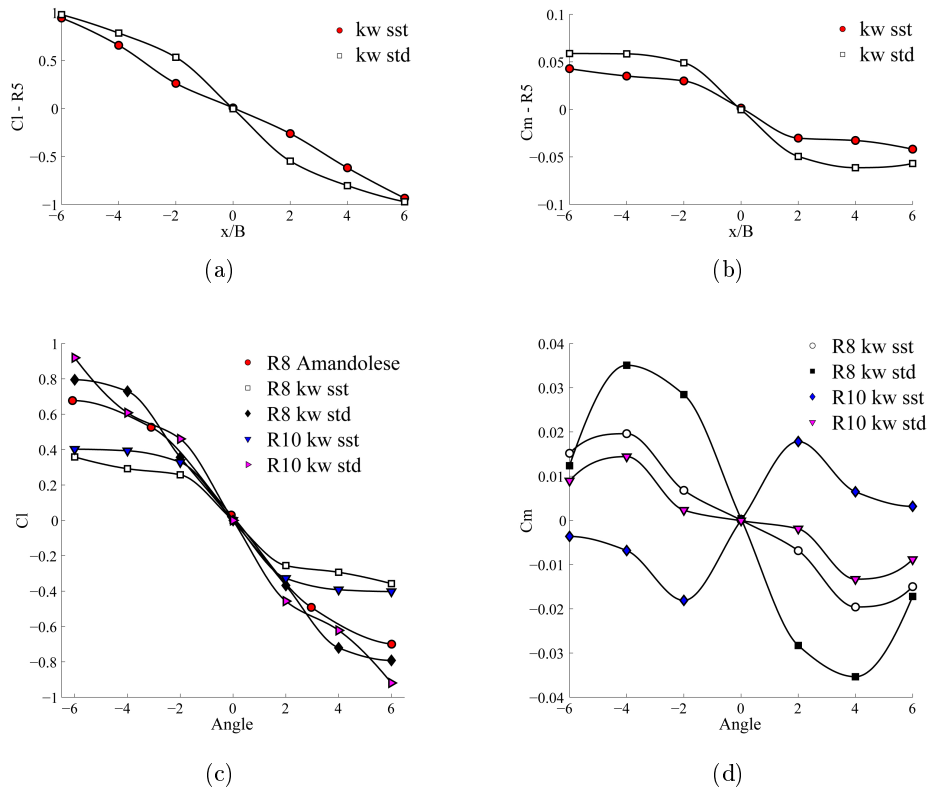


Figure 7.20: Variation of the aerodynamic coefficients with the angle of attack for  $R5$ ,  $R8$  and  $R10$ : (a)  $R5 C_l$ , (b)  $R5 C_m$ , (c)  $R8$  and  $R10 C_l$ , (d)  $R8$  and  $R10 C_m$ .

Figure 7.23 shows the motion-induced pressure distributions. The two turbulence models predict with fair agreement the amplitude of the oscillations, but the location of the peak appears to be insensitive to the reduced velocity, unlike the experimental data [75]. Finally, the phase shift reported in Figs. 7.23 (b) and (d) shows a monotonic decreasing behaviour which is not confirmed by the experimental evidences for  $R8$  and  $R10$ .

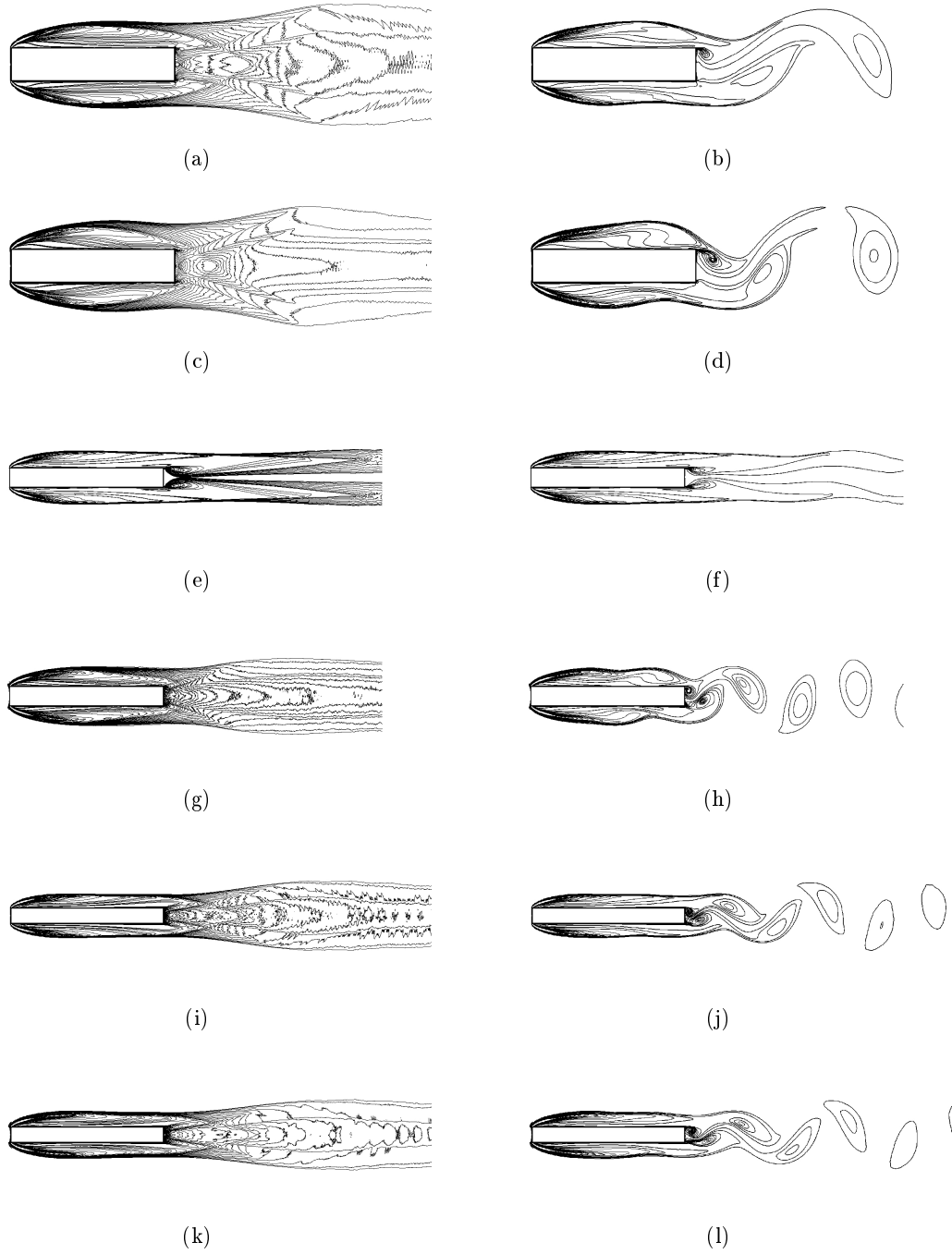


Figure 7.21: Vorticity contours for  $R5$ ,  $R8$  and  $R10$ : (a)  $R5$  time averaged  $k - \omega$  *sst*, (b)  $R5$  instantaneous  $k - \omega$  *sst*, (c)  $R5$  time averaged standard  $k - \omega$ , (d)  $R5$  instantaneous standard  $k - \omega$ , (e)  $R8$  time averaged  $k - \omega$  *sst*, (f)  $R8$  instantaneous  $k - \omega$  *sst*, (g)  $R8$  time averaged standard  $k - \omega$ , (h)  $R8$  instantaneous standard  $k - \omega$ , (i)  $R10$  time averaged  $k - \omega$  *sst*, (j)  $R10$  instantaneous  $k - \omega$  *sst*, (k)  $R10$  time averaged standard  $k - \omega$ , (l)  $R10$  instantaneous standard  $k - \omega$ .

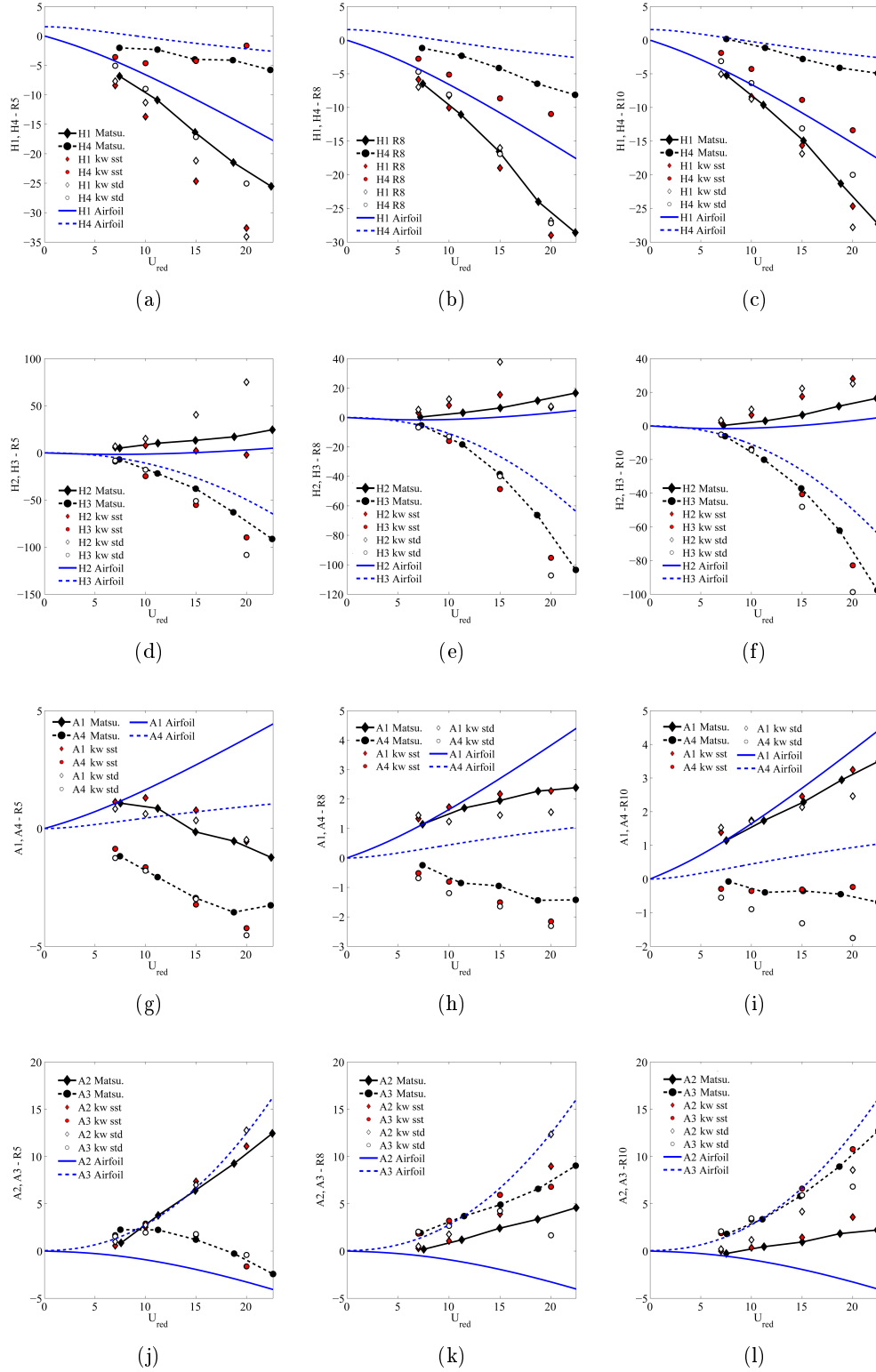


Figure 7.22: Comparison between numerical and experimental flutter derivatives for  $R5$ ,  $R8$  and  $R10$ .

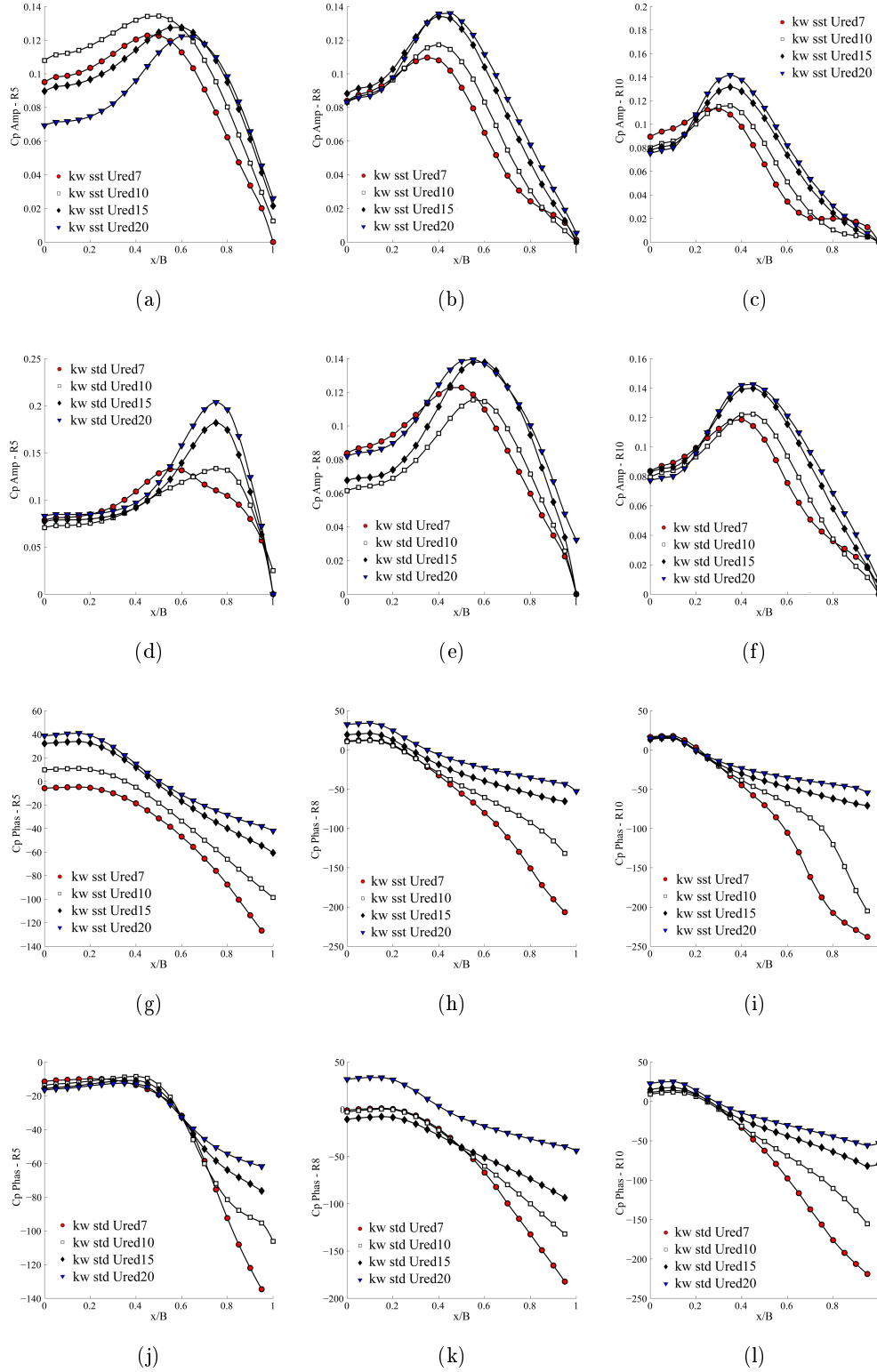


Figure 7.23: Amplitude and phase distribution of the motion induced pressure coefficient for  $R5$ ,  $R8$  and  $R10$ : (a), (b), (c) amplitudes for  $k - \omega$  sst, (d), (e), (f) amplitudes for standard  $k - \omega$ , (g), (h), (i) phases for  $k - \omega$  sst, (j), (k), (l) phases for standard  $k - \omega$ .

		$C_d$ avg	$C_d$ rms	$C_l$ rms	St	$C_{l,\alpha}$	$C_{m,\alpha}$
<i>R12p5</i>	$k - \omega$ <i>sst</i>	1.05	7.9E-3	2.9E-2	0.13	-0.20	2.3E-2
	$k - \omega$ <i>std</i>	1.11	8.6E-3	3.4E-2	0.14	-0.18	5.4E-3
<i>R15</i>	$k - \omega$ <i>sst</i>	1.13	1.3E-2	3.0E-2	0.13	-0.18	3.0E-2
	$k - \omega$ <i>std</i>	1.11	6.9E-3	1.9E-2	0.13	-0.23	2.3E-2
<i>R20</i>	$k - \omega$ <i>sst</i>	1.19	1.8E-2	3.0E-2	0.14	-0.16	3.4E-2
	$k - \omega$ <i>std</i>	1.23	1.2E-2	2.4E-2	0.14	-0.20	3.5E-2

Table 7.5: Global aerodynamic coefficients for *R12p5*, *R15* and *R20*.

### 7.5.5 *R12p5*, *R15* and *R20*

In this section the most elongated cases are presented. The pressure coefficient distributions along the upper side is given in Fig. 7.24 together with its *rms*. From such graphs it can be seen that the detachment located at the leading edge is still apparent for *R20* as the pressure appears to be recovered only at  $x/B = 0.3$ . Once again it appears that the shear layers originated at the leading edge are deeply affecting the flow field, as confirmed by the vorticity contours reported in Fig. 7.25.

The characteristic integral quantities of the flow are reported in Table 7.5. Even though the side ratio is high, the computed  $C_{l,\alpha}$  coefficient is still close to 0.2 while the theoretical value for the thin airfoil is 0.11.

Considering the flutter derivatives in Fig. 7.26 it can be noticed that the experimental values of *R20* are almost coincident with the theoretical thin airfoil case, while the computed ones still show some remarkable differences which are often coherent between the two tested turbulence models and with similar patterns to what is observed for bluffer sections. It is also interesting to notice that while the  $k - \omega$  *sst* model predicts monotonically decreasing values for  $C_{l,\alpha}$  towards the theoretical value, the standard model doesn't exhibit the same regular trend.

Figure 7.27 shows that the  $k - \omega$  *sst* model presents an inversion of the motion-induced pressures phase shift, for high reduced velocities, observed for *R12p5*, while the experimental data [75] indicate this trend already for *R8*. Such behaviour appears to be clearly visible and fully established using the  $k - \omega$  *sst* model for *R15* while, when the standard  $k - \omega$  model is used, it appears only for *R20*.

### 7.5.6 Critical flutter wind speed evaluation

Based on the above remarks, it can be deduced that the two-dimensional simulations performed using RANS turbulence models tend to overestimate the role played by the shear layers and, indeed, the bluntness of the bodies. This is revealed by the occurrence of critical states (like barycentric position of the aerodynamic centre, inversion in the phase shift of the motion-induced pressures along the side and coherence with the airfoil theory) for higher side ratios in the numerical simulations, if compared to the experimental data.

In order to provide a quantification of such effects, the stability of a test structure is investigated and the critical flutter speed determined using both the experimental and

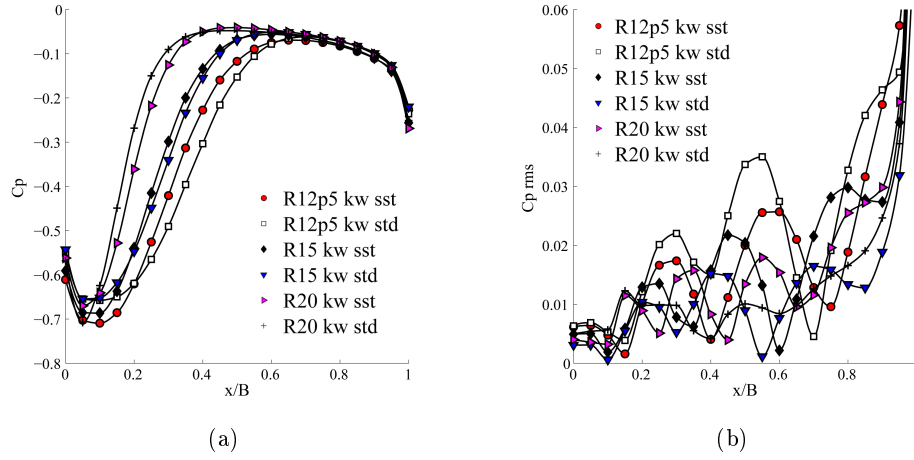


Figure 7.24: Pressure coefficient distribution along the upper side of *R12p5*, *R15* and *R20* at zero angle of attack: (a) time averaged, (b) *rms*.

$\rho$ [ $kg/m^3$ ]	B [ $m$ ]	Mass [ $kg/m$ ]	Inertia [ $kg \cdot m$ ]
1.225	30.0	5.0E4	1.0E7
$Fq_h$ [ $Hz$ ]	$Fq_\alpha$ [ $Hz$ ]	$\xi_h$ [%]	$\xi_\alpha$ [%]
0.1	0.3	0.3	0.3

Table 7.6: Data of the structure used in critical flutter speed calculation.

the numerical flutter derivatives. The characteristics of such structure are reported in Tab. 8.2 and they are chosen such that the critical wind speed always occurs in the range of investigated reduced velocities.

The comparison between the critical flutter speeds obtained with experimental and numerical flutter derivatives, reported in Tab. 7.7, confirms that the latter ones, lead to unfavourable aerodynamic conditions and, indeed, to flutter wind speeds systematically lower than the expected ones, at least in these cases.

## 7.6 Conclusions on rectangular prisms

The aerodynamic behaviour of a wide selection of rectangular prisms have been simulated using a two-dimensional RANS approach in both static and dynamic conditions. The integral flow quantities, the pressure distributions, the flutter derivatives and the

	<i>R12p5</i>	<i>R15</i>	<i>R20</i>
Exp. [75]	110	130	140
$k - \omega$ <i>sst</i>	80	106	123
$k - \omega$ <i>std</i>	68	90	120

Table 7.7: Comparison between critical flutter speed in [ $m/s$ ].

motion-induced pressure distributions obtained with both the  $k-\omega$  *sst* and the standard  $k-\omega$  turbulence models are presented and discussed.

Although the  $k-\omega$  *sst* model often appears to over damp the unsteady flow structures, it proves to be generally more reliable than the standard  $k-\omega$  model, even when the pressure distributions at zero angle of attack is better predicted by the standard model. Such aspect is critical as it shows that global fitting of available results in fixed conditions does not lead automatically to better predictions in other configurations. Indeed, it seems preferable to use a  $k-\omega$  *sst* model as it generally proved to be more robust with respect to variations in the studied configuration.

In general, for high aspect ratios, involving an upstream position of the aerodynamic centre, it is possible to state that the simulations tend to emphasize the bluff feature of the body. Such observation has been confirmed by calculating the flutter wind velocity using the experimental and the numerical flutter derivatives for a test section: numerical flutter derivatives tend to systematically underestimate the critical speed thus being on the safe side.

Figure 7.28 depicts a visual comparison between the results obtained using LES simulations [90] in smooth and turbulent flow together with the RANS simulation (standard  $k-\omega$ ) for  $R2$ . It appears that the shear layers produced at the leading edge, which are the main feature of the investigated flows, are unnaturally stable and coherent in the RANS simulations.

Indeed, this is caused by the high viscosity generated by the RANS model which suppresses the amplification of small disturbances in the shear layers caused by Kelvin-Helmholtz and other shear layer instabilities.

Such flow instabilities are the source of a considerable amount of large and medium scale vortical structures and are responsible for a considerable amount of the turbulence length scales observed around bluff bodies at high  $Re$  number [108, 109].

The fact that small disturbances can be amplified in shear layers is common knowledge but unfortunately such phenomenon is in no way taken into account by currently available RANS turbulence models which are deduced for statistically stationary and isotropic turbulence. The fact that energy might be transferred from the subgrid model to the resolved scales is known as backscatter in the LES approach and it plays a crucial role in the definition of the flow around bluff bodies especially if the turbulence model suppress all the main shear layer instabilities.

When RANS approaches are used, the suppression of such flow feature can drastically change the extent and coherence of shear layers so leading to inaccurate or even unnatural results.

In addition to this, the simulated vortical structures, produced by global instability mechanisms, appear to be extremely stable, their mutual interaction is unnatural and the energy cascade is reduced to the dissipation introduced by the turbulence model. Unfortunately, it appears that such unnaturally stable recirculation zones can deform the average flow field so leading to inaccurate results even for time averaged flow quantities.

This aspect can be highlighted by referring to the local pressure distributions (in terms of the time-averaged amplitude of the motion-induced  $C_p$ ) over rectangular sections with different aspect ratios, and in particular by comparing the experimental data proposed by [75] with proposed numerical results obtained via the  $k-\omega$  *sst* model. In detail, Fig. 7.29 shows that, for  $U_{red} \simeq 20$ , the experimentally-based time-averaged pres-

sure peaks increase in value and move towards the leading edge when the section's aspect ratio increases. Such an evidence is reasonably described by numerical results, but a certain offset of the pressure peaks towards the trailing edge and a not so sharp pattern with respect to the experimental data are obtained, revealing a clear deterioration effect in the solution accuracy.

RANS-based results show also that the predictions of aeroelastic stability performances are generally unfavorable with respect to the experimental observations. This evidence is in agreement with the fact that usually the aeroelastic performances of bridge decks are found more stable under turbulent approaching flows. In this case, in fact, the intrinsic turbulence tends to decrease the stability of the main flow, due to the amplification of the local instability paths of the shear layers, as it has been experimentally highlighted also by [110].

In this view, the possibility to effectively describe the influence of the incoming turbulence, as well as three-dimensionality effects, is extremely limited when RANS approaches are employed. On the contrary, techniques based on Scale Resolving Simulations [29] can be retained to be more promising, since they enable to take into account for the main instabilities affecting the shear layers. In conclusion, although two-equations RANS turbulence models suffer from significant limitations in simulating strongly separated flows in comparison with other (more time-consuming) numerical approaches, proposed results reveal that RANS simulations, based on the standard  $k - \omega$  model and on the  $k - \omega$  *sst* model, can give almost reasonable results with relatively low computational time and effort, especially when applied to evaluate flutter derivatives of elongated cross-sections. In this context, proposed results can be retained a contribution for designers and technical engineers that aim to estimate, by using numerical methods and in the early design stages, flutter derivatives and aeroelastic stability performances of bridge decks.



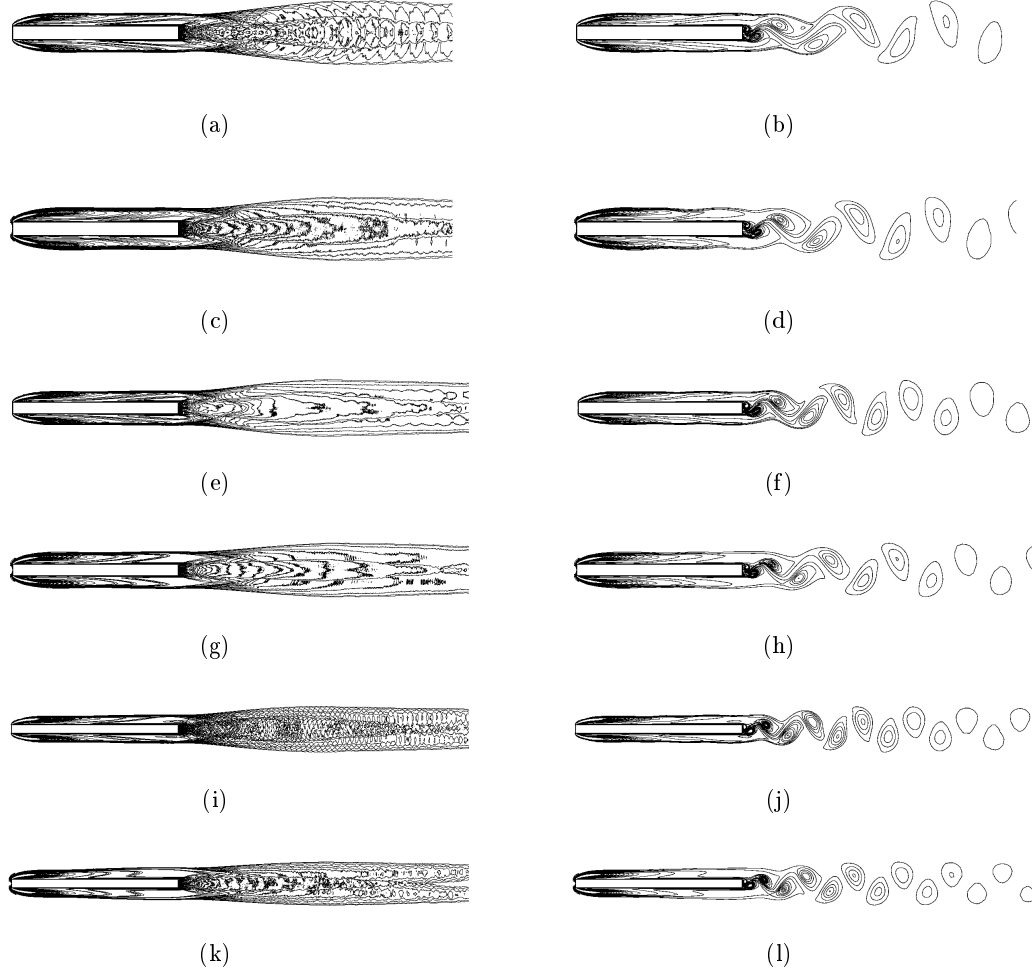


Figure 7.25: Vorticity contours for  $R12p5$ ,  $R15$  and  $R20$ : (a)  $R12p5$  time averaged  $k - \omega$  *sst*, (b)  $R12p5$  instantaneous  $k - \omega$  *sst*, (c)  $R12p5$  time averaged standard  $k - \omega$ , (d)  $R12p5$  instantaneous standard  $k - \omega$ , (e)  $R15$  time averaged  $k - \omega$  *sst*, (f)  $R15$  instantaneous  $k - \omega$  *sst*, (g)  $R15$  time averaged standard  $k - \omega$ , (h)  $R15$  instantaneous standard  $k - \omega$ , (i)  $R20$  time averaged  $k - \omega$  *sst*, (j)  $R20$  instantaneous  $k - \omega$  *sst*, (k)  $R20$  time averaged standard  $k - \omega$ , (l)  $R20$  instantaneous standard  $k - \omega$ .

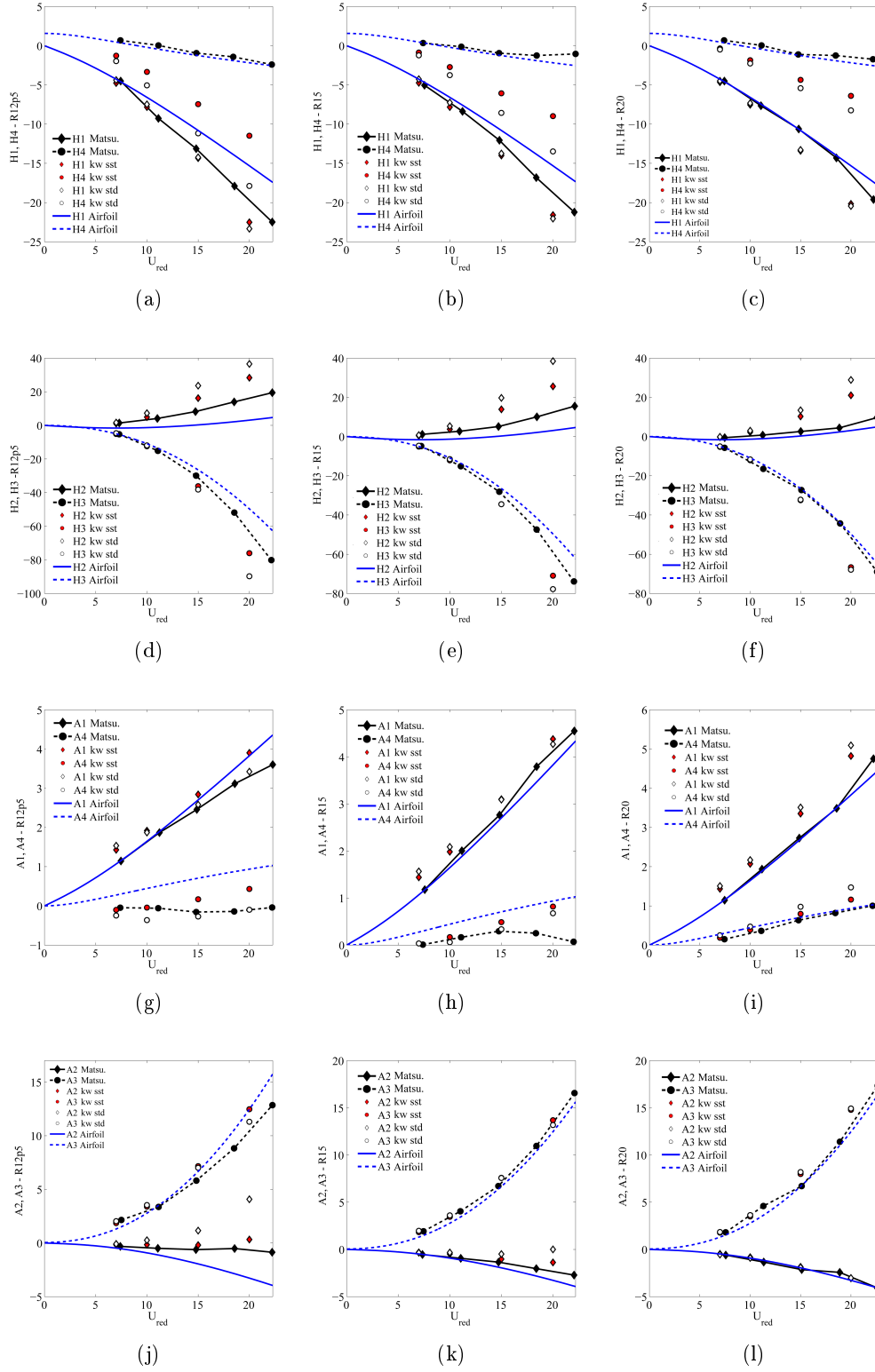


Figure 7.26: Comparison between numerical and experimental flutter derivatives for  $R12p5$ ,  $R15$  and  $R20$ .

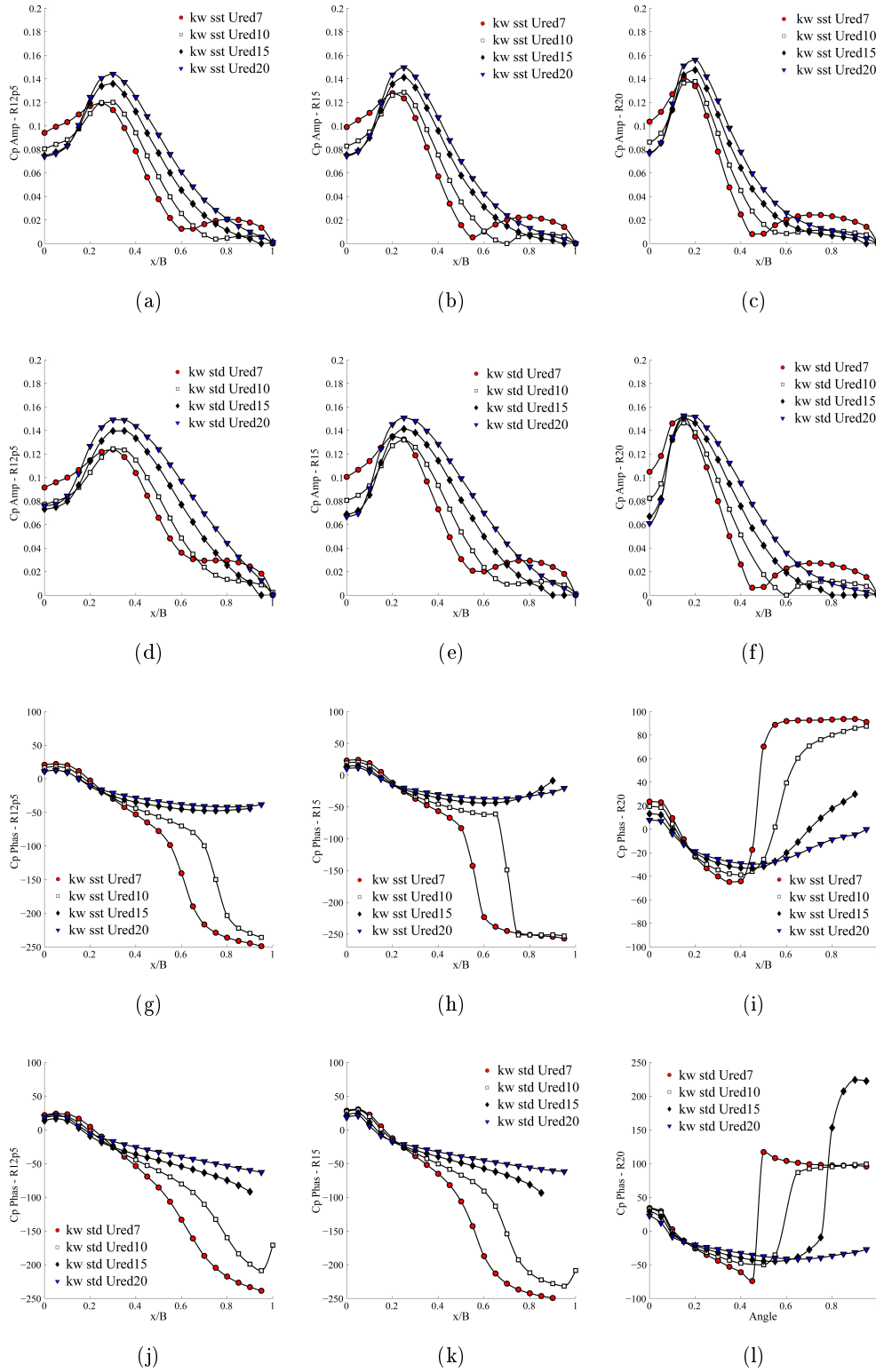


Figure 7.27: Amplitude and phase distribution of the motion induced pressure coefficient for  $R12p5$ ,  $R15$  and  $R20$ : (a), (b), (c) amplitudes for  $k - \omega$  sst, (d), (e), (f) amplitudes for standard  $k - \omega$ , (g), (h), (i) phases for  $k - \omega$  sst, (j), (k), (l) phases for standard  $k - \omega$ .

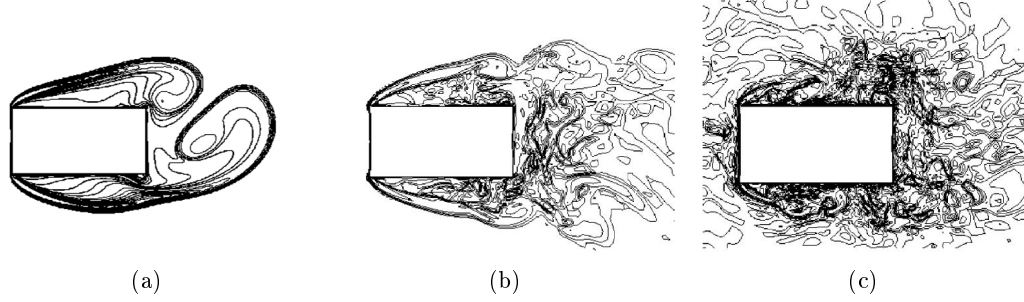


Figure 7.28: Comparison of vorticity contours between (a) RANS, (b) LES with smooth inlet condition and (c) LES with turbulent inlet condition [90] for  $R2$  in fixed condition.

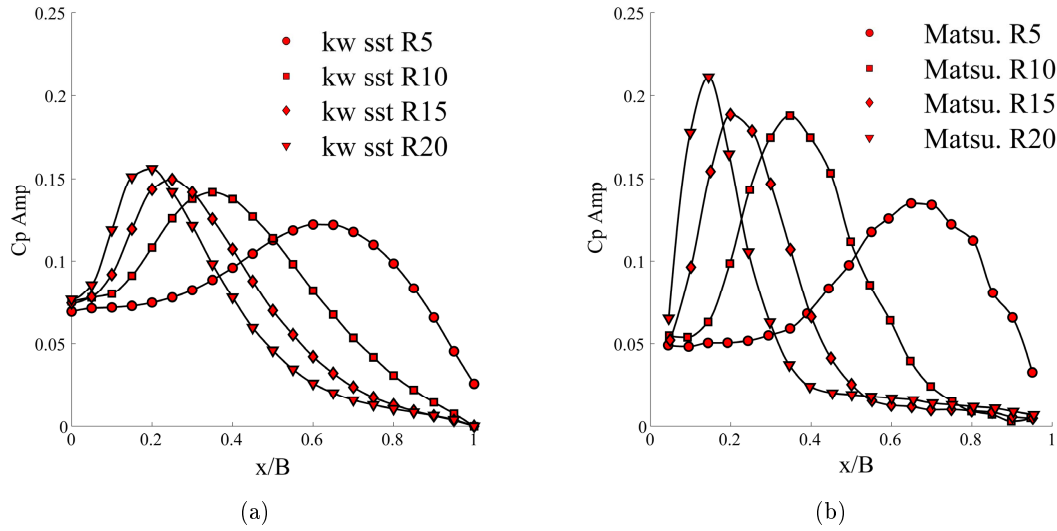


Figure 7.29: Forced angular vibrations of R5, R10, R15 and R20. Sinusoidal angular motion of the section, with an amplitude of 1 degree. (a) Computed distributions of motion-induced mean values of the amplitude for the pressure coefficient  $C_p$  along the upper side of the section, for  $U_{red} = 20$  and considering the  $k - \omega$  *sst* model. (b) Experimental data by [75] ( $U_{red} = 22$ ).



## Chapter 8

# Flutter derivatives extraction: bridge decks

In this chapter the robustness of standard computational fluid dynamics techniques and turbulence models in predicting flutter derivatives and critical flutter wind speed for streamlined and bluff deck sections is tested. In the simple cases presented in the previous chapter (rectangular prisms), remarkable biases were observed between numerical and experimental results. In this chapter the ability of the  $k - \omega$  *sst* turbulence model in assessing the critical flutter speed of various deck typologies is analysed. Each case has been selected in order to test and discuss particular aspects of the simulation strategy and the results interpretation. Systematic comparison with experimental data is provided.

### Contents

---

<b>8.1</b>	<b>Introduction</b>	<b>159</b>
<b>8.2</b>	<b>Investigation results</b>	<b>161</b>
8.2.1	R8	162
8.2.2	Severn	164
8.2.3	Gibraltar	165
8.2.4	Chongqing	167
8.2.5	Tacoma	175
8.2.6	Adige	180
<b>8.3</b>	<b>Conclusions on bridge decks</b>	<b>182</b>

---

### 8.1 Introduction

Based on the results presented in the previous chapter, only the  $k - \omega$  *sst* model has been here tested so also avoiding the problems often encountered in the calibration of the inlet parameters. In fact it is well known that the  $k - \omega$  *sst* model is rather stable with respect to their variation which is indeed a positive feature when no previously obtained experimental data are available.

The  $Re$  number, in the case of bluff bodies with sharp corners, mainly characterizes the stability conditions of shear layers with respect to disturbances. Commonly adopted RANS turbulence models always damp the small flow scales out and account for their effect on the mean flow thanks to the concept of turbulent viscosity. In reality, such small scales can be eventually amplified and effectively decrease the coherence of the shear layers. As a consequence, the shear layer rolling-up is often not accurately described [111] so also compromising the accuracy of the mean flow as it will be later shown.

It is usually observed, both in experiments and in numerical simulations, that the effect of the  $Re$  number is highly non-linear and leads to sudden jumps of the system state between different configurations. Considering that RANS based simulations are expected to account for the  $Re$  number only approximately, it is of interest to verify the system stability with respect to the  $Re$  number for multiple reasons. In fact, on one side, high sensitivity of the simulation results on such parameter might warn that multiple state of the system are possible and that numerical simulations might be unable to correctly select the real one. On the other side, it is interesting to study the dependence of the flow field on the  $Re$  number because its variation might cure some biases introduced by the turbulence model as it will be later shown.

In the following, numerical results will be shown both for  $Re = 1.5E5$  and  $Re = 37.5E5$ . Such variation should not be interpreted only in analogy to a  $Re$  number variation in experiments. Instead, it should be considered as a drastic change in the whole simulation strategy because, from the numerical point of view, it implies a completely different treatment of the boundary layer representation. In fact, the mesh has been kept constant in the two cases so that, for  $Re = 1.5E5$ , the non-dimensional wall distance  $y_{max}^+ \simeq 5.0$  allows direct integration through the boundary layer while, for  $Re = 37.5E5$ ,  $y_{max}^+ \simeq 125.0$  so that wall functions are used (enhanced wall treatment in [51]). Indeed, the two approaches are not directly comparable so that differences between the two simulation strategies should be interpreted as the results of both the  $Re$  number and the wall treatment variation.

From the practical point of view, it should be observed that the simulation time is a function of the mesh only and it is not directly affected by the  $Re$  number. In this context, the two adopted approaches represent the choice that the practitioner engineer have to face in order to keep the simulation time to a reasonable level. Additionally, it is observed that, when sharp corners define the separation point, the role played by the boundary layer in the flow definition might be negligible so affecting the results only marginally.

Summing up, in the following, the  $Re$  number variation has to be seen as a variation of the whole simulation strategy which reflects the choices that practitioners have to face when modelling such flows. From a scientific prospective, this analysis does not intend to study the real variation of the flow field with the  $Re$  number which would be probably misleading using a RANS approach in transcritical conditions. More significantly, the stability of the simulation results with respect to the numerical approach is studied especially because the supercritical condition, which is the operational range for real bridges, is a stable condition with respect to the  $Re$  number and indeed the turbulence production and dissipation.

	$S$	$M$	$E$
Amplitude $\alpha$	$2^\circ$	$5^\circ$	$3^\circ$
Amplitude $h$	$0.01B$	$0.02B$	$0.05B$

Table 8.1: Amplitudes of the forced vibration used for the flutter derivatives extraction.

## 8.2 Investigation results

In the following the numerical results of the present investigation are presented and compared to available experimental data. In particular, the excellent database provided in [37] was taken as reference for all the considered cases, Adige bridge excluded. The flow topology has been represented by vorticity contours. Both the variation of the aerodynamic coefficient with the attack angle and the flutter derivatives have been reported and compared to the experimental ones at different  $Re$  numbers.

It is here observed that the database provided in [37] is particularly attractive for comparison with numerical results. In particular, in that study, all analysed decks are considered without secondary elements, the experimental procedure is clearly explained reporting the motion amplitudes used for the flutter derivative extraction (Forced Vibrations where used) and the  $Re$  number. Additionally, experiments were performed in a water channel so that no translation of the flutter derivative origin is expected due to cancellation of the inertial terms [48] so providing an ideal database for comparison with numerical results.

The amplitude of the forced vibrations used to extract the flutter derivatives have been selected according to the experimental tests as reported in Tab. 8.1. In the following, for the sake of brevity, results mainly extracted with  $M$  amplitudes and  $Re = 2.0E5$  will be shown for flutter derivatives, aiming at reporting the experimental results obtained in the middle range of the available experiments. When discrepancies between numerical and experimental results are analyzed plotting all available data, the experimental  $Re$  and motion amplitudes do not suffice in explaining such differences so that such choice is still justified. It is here also noticed that the motion amplitudes used in the experimental tests appear to be large for rotations and small for heaving. In the author experience a more balanced conditions can be obtained with the amplitudes reported as  $E$  in Tab. 8.1. Nevertheless, in the following, compatibility with the experiments is preserved and only  $S$  and  $M$  settings were actually used.

Considering the Adige bridge, no information was available regarding the variation of the aerodynamic coefficients and flutter derivatives with the  $Re$  number. Nevertheless, the case has been considered in order to test the ability of the model to account for the presence of barriers and to catch the dependence of the flutter derivatives with the average attack angle (the amplitudes of the forced vibrations were unknown and the setting  $M$  have been used).

Finally, with the aim of assessing the usefulness of such procedures in technical applications, the critical flutter speed was calculated for a set of test structures. Such structures have been defined in order to explore various flutter conditions characterized by increasing critical reduced velocity  $U_{red}$ . This has been obtained by considering fixed mass matrix, frequency and damping ratios (reported in Tab. 8.2) and allow the deck



$\rho$ [ $kg/m^3$ ]	Mass [ $kg/m$ ]	Inertia [ $kg \cdot m$ ]
1.225	5.0E4	1.0E7
$Fq_h$ [ $Hz$ ]	$Fq_\alpha$ [ $Hz$ ]	$\xi_h = \xi_\alpha$ [%]
0.1	0.4	1.0

Table 8.2: Data of the structures used in critical flutter speed calculation.

	Str. 1	Str. 2	Str. 3	Str. 4
$B$ [ $m$ ]	30	40	50	60

Table 8.3: Deck along wind length  $B$  for the considered structures.

characteristic length to vary as reported in Tab. 8.3. The flutter analysis have been performed following the procedure described in [52].

The critical flutter wind speed for the considered test structures has been firstly calculated using the Theodorsen flutter derivatives, valid for flat plate of vanishing thickness (namely airfoil) vibrating in an inviscid flow and are reported in Tab. 8.4 for comparison.

In order to avoid extrapolation of the flutter derivatives, the critical flutter speed has been reported only when it fell in the available data range. In the following, when the critical speed is not observed for  $U_{red}$  smaller than the first available one, the symbol  $\otimes$  will be used while, when it is observed for high values of  $U_{red}$ , which would need extrapolation, the symbol  $-$  is reported.

The geometries of the considered decks are reported in Fig. 8.1, for further details reference is made to [37].

### 8.2.1 R8

The vorticity contours of the simulated flows for the case of R8 are depicted in Figs. 8.3 and 8.4. It appears that the  $Re$  number has very little impact on the flow topology at zero attack angle but increasing differences can be observed when higher angles are considered. Such differences cause a shifting of the pressure distribution along the side where the recirculation is observed while the other side is not sensibly affected as reported in Fig. 8.2. Indeed, this stresses the primary role played by the leading edge detachment point in the definition of the aerodynamic characteristics around the whole body.

The drag coefficient variation with the attack angle, reported in Fig. 8.5 (a), is in extremely good agreement with experimental results while the lift coefficient variation is in reasonable agreement for small attack angles but the stall condition is not captured

	Str. 1		Str. 2		Str. 3		Str. 4	
	$U$	$U_{red}$	$U$	$U_{red}$	$U$	$U_{red}$	$U$	$U_{red}$
Airfoil	192	20.5	162	13.6	143	10.0	130	7.8

Table 8.4: Critical flutter speed for the test structures considering Theodorsen flutter derivatives [ $m/s$ ].

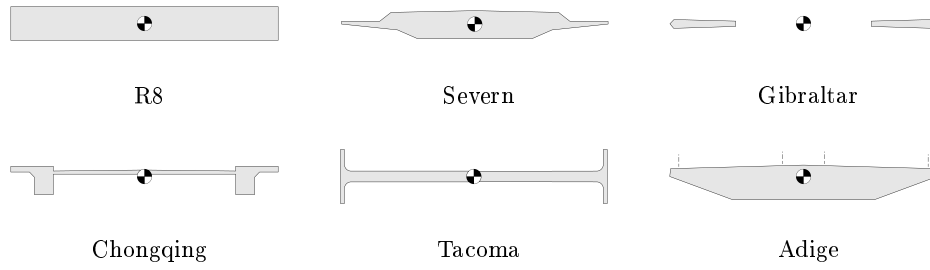


Figure 8.1: Geometry of the considered decks.

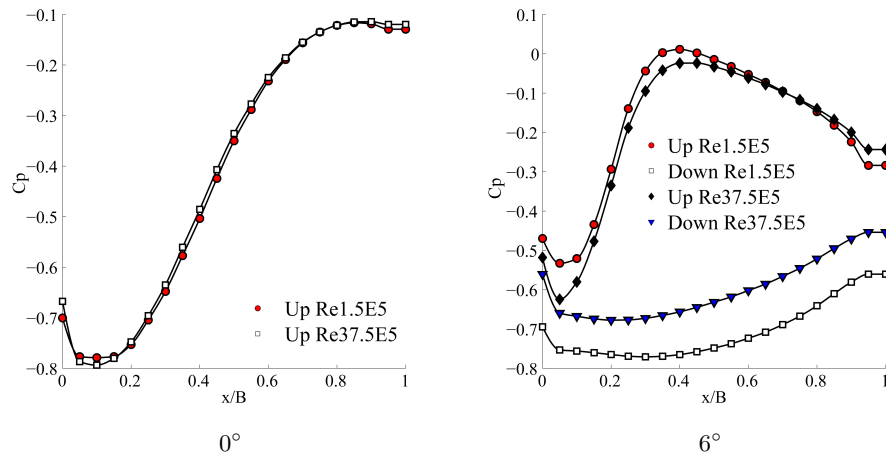


Figure 8.2: Variation of the time averaged pressure coefficient distribution with the attack angle.

correctly Fig. 8.5 (b). The pitching moment appears to be not accurate and the two simulated  $Re$  number provide opposite sign for the coefficient variation Fig. 8.5 (c). This is due to the fact that the considered aspect ratio has an almost symmetric aerodynamic centre so that its position can lead to positive or negative pitching moment when different  $Re$  numbers are considered.

Flutter derivatives in this case appear to be not accurate especially with respect to the  $A_i^*$  terms which are directly influenced by the derivative of the pitching moment coefficient (see Fig. 8.6). In general, in this case the critical flutter speed is sensibly underestimated. This is indeed expected as the aerodynamic centre appears to be centrally located making the section prone to torsional instability. Interestingly, although in static conditions opposite sign are observed for the pitching moment derivative, flutter derivatives are in good agreement between the two tested simulation strategies and appear to be on the safe side as already observed in [111].

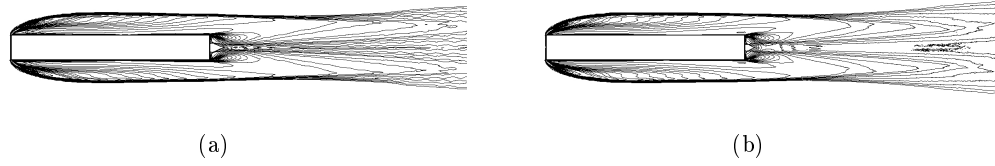


Figure 8.3: Time averaged vorticity contours for R8 at zero attack angle: (a)  $Re = 1.5E5$ , (b)  $Re = 37.5E5$ .

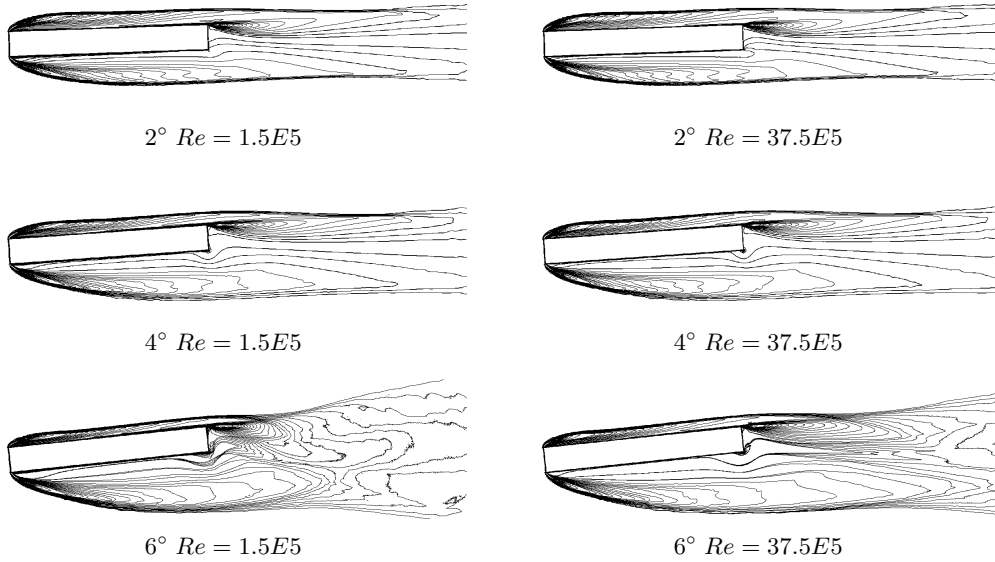


Figure 8.4: Time averaged vorticity contours for R8 at varying attack angle.

### 8.2.2 Severn

The bare deck of the Severn bridge is characterized by a well streamlined cross section. The numerical solution does not develop vortex shedding neither at  $Re = 1.5E5$  nor at  $Re = 37.5E5$  for all the considered attack angles. The flow topology is not visibly affected by the simulation Reynolds number as shown in Fig. 8.7. Such behaviour is observed for all the considered attack angles so that in Fig. 8.8 only the vorticity contours for  $Re = 1.5E5$  are reported in order to characterize the flow topology.

The flow is well attached and experimental and numerical data are in very good agreement as shown in Fig. 8.9. A significant shift in the drag coefficient is observed but, without experimental pressure measurements, it is not possible to individuate the cause of this shift.

The results in this case are accurate and, indeed, the absence of marked unsteady phenomena and the independence of the flow topology with respect to the  $Re$  number indicate that the RANS approach is suitable for such flow.

Considering the experimental flutter derivatives, minor changes are observed between the set extracted considering small, medium and large displacements and no significant

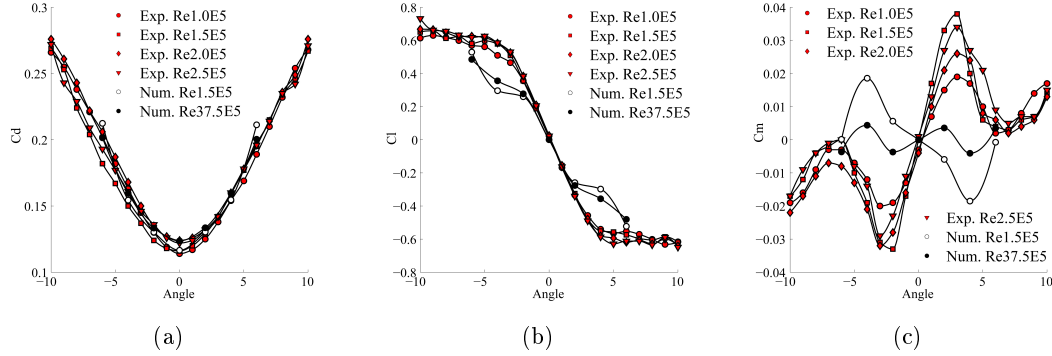


Figure 8.5: Variation of the aerodynamic coefficients with the attack angle for R8: (a) drag, (b) lift, (c) pitching moment coefficients.

	Str. 1		Str. 2		Str. 3		Str. 4	
	$U$	$U_{red}$	$U$	$U_{red}$	$U$	$U_{red}$	$U$	$U_{red}$
Exp. $Re2.0E5 M$	129	11.7	116	8.3	109	6.7	104	5.7
Num. $Re1.5E5 M$	80	6.9	83	5.7	87	5.2	87	4.9
Num. $Re37.5E5 M$	88	7.8	92	6.4	94	5.7	93	5.2

Table 8.5: Comparison between critical flutter speed for R8 in  $[m/s]$ .

effect of the  $Re$  number is experimentally observed. The numerically extracted flutter derivatives are in fair agreement with the experimental results but some biases are observed which have the same direction for both the  $Re$  numbers considered in simulations. Despite such differences, the flutter critical speed calculated with experimental and numerically obtained flutter derivatives is in very good agreement with differences always smaller than 10% and always on the safe side.

### 8.2.3 Gibraltar

The Gibraltar bridge deck has been analysed in order to include in the investigation a twin deck geometry. The flow topology, depicted in Fig. 8.11, shows the strong interaction between the upstream and the downstream deck. The variation of the flow topology with the attack angle is reported in Fig. 8.12. Very good agreement is observed between experimental and numerical results to what it concerns the drag and the lift

	Str. 1		Str. 2		Str. 3		Str. 4	
	$U$	$U_{red}$	$U$	$U_{red}$	$U$	$U_{red}$	$U$	$U_{red}$
Exp. $Re2.0E5 M$	-	-	164	14.0	142	10.0	127	7.7
Num. $Re1.5E5 M$	-	-	154	13.0	137	9.8	124	7.8
Num. $Re37.5E5 M$	-	-	151	12.8	135	9.6	122	7.6

Table 8.6: Comparison between critical flutter speed for Severn bridge in  $[m/s]$ .

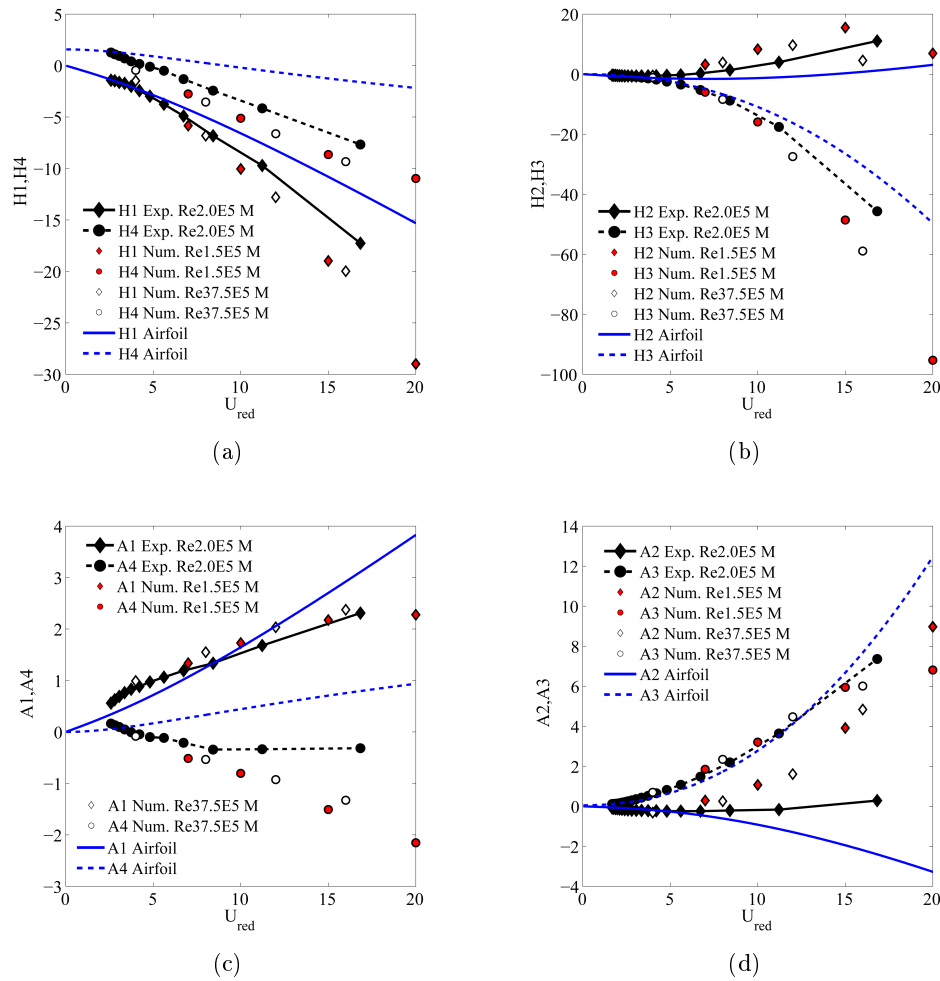


Figure 8.6: Comparison between experimental and numerical flutter derivatives for R8.

coefficients (Fig. 8.13) while the pitching moment does not appear to be accurate. In the experimental results a significant value of the pitching moment is observed at null incidence angle which is not observed in numerical simulations (it was not possible to verify from available experimental data if this is a bias of the experimental procedure or a difference in the flow organization). Nevertheless, it is observed that the pitching moment derivative with the attack angle is in very good agreement with experimental results especially for  $Re = 37.5E5$  at small attack angles.

Considering flutter derivatives, in this case, some dependence of the results with the motion amplitude and with the  $Re$  number is found in the experimental data but such variations do not explain the biases observed in the numerical results. The airfoil flutter derivatives are reported for comparison even though, obviously, major differences are observed as such analytical solution is not representative of twin decks. The overall agreement is good for all terms apart from  $A_2^*$  and  $A_3^*$ . Such condition is indeed expected considering the differences in the pitching moment variation depicted in Fig. 8.13 (c).

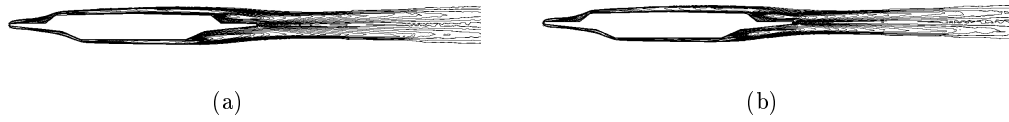


Figure 8.7: Time averaged vorticity contours for Severn bridge at zero attack angle: (a)  $Re = 1.5E5$ , (b)  $Re = 37.5E5$ .

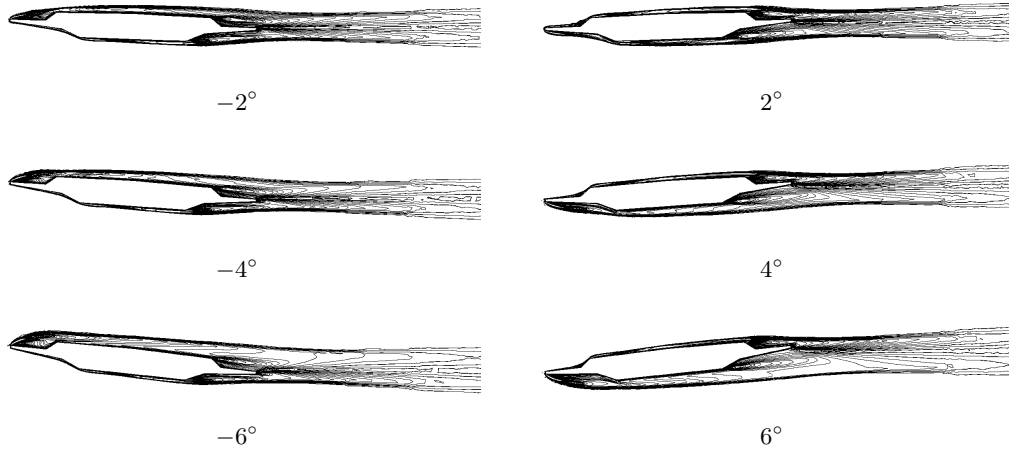


Figure 8.8: Time averaged vorticity contours for Severn bridge at varying attack angle  $Re = 1.5E5$ .

Nevertheless, once again, when the critical flutter speed is calculated, the experimental flutter derivatives leads to instability only for Str. 4 while, using the numerical results, instability is observed also for other test structures. The best accordance, in this case, is obtained for  $Re = 37.5E5$  which led to the best agreement with experimental results in static conditions, but, as it will be later shown, such behaviour should not be generalized.

#### 8.2.4 Chongqing

Such deck has been analysed aiming at including in the simulations a geometry with poor aerodynamic performances. In particular, wide recirculation zones are formed as a consequence of a poor aerodynamic design and non-symmetric conditions between the

	Str. 1		Str. 2		Str. 3		Str. 4	
	$U$	$U_{red}$	$U$	$U_{red}$	$U$	$U_{red}$	$U$	$U_{red}$
Exp. $Re2.0E5$ $M$	-	-	-	-	-	-	227	14.1
Num. $Re1.5E5$ $M$	154	12.9	161	10.3	175	9.3	182	8.6
Num. $Re37.5E5$ $M$	-	-	210	13.8	212	11.9	199	10.6

Table 8.7: Comparison between critical flutter speed for Gibraltar bridge in  $[m/s]$ .

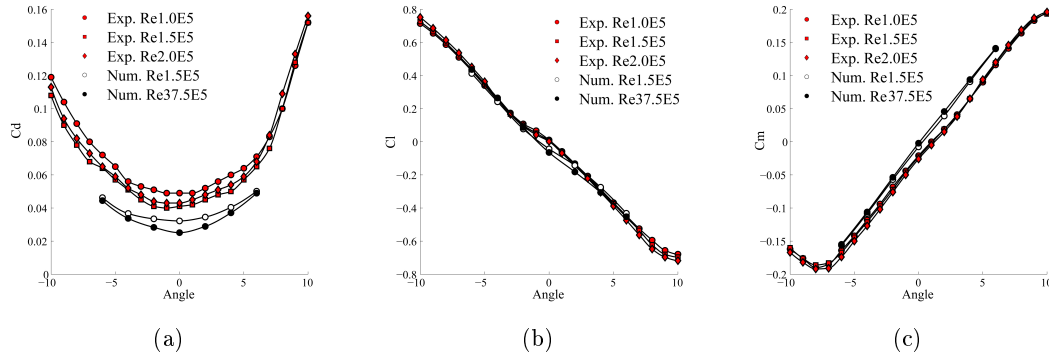


Figure 8.9: Variation of the aerodynamic coefficients with the attack angle for Severn bridge: (a) drag, (b) lift, (c) pitching moment coefficients.

upper and bottom side of the deck increase the flow complexity.

As a first observation, it is noticed that, in this case, the simulation  $Re$  number/simulation strategy has a remarkable effect on the simulated flow organization. In particular, when  $Re = 1.5E5$  is considered, a vortex of considerable dimensions develop on the bottom side just downstream the upstream detachment point (Fig. 8.15 (c) and (d)). Such vortex appear to be extremely stable and grows until it detaches and it is transported downstream. Then, it interacts and it is deformed by the downstream part of the deck and, finally, it is shed in the wake. Unfortunately, in the database [37], no information is provided with respect to the vortex shedding mechanism. Nevertheless, the described vortex appears to grow considerably, probably in a non-physical way, thanks to the artificial stability provided by the turbulence model.

At this point, it is useful to consider the results obtained for  $Re = 37.5E5$ . The flow, in this case, is stable and does not develop any instability at null attack angle due to the extremely high turbulent viscosity provided by the turbulence model (the turbulent viscosity ratio  $\mu_t/\mu \simeq 100$  for  $Re = 1.5E5$  while it increases of one order of magnitude for  $Re = 37.5E5$ ). The comparison between the time averaged vorticity contours for the two cases is reported in Fig. 8.15 (a) and (b).

Surprisingly, looking at the aerodynamic coefficients variation with the attack angle reported in Fig. 8.17, the results obtained with  $Re = 37.5E5$  appear to accurately reproduce all the static experimental results while  $Re = 1.5E5$  is not accurate. It appears that the average flow field, in the case of  $Re = 1.5E5$ , is deformed by the vortex which develop at the leading edge so compromising also the average flow pattern as depicted in Fig. 8.16.

Considering the experimental flutter derivatives, no major differences are observed within the analysed  $Re$  number range while some dependence with the motion amplitude is recorded so that both  $S$  and  $M$  displacements are reported. Indeed, the main trends of the flutter derivatives are captured by both models and the calculated critical flutter speed reported in Tab. 8.8 are in very good agreement with experimental data. It is noticed that results are again mainly on the safe side and that, surprisingly,  $Re = 1.5E5$  provides closer agreement with experimental results, especially for high  $U_{red}$  despite its poor predictions in static conditions.

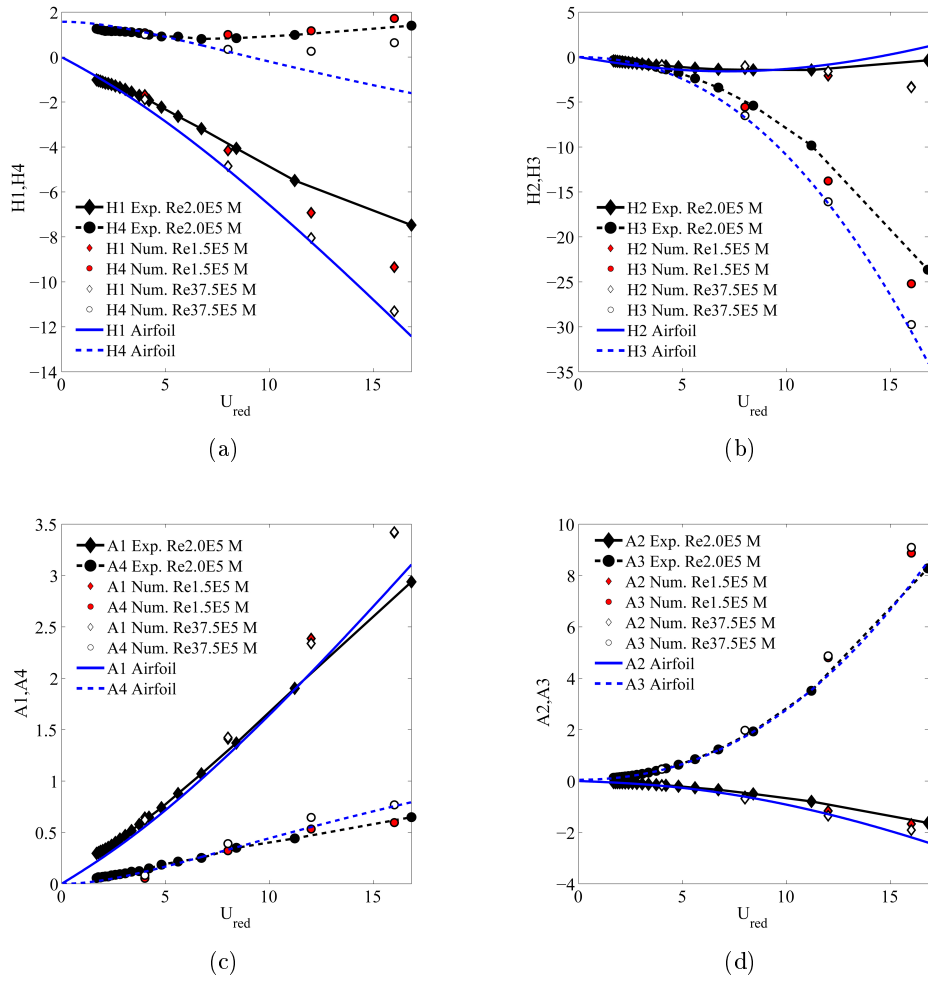


Figure 8.10: Comparison between experimental and numerical flutter derivatives for Severn bridge.



Figure 8.11: Time averaged vorticity contours for Gibraltar bridge at zero attack angle: (a)  $Re = 1.5E5$ , (b)  $Re = 37.5E5$ .



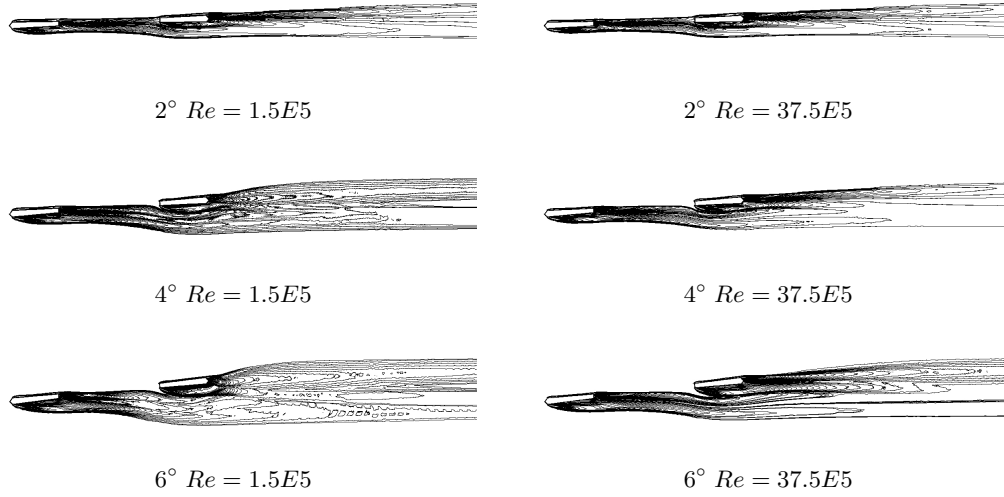


Figure 8.12: Time averaged vorticity contours for Gibraltar bridge at varying attack angle.

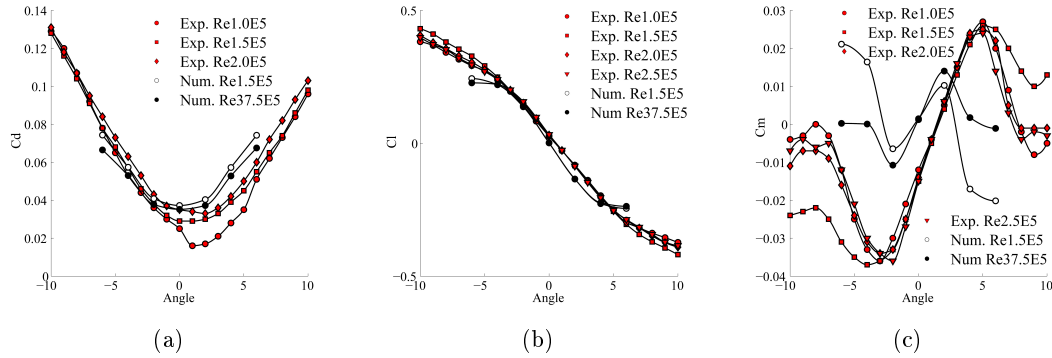


Figure 8.13: Variation of the aerodynamic coefficients with the attack angle for Gibraltar bridge: (a) drag, (b) lift, (c) pitching moment coefficients.

	Str. 1		Str. 2		Str. 3		Str. 4	
	$U$	$U_{red}$	$U$	$U_{red}$	$U$	$U_{red}$	$U$	$U_{red}$
Exp. $Re2.0E5$ $M$	113	9.8	105	7.1	97	5.8	92	4.5
Num. $Re1.5E5$ $M$	109	9.4	100	6.2	95	5.2	90	4.4
Num. $Re37.5E5$ $M$	98	8.1	93	6.2	95	5.2	95	4.6

Table 8.8: Comparison between critical flutter speed for Chongqing bridge in  $[m/s]$ .

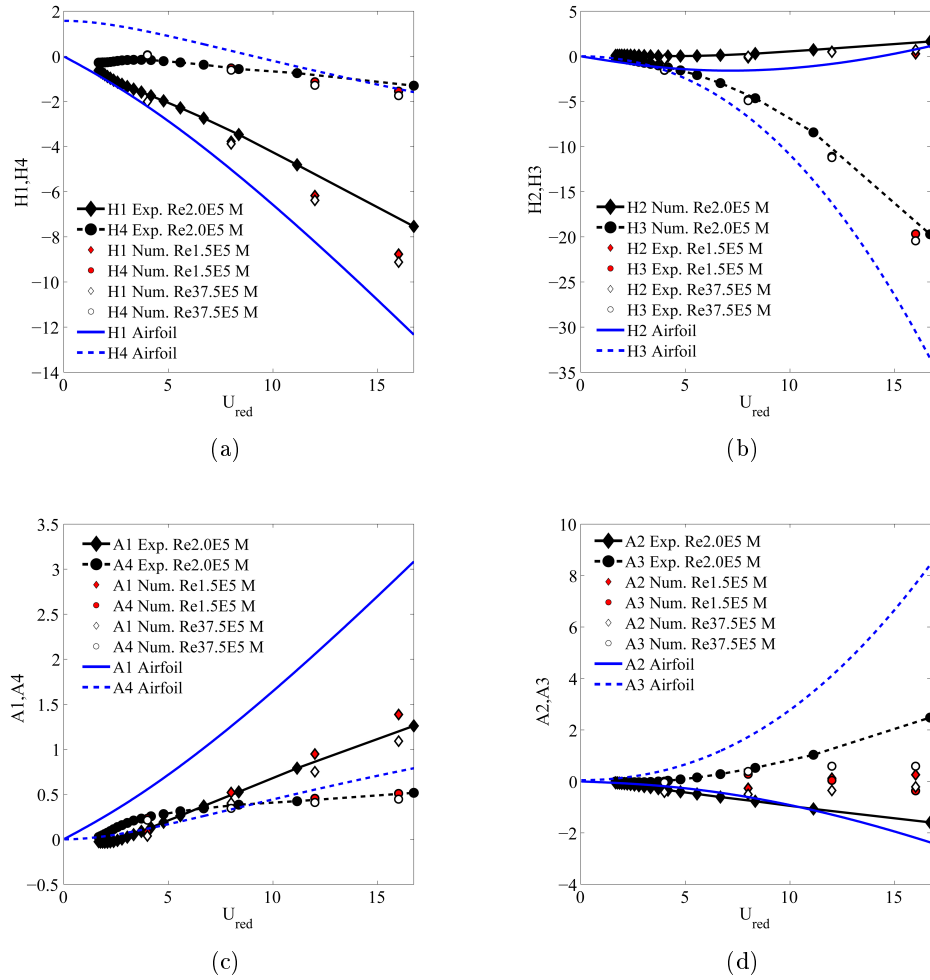


Figure 8.14: Comparison between experimental and numerical flutter derivatives for Gibraltar bridge.

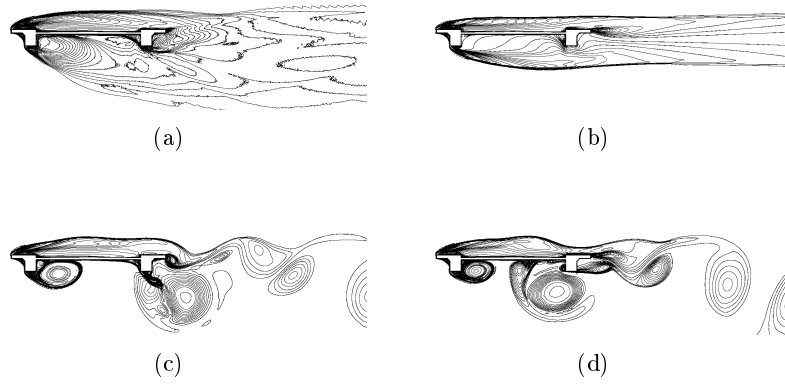


Figure 8.15: Vorticity contours for Chongqing bridge at zero attack angle: (a) time averaged  $Re = 1.5E5$ , (b) time averaged  $Re = 37.5E5$ , (c) instantaneous with maximum lift  $Re = 1.5E5$ , (d) instantaneous with minimum lift  $Re = 1.5E5$ .

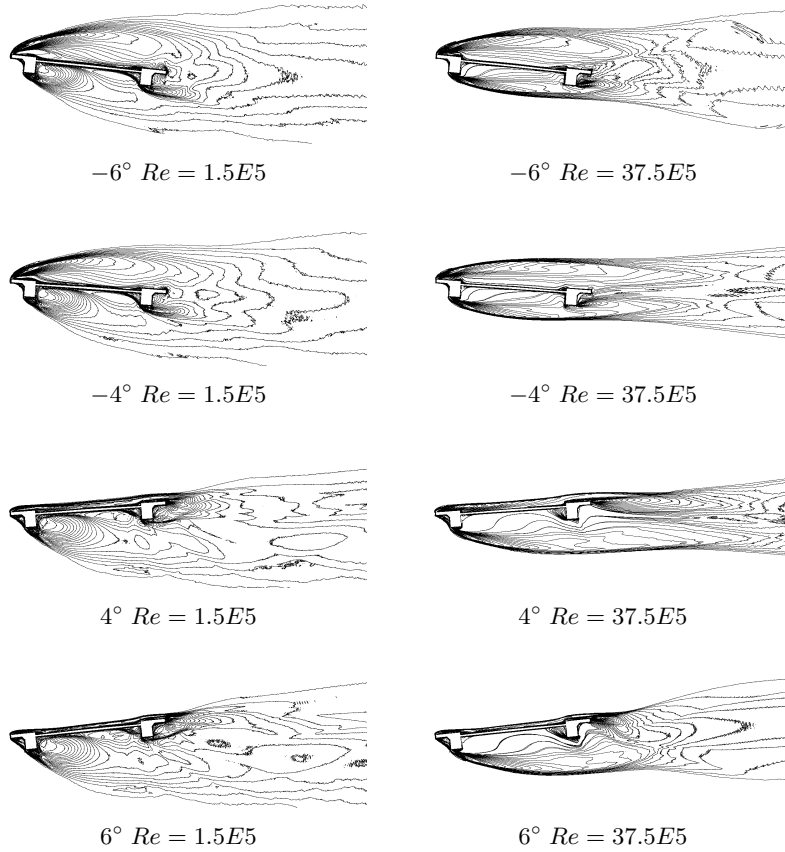


Figure 8.16: Time averaged vorticity contours for Chongqing bridge at varying attack angle.

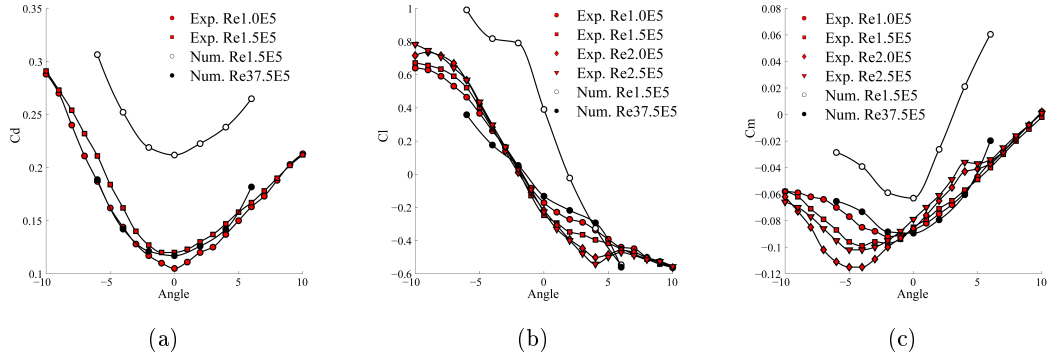


Figure 8.17: Variation of the aerodynamic coefficients with the attack angle for Chongqing: (a) drag, (b) lift, (c) pitching moment coefficients.

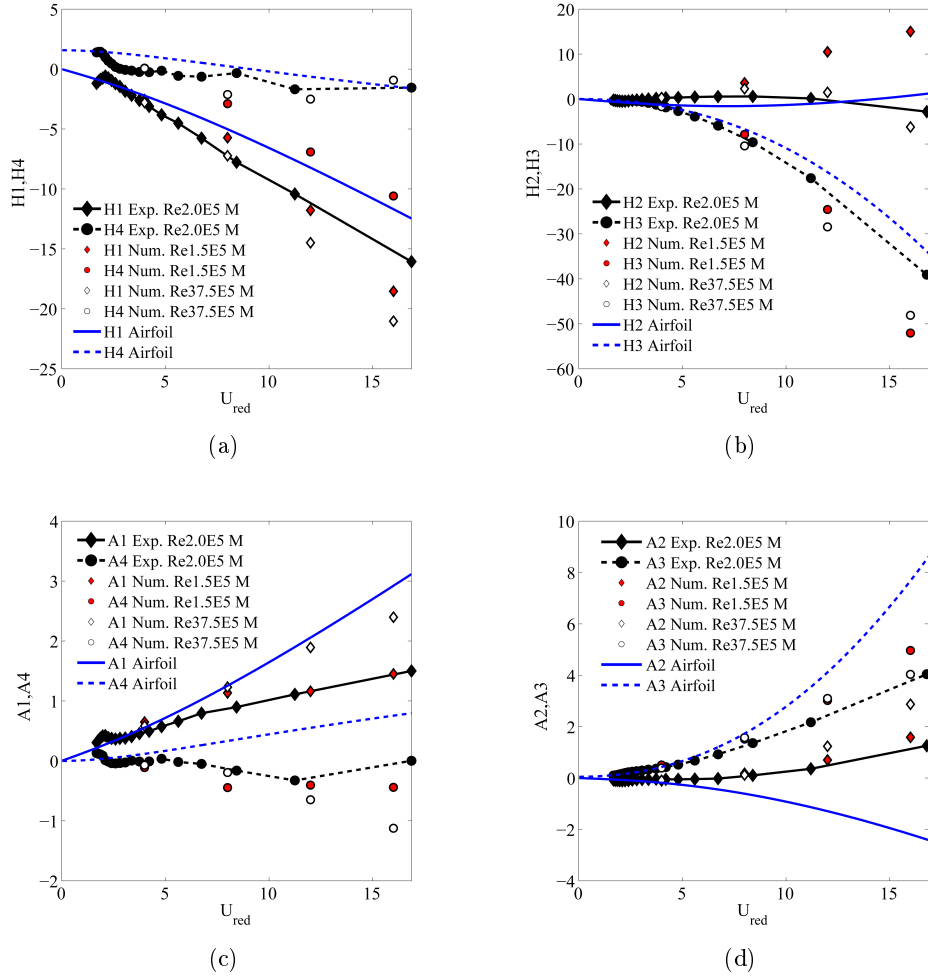


Figure 8.18: Comparison between experimental and numerical flutter derivatives for Chongqing bridge with medium displacements  $M$ .

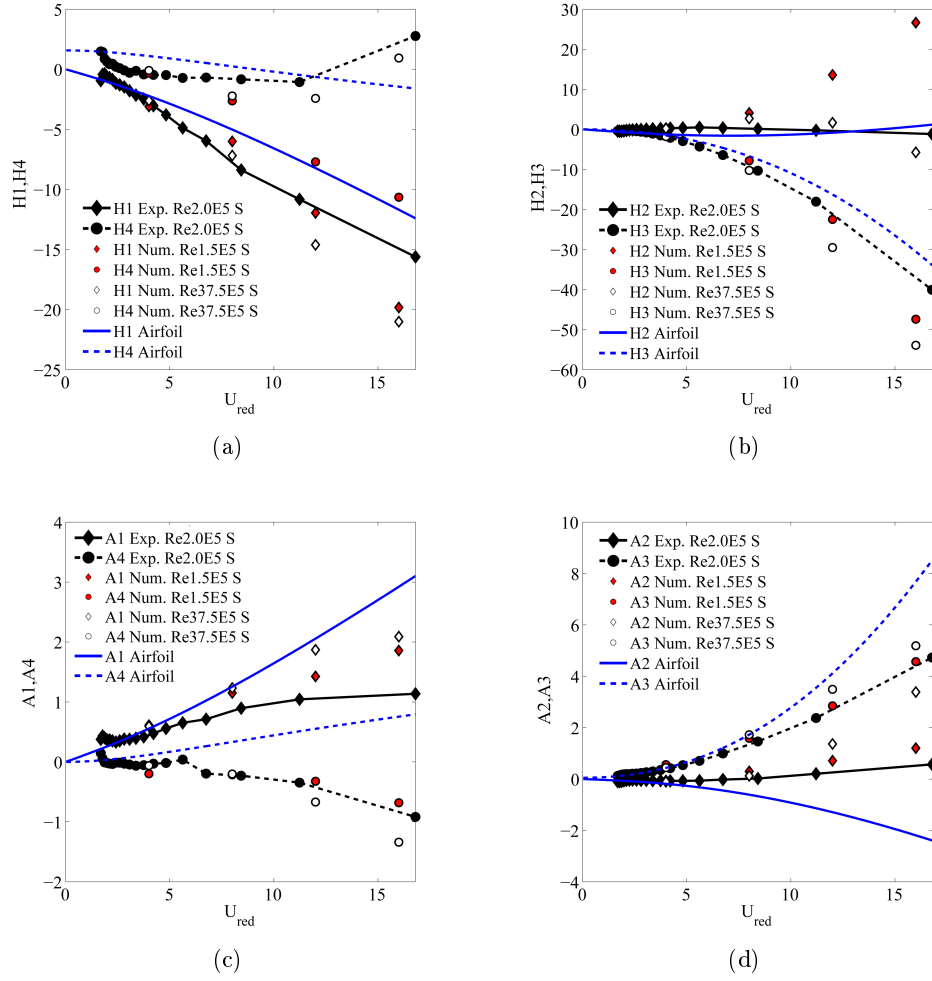


Figure 8.19: Comparison between experimental and numerical flutter derivatives for Chongqing bridge with small displacements  $S$ .

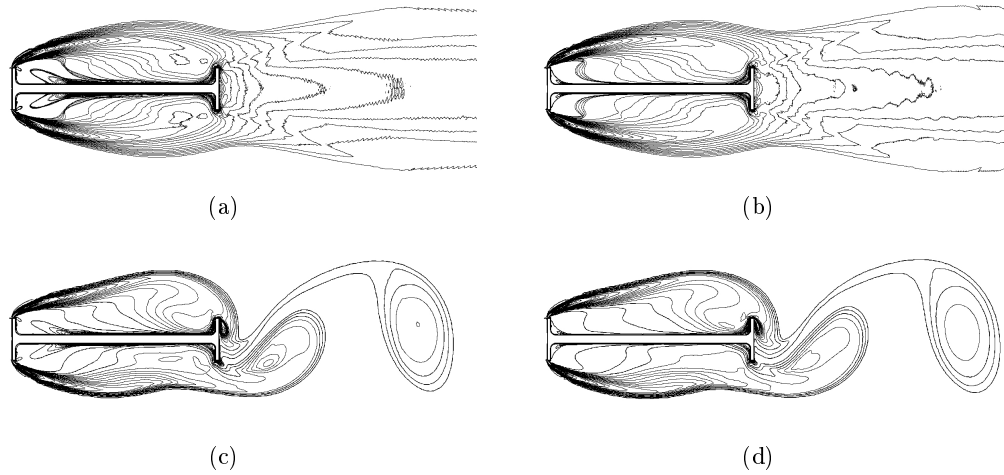


Figure 8.20: Vorticity contours for Tacoma bridge at zero attack angle: (a) time averaged  $Re = 1.5E5$ , (b) time averaged  $Re = 37.5E5$ , (c) instantaneous with maximum lift  $Re = 1.5E5$ , (d) instantaneous with maximum lift  $Re = 1.5E5$ .

### 8.2.5 Tacoma

In this section the Tacoma bridge cross section is analysed. The geometry is here included as an example of massively detached flow, which, at least on theoretical ground, should not be well captured by the RANS approach.

The aerodynamic coefficients variation with the attack angle is reported in Fig. 8.22 showing reasonable agreement with experimental results. It is noticed that the drag at zero attack angle is well captured while its variation with the attack angle is overestimated as a consequence of the overestimation of the lift coefficient variation.

The geometry is known to lead to severe torsional instability as confirmed by the sign of the pitching moment coefficient derivative. Comparison of the numerical flutter derivative with the experimental results in this case is not straightforward as the experimental data appear to be scattered and remarkable variations with the motion amplitude are observed. To provide a reasonably complete picture of the data variability, also in this case, both  $S$  and  $M$  forced vibration amplitudes are reported.

Despite the differences, the critical flutter speed for Str.1 is in good agreement with experimental results and, for the other structures, instability falls in the reduced velocities range 0-4 according to experimental results (in Tab. 8.9 such condition is reported as  $\otimes$  because flutter derivatives are extrapolated in that range and results might be misleading).

It is once again noticed that, overall good agreement with experimental results is observed concerning the critical flutter speed. This is expected because instability is triggered by negative torsional damping and  $A_2^*$  and  $A_3^*$  appear to be accurate. Once again, the calculated critical speed appears to be on the safe side.

It is noticed that peaks are observed in the experimental flutter derivatives for  $U_{red} \simeq 2$ . Such reduced velocity corresponds to the lock-in condition so that the Scanlan loading model cannot be used to evaluate the critical flutter speed in that range

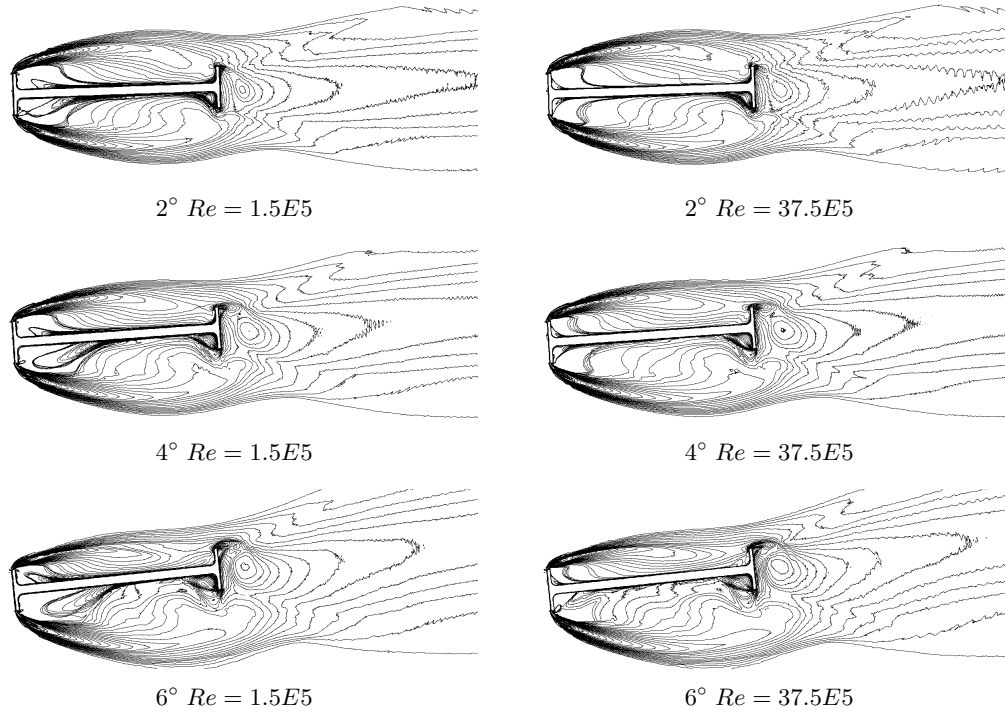


Figure 8.21: Time averaged vorticity contours for Tacoma at varying attack angle.

	Str. 1		Str. 2		Str. 3		Str. 4	
	$U$	$U_{red}$	$U$	$U_{red}$	$U$	$U_{red}$	$U$	$U_{red}$
Exp. $Re2.0E5$ $M$	66	5.6	60	3.9	70	3.8	76	2.6
Num. $Re1.5E5$ $M$	57	4.8	⊗	⊗	⊗	⊗	⊗	⊗
Num. $Re37.5E5$ $M$	60	5.0	⊗	⊗	⊗	⊗	⊗	⊗

Table 8.9: Comparison between critical flutter speed for Tacoma bridge in  $[m/s]$ .

[111]. The numerical model is able to capture such condition and instantaneous vorticity contours for a rotational vibration with  $U_{red} = 2$  are reported in Fig. 8.23. The two simulation strategies  $Re = 1.5E5$  and  $Re = 37.5E5$  lead to very similar results so indicating that the lock-in condition is a stable mechanism with respect to the simulation  $Re$  number. It is here stressed that RANS models are usually able to approximately capture only global flow instabilities like in this case and should not be relied on for local shedding mechanisms. As a last remark, in order to give a better picture of the biases introduced by RANS turbulence models in the shear layer rolling-up and their effect on the mean flow, comparison is here proposed between the experimental flow visualization (hydrogen-bubble) reported in [112] and numerical simulations (see Fig. 8.26). Unfortunately such experiments are performed at  $Re = 1200$  so they are not comparable to the previously presented results. Nevertheless, in the experimental results, local shear layer instabilities (some of them marked with red arrows) are observed. Such instabilities, probably of the Kelvin-Helmholtz kind, leads to the shear layer rolling-up and, finally

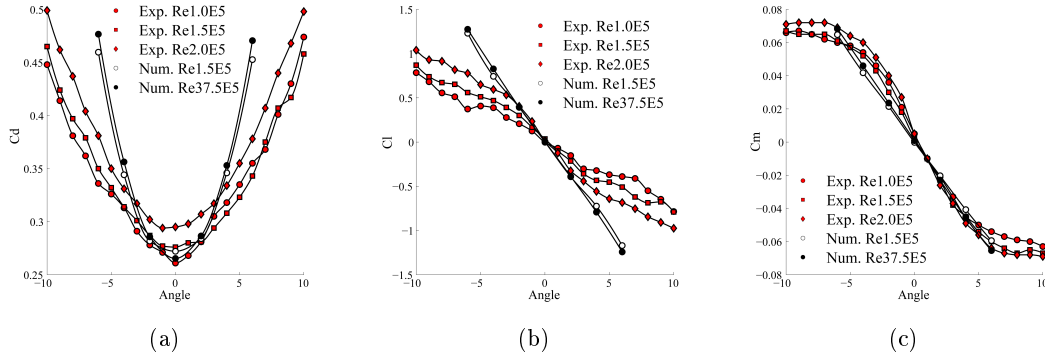


Figure 8.22: Variation of the aerodynamic coefficients with the attack angle for Tacoma: (a) drag, (b) lift, (c) pitching moment coefficients.

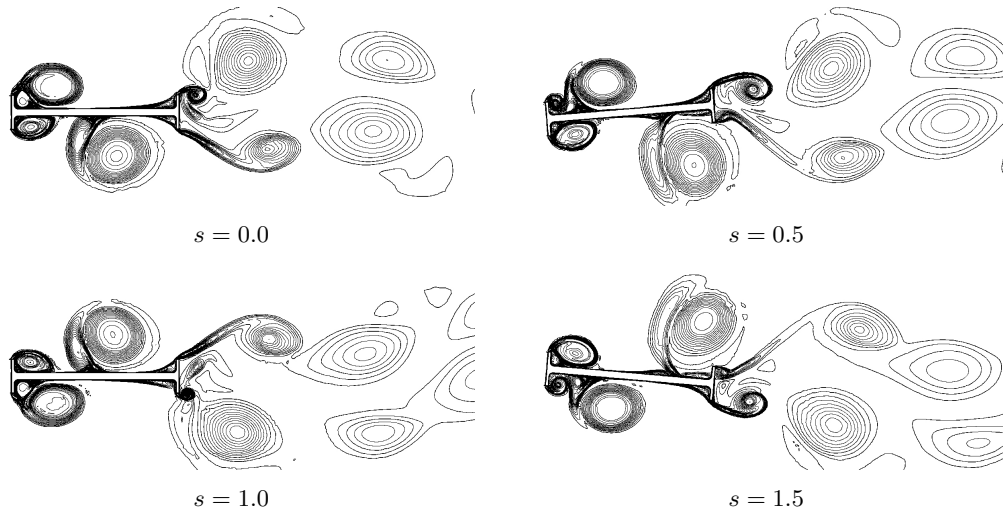


Figure 8.23: Instantaneous vorticity contours for Tacoma bridge in lock-in condition at  $U_{red} = 2$ .

to the reattachment as shown in Fig. 8.26 (a). In the numerical simulations, none of such structures is observed (Fig. 8.26 (b)) and, conversely, the shear layer thickness is remarkably increased. The rolling-up still occurs but as a consequence of the global shear layer instability with a final result which is only roughly similar to the experimental case. Undoubtedly, the mean flow is deeply affected by such discrepancies which were indeed originated by the amplification of small scales due to shear layer instabilities.



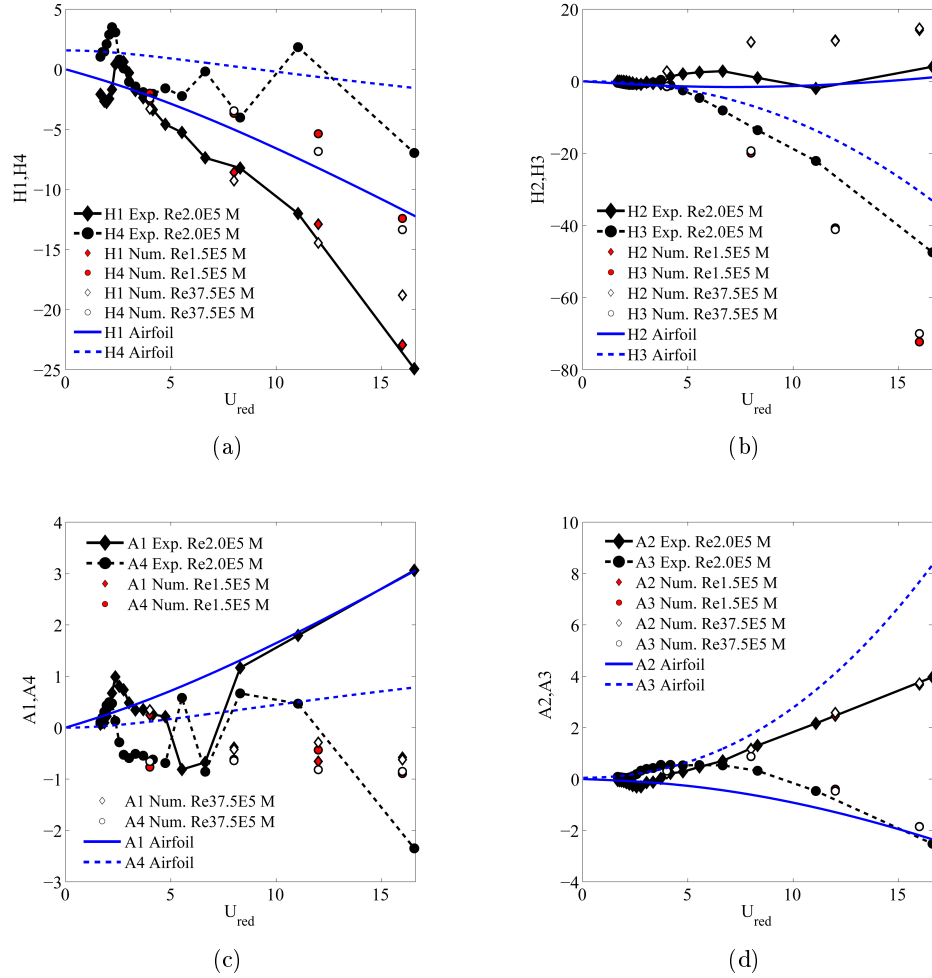


Figure 8.24: Comparison between experimental and numerical flutter derivatives for Tacoma bridge with medium displacements  $M$ .

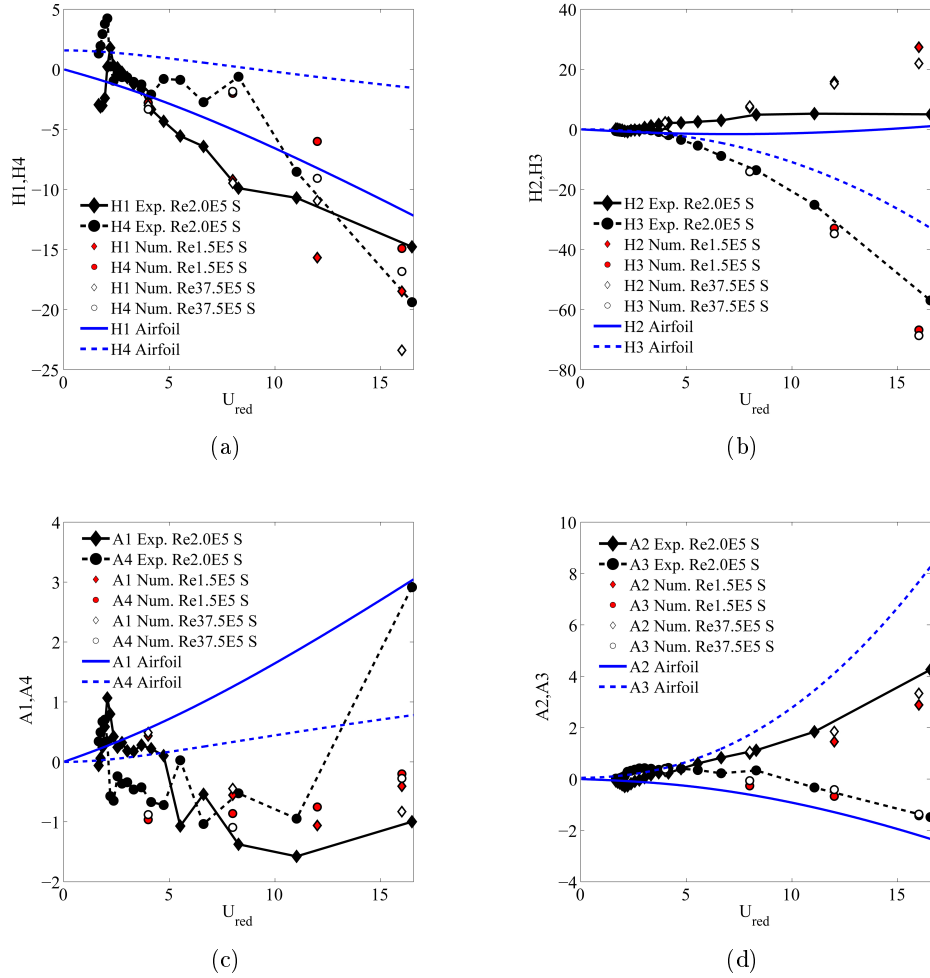


Figure 8.25: Comparison between experimental and numerical flutter derivatives for Tacoma bridge with small displacements  $S$ .

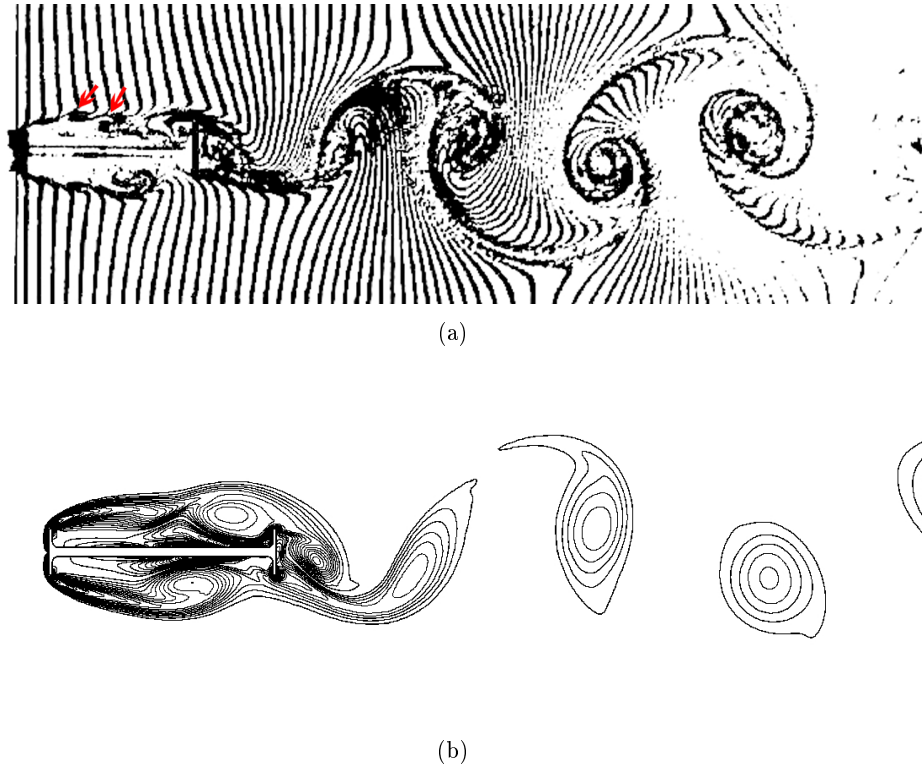


Figure 8.26: Comparison between experimental and numerical flow field at  $Re = 1200$ : (a) experimental [112], (b) numerical.

### 8.2.6 Adige

The Adige bridge deck has been here considered in order to test the model ability to account for simple barriers and its sensitivity to the average attack angle as usually verified in wind tunnel tests.

With respect to the barriers effect, the accuracy of the turbulence model in accounting for such secondary elements is not obvious especially considering that they are inevitably coarsely meshed and they produce a large quantity of turbulence characterized by small length scales.

In order to keep the simulation as simple as possible, the barriers have been modelled as zero thickness walls. The presence of such secondary elements, although extremely simplified, obliges to use very small finite volumes in zones characterized by high velocity so that, in order to limit the Courant number, the time step has to be reduced with respect to the other cases.

In order to assess the ability of the model to correctly incorporate the effects of the barriers, the case has been studied in static conditions also without such secondary elements (simulations indicated as *NB* in the figures).

The interpretation of the results in this case is more complex than the other cases: as it is shown in Fig. 8.28 the lift curve calculated with the barriers shows a local maximum and a sudden jump for  $Re = 37.5E5$  which is not observed in experiments. The instantaneous and time averaged vorticity contours are reported in Fig. 8.27. It

is noticed that, depending on the simulation  $Re$  number, the flow can have different organizations at the bottom side detachment point. Another set of simulations was performed at  $Re = 15.0E5$  in order to have a clearer picture of the results.

Considering Fig. 8.28, it is observed that, roughly speaking, depending on the simulation  $Re$  number, the flow sharply detaches from the bottom rear corner or it adheres to the deck being conveyed toward the centre of the wake (Fig. 8.27). Again, depending on the  $Re$  number, such transition is observed for different attack angles as shown in Fig. 8.29 and more synthetically in Fig. 8.28.

Considering the experimental results for the lift coefficient (Fig. 8.28 (b)), it seems that experiments are closer to the condition reproduced by  $Re = 1.5E5$  where the flow is sharply detached and the jumps are not observed. In general, it seems that the barriers led to an improvement of the flow prediction (especially in the inclination of the pitching moment coefficient variation) but are also responsible for the upward suction that induces the jumps so compromising the simulation accuracy.

Flutter derivatives are better captured by  $Re = 1.5E5$  which has a constant topology. This is expected as the topology variation induces a strong dynamic behaviour to the flow which is not experimentally observed.

To what it concerns the critical flutter speed, results can be still considered to be reasonably accurate but, in general, they are no longer on the safe side (see Tab. 8.10).

As already stated, the case have been also considered in order to test the ability of the turbulence model to capture the variation of the flutter derivatives and, indeed, the stability conditions with the mean attack angle. This has been accomplished, according to standard experimental procedures, by studying the variation of the aeroelastic coefficients when the section has average attack angle equal to  $3^\circ$  and  $-3^\circ$ .

Also in this case, it is observed that the calculated flutter derivatives correctly reproduce the trends of the experimental ones with respect to the attack angle but the estimations are not always conservative, especially for  $Re = 37.5E5$  at  $-3^\circ$ . Inspecting Fig. 8.28 it is noticed that, during the forced vibrations, the deck passes through the attack angles which led to the sudden jump in the flow topology in static condition. The videos of the vorticity show that the flow attaches and detaches periodically so confirming the change in the flow topology during the motion. Although with minor intensity, such behaviour is observed also for  $Re = 1.5E5$  at  $-3^\circ$  and, in fact, for angles smaller than  $-6^\circ$  in static conditions (8.28 (b)) the lift coefficient gradually decreases in numerical simulation reaching the values observed for  $Re = 37.5E5$ . Such behaviour is not observed in experimental results and it compromises the accuracy of the flutter derivatives estimation for  $-3^\circ$  average attack angle.

In this case, the numerically obtained flutter derivative are able to represent the flutter condition only qualitatively and more importantly, they do not provide results uniformly on the safe side (Tab. 8.10).

From a practical point of view, cases characterized by such jumps should be avoided in numerical simulations because RANS turbulence model are not able to accurately capture the flow dynamics with confidence. Additionally, it has been shown that, as expected, when the dynamic behaviour is studied in such a way that the stall angle is reached, RANS based numerical simulations are not able to correctly capture the aeroelastic behaviour with good accuracy.

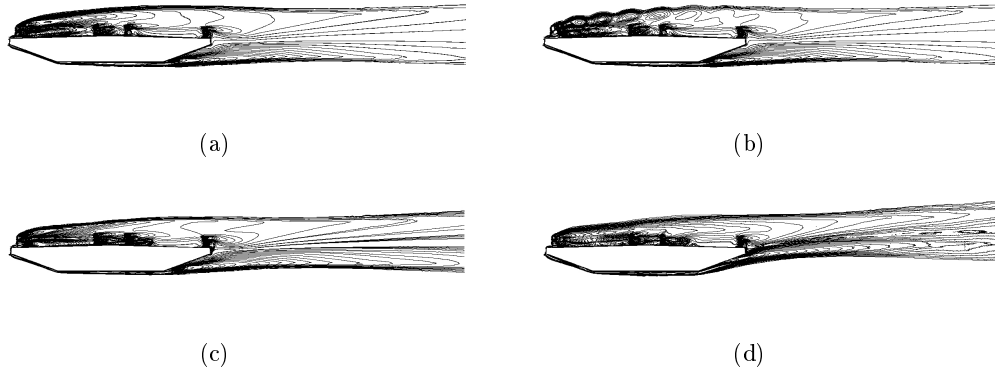


Figure 8.27: Vorticity contours for Adige bridge at zero attack angle: (a) time averaged  $Re = 1.5E5$ , (b) instantaneous  $Re = 1.5E5$ , (c) time averaged  $Re = 15.0E5$ , (d) time averaged  $Re = 37.5E5$ .

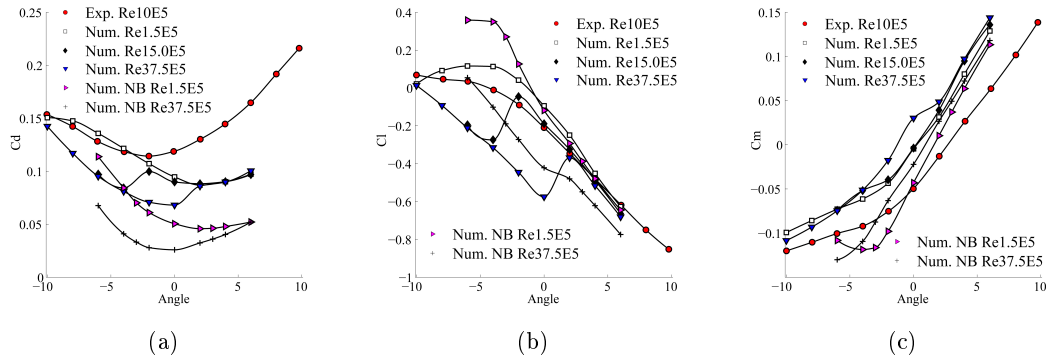


Figure 8.28: Variation of the aerodynamic coefficients with the attack angle for Adige: (a) drag, (b) lift, (c) pitching moment coefficients.

### 8.3 Conclusions on bridge decks

In this chapter a detailed validation of the ability of the  $k - \omega$  *sst* turbulence model to capture the aerodynamic performance of bridge decks both in static and dynamic conditions have been presented.

The eight considered geometries have been selected in order to test the ability of the numerical model to reproduce various conditions encountered in the technical practice. In particular:

- R8 has a very bluff section characterized by reattached flow and almost central aerodynamic centre,
- Severn has a streamlined section characterized by sharp edges,
- Gibraltar has a well streamlined twin deck section,
- Chongqing has a  $\neg$  shaped bluff section with large recirculation zones,

	Str. 1		Str. 2		Str. 3		Str. 4	
	$U$	$U_{red}$	$U$	$U_{red}$	$U$	$U_{red}$	$U$	$U_{red}$
Exp. $Re10.0E5$ $0^\circ$	160	14.8	137	10.0	128	8.0	112	6.3
Num. $Re1.5E5$ $M$ $0^\circ$	-	-	148	11.3	129	8.1	116	6.3
Num. $Re37.5E5$ $M$ $0^\circ$	-	-	141	10.7	124	7.8	114	6.3
Exp. $Re10.0E5$ $3^\circ$	-	-	155	12.2	140	9.3	129	7.5
Num. $Re1.5E5$ $M$ $3^\circ$	-	-	150	11.9	133	8.9	120	7.0
Num. $Re37.5E5$ $M$ $3^\circ$	-	-	157	13.0	139	9.7	125	7.5
Exp. $Re10.0E5$ $-3^\circ$	94	8.1	94	6.3	86	4.7	88	4.2
Num. $Re1.5E5$ $M$ $-3^\circ$	118	10.4	96	6.4	77	4.1	$\otimes$	$\otimes$
Num. $Re37.5E5$ $M$ $-3^\circ$	141	13	125	8.9	115	6.9	102	5.3

Table 8.10: Comparison between critical flutter speed for Adige bridge in  $[m/s]$ .

- Tacoma has a  $\vdash$  shaped bluff section prone to torsional instability,
- Adige has a streamlined section but barriers have been included in the analysis and the effect of the average incidence angle on the flutter derivatives has been studied.

The results have been presented describing in detail the simulation strategy, commenting the obtained results, providing visual inspection of the simulated flow fields and comparison with experimental results.

Despite some biases, it is shown that, following the proposed simulation strategy, numerical simulations, although performed with a standard  $k - \omega$  *sst* turbulence model are able to provide a precious insight in the aerodynamic performance of bridge decks. In fact, although the estimation of the single flutter derivative might be sometimes inaccurate, the global behaviour of the structure has been generally correctly reproduced.

Analysing the aerodynamic coefficients variation with the attack angle in the numerical simulations and comparing results obtained with different simulation strategies, some conditions that should be interpreted with caution have been identified. In particular, when jumps are observed in the flow topology with varying attack angle the aeroelastic behaviour predicted by numerical models might be inaccurate. The same caution should be used when calculating the flutter derivatives close to the stall condition. In the other cases, the critical wind speed calculated from numerically extracted flutter derivatives proved to be surprisingly accurate and mainly on the safe side if compared to experimental evidences.

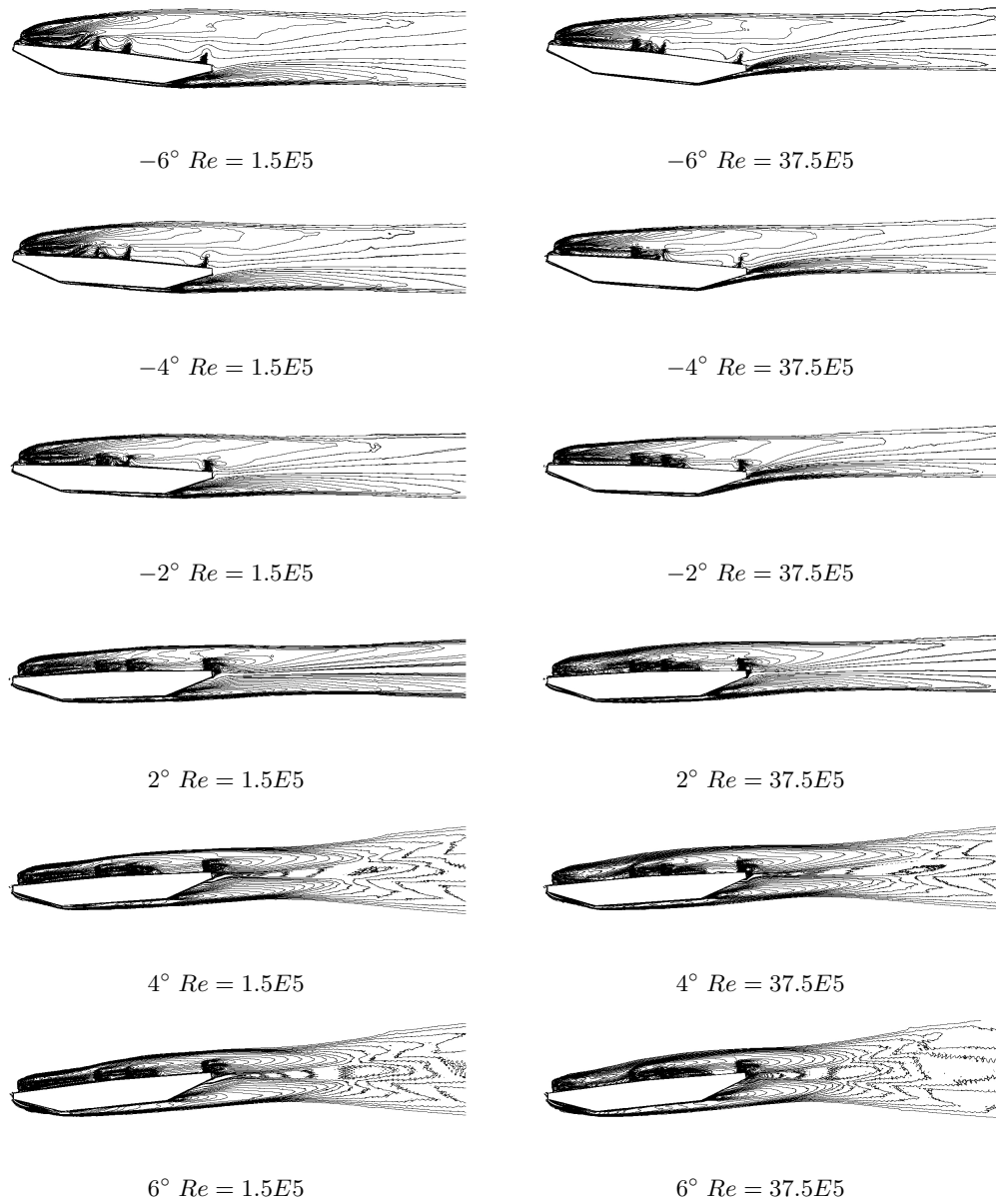


Figure 8.29: Time averaged vorticity contours for Adige bridge at varying attack angle.

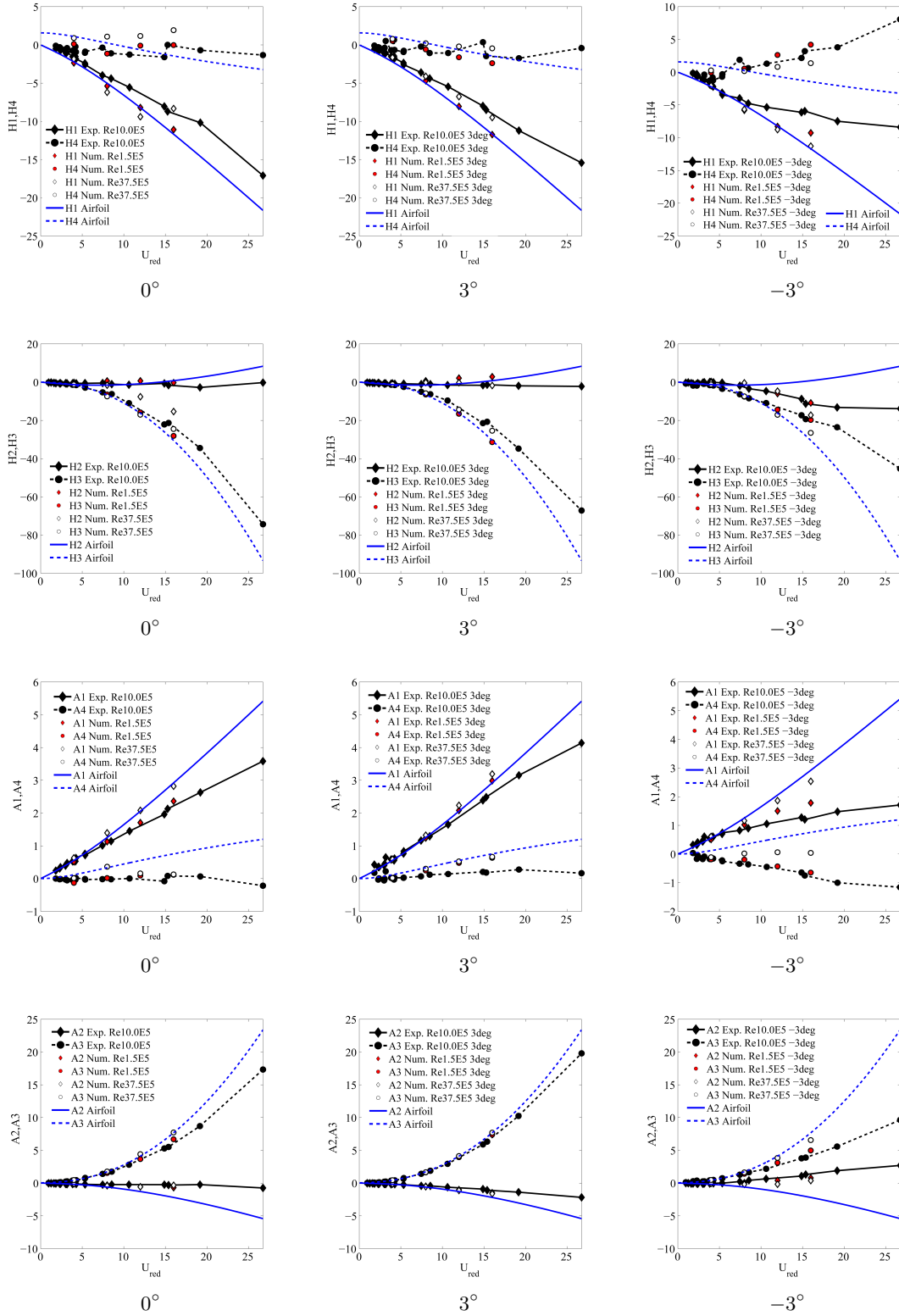


Figure 8.30: Comparison between experimental and numerical flutter derivatives for Adige bridge at varying mean attack angle.





# Conclusions

In this thesis the numerical simulation of aeroelastic loads on bridge decks has been addressed and discussed in details. In particular, in Chapter 2 an overview of aeroelastic phenomena is presented providing a basic description of the generative mechanisms which lead to wind loading and aeroelastic instabilities. The importance of the individuation of the correct scales, representative of the observed phenomena, is highlighted and the main characteristics of the flow fields encountered around bluff bodies presented.

In Chapter 3, the governing equations for inviscid flows are briefly recalled together with some basic concepts of aerodynamic. Such concepts, although not directly useful for applications to bridge decks, constitute an essential requirement in order to build a unitary and consistent approach able to guide the reader in the subsequent chapters. The inconsistencies between theoretical predictions and experimental results are highlighted so naturally leading to the introduction of viscosity and turbulence.

Chapter 3, presents the governing equations for viscous fluids and, focusing the attention on experimental evidences, describes the generative mechanisms of such chaotic flow regime with special attention to external flows around bluff bodies. The most commonly used approaches to turbulence modelling are presented discussing the critical aspects which lead to remarkable differences between numerical predictions and experimental evidences. The attention is mainly focused on RANS model because they are extensively used in subsequent developments.

Flutter derivatives and procedures currently used to assess the stability of bridges are presented in Chapter 5. Standard techniques used for the extraction of flutter derivatives are described highlighting the differences between experimental and numerical procedures. The Scanlan loading model is presented and its relation with Theodorsen and Wagner approaches recognized.

The airfoil theory and its generalization to mildly bluff bodies is the matter of Chapter 6. Here, the analogy between Theodorsen and Wagner approach is described in detail and an extension of the indicial approach, able to incorporate some features of the aerodynamic behaviour of mildly bluff bodies, is proposed according to other works by Scanlan. An effective procedure for the calibration of the model parameters, based on computational fluid dynamics, is presented and the procedure tested on the thin airfoil and a streamlined deck section. Strengths and limitations of the proposed model and calibration procedure are discussed.

Chapters 7 and 8 present a comprehensive assessment of the performance of currently available computational techniques coupled with RANS based turbulence models in predicting flutter derivatives and the critical flutter wind speed. In particular in Chapter 7, forced vibration tests are simulated for rectangular prisms with aspect ratio varying between 2 and 20. Systematic comparison between numerical and experimental results is provided together with data extracted by other authors. The case of rectangular prisms is indeed extremely interesting because the flow is mainly characterised by the presence of strong flow detachments at the leading edge corners and formation of shear layers so representing an ideal test case to study the model performance in predicting the dynamic behaviour of such flow structures.

Finally, in Chapter 8, the ability of RANS based simulations in predicting the flutter derivatives of bridge decks is assessed. The considered geometries have been selected in order to test the ability of the numerical model to reproduce various conditions encountered in the technical practice. Also in this case, systematic comparison with experimental results is provided. By studying the sensitivity of the predictions with the simulation strategy and individuating the conditions which lead to poor model predictions, guidelines are set with the aim of providing practitioner engineers a useful reference for the simulation setup and the interpretation of the results.

Further research work is needed on the topic. In particular, Scale Resolving Turbulence models might lead to a considerable improvement in the numerical models predictive capabilities. The computational time required to systematically extract flutter derivatives for a variety of cases, representative of the typologies encountered in the technical practice, is still nowadays extremely long. Furthermore, when such models are used, the results become extremely sensitive to the mesh size so that convergence studies would be necessary (so increasing the computational cost). Many studies in literature proposed LES simulations with inadequate space and time resolving capabilities. In order to reach meaningful results the shear layers should become unstable providing the large and medium size turbulent scales. Unfortunately, the stability of the shear layers is deeply affected by the mesh size in a non-linear way: if the initial mesh is too coarse, even doubling the mesh resolution does not provide useful indications. Indeed, the danger is that coarse meshes might tend to underestimate the critical flutter speed similarly to RANS models, while fine meshes might overestimate it significantly so that a detailed investigation of Scale Resolving models in such application is needed before its practical application.

# References

- [1] S. Kumar and G. Laughlin. Online page of aps physics. <http://www.aps.org/units/dfd/pressroom/gallery/2009/kumar09.cfm>.
- [2] S.A. Kinnas. Online page of the university of texas at austin. <http://www.ce.utexas.edu/prof/kinnas/>.
- [3] J.D. Anderson. *Fundamentals of aerodynamics, 3rd ed.* McGraw-Hill, New York, 2001.
- [4] G. Schewe and A. Larsen. Reynolds number effects in the flow around a bluff bridge deck cross section. *J. Wind Eng. Ind. Aerodyn.*, 74-76:829–838, 1998.
- [5] C. Dyrbye and S.O. Hansen. *Wind loads on structures*. Wiley, Chichester, UK, 1997.
- [6] R.H. Scanlan and E. Simiu. *Wind Effects on Structures*. John Wiley and Sons Inc., 1996.
- [7] H. K. Versteeg and W. Malalasekera. *An Introduction to Computational Fluid Dynamics: The Finite Volume Method*. Longman, Edinbrugh Gate, Harlow, England, 2006.
- [8] H.K. Versteeg and W. Malalasekera. *An introduction to computational fluid dynamics: the finite volume method*. Pearson Education Limited, Harlow, 2007.
- [9] T. Ruggeri. *Introduzione alla termomeccanica dei continui*. Monduzzi, 2013.
- [10] Cenedese A. *Meccanica dei fluidi*. McGraw-Hill, Milano, 2003.
- [11] [http://www.finot.com/ecrits/Damien Lafforgue/article\\_voiles\\_english.html](http://www.finot.com/ecrits/Damien Lafforgue/article_voiles_english.html).
- [12] P. Luchini and M. Quadrio. *Aerodinamica*. Freely available at <http://www.aero.polimi.it/quadrio/it/Didattica/dispensenuove.html>, Politecnico di Milano.
- [13] R.L. Bisplinghoff, H. Ashley, and R.L. Halfman. *Aeroelasticity*. Courier Dover Publications, New York, 1996.
- [14] T. Theodorsen. General theory of aerodynamic instability and the mechanism of flutter. *NACA Report*, page 496, 1935.

- 
- [15] H. Wagner. Über die entstehung des dynamischen auftriebes von tragflügeln. *ZAMM - Journal of Applied Mathematics and Mechanics*, 5:17–35, 1925.
  - [16] Y.C. Fung. *An Introduction to the Theory of Aeroelasticity*. Courier Dover Publications, New York, 1993.
  - [17] I.E. Garrick. On some reciprocal relations in the theory of nonstationary flows. *NACA Report*, page 629, 1938.
  - [18] D.C. Wilcox. *Turbulence Modeling for CFD*. DCW Industries Inc., La Canada, CA, USA, 1998.
  - [19] F.M. White. *Viscous Fluid Flow*. McGraw-Hill, New York, 1991.
  - [20] <http://www.wikipedia.com>.
  - [21] R.S. Rogallo and P. Moin. Numerical simulation of turbulent flows. *Annual review of fluid mechanics*, 16:99–137, 1984.
  - [22] H.L. Grant, R.W. Stewart, and Moilliet A. Turbulence spectra from a tidal channel. *Journal of Fluid Mechanics*, 12:241–268, 1962.
  - [23] F. R. Menter, M. Kuntz, and R. Langtry. Ten years of industrial experience with the SST turbulence model. *Turbulence Heat and Mass Transfer*, 4, 2003.
  - [24] F.R. Menter. Turbulence modeling for engineering flows. *Technical paper from Ansys Inc.*, 2011.
  - [25] P.A. Durbin and B.A. Patterson-Reif. *Statistical Theory and Modeling for Turbulent Flow*. Wiley, Chichester, West Sussex, UK, 2001.
  - [26] A. Leonard. Energy cascade in large-eddy simulations of turbulent fluid flows. *Advances in Geophysics*, 18:237–248, 1974.
  - [27] J.H. Ferziger. Large Eddy Numerical Simulations of Turbulent Flows. *AIAA Paper*, pages 76–374, 1976.
  - [28] S. Som, D.E. Longman, Z. Luo, M. Plomer, T. Lu, Senecal P.K., and E. Pomraning. Simulating flame lift-off characteristics of diesel and biodiesel fuels using detailed chemical-kinetic mechanisms and LES turbulence model. *Proc. ASME 2011 Internal Combustion Engine Division Fall Technical Conference*, 2011.
  - [29] Y. Ergorov and F.R. Menter. The Scale-Adaptive Simulation Method for Unsteady Turbulent Flow Predictions. Part 1: Theory and Model Description. *Flow Turbulence and Combustion*, 85:113–138, 2010.
  - [30] Y. Ergorov, F.R. Menter, R. Lechner, and D. Cokljat. The Scale-Adaptive Simulation Method for Unsteady Turbulent Flow Predictions. Part 2: Application to Complex Flows. *Flow Turbulence and Combustion*, 85:139–165, 2010.
  - [31] K.F.. Liaw. *Simulation of Flow around Bluff Bodies and Bridge Deck Sections using CFD*. Ph.D. Thesis, University of Nottingham, 2005.

- 
- [32] R.H. Scanlan. Aerodynamics of cable-supported bridges. *Journal of Constructional Steel Research*, 39:51–68, 1996.
  - [33] R.H. Scanlan and J.J. Tomko. Airfoil and bridge deck flutter derivatives. *Journal of the Engineering Mechanics Division ASCE*, 97:1717–1737, 1971.
  - [34] R.H. Scanlan. Problematics in the formulation of wind-force models for bridge decks. *Journal of the Engineering Mechanics Division ASCE*, 119:1353–1375, 1993.
  - [35] R.H. Scanlan. Reexamination of sectional aerodynamic force functions for bridges. *Journal of Wind Engineering and Industrial Aerodynamics*, 89:1257–1266, 2001.
  - [36] A. Šarkić, R. Fisch, R. Höffer, and Bletzinger K.U. Bridge flutter derivatives based on computed, validated pressure fields. *Journal of Wind Engineering and Industrial Aerodynamics*, 104-106:141–151, 2012.
  - [37] U. Starossek. Online page of Technische Universität Hamburg-Harburg <http://www.tuhh.de/sdb/starossek/>.
  - [38] Fujino Y. Iwamoto, M. Identification of flutter derivatives of bridge deck from free vibration data. *J. Wind Eng. Ind. Aerodyn.*, 54:55–63, 1995.
  - [39] Gu M., R. Zhang, and H. Xiang. Identification of flutter derivatives of bridge decks. *Journal of Wind Engineering and Industrial Aerodynamics*, 84:151–162, 2000.
  - [40] A. Chen, X. He, and H. Xiang. Identification of 18 flutter derivatives of bridge decks. *Journal of Wind Engineering and Industrial Aerodynamics*, 90:2007–2022, 2002.
  - [41] A.G. Chowdhury and Sarkar P.P. A new technique for identification of eighteen flutter derivatives using a three-degree-of-freedom section model. *Engineering Structures*, 25:1763–1772, 2003.
  - [42] Gu M. and X.R. Qin. Direct identification of flutter derivatives and aerodynamic admittances of bridge decks. *Engineering Structures*, 26:2161–2172, 2004.
  - [43] J.M.W. Brownjohn and Bogunovic Jakobsen J. Strategies for aeroelastic parameter identification from bridge deck free vibration data. *Journal of Wind Engineering and Industrial Aerodynamics*, 89:1113–1136, 2001.
  - [44] M. Deistler, K. Peternell, and W. Scherrer. Consistency and relative efficiency of subspace methods. *Automatica*, 31:1865–1875, 1995.
  - [45] A. Chiuso and G. Picci. Subspace identi.
  - [46] L. Lin, B. Xi, and Z. Lv. Modal parameter identification based on singular value decomposition and backward prediction. In *8th IEEE International Conference on Control and Automation*, Xiamen, China, 2010.
  - [47] G. Vairo. A numerical model for wind loads simulation on long-span bridges. *Simulation Modelling Practice and Theory* 11, pages 315–351, 2003.

- 
- [48] F. Brusiani, S. de Miranda, L. Patruno, F. Ubertini, and P. Vaona. On the evaluation of bridge deck flutter derivatives using rans turbulence models. *Journal of Wind Engineering and Industrial Aerodynamics*, 119:39–47, 2013.
- [49] F. Brusiani, G. Cazzoli, S. de Miranda, F. Ubertini, and P. Vaona. Application of the  $k - \omega$  turbulence model to assess the flutter derivatives of a long span bridge. *Proc. 6th Subrata Chakrabarti International Conference on Fluid Structure Interaction*, 2011.
- [50] L. Huang, L. Haili, W. Bin, and L. Yongle. Numerical simulation for aerodynamic derivatives of bridge deck. *Simulation Modelling Practice and Theory*, 17:719–729, 2009.
- [51] Ansys. *Ansys Fluent Manual Release 14.0*. Ansys, Inc., Canonsburg, PA, USA, 2011.
- [52] J.A. Jurado, S. Hernández, F. Nieto, and A. Mosquera. *Bridge aeroelasticity: sensitivity analysis and optimal design*. WITpress, Southampton, UK, 2011.
- [53] C. Mannini. *Flutter Vulnerability Assessment of flexible bridges*. Ph.D. Thesis, Technical University Carolo-Wilhelmina and University of Florence, 2006.
- [54] R.H. Scanlan, J.G. Béliveau, and K. Budlong. Indicial aerodynamics functions for bridge decks. *Journal of the Engineering Mechanics Division ASCE*, 100:657–672, 1974.
- [55] D.A. Peters. Two-dimensional incompressible unsteady airfoil theory - an overview. *Journal of Fluids and Structures*, 24:295–312, 2008.
- [56] L. Cararcoglia and N.P. Jones. Time domain vs. frequency domain characterization of aeroelastic forces for bridge deck sections. *Journal of Wind Engineering and Industrial Aerodynamics*, 91:371–402, 2003.
- [57] R.H. Scanlan and N.P. Jones. A form of aerodynamic admittance for use in bridge aeroelastic analysis. *Journal of Fluids and Structures*, 13:1017–1027, 1999.
- [58] R.T. Jones. The unsteady lift on a wing of finite aspect ratio. *NACA Report*, 681, 1940.
- [59] R.H. Scanlan. Motion-related body-force functions in two-dimensional low-speed flow. *Journal of Fluids and Structures*, 14:49–63, 2000.
- [60] C. Costa and C. Borri. Application of indicial functions in bridge decks aeroelasticity. *Journal of Wind Engineering and Industrial Aerodynamics*, 94:859–881, 2006.
- [61] C. Costa. Aerodynamic admittance functions and buffeting forces for bridges via indicial functions. *Journal of Fluids and Structures*, 23:413–428, 2007.
- [62] S. de Miranda, L. Patruno, F. Ubertini, and G. Vairo. Indicial functions and flutter derivatives: a generalized approach to the motion-related wind loads. *J. of Fluids and Structures*, 42:466–487, 2013.

- 
- [63] N.P. Jones, J.D. Ragget, and E. Ozkan. Prediction of cable-supported bridge response to wind: coupled flutter assessment during retrofit. *Journal of Wind Engineering and Industrial Aerodynamics*, 91:1445–1464, 2003.
- [64] T. Yoshimura and Y. Nakamura. On the indicial aerodynamic moment responses of bridge deck sections. *Proceedings of the Fifth International Conference on Wind Engineering, Fort Collins, CO, USA*, 2:877–885, 1979.
- [65] L. Caracoglia and N.P. Jones. A methodology for the experimental extraction of indicial functions for streamlined and bluff deck sections. *Journal of Wind Engineering and Industrial Aerodynamics*, 91:609–636, 2003.
- [66] D. Lesieutre, P. Reisenthel, and M. Dillenius. A practical approach for calculating aerodynamic indicial functions with a Navier-Stokes solver. *AIAA Paper 94-0059*, 1994.
- [67] L. Bruno and D. Fransos. Evaluation of Reynolds number effects on flutter derivatives of a flat plate by means of a computational approach. *Journal of Fluids and Structures*, 24:1058–1076, 2008.
- [68] P. Brar, R. Raul, and R. Scanlan. Numerical calculation of flutter derivatives via indicial functions. *Journal of Fluids and Structures*, 10:337–351, 1996.
- [69] R. Singh and J. D. Baeder. The direct calculation of indicial lift response of a wing using computational fluid dynamics. *Journal of Aircraft*, 34:465–471, 1997.
- [70] J. Sitaraman and J.D. Baeder. Computational-fluid-dynamics-based enhanced indicial aerodynamic models. *Journal of Aircraft*, 41:798–810, 2004.
- [71] K. Yee, S. Hong, and D.H. Lee. Numerical investigation on the directionality of nonlinear indicial responses. *Journal of mechanical science and technology*, 21:1293–1305, 2007.
- [72] J.B. Frandsen. Numerical bridge deck studies using finite elements. part I: flutter. *Journal of Fluids and Structures*, 19:171–191, 2004.
- [73] X. Amandolèse and C. Crémona. Analysing fluid loadings on moving bluff bodies using proper orthogonal decomposition. *Journal of Fluids and Structures*, 20:577–587, 2005.
- [74] D. Fransos and L. Bruno. Determination of the aeroelastic transfer functions for streamlined bodies by means of a Navier-Stokes solver. *Mathematical and computer modelling*, 43:506–529, 2006.
- [75] M. Matsumoto. Aerodynamic damping of prisms. *Journal of Wind Engineering and Industrial Aerodynamics*, 59:159–175, 1996.
- [76] M. Matsumoto, Y. Daito, F. Yoshizumi, Ichikawa Y., and T. Yabutani. Torsional flutter of bluff bodies. *Journal of Wind Engineering and Industrial Aerodynamics*, 69-71:871–882, 1997.



- 
- [77] L. Singh. *Experimental determination of aeroelastic parameters of long-span bridges, Ph.D. Dissertation*. The Johns Hopkins University, Baltimore, 1997.
- [78] A. Chen, X. He, and H. Xiang. Identification of 18 flutter derivatives of bridge decks. *Journal of Wind Engineering and Industrial Aerodynamics*, 90:2007–2022, 2002.
- [79] A. Larsen and J.H. Walther. Discrete vortex simulation of flow around five generic bridge deck sections. *Journal of Wind Engineering and Industrial Aerodynamics*, 77-78:591–602, 1998.
- [80] F. Maceri and G. Vairo. Modelling and simulation of long-span bridges under aerodynamic loads. In: *Novel Approaches in Civil Engineering. Lect. Notes Appl. Comput. Mech.*, 14:359–376, 2004.
- [81] C.S. Cai and P. Albrecht. Flutter derivatives based random parametric excitation aerodynamic analysis. *Computers & Structures*, 75:463–477, 2000.
- [82] C. Borri, C. Costa, and W. Zahlten. Non-stationary flow forces for the numerical simulation of aeroelastic instability of bridge decks. *Computers & structures*, 80:1071–1079, 2002.
- [83] X. Chen and A. Kareem. Advances in modeling aerodynamic forces on bridge decks. *Journal of engineering mechanics ASCE*, 128:1193–1205, 2002.
- [84] E.F. Crawley, H.C. Curtiss, H.C. Peters, R.H. Scanlan, and F. Sisto. A modern course in aeroelasticity. *E.H. Dowell Editor*, 1995.
- [85] F. Tubino. Relationships among aerodynamic admittance functions, flutter derivatives and static coefficients for long-span bridges. *Journal of Wind Engineering and Industrial Aerodynamics*, 93:929–950, 2005.
- [86] W.D. Iwan and R.D. Blevins. A model for vortex-induced oscillation of structures. *Journal of Applied Mechanics. Transactions ASME*, 41:581–585, 1974.
- [87] Brinch M. Damsgaard A. Reinhold, T.A. Wind tunnel tests for the Great Belt Link. *Proceedings 1st Int. Symposium on Aerodynamics of Large Bridges, eds. Larsen, A. Copenhagen, Denmark*, 1992.
- [88] D. Sun, J.S. Owen, and N.G. Wright. Application of the  $k-\omega$  turbulence model for a wind-induced vibration study of 2D bluff bodies. *J. Wind. Eng. Ind. Aerodyn.*, 97:77–87, 2009.
- [89] A. Lavenille and L.Z. Yong. Mean flow patterns around two-dimensional rectangular cylinders and their interpretation. *J. Wind. Eng. Ind. Aerodyn.*, 14:387–398, 1983.
- [90] T. Tamura and Y. Ono. LES analysis on aeroelastic instability of prisms in turbulent flow. *J. Wind. Eng. Ind. Aerodyn.*, 91:1827–1846, 2003.

- 
- [91] L. Bruno, D. Fransos, N. Coste, and A. Bosco. 3D flow around a rectangular cylinder: a computational study. *J. Wind. Eng. Ind. Aerodyn.*, 98:263–276, 2010.
- [92] F.R. Menter. Best Practice: Scale-Resolving Simulations in ANSYS CFD Version 1.0. *ANSYS Germany GmbH*, 2012.
- [93] M. Shur, P.R. Spalart, K.D. Squires, M. Strelets, and A. Travin. Three dimensionality in Reynolds-Averaged Navier-Stokes solutions around two-dimensional geometries. *AIAA Journal*, 43:1230–1242, 2005.
- [94] D. Yu and A. Kareem. Two-dimensional simulation of flow around rectangular prisms. *J. Wind. Eng. Ind. Aerodyn.*, 62:131–208, 1996.
- [95] D. Yu and A. Kareem. Parametric study of flow around rectangular prisms using LES. *J. Wind. Eng. Ind. Aerodyn.*, 77&78:653–662, 1998.
- [96] D. Bouris and G. Bergeles. 2D LES of vortex shedding from a square cylinder. *J. Wind. Eng. Ind. Aerodyn.*, 80:31–46, 1999.
- [97] <http://code-saturne.org/cms/>.
- [98] D.R. Laurence, J.C. Uribe, and S.V. Utyuzhnikov. A robust formulation of the v2-f model. *Flow Turbulence and Combustion*, 73:169–185, 2004.
- [99] P. Sagaut. *Large Eddy Simulation for Incompressible Flows*. Springer, 2006.
- [100] K. Shimada and T. Ishihara. Application of a modified  $k-\epsilon$  model to the prediction of aerodynamic characteristics of rectangular cross-section cylinders. *J. of Fluids and Structures*, 16:465–485, 2002.
- [101] F.R. Menter. Two-Equation Eddy-Viscosity Turbulence Models for Engineering Applications. *AIAA-Journal*, 32:269–289, 1994.
- [102] Y. Ohtsuki. Wind tunnel experiments on aerodynamic forces and pressure distributions of rectangular cylinders in a uniform flow. *Proc. 5th Symposium on Wind Effects on Structures*, 1978.
- [103] M. Miyazaki and T. Miyata. Effect of turbulence scale on aerodynamic response of rectangular cylinders. *Flow Turbulence and Combustion*, 85:113–138, 1978.
- [104] T. Miyata and M. Miyazaki. Turbulence effects on aerodynamic response of rectangular bluff cylinders. *J.E. Cermak (Ed.), Wind Engineering, Proc. Fifth Int. Conf., Fort Collins, Colorado, USA*, pages 631–642, 1979.
- [105] A. Okajima. Strouhal numbers of rectangular cylinders. *J. Fluid Mech.*, 123:379–398, 1982.
- [106] T. Mizota, H. Yamada, Y. Kubo, A. Okajima, C.W. Knisely, and H. Shirato. Aerodynamic characteristics of fundamental structures, part 1, section 2. *J. Wind Eng.*, 36:50–52, 1988.

- [107] M.X. Amandolese. *Contribution à l'étude des chargements fluides sur des obstacles non profilés fixes ou mobiles: application aux tabliers de pont*. Ph.D. Thesis, École Nationale des Ponts et Chaussées, 2001.
- [108] A. Prasad and C.H.K. Williamson. The instability of the shear layer separating from a bluff body. *J. Fluid Mech.*, 333:375–402, 1997.
- [109] C.H.K. Williamson. Advances in our understanding of vortex dynamics in bluff body wakes. *J. Wind. Eng. Ind. Aerodyn.*, 69-71:3–32, 1997.
- [110] M. Novak and A.G. Davenport. Aeroelastic instability of prisms in turbulent flow. *Journal of the Engineering Mechanics Division*, 96:17–39, 1970.
- [111] S. de Miranda, L. Patruno, F. Ubertini, and G. Vairo. On the identification of flutter derivatives of bridge decks via rans-based numerical models: benchmarking on rectangular prisms. *Under review*, -:-, 2014.
- [112] Y. Nakamura and M. Nakashima. Vortex excitation of prisms with elongated rectangular,  $\vdash$  and  $\vdash$  cross-sections. *J. Fluid Mech.*, 163:149–169, 1986.